

Andrzej Sołtan Institute for Nuclear Studies

# Direct and Indirect Search for Dark Matter

Piotr Mijakowski

*Ph.D. thesis written under supervision  
of Prof. dr hab. Ewa Rondio*



February 2011



## Abstract

Direct and indirect searches for dark matter (DM) particles are discussed. The search for a diffuse signal from DM annihilation in the Milky Way is presented using the atmospheric neutrino data from Super-Kamiokande-I, -II, -III. The analysis focuses on the model independent scenario with DM particles annihilating directly into pairs of neutrinos and anti-neutrinos. No signal contribution is allowed by the Super-Kamiokande data for considered masses of DM particles in the range from 3 GeV to 3 TeV. The upper limit on DM-induced neutrino flux has been obtained as a function of the mass of relic particles. The corresponding limit on the DM self-annihilation cross section  $\langle\sigma_A V\rangle$  has been evaluated. With this analysis, the existing limit on the value of  $\langle\sigma_A V\rangle$  has been significantly improved for DM particle masses below 100 GeV as compared to previous constraints based on neutrino interactions data. Presented search can be also related to the concept of the decay of DM particles. The limit on DM decay lifetime  $\tau_{DM}$  has been derived. Finally, studies related to direct DM detection are presented. The results of simulations of neutron background for the Argon Dark Matter (ArDM) experiment are shown.



# Contents

<b>List of Figures</b>	<b>v</b>
<b>List of Tables</b>	<b>ix</b>
<b>List of Abbreviations</b>	<b>xi</b>
<b>Acknowledgements</b>	<b>xv</b>
<b>Introduction</b>	<b>1</b>
<b>1 Dark Matter</b>	<b>4</b>
1.1 Dark Matter in the Universe . . . . .	4
1.2 Standard Cosmological Model . . . . .	5
1.3 Dark Matter Candidates . . . . .	7
1.3.1 Neutralino – Supersymmetric Dark Matter Candidate . . . . .	8
1.4 Overview of WIMP Searches . . . . .	10
1.5 Direct Detection . . . . .	10
1.5.1 Status of Direct Detection Experiments . . . . .	12
1.6 Indirect Detection . . . . .	14
1.6.1 Status of Indirect Detection Experiments . . . . .	16
1.7 Summary of Dark Matter Searches . . . . .	18
<b>2 Neutrinos</b>	<b>20</b>
2.1 Introduction . . . . .	20
2.2 Neutrino Interactions with Matter . . . . .	20
2.3 Neutrino Oscillations . . . . .	25
2.3.1 Neutrino Oscillation Formalism . . . . .	26
2.4 Neutrino Sources . . . . .	28
2.4.1 Natural sources . . . . .	29
2.4.2 Artificial sources . . . . .	32
2.5 Atmospheric Neutrino Properties . . . . .	33
<b>3 Neutrinos from Dark Matter Annihilation</b>	<b>37</b>
3.1 Neutrinos from DM Annihilation in Earth, Sun and Galactic Center . . . . .	38
3.1.1 Results from Super-Kamiokande . . . . .	39
3.1.2 Comparison with Direct Detection Results . . . . .	42
3.2 Neutrinos from Diffuse Dark Matter Annihilation . . . . .	45
3.2.1 Galactic Neutrino Flux from Dark Matter Annihilation . . . . .	46

3.2.2	Limit on Dark Matter Self-Annihilation Cross Section . . . . .	51
3.2.3	Prospects for Dark Matter Diffuse Annihilation Search . . . . .	51
3.3	Neutrinos from Dark Matter Decay . . . . .	52
<b>4</b>	<b>Super-Kamiokande Detector</b>	<b>54</b>
4.1	Introduction . . . . .	54
4.2	Principle of Operation . . . . .	56
4.3	History . . . . .	60
4.4	DAQ Monitoring Software for SK-IV . . . . .	61
<b>5</b>	<b>Atmospheric Neutrinos at Super-Kamiokande</b>	<b>63</b>
5.1	Data Samples . . . . .	63
5.2	Data Selection . . . . .	67
5.3	Monte Carlo Simulation of Atmospheric Neutrino Interactions . . . . .	70
5.4	Monte Carlo Simulation of Tau Neutrino Interactions . . . . .	72
5.5	Atmospheric Neutrino Oscillation Analysis . . . . .	73
5.5.1	Livetime of Data Samples . . . . .	73
5.5.2	Fit . . . . .	73
5.5.3	Sources of systematic uncertainty . . . . .	76
5.5.4	Results . . . . .	76
<b>6</b>	<b>Methodology of Search for Diffuse Dark Matter Annihilation Signal</b>	<b>78</b>
6.1	Introduction . . . . .	78
6.2	Simulation of Diffuse Dark Matter Annihilation Signal . . . . .	79
6.3	Methodology . . . . .	84
6.4	Search for Low Energy Signal . . . . .	85
6.5	Search for High Energy Signal . . . . .	91
6.6	Upper Limit on Fitted Number of DM-Induced Neutrinos . . . . .	93
6.7	Summary . . . . .	96
<b>7</b>	<b>Search for Diffuse DM Annihilation Signal at Super-Kamiokande</b>	<b>97</b>
7.1	Diffuse Dark Matter Annihilation Search . . . . .	97
7.1.1	Data Sample . . . . .	98
7.1.2	Dark Matter Induced Signal . . . . .	98
7.1.3	Fit . . . . .	103
7.2	Fitted Number of Dark Matter Induced Neutrinos . . . . .	105
7.2.1	Upper Limit on DM-Induced Neutrinos . . . . .	107
7.3	Upper Limit on DM-Induced Neutrino Flux . . . . .	107
7.4	Limit on Dark Matter Lifetime . . . . .	109
7.5	Limit on Dark Matter Self-Annihilation Cross Section . . . . .	110
<b>8</b>	<b>Neutron Background Studies for ArDM</b>	<b>114</b>
8.1	Dark Matter Search with ArDM Detector . . . . .	114
8.1.1	Detector Description . . . . .	114
8.1.2	Experimental Background . . . . .	116
8.1.3	ArDM prospects . . . . .	117
8.2	Neutron Background Studies . . . . .	118
8.2.1	Rock Neutron Simulations for Canfranc . . . . .	119

8.2.2	Muon-Induced Neutron Simulations . . . . .	124
8.2.3	Conclusions on the neutron background studies for ArDM . . . . .	126
	<b>Summary and outlook</b>	<b>128</b>
	<b>Bibliography</b>	<b>130</b>

# List of Figures

1.1	Best fit power law $\Lambda$ CDM model as compared to the temperature of angular power spectrum measured by WMAP. . . . .	6
1.2	Comoving number density of a thermal relic particle in the early Universe. . . . .	7
1.3	Feynman diagrams which contribute to neutralino-quark scalar interactions (spin-independent). . . . .	9
1.4	Feynman diagrams which contribute to neutralino-quark axial vector interactions (spin-dependent). . . . .	9
1.5	Different ideas for DM particle detection. . . . .	10
1.6	Illustration of various detection methods of a recoil energy. . . . .	11
1.7	Annual modulation of a signal from DAMA experiment. . . . .	12
1.8	Upper limits on the value of spin-independent WIMP-nucleon cross section as a function of WIMP mass. . . . .	14
1.9	Gamma spectrum obtained in the analysis of EGRET data. . . . .	16
1.10	Positron fraction and antiproton to proton ratio measurements in the cosmic rays by PAMELA. . . . .	17
1.11	Energy spectrum of $(e^+ + e^-)$ obtained by ATIC . . . . .	18
1.12	The FERMI LAT cosmic ray electron spectrum and gamma spectrum . . . . .	19
2.1	Ratio of total charged current neutrino cross section and neutrino energy $(\sigma_T/E_\nu)$ for the muon neutrinos and anti-neutrinos interacting on nucleons as a function of neutrino energy. . . . .	21
2.2	Examples of interactions involving neutrinos. . . . .	22
2.3	Relation between direction of a charged lepton produced in neutrino interaction and direction of a parent neutrino. . . . .	23
2.4	Contribution from different processes to charged current $\nu_\mu$ interactions as a function of neutrino energy. . . . .	24
2.5	Energy spectra and fluxes of neutrinos at the surface of the Earth calculated for different neutrino sources. . . . .	30
2.6	Schematic view of neutrinos' creation in the atmosphere. . . . .	31
2.7	Atmospheric neutrino energy spectrum for $(\nu_\mu + \bar{\nu}_\mu)$ and flux ratio of $(\nu_\mu + \bar{\nu}_\mu)$ to $(\nu_e + \bar{\nu}_e)$ . . . . .	34
2.8	The flux of atmospheric neutrinos versus zenith angle calculated for Kamioka Observatory location for several neutrino energies. . . . .	35
3.1	Illustration of a cone half-angle $\Phi$ used to investigate the value of neutrino flux from a given angular region around the position of DM annihilation source. . . . .	39

3.2	Zenith angle distributions of upward through-going muons at Super-K based on 1679.6 live days of exposure. Distributions with respect to the center of the Earth (a), the Sun (b) and the Galactic Center (c) are shown.	40
3.3	Super-Kamiokande DM-induced upward-going muon flux limits as a function of $M_\chi$ for neutralino annihilations in the Earth's core (a), the Sun's core (b) and in the Galactic Center (c).	41
3.4	Upper limit on WIMP-nucleon cross section for spin-independent interactions obtained in the analysis of upward-going muon events at Super-Kamiokande.	43
3.5	Upper limit on WIMP-nucleon cross section for spin-dependent interactions obtained in the analysis of upward-going muon events at Super-Kamiokande.	44
3.6	Illustration of expected signal from the diffuse annihilation of a 100 GeV DM particle.	45
3.7	Dark matter density as a function of radius for different halo profiles considered.	47
3.8	Illustration of line of sight $l$ and viewing angle $\psi$ in the coordinate system related to the Galactic Center.	48
3.9	Line of sight integration $\mathcal{J}(\psi)$ as a function of the pointing angle $\psi$ with respect to the Galactic Center and its average, $\mathcal{J}_{\Delta\Omega}$ , inside a cone with half-angle $\psi$ around the GC as a function of the visible fraction of the whole sky.	50
3.10	Upper limit on the DM total self-annihilation cross section $\langle\sigma_AV\rangle$ from various components of the Milky Way halo from Ref. [90].	52
4.1	A schematic view of the Super-Kamiokande detector and the experimental hall.	55
4.2	Construction of the wavefront of Cherenkov radiation.	56
4.3	Inside view of the Super-Kamiokande detector during the maintenance in 2006 and illustration of Cherenkov ring produced in a charged current $\nu_e$ interaction in water.	57
4.4	An example event display of a single-ring $\mu$ -like and e-like events.	58
4.5	Particle identification likelihood distribution (PID).	59
4.6	<i>Skhist</i> application window.	62
5.1	The simulated parent neutrino energy distributions for the fully-contained, partially-contained, upward stopping muon and upward through-going muon event samples of atmospheric neutrinos.	66
5.2	The number of hits in the largest outer detector cluster (nhitac).	68
5.3	An example of event display of partially-contained and upward through-going muon events.	69
5.4	The illustration of the zenith angle and momentum distributions of the data samples used in the neutrino oscillation analysis.	75
5.5	Best fit contour for the values $\Delta m_{23}^2$ and $\sin^2 2\theta_{23}$ oscillation parameters in the 2 flavor analysis of SK-I+II+III data.	77
6.1	Number of events in atmospheric neutrino Monte Carlo as a function of true neutrino energy.	80

6.2	Zenith angle distribution of simulated $\nu_\mu$ , $\bar{\nu}_\mu$ , $\nu_e$ , and $\bar{\nu}_e$ atmospheric neutrinos of the energy of 4 GeV. . . . .	81
6.3	The ratio of the charged current $\nu_\tau$ cross section to $\nu_\mu$ cross section a function of neutrino energy. . . . .	83
6.4	The zenith angle distributions of a $\nu_\tau\bar{\nu}_\tau$ signal from annihilation of 10 GeV DM particle as seen in SK data samples. . . . .	84
6.5	Zenith angle distribution of SK-I PC events. . . . .	86
6.6	Visible energy distribution of SK-I PC events. . . . .	87
6.7	Zenith angle distribution (left panel), visible energy distribution (middle panel) of SK-I PC events and resulting $\chi^2$ contour (right panel) of a fit of $\alpha$ and $\beta$ parameters to the zenith and visible energy distributions. . . . .	88
6.8	Simultaneous fit of the signal from annihilation of 5.6 GeV DM particle to PC and FC samples. . . . .	89
6.9	Fitted number of DM-induced ( $\nu_\mu + \bar{\nu}_\mu$ ) events for various masses of relic particles considered in the search. . . . .	90
6.10	Visible energy distribution of SK-I PC (left plot) and SK-I FC (right plot) events for various DM particle masses. . . . .	91
6.11	The zenith angle distributions of UPMU stopping and through-going events for SK-I. . . . .	92
6.12	90% CL upper limit on the number of DM-induced ( $\nu_\mu + \bar{\nu}_\mu$ ) events in SK-I	93
6.13	Calculation of an upper limit for the values in the unphysical region [115].	94
6.14	Application of the Bayesian scheme shown in Fig. 6.13 to the case of Gaussian $f(\hat{\alpha} \alpha)$ . . . . .	95
7.1	Illustration of a signal from annihilation of 5.6 GeV DM particle in SK data samples. . . . .	99
7.2	Illustration of a signal from annihilation of 1.3 GeV DM particle in SK data samples. . . . .	101
7.3	Illustration of a signal from annihilation of 20 GeV DM particle in SK data samples. . . . .	101
7.4	Illustration of a signal from annihilation of 40 GeV DM particle in SK data samples. . . . .	102
7.5	[Illustration of a signal from annihilation of 130 GeV DM particle in SK data samples. . . . .	102
7.6	Illustration of a fit for a signal from annihilation of 90 GeV DM particle. .	104
7.7	Fitted number of ( $\nu_\mu + \bar{\nu}_\mu$ ) events from DM annihilation per 1000 days of exposure of Super-Kamiokande detector. . . . .	105
7.8	Number of ( $\nu_\mu + \bar{\nu}_\mu$ ) events from DM annihilation obtained in the <i>global approach</i> (blue points), in the <i>simplified approach</i> described in Chapter 6, Fig. 6.10 (red points) and in the fit without systematic uncertainty terms (green points). . . . .	106
7.9	Upper limit on the number of ( $\nu_\mu + \bar{\nu}_\mu$ ) from DM annihilation per 1000 days.	108
7.10	Upper limit on DM-induced neutrino flux. . . . .	109
7.11	Lower limit on DM lifetime. . . . .	110
7.12	Upper limit on DM self-annihilation cross section $\langle\sigma_A V\rangle$ . . . . .	111
8.1	Principle of operation of the ArDM detector. . . . .	115

8.2	Schematic view of the ArDM detector and its main components. . . . .	116
8.3	Event rates expected in ArDM. . . . .	117
8.4	Energy spectra of neutrons produced in the rock and obtained at the walls of the Boulby laboratory. . . . .	120
8.5	Illustration of the geometry included in the simulation of neutrons related to radioactivity in the rock of the Canfranc laboratory. . . . .	120
8.6	Illustration of the simulated polyethylene shield setup for the ArDM detec- tor and example of an event display of a neutron related to radioactivity in the rock. . . . .	121
8.7	The positions of the hits of neutrons on the detector external container for the two considered configurations of the shield setup: (a) with holes and (b) without holes. . . . .	123
8.8	Energy spectrum of neutrons related to radioactivity in the wall of the experimental hall while they enter the external detector container after passing a shield. . . . .	124
8.9	Average number of neutrons produced by a muon per unit path length (1/g/cm <sup>2</sup> ) in scintillator as a function of muon energy. . . . .	125
8.10	Results of the simulation of a neutron production by muons in the rock as a function of muon energy. . . . .	126
8.11	Energy spectrum of neutrons produced by muons and distance of a neutron production point from muon trajectory . . . . .	127

# List of Tables

1.1	Spectrum of particles and fields in the MSSM. . . . .	8
3.1	Parameters of DM halo models. . . . .	47
3.2	Estimation of the various signal intensity factors for different DM halo models. . . . .	49
5.1	Classification of the Super-Kamiokande atmospheric neutrino data samples.	65
5.2	Reduction efficiency for each category of events in SK-I, SK-II and SK-III.	71
5.3	Livetime of SK-I, SK-II and SK-III data sets. . . . .	73
6.1	Number of observed events in atmospheric MC (SK-I+II+III) and tau MC (SK-I+II+III) sets. . . . .	82
6.2	Fraction of $\nu_\tau\bar{\nu}_\tau$ events contributing to Multi-GeV and Multi-Ring e-like samples. . . . .	83
8.1	Summary of the simulation of neutrons related to radioactivity in the rock of the new Canfranc hall. . . . .	122

# List of Abbreviations

<b>AGN</b>	Active Galactic Nuclei
<b>AMANDA</b>	Antarctic Muon and Neutrino Detector Array
<b>ArDM</b>	Argon Dark Matter
<b>ATIC</b>	Advanced Thin Ionization Calorimeter
<b>CC</b>	Charged Current
<b>CDM</b>	Cold Dark Matter
<b>CDMS</b>	Cryogenic Dark Matter Search
<b>CL</b>	Confidence Level
<b>CMB</b>	Cosmic Microwave Background
<b>CNGS</b>	CERN Neutrinos to Gran Sasso
<b>CoGeNT</b>	Coherent Germanium Neutrino Technology
<b>DM</b>	Dark Matter
<b>DAMA</b>	Dark Matter Search Experiment
<b>EGRET</b>	Energetic Gamma Ray Experiment Telescope
<b>DAQ</b>	Data Acquisition
<b>FC</b>	Fully-contained
<b>FERMI-LAT</b>	Fermi Large Area Telescope
<b>GC</b>	Galactic Center
<b>GPS</b>	Global Positioning System

<b>HE</b>	High Energy
<b>HV</b>	High Voltage
<b>ID</b>	Inner Detector
<b>K2K</b>	KEK to Kamioka
<b>LE</b>	Low Energy
<b>LAr</b>	Liquid argon
<b>LEM</b>	Large Electron Multiplier
<b>LEP</b>	Large Electron-Positron Storage Ring
<b>LSP</b>	Lightest Supersymmetric Particle
<b>MACRO</b>	Monopole and Cosmic Ray Observatory
<b>MC</b>	Monte Carlo
<b>MSSM</b>	Minimal Supersymmetric Model
<b>MW</b>	Milky Way
<b>NC</b>	Neutral Current
<b>NDF</b>	Number of Degrees of Freedom
<b>NUMI</b>	Neutrinos at the Main Injector
<b>OD</b>	Outer Detector
<b>PAMELA</b>	Payload for Antimatter Matter Exploration and Light-nuclei Astrophysics
<b>PC</b>	Partially-contained
<b>PMT</b>	Photomultiplier
<b>ppb</b>	parts per billion
<b>SK or Super-K</b>	Super-Kamiokande
<b>SUSY</b>	Supersymmetry

**T2K** Tokai to Kamioka  
**UPMU** Upward-going Muon  
**VUV** Vacuum Ultraviolet (wavelength below 200 nm)  
**WIMP** Weakly Interacting Massive Particle



# Acknowledgements

I would like to cordially thank my supervisor, prof. Ewa Rondio, for a lot help and guidance which I have received from her during my Ph.D. studies. I could always count on her exceptional advice and encouragement during preparation of this thesis. I want to thank prof. Danuta Kielczewska who also supervised my work and help me a lot with my studies. Without the support of Ewa and Danka this thesis would have never come into existence. Thank you!

I am grateful to prof. Edward Kearns who has given me opportunity to work in a wonderful experiment and in the interesting field of dark matter search. I would also like to thank prof. Henry Sobel who supported my stays in Japan making my work for the Super-Kamiokande possible.

I am grateful to prof. Andre Rubbia who has given me a chance to work in another great experiment. My adventure with particle physics and dark matter started with the ArDM.

I would like to express my greetings to dr Roger Wendell for all the advices, help and discussions regarding details of the SK experiment and analyses of its data. And I feel indebted to him for the Osc3++/ package he has developed, it is worth millions!

During my stays in Japan and work for the experiment I have received help from many people. I am especially grateful to dr Shunichi Mine, dr Michael Smy, and prof. William Kropp for their help to arrange things.

I received a lot of help from dr Jennifer Raaf who was patiently answering all of my questions regarding the experiment and from dr Fanny Dufour who was educating me on the data selection process. I would also like to thank other members of the data reduction groups: prof. Shigetaka Moriyama, prof. Kate Scholberg, dr Naho Tanimoto.

I want to thank prof. Yoshihisa Obayashi for a guidance on the DAQ software development.

I am also grateful to prof. Masato Shiozawa and prof. Chris Walter for a helpful discussions during our analysis group meetings. For the same reason I am also indebted to members of Warsaw Neutrino Group, especially to prof. M. Szeptycka and dr Tadeusz Kozłowski. I also thank prof. John Beacom for providing a conceptual impulse for my analysis and exchanging with me opinions regarding obtained results.

I would like to pass cheers to Paweł Przewłocki, Magda Posiadała, Beata Brzozowska, Robert Sulej, Tomek Palczewski and Justyna Łagoda for having fun together during work and studies at our Institute.

My cheers go also to all my Japanese and American colleagues with whom I have a great time while being in Japan and US.

This work has been supported by the State Committee for Scientific Research in Poland, grant N N202 175735.



# Introduction

The present understanding of the Universe suggests that more than 73% of its mass is in the form of dark energy, about 23% is non-baryonic, non-relativistic dark matter (DM) and only a remaining fraction, below 4%, is ordinary baryonic matter with a very little amount of antimatter [1, 2]. What forms the unknown dark energy and dark matter component is the most important missing piece in our understanding of the Universe. Revealing its nature is a challenging goal of contemporary particle physics and astrophysics.

Theoretical explanation of DM origin usually requires mechanisms going beyond the Standard Model. Dark matter presumably comprises a new type of an elementary particle. One of the commonly mentioned candidates is referred to as the Weakly Interacting Massive Particle (WIMP). That is a collective name describing a particle which is massive (expected mass ranging from several tens of GeV to several TeV); interacts only via the weak and gravitational force; interacts very rarely with baryons; and is abundant in the Universe [1]. The lightest supersymmetric particle (LSP), usually referred to as neutralino ( $\chi$ ), is a very promising WIMP candidate [2]. It is promising in terms of observation possibilities at future and ongoing experiments. There are worldwide efforts aiming to detect these particles in experiments searching for their existence in the Universe as well as trying to produce them in collisions of high energy particles.

In the following thesis, the search for DM particles such as neutralinos is described. However, the discussion presented here would be valid also for any other dark matter candidate with the same phenomenology as neutralino. The term DM particle is being interchangeably used throughout the thesis with a term WIMP, neutralino, or a relic particle. The convention of expressing momenta and masses of particles in units of energy is adopted (assuming system of natural units,  $\hbar = c = k_B = 1$ ).

The material presented in the thesis is related to two different approaches to the search for DM particles: (1) direct detection of DM particles scattering off nuclei in the detector and (2) indirect detection which aims at observation of products of DM annihilation or decay. The author has been involved in two projects searching for dark matter in the Universe: direct detection experiment Argon Dark Matter (ArDM) [3], and Super-Kamiokande (also SK or Super-K) where dark matter can be investigated indirectly [4, 5].

The author's activities in the ArDM concerned Monte Carlo simulations of interactions and propagation of neutrons. The observed signal from interactions of neutrons in the detector is expected to be the main background for the WIMP-induced signal. Therefore, it is important to investigate sources of neutrons and to estimate the event rate of this background particles in the experiment. The author started work for the ArDM in 2004, during a preparation of his M.Sc. thesis. He contributed to the development of the detector's simulation, studies of neutron interactions in liquid argon (LAr) and to simulations related to various sources of a neutron background. He partially continued this activities

during Ph.D. studies which started at the end of 2005.

After the delay of the ArDM detector installation at the Canfranc laboratory, the data for DM search were not expected to be available within the time scale of this thesis. Therefore, the author started to work on the analysis of the data from the Super-Kamiokande experiment, where he took responsibility for a search for diffuse signal from DM annihilation in the Milky Way. The outcome of this study is the main result presented in the thesis.

The author joined the Super-K collaboration in 2007. He contributed to the experiment in various ways. He developed an *online* software which is used to monitor the quality of recorded data. This application has been used during shifts at the detector since 2008. It helps to control trigger rates and other variables related to status of the realtime data. Second service task for the experiment concerned the selection of neutrino interaction events in SK data (selection of partially-contained events). That required also an evaluation of the corresponding systematic uncertainties and preparation of the official data sets for the collaboration. In 2006, before becoming a SK collaborator, the author took part in the reconstruction work at the detector, and contributed to the installation of new photomultiplier tubes.

The main author's activity in the Super-Kamiokande collaboration has been related to the search for a diffuse DM annihilation signal using neutrino data collected with the detector from 1996 to 2008. The other type of DM analysis, where one is investigating the Earth's core, the Sun and the region of the Galactic Center as potential sources of DM-induced neutrinos, has been conducted at the same time by his Japanese colleague. The author has been reporting the progress of his work on a regular basis at the SK collaboration meetings and on numerous meetings of the analysis group. He also presented the preliminary results of this analysis as posters at the 31st International Cosmic Ray Conference held in Łódź in 2009 and at the 24th International Conference on Neutrino Physics and Astrophysics in Athens in 2010. The publication of the final results is planned.

In addition to work for the ArDM and the Super-Kamiokande collaborations, the author has been an active member of the T2K collaboration [6]. He performed a simulation of propagation and interactions of muons at the shallow underground location of the ND280 which is a near detector of T2K [7]. Muons are produced in the atmosphere in showers initiated by cosmic rays and therefore are often referred to as cosmic ray muons. Using the information on their flux, energy and angular characteristics, the author developed a simulation of a cosmic ray muon propagation underground for the ND280 geometry. These studies enabled to evaluate the rate of muons at the near detector station and to determine the requirements for a cosmic ray trigger.

The thesis starts with an overview of dark matter concept in Chapter 1. The evidences for DM existence are discussed there as well as expected properties of DM particles and strategies for their detection. As the search for DM signal presented in this thesis is based on neutrino data, Chapter 2 contains an overview of neutrino interactions, oscillations and sources of neutrinos in nature. In Chapter 3, the results of current searches for DM-induced neutrinos are shown. This chapter contains also the discussion on the expected DM distribution in the Milky Way. Chapter 4 contains SK detector description. The principle of operation of a water Cherenkov detector is explained there. In Chapter 5, it is discussed how the SK data are categorized into different samples based on the topology of observed events. It is also explained how the collected data are modeled using Monte Carlo simulations. Later, it is shown how the data and Monte Carlo samples

---

are used in the search for oscillation effect of neutrinos produced in the atmosphere. The oscillation analysis presented there is based on the results published by the collaboration. The similar methodology in case of the oscillation analysis is applied later in the search for dark matter signal which is presented in the next chapters. Chapters 6 and 7 show the diffuse DM search analysis conducted by the author. The goal of Chapter 6 is to explain the method of the analysis – results presented there are based on a limited number of SK data samples and sources of systematic uncertainty are not addressed at this stage. The purpose is to test the capacity of SK data for a potential signal contribution and to understand the analysis procedure. Chapter 7 contains the final results of the search for diffuse DM annihilation signal using all available information on the SK data. It has been found that no signal contribution is allowed by the Super-Kamiokande data for the considered masses of DM particles in a range from 3 GeV to 3 TeV. Therefore, the corresponding limits on DM-induced neutrino flux and DM self-annihilation cross section  $\langle\sigma_A V\rangle$  have been derived as a function of mass of relic particles <sup>1</sup>. With these results, existing limit on the value of  $\langle\sigma_A V\rangle$ , presented at the end of Chapter 3, has been improved. This analysis is recognized by the Super-Kamiokande collaboration as official and its results are being currently shown at conferences. Chapter 8 concerns the ArDM experiment and simulations of a neutron background. That is a separate material which shows the results of author's work related to estimation of the requirements for a neutron shield of the ArDM detector. Some considerations regarding production of neutrons by muons are also presented. Finally, in the last chapter (Summary and outlook), most important results obtained in this thesis are listed and discussed in the context of the current knowledge and plans of the DM searches.

---

<sup>1</sup> $\langle\sigma_A V\rangle$  stands for a cross section for DM annihilation averaged over the relative velocity of annihilating particles. It is expected that root mean square of the DM velocity distribution in the galactic halos is at the level of 1/1000 of a speed of light.

# Chapter 1

## Dark Matter

There is compelling evidence that ordinary baryonic matter composes only 4% of the matter in the Universe. The rest is dominated by dark energy (73%) and dark matter (23%) components of unknown nature [1, 8]. Various astrophysical observations indicate the presence of the large cosmological dark matter structures in the Universe [8, 10, 11, 12, 13, 14]. It is also reported that dark matter forms a non-luminous halo surrounding galaxies [16, 17, 18]. It is expected that dark matter is composed of a new type of elementary particle [1, 2]. Understanding of its nature is a key issue in the contemporary particle physics.

### 1.1 Dark Matter in the Universe

Dark matter has manifested its presence so far only via gravitational interactions with surrounding baryonic matter. Due to large abundance it seems to influence evolution of the Universe. Its existence can be derived from the following observations:

- Motion of the galaxies – The problem of invisible matter component in the Universe, was first raised by F. Zwicky in 1933 based on the observation of the velocities of galaxies in the Coma cluster [11]. The observed motions of galaxies could not be explained by taking into account only the visible mass which is proportional to light emitted by stars. Observed velocities were too high and only the presence of the unknown, invisible matter component could explain the fact that investigated system is gravitationally bound.
- Rotational speeds of galaxies – The distribution of the radial velocities of the galactic components as a function of distance from the galaxy center is not in agreement with the expectation based on distribution of visible mass in the galaxies [10]. It indicates that some additional, invisible mass is present in there. It is distributed uniformly and reaching even beyond visible size of the galactic disks.
- Gravitational lensing – Dark matter existence could be inferred from observations of the galactic clusters, like the *Bullet Cluster* [19]. The total mass contained in the observed region can be derived based on the gravitational lensing effect and is not in agreement with the evaluation based on the visible components. This technique has been also used to create first 3 dimensional maps of DM distribution in the cosmic space [20].

- Cosmic Microwave Background (CMB) – Measurements of the CMB help to derive the value of the total mass-energy contained in the Universe and contribution to this mass of various matter components by studying anisotropies in the distribution of matter at the stage of early Universe. According to this observation the total contribution of matter to the mass-energy of the Universe is at the level of 23%, the contribution of the baryonic matter is around 4% [8]. That issue is discussed more in Section 1.2.
- Nucleosynthesis models – In this models one can indirectly constrain the baryonic contribution to the total mass contained in the Universe. Based on the measurements of light elements in cosmic rays, the abundance of all elements and particles in the Universe can be derived [13].
- Evolution of large cosmic structures – Dark matter seems to be necessary in the simulations of formation of the large scale structures [14]. It catalyzes the formation of the galaxies by attraction of baryonic matter to some regions in the cosmic space.

## 1.2 Standard Cosmological Model

Standard Cosmology is based on the assumptions that the Universe evolved from a state of infinitely hot and infinitely dense matter. That process has been named the Big Bang and is one the most famous concepts of science. The large scale structure of the Universe is determined by gravitational interactions, and it is assumed that the Universe is homogenous and isotropic at very large scales. The geometry of the Universe depends on the amount of mass-energy. Detailed description of the Big Bang cosmology model can be found in Ref. [15].

Cosmological model assumes that there were small deviations from homogeneity and structures in the Universe were formed by gravitational agglomeration around these perturbations. Density fluctuations can be probed using observations of cosmic microwave background anisotropies, gravitational lensing, gas clouds which absorb quasar light (called Lyman- $\alpha$  forest) over a wide range of scales and redshifts. These density perturbations are characterized by a power spectrum which describes the fluctuations in the CMB [8].

The measurement of a power spectrum using the latest CMB data from the WMAP experiment and based on other astrophysical observations allows to determine values of cosmological parameters such the total mass-energy content of the Universe  $\Omega_{tot}$ , the density of dark matter  $\Omega_\chi$ , the density of baryons  $\Omega_b$ , the density of dark energy  $\Omega_\Lambda$ , the expansion rate of the universe  $H$  (Hubble constant) *etc.*. Density of these various matter-energy components is expressed in units of the critical density,  $\rho_{crit}$ , which is defined as a density of the Universe for which it is spatially flat. The results indicate that the value of  $\Omega_{tot} = \rho_{tot}/\rho_{crit} = 1$ . Density of baryons (fraction of the critical density made up of baryons) has been estimated as  $4.55 \pm 0.3\%$  of the  $\rho_{crit}$ . [8]. The dark matter contribution  $\Omega_\chi = 22.8 \pm 3\%$  of  $\rho_{crit}$ , and the density attributed to dark energy  $\Omega_\Lambda = 72.7 \pm 3\%$  [8].

The remarkable agreement of various astrophysical measurements has led to the concordance model, referred to as Lambda Cold Dark Matter model ( $\Lambda$ CDM). Its predictions fit the measurements of the power spectrum (compare Fig. 1.1) and determine properties of the Universe. Dark energy component can be interpreted as a cosmological constant and causes the Universe to accelerate due to negative pressure. Dark matter should

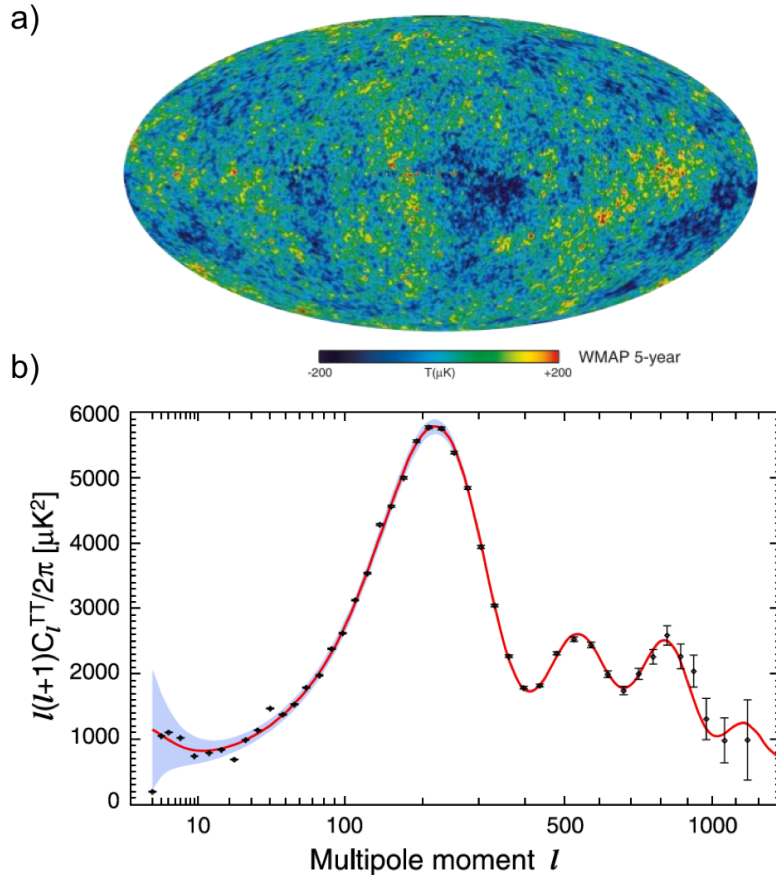


Figure 1.1: (a) The map of the anisotropies in the Cosmic Microwave Background temperature spectrum as observed by the WMAP satellite [9]. Colors represent the relative change of temperature with respect to 2.7 K (red color indicates warmer regions, blue color colder areas). (b) Best fit power law  $\Lambda$ CDM model as compared to the temperature of angular power spectrum measured by WMAP [8]. The results are shown as a function of multipole moment of the spectral functions that are used to quantify the angular size of the fluctuations observed by WMAP and shown in (a).

be composed of some relic particles which had non-relativistic velocities when galaxies were formed (Cold Dark Matter).

According to the thermal models of the Universe evolution, it can be shown that stable, massive and weakly interacting particles should give the expected contribution to  $\Omega_\chi$  [2]. If one considers a particle with a mass  $M_\chi$  which is in thermal equilibrium in the early Universe, the evolution of its numerical density ( $n_\chi$ ) is governed by Fermi-Dirac or Bose-Einstein distribution (depending on whether it is a fermion or a boson). The equilibrium is maintained by this particle through annihilation into lighter particles and its creation in interaction of other particles. As the temperature of the Universe decreases during expansion, at a certain point these relic particle ceases to annihilate, and its co-moving equilibrium abundance freezes and it drops out of the thermal equilibrium. This happens sooner if the value of the self-annihilation cross section of these particles  $\langle\sigma_A V\rangle$  is very weak as then the balance between annihilation and creation of relic particles cannot be maintained any longer. The  $\langle\sigma_A V\rangle$  is the thermal average of the dark matter pair annihilation cross section times their relative velocity. When a calculation is done for a

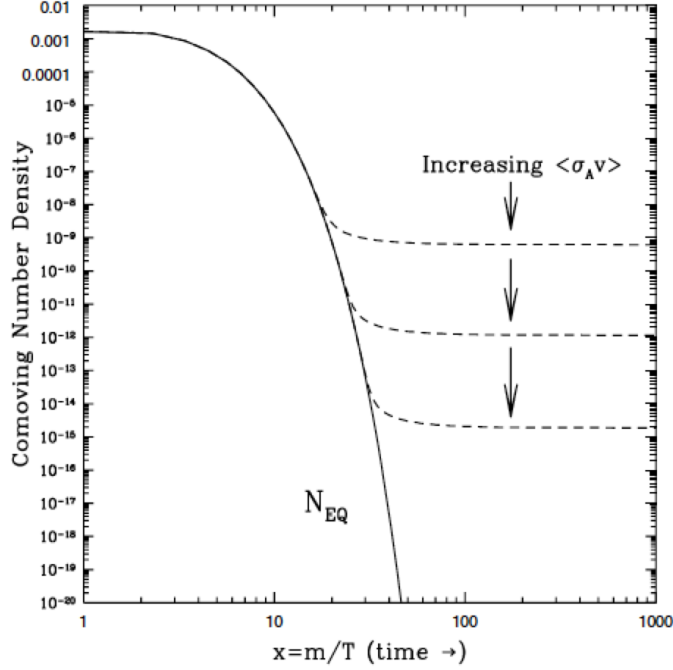


Figure 1.2: Comoving number density of a thermal relic particle in the early Universe. The dashed curves indicate the expected abundance, and the solid curve is the equilibrium abundance [21].

relic particle with a weak-scale interactions, the particle drops out of thermal equilibrium at non-relativistic velocities and its relic abundance is just about the same as expected for cold dark matter. The evolution of number density is shown in Fig. 1.2 as a function of  $M_\chi/T$ . The resulting density of relic particles after "freeze-out" is given by [21]:

$$\Omega_\chi h^2 = \frac{M_\chi n_\chi}{\rho_c} \cong \left( \frac{3 \times 10^{-27} \text{cm}^3 \text{s}^{-1}}{\langle\sigma_A V\rangle} \right), \quad (1.1)$$

where  $h$  is the Hubble constant scaled by 100 km/s/Mpc. In the first approximation, the relic abundance is independent of the relic particle mass and mainly depends on the DM self-annihilation cross section  $\langle\sigma_A V\rangle$ . Because, the value of  $\Omega_\chi h^2$  (physical dark matter density) measured by WMAP is  $0.11 \pm 0.05$  [8], this leads to the conclusion that the DM self-annihilation is required to be  $\langle\sigma_A V\rangle \approx 3 \times 10^{-26} \text{cm}^3 \text{s}^{-1}$ .

### 1.3 Dark Matter Candidates

The main candidate for a cold dark matter particle is a Weakly Interacting Massive Particle (WIMP). That is a collective name describing neutral stable particles with masses of around hundreds of GeV which are predicted to have electro-weak scale cross sections for interactions with matter [1, 2]. It is a remarkable coincidence that such relic particles have just the relevant abundance and decoupling temperatures to be a cold dark matter. One of the most popular WIMP candidates which is considered in the community is provided by the Supersymmetry (SUSY) theory. That is a lightest supersymmetric particle (LSP), namely neutralino ( $\chi$ ).

Table 1.1: Spectrum of particles and fields in the MSSM.

Standard Model particles		SUSY partners	
Symbol	Name	Symbol	Name
$u, c, t$	up-quarks	$\tilde{q}_u^1 \dots \tilde{q}_u^6$	up squarks
$d, s, b$	down-quarks	$\tilde{q}_d^1 \dots \tilde{q}_d^6$	down squarks
$e, \mu, \tau$	leptons	$\tilde{l}^1 \dots \tilde{l}^6$	sleptons
$\nu_e, \nu_\mu, \nu_\tau$	up-quarks	$\tilde{\nu}_1 \dots \tilde{\nu}_3$	sneutrino
$g$	gluon	$\tilde{g}$	gluino
$W^\pm$	W boson		
$H^\pm$	charged Higgs boson	$\chi_1^\pm, \chi_2^\pm$	charginos
$B$	B-field (photon)	$\tilde{B}$	bino
$W^3$	$W^3$ -field ( $Z^0$ )	$\tilde{W}^3$	wino
$H_1^0, H_2^0, H_3^0$	Higgs bosons	$\tilde{H}_1^0, \tilde{H}_2^0$	higgsinos

The nature of the neutralino in the context of the SUSY is discussed further in this section. At this point, it shall be mentioned that neutralinos are not the only considered candidates for the dark matter particle. For example, neutrinos were considered a good DM particle candidate since it has been proven that they have mass. As neutrinos are abundant in the Universe there would be no need to invent new type of particle in order to have a candidate. However, neutrinos were excluded from being a dark matter because they were relativistic at the time of the Universe formation and would prevent structure formation.

Axions, introduced in an attempt to solve the problem of CP violation in particle physics, have been also often discussed as candidates well motivated by theory. Axions are expected to interact extremely weakly with ordinary particles, which implies that they were not in thermal equilibrium in the early universe. Moreover, if they are forming a relic remnant they have to be very abundant as their expected mass is in the range  $10^{-6} - 3 \cdot 10^{-2}$  eV [24]. The searches for these particles are ongoing [24].

There are also other exotic DM candidates like WIMPzillas, Kaluza-Klein Dark Matter, Mirror Dark Matter, or self Interacting Dark Matter. Their overview can be found elsewhere, e.g. [1, 25].

### 1.3.1 Neutralino – Supersymmetric Dark Matter Candidate

Supersymmetry is widely considered extension to the Standard Model of particle physics. Details on that theory can be found in Ref. [2].

SUSY assumes that for each known particle a *supersymmetric* partner particle exists, referred to as sparticle. Sparticles would have spin different than particles by  $1/2$ . Therefore, sfermions would be bosons and sbosons would be fermions. The spectrum of *supersymmetric* particles which is introduced in one of the simplest SUSY models, Minimal Supersymmetric Standard Model (MSSM), is shown in Table 1.1. The MSSM contains two Higgs doublets needed to give mass to up and down squarks. There two squarks for each quark. The superpartners of the  $W$  and charged Higgs bosons, the charged higgsino and gaugino, mix after electro-weak symmetry breaking and create two mass eigenstates which

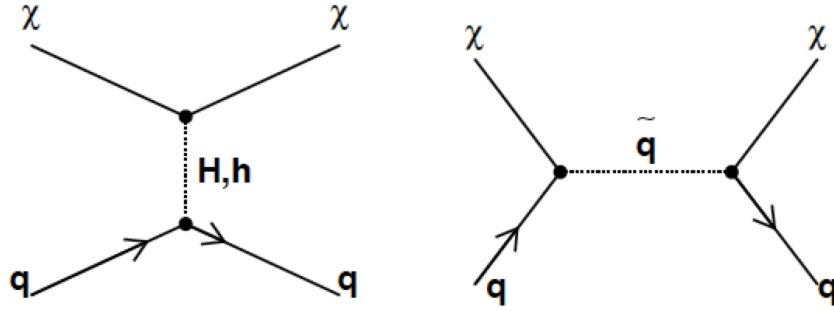


Figure 1.3: Feynman diagrams which contribute to neutralino-quark scalar interactions (spin independent) [2].

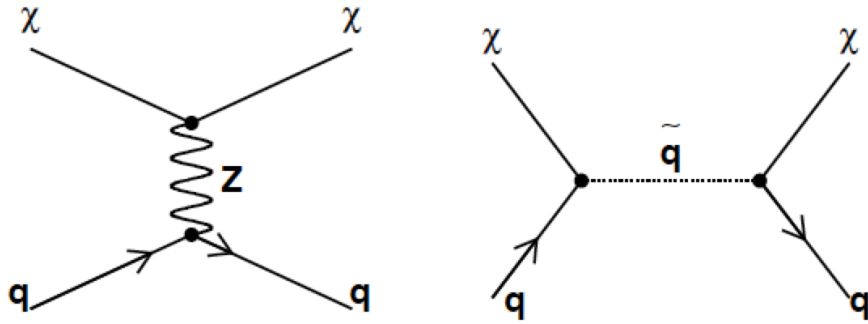


Figure 1.4: Feynman diagrams which contribute to neutralino-quark axial vector interactions (spin dependent) [2].

are called charginos ( $\chi^\pm$ ). The same thing happens for the superpartners of the photon,  $Z$  boson, and two neutral Higgs bosons. The following fields are produced:  $\tilde{B}$  (photino),  $\tilde{W}^3$  (wino) and  $\tilde{H}_1^0, \tilde{H}_2^0$  (higgsinos). These fields create 4 mass eigenstates called neutralinos:

$$\tilde{\chi} = a_1 \tilde{B} + a_2 \tilde{W}^3 + a_3 \tilde{H}_1^0 + a_4 \tilde{H}_2^0. \quad (1.2)$$

The lightest neutralino is most likely the LSP and is considered the best motivated WIMP candidate. The LSP is stable in the MSSM because theory contains a multiplicatively conserved quantum number called  $R$ -parity (which serves to prevent rapid proton-decay). The value of  $R$  is -1 for sparticles and 1 for particles. The LSP has to be stable since it can no longer decay into lighter SUSY particles and neither it can decay into particles from the Standard Model only (due to  $R$ -parity conservation).

The limits on the neutralino mass ( $M_\chi$ ) depend on the model assumed for the SUSY breaking, constraints from searches for sparticles at LEP  $e^+e^-$  and Tevatron hadron colliders, and are based on the cosmological considerations. The lower limit for  $M_\chi$  is around 7-10 GeV and can be derived from searches for *supersymmetric* particles at accelerators [22]. The upper limit on neutralino mass, from cosmology, is approximately 7 TeV [23]. These limits should be considered as a general indication of scale of WIMP masses as vari-

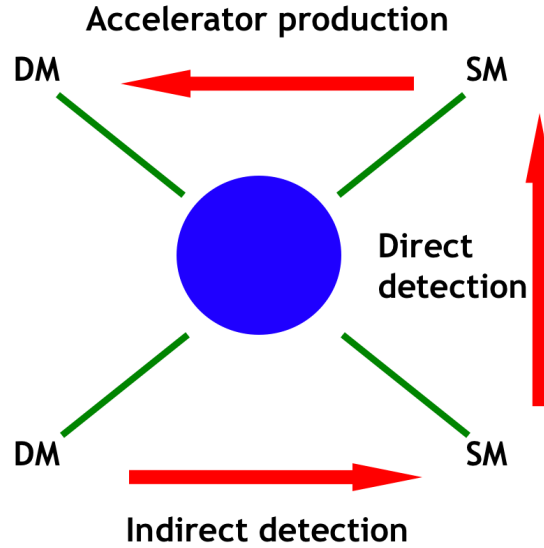


Figure 1.5: Drawing resembling a Feynman diagram which illustrates different ideas for DM particle detection. Depending on the direction of the time axis, different type of a search can be recognized. SM stands for the Standard Model particle, DM for the dark matter particle.

ation of the SUSY and Universe evolution models can yield slightly different constraints.

Neutralinos are expected to have only the electroweak scale interactions with ordinary matter. One could distinguish two types of their interactions: spin-dependent (SD) and spin-independent (SI) [2]. In the first case  $\chi$  couple to the spin of the target nucleus (axial vector interactions). That is mainly the case for neutralino interactions with nuclei which have odd number of nucleons (spin is unpaired). In case of spin-independent reactions WIMPs couple to the mass of the target nucleus (scalar interactions). Figures 1.3, 1.4 show the corresponding Feynman diagrams for these interactions.

## 1.4 Overview of WIMP Searches

There are ongoing worldwide efforts aimed to detect dark matter particles. Three main strategies for a search of WIMPs can be recognized: (1) direct detection experiments, designed to observe interactions of DM particles which are expected to scatter off nuclei in the detectors; (2) searches for DM and associated *supersymmetric* particles at accelerators; (3) indirect detection experiments in which products of DM annihilation (or decay) such as gamma rays, neutrinos, positrons, antiprotons, antideuterons can be observed.

Direct and indirect detection of DM particles is discussed in the following sections. Experiments at which *supersymmetric* particles, including neutralinos, could be produced in the collisions of high energy particles are ongoing [26]. Figure 1.5 summarizes different ideas for DM particle detection.

## 1.5 Direct Detection

Direct observation of dark matter present in the local galactic halo is very challenging task. The experimental idea is based on the observation of WIMP elastic scattering with nuclei

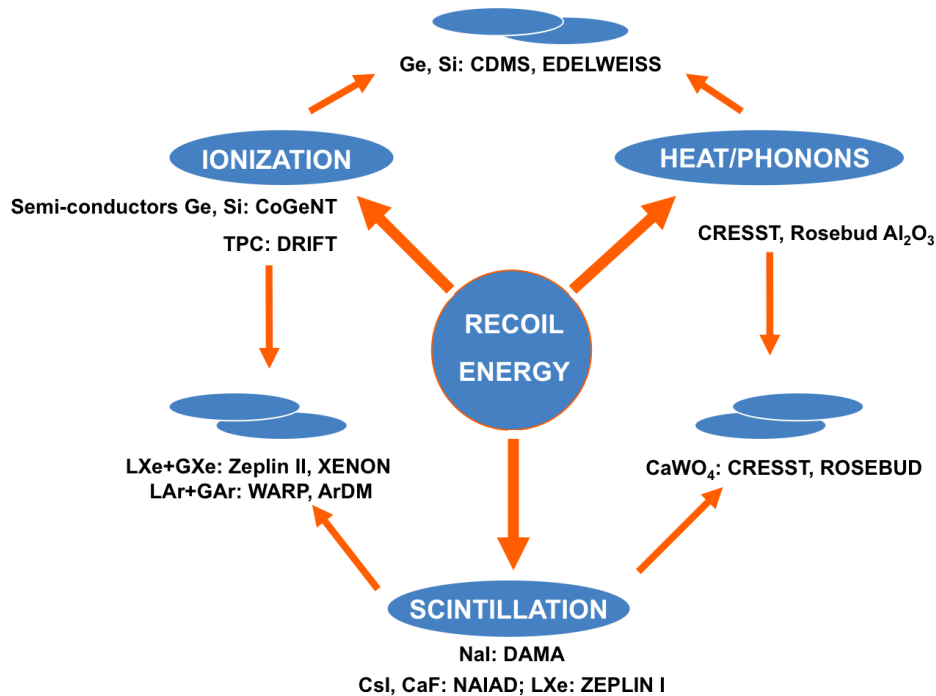


Figure 1.6: Illustration of various detection methods of a recoil energy. Selected experiments which realize different detection techniques are shown.

in the detector. The expected energy of nuclear recoils induced by WIMP interactions is in the range from several keV to several hundreds of keV depending on the  $M_\chi$  and type of nuclei in the detector [27]. Since very low rates of WIMP-induced events are expected in the experiment due to very low WIMP-nucleon cross section, experiments are sensitive to backgrounds which can limit the detector's capabilities to recognize events due to DM particles.

The sources of background for direct DM searches are related mostly to radioactivity and cosmic ray muons (and products of their interactions). The level of background is much higher at the Earth's surface than underground where the flux of cosmic ray muons is largely suppressed and level of natural radioactivity is lower. Therefore, DM detectors are installed in underground laboratories and usually are equipped with multi-layer system of shields and active veto detectors that can recognize passing muons. The dominant background at various underground locations consists of electrons from  $\beta$  decays of radioactive isotopes present in the rock and in the construction materials and of electrons produced in interactions of muons underground. The flux of neutrons and  $\alpha$  particles from radioactive decays and associated with muons is approximately six orders of magnitude lower than flux of electrons. However, interactions of neutrons and  $\alpha$  particles are expected to yield similar signatures as a WIMP-induced signal. Only the multiple scattering of neutrons/ $\alpha$ 's in the detector allows to distinguish them from interactions of WIMPs which are not expected to scatter more than once.

It is usually possible to recognize in the experiment the dominant background events due to electrons/gammas. Electrons interact mainly with the atomic electron cloud and produce electron recoils. Neutrons and  $\alpha$  particles scatter on nuclei. Electron and nuclear recoils lead to production of scintillation light, ionization, change of the temperature in the detector medium or vibrations of the crystal structures (phonons). The fact that

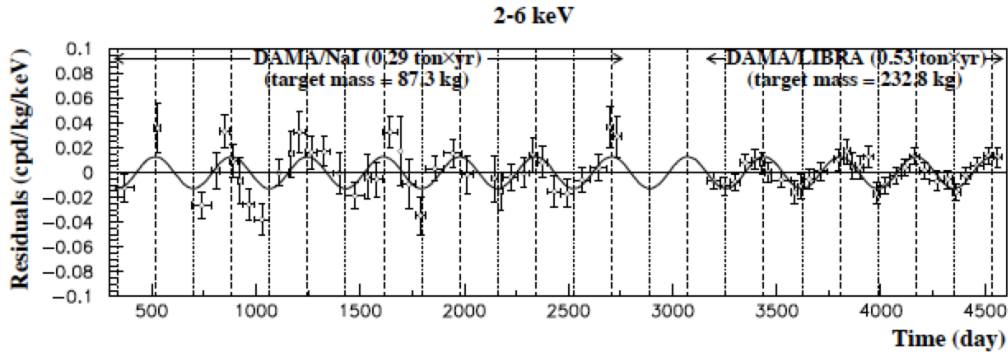


Figure 1.7: Annual modulation of a signal from DAMA experiment [28]. Number of recorded events compared to the mean number of events in a long time period (residuals) are shown for energy of recoils in a range 2-6 keV.

energy of recoils can be recorded in detector in many various ways, depending on the choice of the active material, implies that many kind of direct detection experiments can be realized. Various experimental methods that can be used to detect the energy of recoils are illustrated in Fig. 1.6 with examples of the experiments which are based on a given technique. For example, electrons interacting in the semiconductor detector deposit energy in form of the ionization and phonons. In case of electron recoils more energy is transferred into ionization then vibrations of the crystal lattice. That is opposite for heavy recoils induced by neutrons or expected for WIMPs in the same type of detector. Nuclear recoils produce less ionizing charges due to the quenching effect as compared to energy which they deposit as phonons. Based on this example it is seen that by combining many readout options it is possible to effectively reduce dominant electron background in the experiment.

### 1.5.1 Status of Direct Detection Experiments

Currently, only two direct detection experiments, DAMA (Dark Matter) [28, 29] and CoGeNT (Coherent Germanium Neutrino Technology) [31], are reporting the detection of dark matter.

DAMA has been in operation since 1996 at the Gran Sasso underground laboratory in Italy. It uses NaI crystals to record the scintillation light produced in recoils induced by all types of particles that interact in the scintillator. There is no active selection of recorded events, therefore interactions of background particles (like electrons) cannot be rejected based on signal characteristics. However, advanced system of shields and active veto detector are part of the experimental setup. In the first phase of the operation, referred to as DAMA NaI and spanning the years 1996-2002, around 100 kg of the target material was used. The upgraded setup, LIBRA (Large sodium Iodide Bulk for RAre processes) uses 250 kg of NaI scintillator and has been operating since 2008. The data collected with two DAMA setups correspond to very high exposition of 0.82 ton-years. DAMA observes an annual modulation of the signal as shown in Fig. 1.7 and it claims that this effect is induced by collisions of WIMPs in the detector [28].

The periodical character of the recorded number of counts in DAMA is confirmed at  $8.3 \sigma$  confidence level (CL) and it matches some expectations for the DM-induced

signal. Flux of DM particles at the detector depends on the relative speed of the Earth with respect to the DM halo. The mean velocity of DM particles in the halo is expected to be zero with respect to the galactic plane with the dispersion of that speed at the level of around 200–300 km/s [16]. The Solar System moves with respect to the galactic plane (and DM halo) with a speed of 230 km/s. Hence, the Earth moves with respect to the DM halo with a velocity that changes during a year due to its motion around the Sun. The maximum effective speed of the Earth with respect to DM halo is in June and minimum in December. The observed annual modulation by DAMA matches the expected amplitude of an event rate change in a scale of a year with a correct phase corresponding to June/December. Despite this evidence, critics argue that DAMA experiment has not proven that observed low energy signal is not due to seasonal variation of electron/gamma background in the detector’s vicinity.

The other experiment claiming DM observation, CoGeNT, uses semiconductor Ge detectors. It reports detection of low mass WIMPs (below  $\sim 11$  GeV) which are inducing energy recoils in the same energy range where internal detector noise is partially present [31]. Based on the statistical background estimation authors claim that their result can be explained by some external source such as interactions of WIMPs. The significance of CoGeNT result is so far very low due to small exposition (several tens of kg · days).

Figure 1.8 contains the current limits on the value of spin-independent  $\sigma_{\chi N}$ , obtained in various direct detection experiments as a function of WIMP mass. The best fit to DAMA/LIBRA observation (as interpreted in Ref. [30]) and to CoGeNT results are also shown there. Two preferred DAMA regions correspond to interactions on sodium or iodine. It is seen that other groups have set the limits on the values of WIMP-nucleon cross section which are excluding the DAMA result. The region of WIMP masses and values of  $\sigma_{\chi N}$  preferred by CoGeNT cannot be addressed by most of the existing experiments because they are not sensitive for such low mass WIMPs. The strongest current limits are from the XENON [33] and CDMS [32] (Cryogenic Dark Matter Search) experiments. The CDMS collaboration observed two events having the characteristics expected for the DM signal with the expectation on the neutron background level of  $0.8 \pm 0.1(\text{stat}) \pm 0.2(\text{syst})$  event [32]. The estimated probability of obtaining 2 or more background events in their measurement was derived as 23%. According to the group, obtained result cannot be interpreted as significant evidence for WIMP interactions and corresponding limit on the  $\sigma_{\chi N}$  was derived. Their positive signal was not confirmed by the XENON experiment. The XENON collaboration uses a 100 liter liquid xenon detector and excluded spin-independent WIMP-nucleon elastic scattering cross sections above  $3.4 \cdot 10^{-44}$  cm<sup>2</sup> for 55 GeV WIMPs at 90% confidence level placing slightly better constraints than the CDMS (see Fig. 1.8). It also excluded the preferred low mass WIMPs region of CoGeNT experiment.

The spin-dependent WIMP interactions can be probed by a certain direct detection experiments which contain isotopes with odd number of nucleons (having unpaired spin). The spin-dependent limit on the value of  $\sigma_{\chi N}$  is shown later in Section 3.1.2 along with the explanation how to link results from direct detection experiments with indirect detection searches which have the capability to investigate spin-dependent reactions of WIMPs on hydrogen in the Sun.

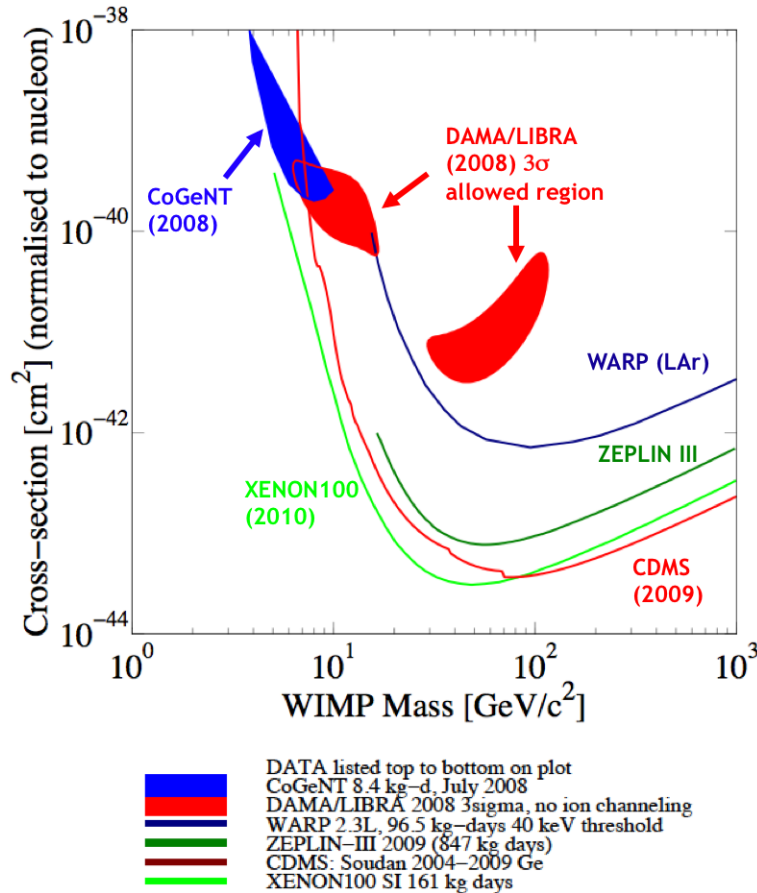


Figure 1.8: Upper limits on the value of spin-independent WIMP-nucleon cross section as a function of WIMP mass. The region above the line is excluded by a certain experiment at 90% confidence level. DAMA/LIBRA result is indicated as a red region as interpreted in Ref. [30]. Preferred CoGeNT region is indicated as blue area. Figure based on Ref. [34].

## 1.6 Indirect Detection

In parallel to the direct detection experiments, a wide range of indirect detection projects have been developed to search for the annihilation products of the dark matter particles. In these searches the value of DM self-annihilation cross section  $\langle\sigma_A V\rangle$  is constrained. Annihilation rate  $\Gamma_A$  is proportional to the  $\langle\sigma_A V\rangle$  and numerical density ( $n_\chi$ ) squared of the relic particles:

$$\Gamma_A \propto \langle\sigma_A V\rangle \times n_\chi^2 = \langle\sigma_A V\rangle \times \frac{\rho_\chi^2}{M_\chi^2}, \quad (1.3)$$

where  $\rho_\chi$  indicates the density of DM particles in the local halo.

In the typical *supersymmetric* models, annihilating WIMPs most likely couple to the particles with masses closest to their mass [2]. Depending on the mass of neutralinos, annihilation would lead to production of  $\tau$  leptons,  $b$ ,  $c$  and  $t$  quarks, gauge bosons or Higgs bosons. As a result of subsequent decays of the primal annihilation products, many kinds of particles will be created. Indirect searches are focused on the detection of the following ones:

- Antimatter – in the search for DM signal from a cosmic space it is better to investigate the flux of antimatter particles than the flux of matter particles because there are not many sources of antimatter in the galaxies. The primary cosmic rays consists mainly of protons. Hence, it would be difficult to observe any excess of DM-induced matter particles in the flux of primary cosmic rays. Furthermore, to reduce the background due to antimatter particles produced in the showers initiated by primary cosmic rays in the atmosphere, it is necessary to take measurements at high altitudes or in the cosmic space. Searches for antimatter particles, mostly positrons and antiprotons, from dark matter annihilation in the galactic halo are conducted by experiments located on satellites (for example, FERMI-LAT [35], PAMELA [36]) or balloons (ATIC [37], HEAT [38]). Propagation of charged particles from DM annihilation is affected by the galactic magnetic field which results in their diffuse spectrum observed at the Earth. Also, these particles cannot reach us from the long distances, larger than few kiloparsecs (kpc), due to interactions with the interstellar medium and energy loss in inverse Compton interactions and via synchrotron radiation.
- Photons – they propagate in the galaxy without any appreciable deflection due to the magnetic field. They are also only weakly attenuated over the large galactic distance scales, thus their energy spectra observed at the Earth would be close to the spectra generated in DM annihilation. For these reasons, photons can potentially provide good angular information on the position of the source and energy spectrum of annihilation products. Experiments are searching for gammas originating in the center of the Milky Way or are focused on the diffuse flux of photons of the cosmic origin. Several such experiments have been conducted, for example: EGRET [39], FERMI-LAT [35], HESS [40], MAGIC [41].
- Neutrinos – Neutrinos provide very good information about their source as their energy and direction remains completely unchanged during propagation in space and through matter. There is practically no background related to cosmic neutrinos. However, due to only weak interactions, neutrino detection is challenging and realized with large detectors located on the Earth where the background comprised of neutrinos produced in the atmosphere contributes. Neutrinos could be related to dark matter annihilations in the Sun, core of the Earth, or in the center of the Milky Way where DM density is expected to be greater what would lead to enhanced annihilation rate. Among all Standard Model particles that can be produced in DM annihilation, only neutrinos can escape from such a dense objects like the core of the Sun or the Galactic Center (GC). It is also expected that DM annihilation in the entire volume of the galaxy and in cosmic space will produce a diffuse flux of neutrinos which one can attempt to observe. The searches for DM-induced neutrinos are conducted at the following neutrino telescopes: ANTARES [42], AMANDA/Ice-Cube [43], Super-Kamiokande [44]. The results of DM searches using neutrino data from the Super-Kamiokande detector are presented in this thesis in Chapters 3, 6, and 7.

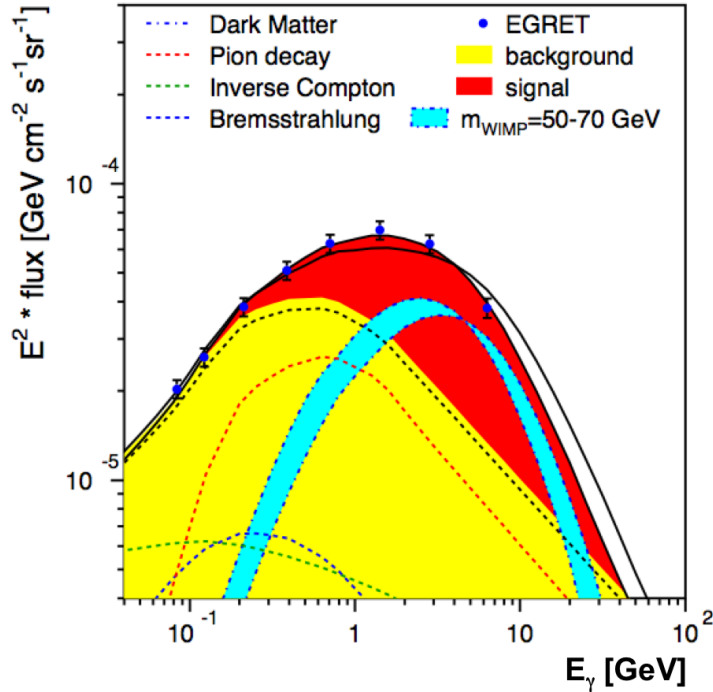


Figure 1.9: Gamma spectrum obtained in the analysis of EGRET data compared with the expected contribution from known natural sources (yellow) and potential WIMP annihilation signal (red) [39].

### 1.6.1 Status of Indirect Detection Experiments

At the time of writing, there are several experiments which observed an excess of events over the expected contribution from cosmic rays and their results could be attributed to DM annihilation [36, 37, 39]. The most prominent results are outlined below:

- EGRET (Energetic Gamma Ray Experiment Telescope) – The gamma ray data from this satellite mission were analyzed in a search for signal from WIMP annihilations in the Milky Way. The observed diffuse spectrum of photons is presented in Fig 1.9 and compared with the spectrum from known galactic gamma sources obtained using a GALPROP code [45]. Authors claimed that surplus of events over the expected contribution can be explained as annihilation of WIMPs with a mass between 50 and 100 GeV [39]. This interpretation was widely discussed in the community. Recently, it has been shown that excess of cosmic gammas observed by EGRET can be explained when a model which is used to derive the expectation on production and propagation of photons in the Milky Way is extended [46].
- PAMELA (Payload for Antimatter Matter Exploration and Light-nuclei Astrophysics) – The PAMELA is a satellite based experiment launched in 2006. The multi-purpose detector, consisting of spectrometer, calorimeter, neutron detector and time of flight counters, is capable to measure different species of particles in cosmic ray flux – antiprotons, protons, electrons, positrons. The experiment observed an excess of positrons (specifically the  $e^+/(e^+ + e^-)$  ratio) in the 10-100 GeV range [36] over the expected background due to production of positrons in interactions of primary

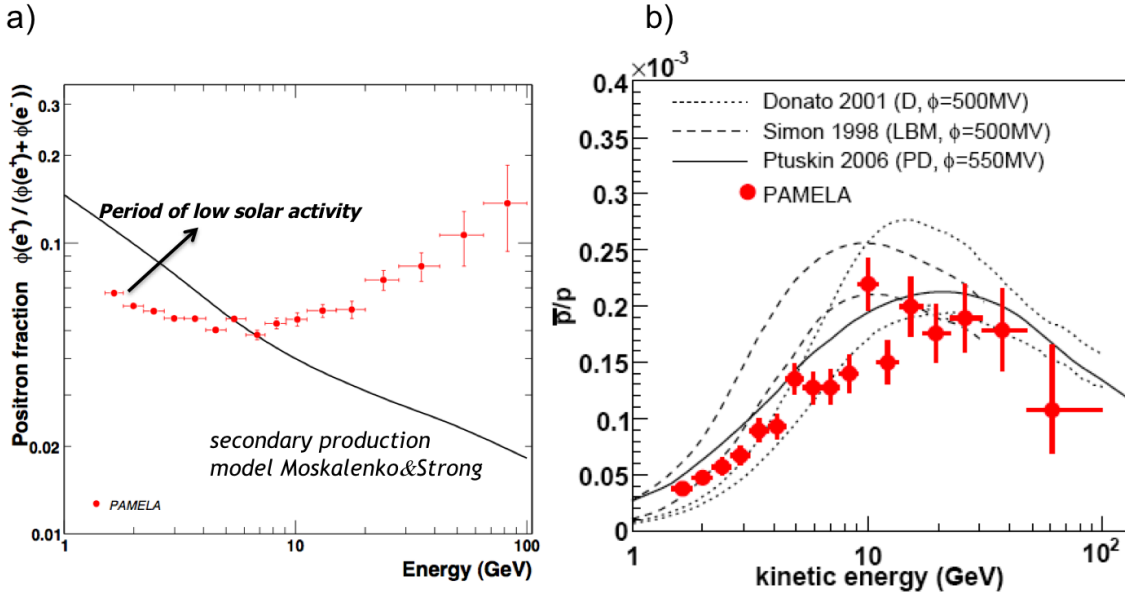


Figure 1.10: (a) Positron fraction measurement in the cosmic rays by PAMELA [36]. The line indicates the prediction due to the production of positrons (and electrons) in the interactions of primary cosmic rays with the inter-stellar medium [47]. (b) Antiproton to proton ratio measured by PAMELA [49] as compared with various expectations due to natural sources.

cosmic rays with the inter-stellar medium [47]. This result is shown in Fig. 1.10(a) and it launched a great discussion in the community. There are numerous publications which interpreted observed excess in the positron fraction as an evidence for dark matter annihilation within distance a few kpc from the Solar System. Models that try to fit the observed PAMELA spectrum with positrons from DM annihilation usually consider some 'boost factors' at the level of  $10^2 - 10^5$  in order to match the strength of the observed excess with annihilation rate. The 'boost factors' are related either to increased value of  $\langle \sigma_A V \rangle$  (as compared to thermal relic cross section value) or increased DM density (as compared to standard DM halo density), e.g. [48]. However, typical *supersymmetric* models require also that positron creation should be associated with production of other particles like antiprotons (protons), gammas and neutrinos in the annihilation of WIMPs. The results of a measurement of the antiproton to proton ratio ( $\bar{p}/p$ ) in the cosmic flux were available from PAMELA [49] shortly after the publication of the positron fraction measurement. They showed agreement with the expectation as presented in Fig. 1.10(b). This fact makes the DM related explanations of positron excess more difficult to justify. The PAMELA results could be related to DM only when non standard models are assumed in which WIMPs would directly couple to leptons [50, 51].

- ATIC (Advanced Thin Ionization Calorimeter) – This balloon experiment measured the  $(e^+ + e^-)$  flux over the Antarctica showing an anomalous shape of the obtained spectrum (see Fig. 1.11.) [37]. The observed excess is in the range of 300–800 GeV. This is not consistent with the PAMELA result on the positron fraction measurement which indicates the disagreement with expectations in different energy region (compare Fig 1.10(a)). ATIC collaboration claims that their result can be explained

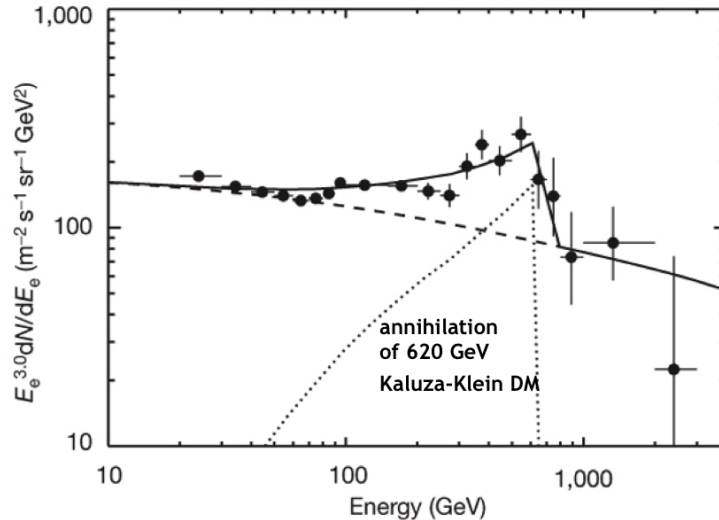


Figure 1.11: Energy spectrum of  $(e^+ + e^-)$  obtained by ATIC [37]. The dashed line shows the background level expectation, the dotted line hypothetical contribution from annihilation of Kaluza-Klein particle of a mass of 620 GeV. Solid line is a sum of a background and DM signal contribution.

with an annihilation of a massive Kaluza-Klein Dark Matter particle into electron and positron pairs. Resulting monoenergetic signal can reproduce such a sharp shape of the observed spectrum. The Kaluza-Klein relic particle is considered an exotic alternative to commonly mention DM candidates. It is related to hypothetical extra dimensions and theoretical models favors its coupling to leptons [52].

- FERMI – It is a satellite detector launched by NASA in 2008. The apparatus consists of two instruments: Large Area Telescope (LAT) which contains a tracker and calorimeter detectors and Gamma Burst Monitor with NaI crystal detectors. The LAT detector measured the cosmic ray  $(e^+ + e^-)$  spectrum with an unprecedented precision for electron energies ranging from 20 GeV to 1 TeV. The result is shown in Fig 1.12(a). Obtained spectrum deviates slightly from a standard expectation [46] but does not confirm the anomalous shape of the ATIC data (also shown in Fig 1.12(a)). In addition to cosmic ray electron spectrum, Fermi measured the gamma spectrum which is shown in Fig 1.12(b). The strong excess observed by EGRET is not confirmed with this FERMI result.

## 1.7 Summary of Dark Matter Searches

Different searches for dark matter particles discussed in this chapter seem to be complementary and observation of DM signal in only one of them is not sufficient to identify the nature of relic particles. The direct or indirect detection of DM particles in the galactic halo is not likely to provide enough information to reveal all their physical properties. In contrast, accelerator experiments may be able to identify neutralinos, shed more light on the underlying theoretical model of their interactions but cannot prove that these are the same particles that are abundant in the Universe. Therefore, only by combining the information from different searches the nature of dark matter can hopefully be revealed

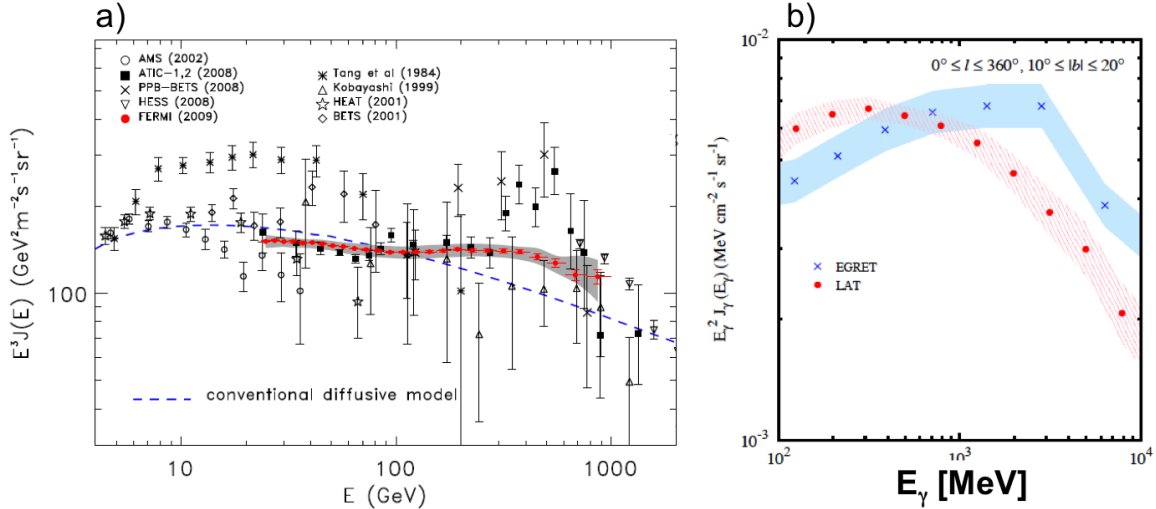


Figure 1.12: (a) The FERMI LAT cosmic ray electron spectrum (red filled circles) [35]. Systematic errors are indicated with the gray band. Results of the other measurements and expectation due to conventional diffuse model [46] are shown. (b) Gamma spectrum obtained by FERMI compared to the result based on EGRET data. Bands correspond to systematic errors.

and understood in future.

So far, the results of the searches are not conclusive. There are two direct detection experiments, DAMA and CoGeNT, claiming the discovery of DM particles [28, 31] while other searches already excluded regions containing their results [32, 33]. It may be the case that different experiments are sensitive to different physics of WIMP interactions which is poorly predicted by theoretical models and some effects regarding their interactions are not taken into account while comparing different results. Other searches are planned to confirm the hypothetical DM detection signals with similar materials used for the detection as experiments claiming the DM observation, but with different background detection capabilities. Newly constructed direct detection experiments based on a noble liquids and the currently operating ones should be able to probe the range of WIMP-nucleon cross sections a few orders of magnitude lower than current limits due to longer exposition and higher mass.

Some results of indirect searches are also difficult to interpret. The observed excess in cosmic ray fraction of positrons by PAMELA [36] and anomalous shape of the electron spectra in ATIC data [37] are not consistent with each other and the latter one is not confirmed in the FERMI measurement [35]. There are various explanations of the origin of excesses observed in cosmic ray electrons/positrons. The effect can be explained by other cosmic sources such as pulsars [53]; or it is claimed that models used to estimate the background level in these searches are incomplete; or the excess can be induced by DM annihilation. In the latter case a leptophilic WIMPs [50, 51] are required in order to be consistent with a null indication of DM signal in the antiproton data. Leptophilic dark matter would lead to production of large cosmic fluxes of neutrinos from decays of muons and tau leptons or even neutrinos from direct annihilation of WIMP into neutrino and anti-neutrino pairs. The search for diffuse DM annihilation signal from the Milky Way using neutrino data from the Super-Kamiokande experiment is presented in this thesis.

# Chapter 2

## Neutrinos

The goal of this chapter is to provide an overview of neutrino properties. First, interactions of neutrinos with matter and then the sources of neutrinos are briefly discussed. In the last part of the chapter the properties of neutrinos produced in the Earth's atmosphere are presented. This type of neutrinos constitute a background in the search for DM-induced neutrino signal which is presented in Chapters 6 and 7.

### 2.1 Introduction

Neutrinos were first postulated by Wolfgang Pauli in 1930 to explain the continuous energy spectrum of electrons observed in nuclear  $\beta$  decay [54]. This process was believed to be a two-body decay involving only an outgoing electron and recoiling nucleus in the final state. Since the energy of electrons in case of a decay at rest shall be fixed and their observed spectrum was continuous, it suggested either the violation of energy conservation law or a third *invisible* particle present in the final state. In order to solve the puzzle, Pauli proposed a new, massless and electrically neutral particle that was carrying the lacking part of the energy of the system. That particle was named the *neutrino* by Enrico Fermi a few years later [55].

According to precise measurements of LEP experiment, 3 generations of neutrinos (leptons) exists in nature [56]. There are called electron neutrino ( $\nu_e$ ), muon neutrino ( $\nu_\mu$ ) and tau neutrino ( $\nu_\tau$ ). For each one the corresponding anti-neutrino exists ( $\bar{\nu}_e, \bar{\nu}_\mu, \bar{\nu}_\tau$ ).

### 2.2 Neutrino Interactions with Matter

Neutrino interactions are described by the rules of Standard Model of particle physics and according to this model neutrinos interact only weakly with other particles. Typical cross section for neutrino interactions is 6 orders of magnitude smaller than for electromagnetic interactions. That means neutrino interactions are very rare. The mean free path for a neutrino, which has energy in a GeV range, traversing the infinite block of lead, is of the order of a light year.

Neutrinos with energies above hundreds of MeV, while traversing through matter, interact mainly with nucleons (N). Their couplings to atomic electrons are typically 3 orders of magnitude smaller and can be neglected in most experimental cases. The value of cross section is proportional to the energy of neutrino. For instance, for muon neutrinos

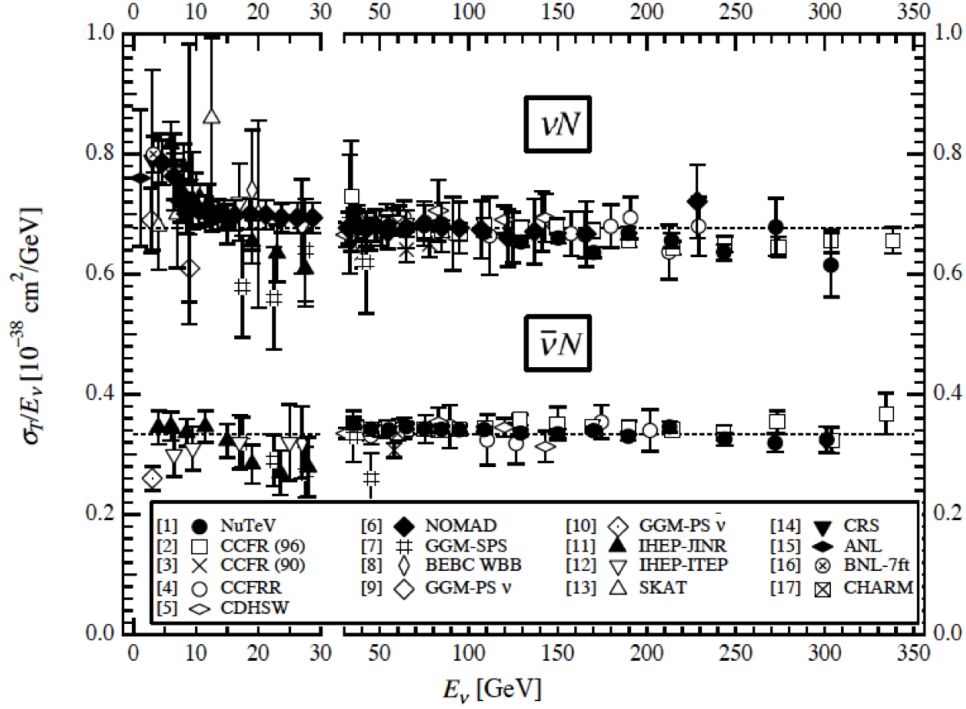


Figure 2.1: Ratio of total charged current neutrino cross section and neutrino energy ( $\sigma_T/E_\nu$ ) for the muon neutrinos and anti-neutrinos interacting on nucleons as a function of neutrino energy [56]. Points indicate various measurements. For the reference of the experiments see [56]. The error bars include both statistical and systematic errors.

interacting with nucleons, the ratio of the total cross section to neutrino energy,  $\sigma_T/E_\nu$ , is of the order of  $\sim 0.68 \cdot 10^{-38} \text{ cm}^2/\text{GeV}$  and remains constant for  $E_\nu > 10 \text{ GeV}$  [56] (see Fig. 2.1). It can also be inferred that the ratio of neutrino to anti-neutrino cross section is approximately 2.

Detection of neutrinos is a challenging task due to the low value of their interaction cross section. It requires high intensity neutrino sources and large neutrino detectors associated with long exposition time to gather high number of events. For example, in Cherenkov detectors like Super-Kamiokande (described in Chapter 4.1) or Ice-Cube [57] the number of observed atmospheric neutrinos is at the level of  $\sim 1$  event per day per kiloton of the detector material. It is also important to mention that neutrinos are not detected directly as they are electrically neutral. One detects the products of their interactions.

In weak interactions, the  $W^\pm$  and  $Z^0$  gauge bosons are interchanged between quarks and leptons. Depending on the boson exchanged two types of neutrino reactions can be distinguished:

- *neutral current (NC interactions)* –  $Z^0$  is exchanged (Fig. 2.2(b)). These are the reactions of type:

$$\nu + N \rightarrow \nu + N' + \dots,$$

where  $N$  is a nucleon and  $N'$  indicates a nucleon with modified momentum or/and in excited state.

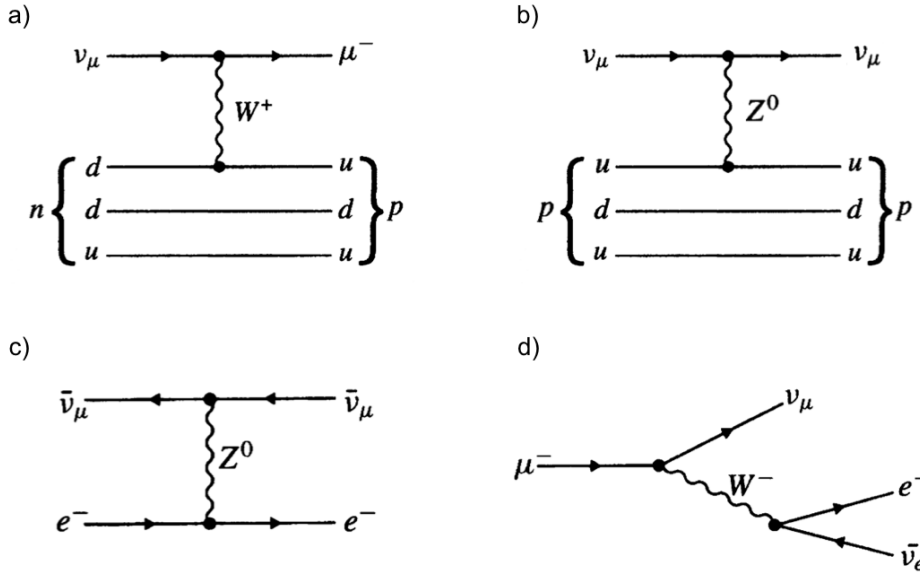


Figure 2.2: Examples of interactions involving neutrinos: (a) charged current (CC) interaction with a nucleon’s quark, (b) neutral current (NC) interaction with a quark, (c) neutral current interaction with an electron, (d) muon decay. [71].

- *charged current (CC interactions)* –  $W^\pm$  boson is exchanged (Fig. 2.2(a)). These are the reactions of type:

$$\nu + N \rightarrow l + N' + \dots,$$

where  $l$  is a charged lepton of the same flavor as interacting neutrino.

Apart from the neutrino or charged lepton and recoiling nucleon present in the final state also some other particles could be produced in NC and CC processes. These are mainly pions. Neutrino interactions with matter depend mainly on the energy of incoming  $\nu$ . More details on the neutrino interaction formalism can be found in [59].

Neutral current processes are usually difficult to reconstruct as part of the energy available in the final state is carried by unobservable neutrino. Hence, neutrino detection is based mostly on the detection of a lepton produced in charged current interactions. If one is able to measure the direction and momentum of this outgoing lepton (along with momentum and direction of associated pions if they were also produced), the energy and the direction of a parent neutrino could be reconstructed as well.

There is a correlation between the direction of a parent neutrino and direction of a charged lepton produced in the neutrino interaction. The more energetic the neutrino is, the closer the lepton follows the original direction of its parent neutrino. That dependence is illustrated in Fig. 2.3 as a function of parent neutrino energy.

As it was stated in Chapter 1, dark matter induced neutrinos are most likely to be in the energy range from several GeV up to several TeV. In this range there are different types of CC and NC reactions that those neutrinos could undergo in the detector medium. The most important ones are discussed below. The values of neutrino-nucleon cross section for different types of CC interactions of muon neutrinos are shown in Fig. 2.4 as a function of neutrino energy. Contribution from different processes to the total neutrino-nucleon cross section could be derived from there.

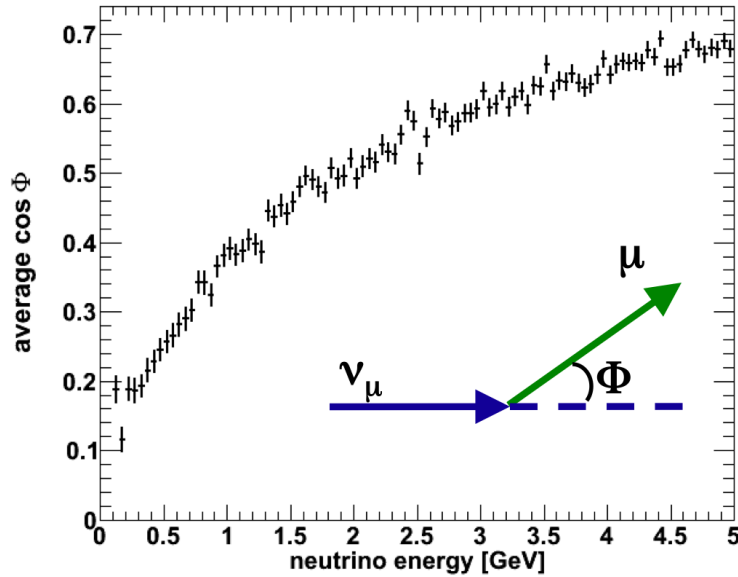


Figure 2.3: Relation between direction of a charged lepton produced in neutrino interaction and direction of a parent neutrino. Vertical axis corresponds to the average value of cosine of an angle between neutrino and lepton directions ( $\Phi$ ). Vertical errors on the points are associated with root mean square (rms) of the average value of  $\cos \Phi$  obtained in the given bin. Horizontal axis indicates the neutrino energy. The plot is based on generated CC quasi-elastic interactions of muon neutrinos having a flat energy distribution. The simulation procedure is described in Chapter 5 of Ref. [60].

- *Neutral current elastic (NCE) and charged current quasi elastic interactions (CCQE).* These are the processes that don't lead to production of any additional particles in the final state apart from the outgoing neutrino (NC) or a charged lepton  $l$  (CC) and recoiling nucleon  $N'$ :

$$NCE : \nu + N \rightarrow \nu + N',$$

$$CCQE : \nu + N \rightarrow l + N'.$$

NCE and CCQE processes are dominant interaction modes for neutrino energies below 1 GeV. They significantly contribute to the total cross section up to around 10 GeV of neutrino energy as it is shown in Fig. 2.4 for CCQE processes (referred there to as  $QE$  line and red points).

- *Neutrino scattering off nucleons with production of resonances (resonant production, RES).* In this type of neutrino interaction with nucleon an excited baryon resonance is produced. The resonance decays then into nucleon and one or more mesons:

$$NC \text{ RES} : \nu + N \rightarrow \nu + r^* \rightarrow \nu + N' + meson(s),$$

$$CC \text{ RES} : \nu + N \rightarrow l + r^* \rightarrow l + N' + meson(s),$$

where  $r^*$  indicates a produced resonance. The most prominent resonance is  $\Delta(1232)$ , but some others may also contribute. Mesons are usually charged or neutral pions,

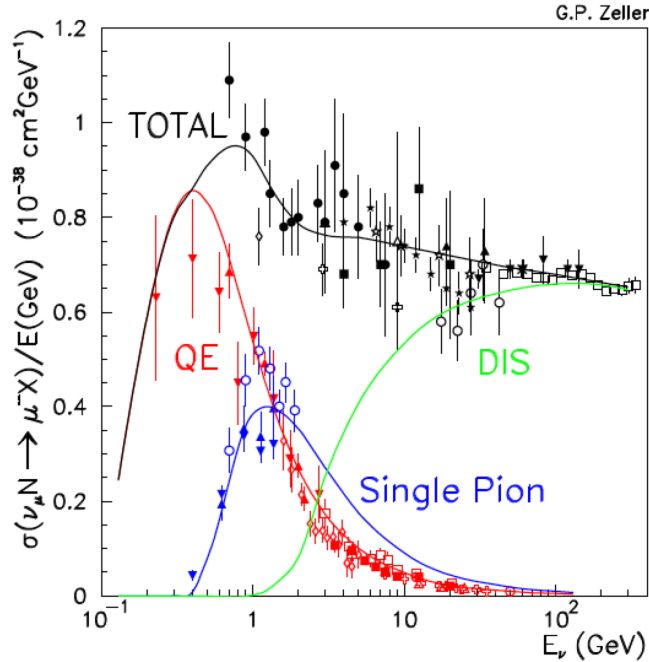


Figure 2.4: Value of the *charged current*  $\nu_\mu$  cross section divided by neutrino energy. Contribution from different processes (CCQE, resonant single pion, and DIS) is shown based on a variety of past experiments [61] as a function of neutrino energy. The prediction from the NUANCE event generator is indicated with lines [62].

less abundant are kaons,  $\rho$  mesons and other heavier particles. Production of many charged particles leads to complex topology observed in the detector. Neutrino interaction events of this type are more difficult to identify than the ones resulting from CCQE reactions. The resonant production processes start to play role in neutrino interactions for  $E_\nu$  from around 1 GeV up to several GeV. The value of CC cross section for resonant single pion production is shown in Fig. 2.4 as a *Single Pion* line and blue points).

- *Coherent scattering off nuclei (COH)*. Here, neutrino interacts with a target nucleus as a whole. As a result a charged lepton and a meson (most probably pion) are produced:

$$NC \text{ COH} : \nu + A \rightarrow \nu + A + \text{meson},$$

$$CC \text{ COH} : \nu + A \rightarrow l + A + \text{meson}.$$

The characteristic feature of *COH* interaction is that the nucleus (A) receives a negligible energy transfer and remains at its ground state. Thus, there is also no nucleon "kicked out" from nucleus. These interactions experimentally manifest themselves the same way as in case of the resonant production mode but are associated with single meson production only. They contribute the most to the total neutrino cross section at energy of a few GeV and at low energy transfers.

- *Deep inelastic scattering (DIS)*. These interactions usually result in a production of many particles in the course of neutrino interactions with partons (quarks and gluons) inside nucleons. Deep inelastic reactions could be both of CC and NC type

and they are dominant for neutrino energies of several tens of GeV and higher. In Fig. 2.4, the simulated contribution of DIS processes to the total value of CC cross section is described with the green line.

$$NC \text{ DIS} : \nu + N \rightarrow \nu + \text{otherparticles},$$

$$NC \text{ DIS} : \nu + N \rightarrow l + \text{otherparticles}.$$

It is now seen that neutrinos could give various experimental signatures in neutrino detectors depending on their energy and underlying interaction mode. Especially, in the range of several GeV many kinds of interaction modes contribute resulting in different characteristics of observed events in the experiment. That typically leads to distinction of many event samples that can be used in the analysis. Classification of experimental event samples, which span many orders of magnitude of neutrino energy, is provided in Chapter 5 based on the data collected with the Super-Kamiokande detector.

Neutrino interactions are bound by a lepton number conservation. Not only the total number of leptons in any reaction has to be conserved. It is also necessary that the number of leptons of a given flavor remain the same. Thus, in charged current processes described above,  $\nu_e/\bar{\nu}_e$ ,  $\nu_\mu/\bar{\nu}_\mu$  and  $\nu_\tau/\bar{\nu}_\tau$  interactions are associated with a production of corresponding charged lepton  $e^\pm$ ,  $\mu^\pm$  or  $\tau^\pm$ . Neutrinos are not allowed to change flavor in the Standard Model. However, over the last 20 years some strong experimental proofs have been gathered of a phenomenon which violates this rule. It affects neutrino propagation and is referred to as neutrino oscillations.

## 2.3 Neutrino Oscillations

The phenomenon of neutrino oscillations was introduced to explain the experimental observation of a deficit of neutrinos of certain flavors as compared to the precise expectations on their rate (*disappearance effect*). The effect was confirmed in the measurements of solar [63, 64], atmospheric [65, 5] and also man-made, reactor [66] and accelerator [79], neutrinos. Experiments aiming at direct confirmation of the *appearance effect*, that is the transition of neutrinos of a one flavor into another, are currently in progress [6, 67].

Neutrino oscillation is the quantum effect caused by the fact that flavor eigenstates in which neutrinos are detected and produced, like  $\nu_\mu$  or  $\nu_\tau$ , are not the same as their mass eigenstates (often denoted as  $\nu_1, \nu_2$  etc). For example, neutrinos produced in decays of muons, that is muon neutrinos, would have certain composition of mass eigenstates, different than in case of electron or tau neutrinos. These constituting mass eigenstates propagate in space with different velocities, as they have different mass. Therefore, at the point of detection their composition could be different than at the point of creation. In other words, there is a probability that a muon neutrino could be detected as the electron or tau neutrino after traversing some distance from the point of production due to the change of proportions of mass eigenstates. This probability is a function of travelled distance and has a periodical character, and this is the reason why the effect is being referred to as oscillation.

The idea of neutrino mixing was first proposed by Bruno Pontecorvo in the late 50's in the analogy with neutral kaon oscillations [68]. The formalism was developed later by

many physicists. Among them the most denoted work has been done by collaboration of Maki, Nakagawa, Sakata [69] and Pontecorvo with Bilenky [70].

The effect of neutrino oscillations has been confirmed already by a number of experiments. The analysis of oscillations of atmospheric neutrinos based on the Super-Kamiokande data is discussed in Chapter 5.

Because atmospheric neutrinos constitute the main background in the search for diffuse dark matter signal, a brief explanation of oscillation formalism is given below. In this case, the dominant transitions are between two flavors,  $\nu_\mu \leftrightarrow \nu_\tau$ . So, the two flavor approximation of neutrino oscillation formalism is sufficient to understand the effect of neutrino mixing in the atmospheric sector.

### 2.3.1 Neutrino Oscillation Formalism

Let's consider oscillations of  $\nu_\mu$  and  $\nu_\tau$  neutrinos in vacuum. Each of these neutrino flavor eigenstates could be described as a linear combination of two mass eigenstates  $\nu_1$  and  $\nu_2$  [71]:

$$\begin{pmatrix} \nu_\mu \\ \nu_\tau \end{pmatrix} = \begin{pmatrix} \cos \theta & \sin \theta \\ -\sin \theta & \cos \theta \end{pmatrix} \begin{pmatrix} \nu_1 \\ \nu_2 \end{pmatrix}$$

where  $\theta$  is a mixing angle. The wave functions of neutrino flavor are orthonormal:

$$\nu_\mu = \cos \theta \cdot \nu_1 + \sin \theta \cdot \nu_2$$

$$\nu_\tau = -\sin \theta \cdot \nu_1 + \cos \theta \cdot \nu_2$$

We would like to see how the flavor eigenstates propagate in space and what is the probability that neutrino of a given flavor, let it be  $\nu_\mu$ , will change its flavor to  $\nu_\tau$  during the propagation. The time evolution of mass eigenstates is given by (in  $\hbar = c = 1$ ):

$$\nu_1(t) = \nu_1(0) \cdot e^{-iE_1 t}$$

$$\nu_2(t) = \nu_2(0) \cdot e^{-iE_2 t}$$

Momentum  $p$  of mass eigenstates is fixed and doesn't change during the propagation. Momentum is related to energy by this common relativistic formula:

$$E^2 = p^2 + m^2$$

Assuming small neutrino masses  $m_i \ll E_i$  (where  $i = 1, 2$ ) and equal momentum for each mass eigenstate, we get:

$$E_i = \sqrt{p^2 + m_i^2} \approx p + \frac{m_i^2}{2p}$$

Let's consider the case in which we have a pure muon neutrino source. Initial conditions at  $t = 0$  are as follows:

$$\nu_\mu(0) = 1$$

$$\nu_\tau(0) = 0$$

Then:

$$\nu_1(0) = \cos \theta \cdot \nu_\mu(0)$$

$$\nu_2(0) = \sin \theta \cdot \nu_\mu(0)$$

We would like to see what happens after time  $t$ :

$$\nu_\mu(t) = \cos \theta \cdot \nu_1(t) + \sin \theta \cdot \nu_2(t)$$

Probability that a muon neutrino is still a muon neutrino at the time  $t$  is given by:

$$P(\nu_\mu \rightarrow \nu_\mu) = \left| \frac{\nu_\mu(t)}{\nu_\mu(0)} \right|^2 = \left| \cos^2 \theta e^{-iE_1 t} + \sin^2 \theta e^{-iE_2 t} \right|^2 = 1 - \sin^2 2\theta \sin^2 \frac{(E_2 - E_1)t}{2}$$

One can reformulate  $(E_2 - E_1)t/2$  argument introducing  $\Delta m^2 = m_2^2 - m_1^2$ ,  $t = L$ ,  $E_i = p + m_i^2/2p$  and assuming  $E = p$ . Then we get:

$$\frac{(E_2 - E_1)t}{2} \Rightarrow \frac{\Delta m^2 L}{4 E}$$

If one now introduces  $\hbar$  and  $c$ , express a traveled distance  $L$  in meters,  $\Delta m^2 c^4$  in  $\text{eV}^2$  and  $E$  in MeV, then the above expression would result in:

$$\frac{\Delta m^2 c^4 L}{4 \hbar c E} \Rightarrow 1.27 \frac{\Delta m^2 L}{E}$$

The final formulae for the oscillation probability are the following:

$$P(\nu_\mu \rightarrow \nu_\mu) = 1 - \sin^2 2\theta \sin^2 \left( 1.27 \frac{\Delta m^2 L}{E} \right) \quad (2.1)$$

$$P(\nu_\mu \rightarrow \nu_\tau) = 1 - P(\nu_\mu \rightarrow \nu_\mu) = \sin^2 2\theta \sin^2 \left( 1.27 \frac{\Delta m^2 L}{E} \right) \quad (2.2)$$

Formula 2.1 describes the probability that a muon neutrino of a given energy  $E$  will remain at its flavor after traveling a distance  $L$  in vacuum. And equation 2.2 is associated with probability that this muon neutrino will change into tau neutrino. Additional effects shall be introduced when the neutrino propagation is in matter instead of vacuum [56].

Formulae 2.1, 2.2 depend on the oscillation parameters  $\theta$  and  $\Delta m^2$ . The first one controls the amplitude of oscillations, the second one its periodicity. While parameters  $\Delta m^2$ ,  $\theta$  are nature's constants, the other terms  $E$  and  $L$  are associated with a given neutrino source and sometimes can be controlled in the experiment.

Equations 2.1, 2.2 are valid in the approximation of 2 flavor transitions. In case of 3 flavors the mixing could be described by  $3 \times 3$  unitary matrix  $U$ , called Maki-Nakagawa-Sakata (MNS) matrix [56, 58]:

$$U = \begin{pmatrix} c_{12}c_{13} & s_{12}c_{13} & s_{13}e^{-i\delta} \\ -s_{12}c_{23} - c_{12}s_{23}s_{13}e^{+i\delta} & c_{12}c_{23} - s_{12}s_{23}s_{13}e^{+i\delta} & s_{23}c_{13} \\ s_{12}s_{23} - c_{12}c_{23}s_{13}e^{+i\delta} & -c_{12}s_{23} - s_{12}c_{23}s_{13}e^{+i\delta} & c_{23}c_{13} \end{pmatrix} \times \begin{pmatrix} 1 & 0 & 0 \\ 0 & e^{i\alpha} & 0 \\ 0 & 0 & e^{i\beta} \end{pmatrix}$$

where  $c_{ij} = \cos \theta_{ij}$  and  $s_{ij} = \sin \theta_{ij}$ ,  $\delta$  is Dirac phase and  $\alpha, \beta$  are Majorana phases. If CP violation occurs these phases are non-zero. If neutrinos are Dirac particles then Majorana phases vanish and one can disregard the matrix on the right hand side of the formula. Then, the MNS can be split into three components describing rotations around three orthogonal axes:

$$U = \begin{pmatrix} 1 & 0 & 0 \\ 0 & c_{23} & s_{23} \\ 0 & -s_{23} & c_{23} \end{pmatrix} \begin{pmatrix} c_{13} & 0 & s_{13}e^{-i\delta} \\ 0 & 1 & 0 \\ -s_{13}e^{-i\delta} & 0 & c_{13} \end{pmatrix} \begin{pmatrix} c_{12} & s_{21} & 0 \\ -s_{12} & c_{21} & 0 \\ 0 & 0 & 1 \end{pmatrix}$$

The first component in matrix  $U$  includes  $\theta_{23}$  mixing angle which corresponds to mixing in the atmospheric neutrino sector. The last term including  $\theta_{12}$  probes the solar neutrino mixing. The middle term contains a CP violation phase  $\delta$  and  $\theta_{13}$  which is currently the least constrained mixing parameter.

The probability of oscillations in case of three flavors is given by complex formulae which can be found elsewhere [56]. They depend on the three mixing angles  $\theta_{13}$ ,  $\theta_{12}$ ,  $\theta_{23}$ . However, due to the small value observed for  $\theta_{13}$  ( $\sin^2 \theta_{13} \leq 0.034$  at 90% confidence level [72]) these formulae could be simplified and oscillations in atmospheric and solar sectors could be studied separately as effective 2 flavor transitions. Then, the formulae for oscillation probability are analogous to equations 2.1 and 2.2. They are only a function of one mixing angle and one squared mass difference –  $\theta_{23}, \Delta m_{23}^2$  (atmospheric neutrinos) or  $\theta_{13}, \Delta m_{13}^2$  (solar neutrinos). The example of analysis in which oscillation parameters  $\theta_{23}$  and  $\Delta m_{23}^2$  are constrained is presented in Chapter 5. Here, the  $\nu_\mu \leftrightarrow \nu_\tau$  transitions are dominant and the atmospheric  $\nu$  events are the background for diffused DM search. In case of solar neutrinos dominant transitions are  $\nu_e \rightarrow \nu_\mu$ . Solar neutrinos are not a background in a search for dark matter induced neutrinos due to their low energy, below 15 MeV.

## 2.4 Neutrino Sources

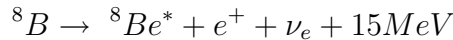
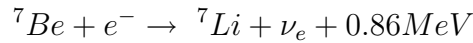
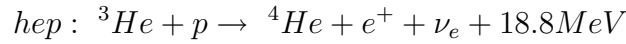
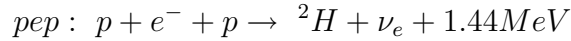
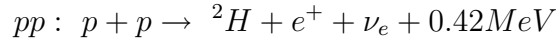
Neutrinos are abundant in the Universe. On average, there is only 3 times less neutrinos than photons in the cosmic space. According to the Big Bang cosmology, when neutrinos had decoupled from the state of thermal equilibrium in which all particles in the early Universe existed, they have formed a relic remnant similar to the cosmic microwave background. At the present stage of the Universe expansion these relic neutrinos have very small energies making them very difficult, if not even impossible, to detect (compare Fig. 2.5, referred there to as *cosmological*).

Moreover, there are number of processes in nature in which neutrinos are created. For instance, they are produced in thermonuclear reactions, radioactive decays, weak decays of mesons and muons. The most important natural and human-made neutrino sources are briefly discussed below. In Section 2.5 more information on atmospheric neutrinos is given as they constitute important source of background for the analysis presented in this thesis.

### 2.4.1 Natural sources

#### Solar neutrinos

The Sun and the other stars are natural nuclear fusion reactors. Neutrinos are created there mostly in proton–proton chain reactions of following types:



Neutrinos are also produced in so called *CNO* chain reactions which are mainly based on fusion of protons with carbon, nitrogen and oxygen.

In the course of thermonuclear fusion reactions only electron neutrinos are produced. They could travel from the Sun's core through its outer layers and outside without any appreciable absorption. Maximum energy of neutrinos produced in the Sun is around 15 MeV. However, most of them have energies below 1 MeV [56]. Neutrinos produced in stars other than the Sun have too low flux to be effectively observed on the Earth.

Experiments aimed at the detection of solar neutrinos gave a first hint on the neutrino oscillation phenomenon in the 1960's. Measured flux of electron neutrinos was lower than predicted by the Standard Solar Model (SSM) [74]. The first experiment reporting this effect was Homestake which started running in 1968 [75]. Next generation of experiments like SNO [63] and Super-Kamiokande [64] confirmed that part of electron neutrinos produced in the Sun transform into other neutrino flavors on their way to the Earth.

#### Atmospheric neutrinos

The primary source of atmospheric neutrinos is the decay of pions and kaons produced by cosmic ray collisions in the atmosphere. Cosmic rays, consisting of protons and ions, interact with nuclei in the upper layers of the atmosphere. That leads to production of hadronic showers, containing mostly pions. The pions (kaons) decay to a muon and a muon neutrino. The muons decay to an electron, a muon neutrino, and an electron neutrino (as shown in Fig. 2.2(d)). The creation of neutrinos in those processes is summarized in Fig. 2.6.

A flux ( $\phi$ ) of tau neutrinos expected from decays of charmed mesons, which are also produced in cosmic ray showers, is estimated to be several orders of magnitude lower than a flux of muon neutrinos and could be considered negligible in this discussion [86, 87].

Atmospheric neutrinos are mostly produced 15–30 km above the Earth's surface. Their average energy is much higher than solar neutrinos – mean energy is of several hundreds of MeV and the energy spectra has a long high energy tail reaching TeV scale (compare Fig 2.5).

Based on the simple neutrino production model derived above, one predicts a flux ratio of 2:1 for muon neutrinos to electron neutrinos. This is modified slightly in detailed calculations. There are also kaons produced in the hadronic showers which could decay to a neutral pion, an electron and an electron neutrino (for example,  $K^+ \rightarrow \pi^0 e^+ \nu_e$ ).

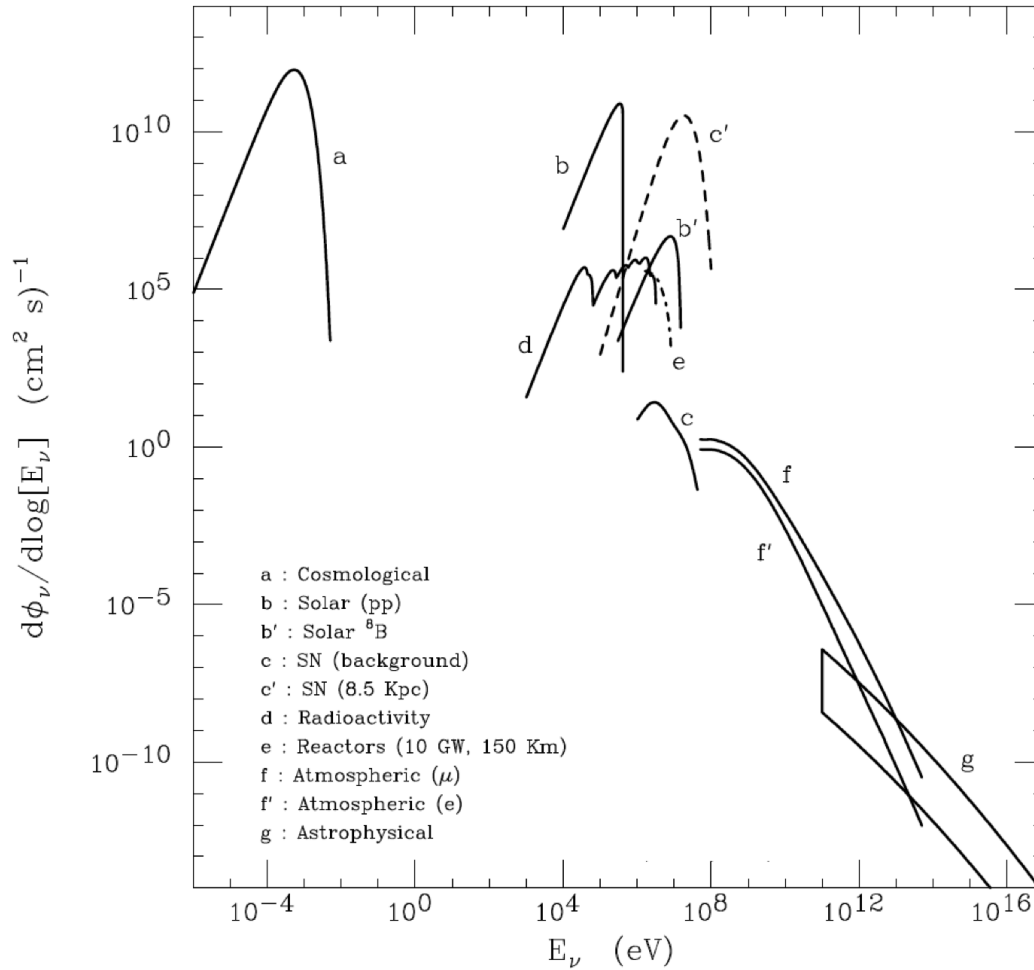


Figure 2.5: Energy spectra and fluxes of neutrinos at the surface of the Earth calculated for different neutrino sources [73].

There is 5% branching ratio (BR) for that process, while the BR for modes with a muon and a muon anti-neutrino production is 67% in case of kaons. Also, at high energy, some muons live long enough (due to Lorentz time dilatation) that they are stopped in the Earth before decaying in flight into high energy neutrinos. Despite these corrections, one generally expects to observe twice as many muon neutrinos than electron neutrinos but that was not confirmed experimentally. The measured ratio was smaller than expected by 63 – 65%, depending on the considered energy of neutrinos [65].

The other effect observed while studying atmospheric neutrinos, was the significant up-down asymmetry in the flux of high energy muon neutrino events [65]. There were more neutrinos coming from above the horizon than from below, *i.e.* from the other side of the Earth. That deficit was unexpected as absorption of neutrinos by matter should be negligible due to their very low interaction cross section with nucleons.

The unresolved mysteries of up-down asymmetry and flux ratio of muon to electron neutrinos turned out to be another evidences for neutrino oscillations. In this case  $\nu_\mu$  changes flavor to  $\nu_\tau$ . That reduces expected number of muon neutrino events. Hence, the flux ratio of  $\phi(\nu_\mu + \bar{\nu}_\mu)/\phi(\nu_e + \bar{\nu}_e)$  would be then lower than calculated in the scenario

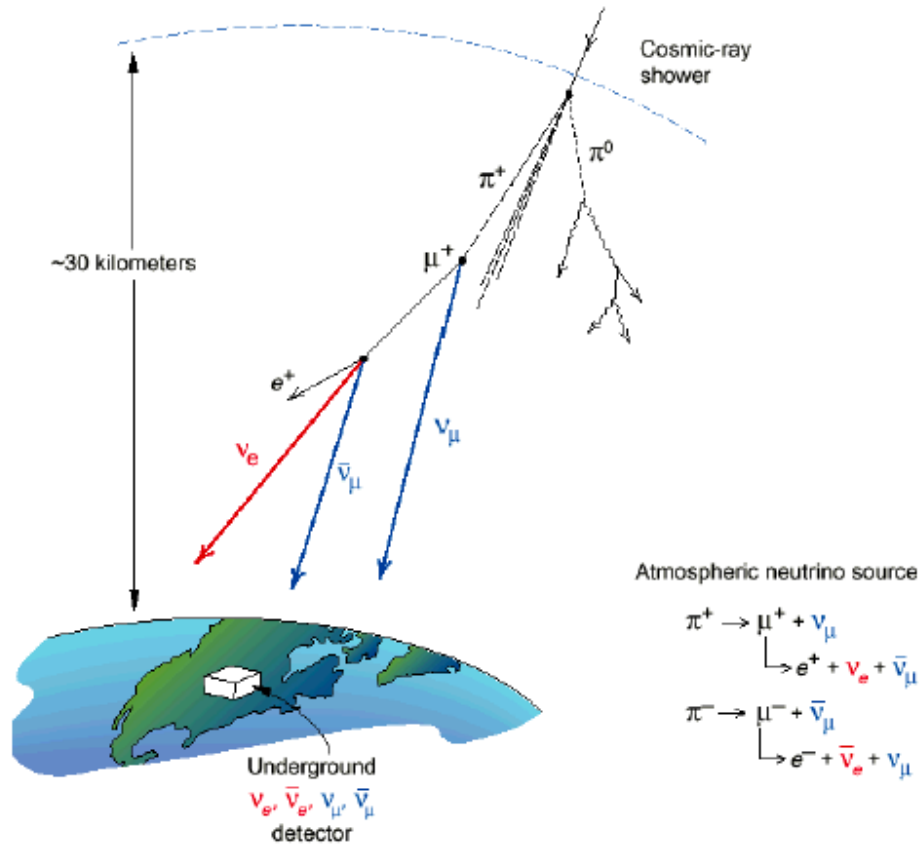


Figure 2.6: Schematic view of neutrinos' creation in the atmosphere.

without oscillations. Also, there would be less muon neutrinos coming from the direction below the horizon as they have a longer distance to travel than neutrinos produced in the atmosphere above the detector and this longer path enables flavor transitions to occur.

### Cosmic neutrinos

Neutrinos could be abundantly produced during the last stages of a stellar evolution which ends as supernova explosion. Here, so called *prompt* and *thermal* neutrinos are created. The first ones appear during core's collapse in a process when a proton absorbs an electron and transforms into a neutron and a neutrino. *Thermal* neutrinos are produced in annihilations of electrons and positrons. That could lead to creation of neutrino and anti-neutrino pairs of all flavors. Mean energy of supernova neutrinos is of the order of ten-odd of MeV. First neutrinos of that kind were observed directly on 23rd of February 1987 by Kamiokande, IMB, Baksan and LSD experiments during supernova explosion (SN1987A) which occurred in the Large Magellanic Cloud [80].

Apart from that, cosmic neutrinos are believed to be produced also during acceleration of relativistic plasma in some galaxies. That class of galaxies is being referred to as Active Galactic Nucleus (AGN) [81]. These type of galaxies contains a massive central Black Hole which attracts the surrounding matter and leads to production of relativistic jets of particles. In the process of acceleration, which is taking place inside relativistic jets,

the particles interact at high energies. New particles could be then created, including mesons that could later decay into high energy neutrinos. Neutrinos of this kind have not been detected so far, however their existence is well motivated. Their flux at the Earth is expected to be very low, see Fig. 2.5.

The other source of cosmic neutrinos could be annihilation or decay of DM particles. Search for such a signal is the goal of the analysis presented in this thesis.

### Geo-neutrinos

It is expected that large amounts of electron anti-neutrinos originate from  $\beta$  decays in the radioactive chains of  $^{238}\text{U}$ ,  $^{232}\text{Th}$  and  $^{40}\text{K}$ . Study of anti-neutrinos produced by these radioactive isotopes in the Earth's crust and mantle may help to understand the composition of our planet's interior and cross check heat flow models. There is also an interesting question whether there is an active geo-reactor running in the Earth's core. Study of geo-neutrinos could bring answer to this question.

Geo-neutrinos have typically energies of a few MeV which is at least significantly lower than expected for dark matter induced neutrinos. Therefore, they rather do not interfere with any search for neutrino signal from dark matter annihilation. Interesting results on the search for geo-neutrinos were already published by Kamland [76] and Borexino collaborations [77].

## 2.4.2 Artificial sources

### Reactor neutrinos

Reactors in nuclear power plants emit electron anti-neutrinos originating from  $\beta$  decays. Large reactor can produce even up to  $6 \cdot 10^{20} \bar{\nu}_e$  per second. Their emission is isotropic therefore the flux decreases with a square of distance from the reactor. Typical energy of reactor neutrinos is of several MeV. Thus, their energy is different than expected for DM-induced neutrinos and, similarly to geo-neutrinos, they do not constitute a background in the search for possible signal from dark matter.

### Accelerator neutrinos

It is possible to create a beam of neutrinos in the laboratory in the same way as neutrinos in the atmosphere are produced. Accelerated protons can produce mesons and kaons in the collisions on a fixed target. That mesons could be magnetically collimated and focused into a long tunnel where they decay in flight. Because of the relativistic boost of the decaying particles, neutrinos rather form a beam than are emitted isotropically. Experimental techniques of neutrino beams production are already well advanced and allow to control direction and energy of neutrinos with a good accuracy. Therefore, control over  $E$  and  $L$ , present in equations 2.1, 2.2, allows precise investigation of neutrino oscillation effects.

The studies of neutrino oscillation phenomena using accelerator neutrinos could be divided into the *appearance* and *disappearance* searches. In the first case one tries to observe neutrinos of a flavor different than the one with which they were originally produced. That could directly prove their spontaneous transitions into the neutrinos of the other flavor during propagation. In the *disappearance* studies, one is measuring the

flux of neutrinos of the initial flavor at the near detector before oscillations could occur and then comparing it with a flux measured at the far detector. If there were no oscillations, then the flux measured at the far detector should be in agreement with the expected flux calculated from the one measured at the near detector. The decrease in the flux observed at the far detector depends on the value of oscillation parameters.

Many oscillation studies based on accelerator neutrinos have already been performed or are in progress. To mention only a few such as NUMI (beam from FermiLab to Sudbury Mine in the Minnesota) [78], K2K (KEK to Kamioka) [79], CNGS (CERN to Gran Sasso) [67], T2K (Tokai to Kamioka) [6]. The last project is currently in operation with a great involvement of Polish groups, including author of this thesis. During his Ph.D. studies author has been involved in the simulations of cosmic ray muons underground for a shallow location of ND280 detector [7], which is the near detector of T2K experiment. These studies were used to evaluate the cosmic ray muon rate at the Side Muon Range Detector of ND280 and to determine the requirements for a cosmic ray trigger [82].

The average energy of neutrinos produced in T2K is around 800 MeV. These neutrinos are detected at Super-Kamiokande which is a far detector of T2K. Super-Kamiokande was also a far detector in K2K accelerator experiment which collected data from June 1999 until November 2004 with the mean energy of neutrino beam 1.3 GeV. Even though the energy of neutrinos from a beam could be relevant in case of low mass WIMP search, these neutrinos do not contribute to the samples used in the analyses presented in this thesis. Interactions of neutrinos related to K2K/T2K beam can be tagged according to the GPS system. In the periods of time when neutrino events from a beam were expected at SK, the recorded events contributed only to the K2K/T2K specific data samples. They are not used in any other analyses than specific to the oscillation studies of accelerator neutrinos.

In summary, various sources of neutrinos are listed in this section. Among them, only atmospheric neutrinos constitute the background in the search for DM-induced neutrinos from annihilation or decay of WIMPs. Energy of atmospheric neutrinos correspond to the range of masses expected for neutralinos (from several GeV to several TeV). The energy of solar neutrinos, geo-neutrinos, reactor neutrinos and neutrinos from a supernovae is below several tens of MeV. Event rate from neutrinos produced in the AGNs is expected to be negligible and direction of these neutrinos would be strongly correlated with the position of their source on the sky map. Interactions of neutrinos produced in the accelerators contribute only to selected samples based on the accurate expectation on the time of their arrival at the detector. In the following section more detailed information on the characteristics of atmospheric neutrinos is given.

## 2.5 Atmospheric Neutrino Properties

More detailed characteristics of atmospheric neutrinos are presented in this section. It would be good to know the flux of atmospheric neutrinos without oscillations before the searches for dark matter and studies of neutrino oscillations in the atmospheric sector are described in the next chapters.

There are several calculations of fluxes of atmospheric neutrinos and in the analyses presented in this thesis, related to the Super-Kamiokande experiment, the calculations by Honda *et al.* are used [83]. It is essential to have a dedicated flux prediction for the

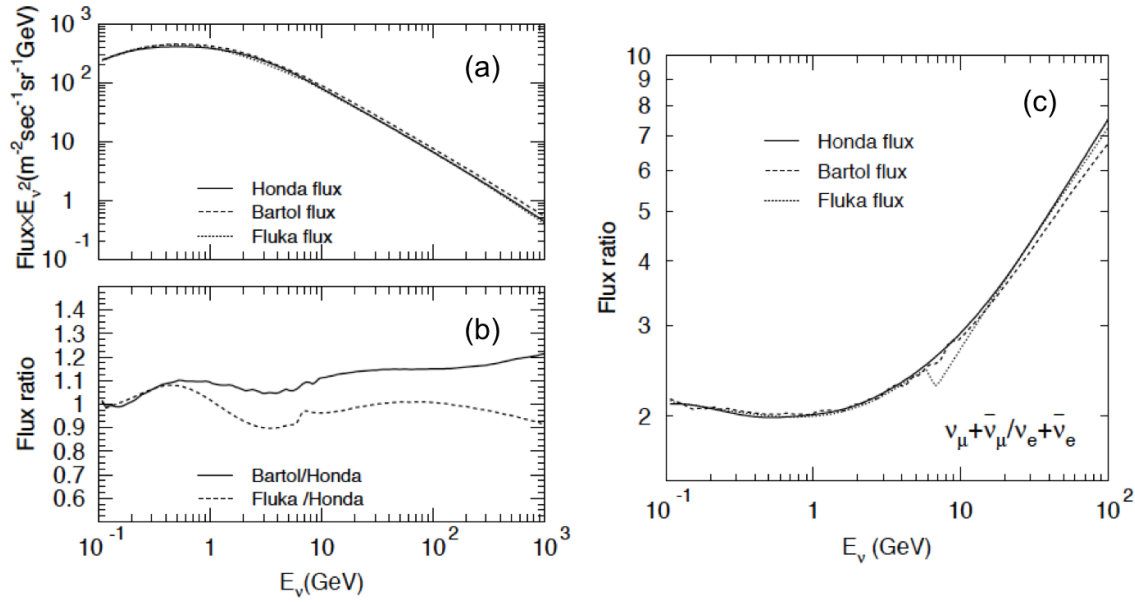


Figure 2.7: *Left panel* – (a) The direction averaged atmospheric neutrino energy spectrum for  $(\nu_\mu + \bar{\nu}_\mu)$  calculated by several authors. (b) The ratio of the calculated neutrino fluxes. *Right panel* – (c) The flux ratio of  $(\nu_\mu + \bar{\nu}_\mu)$  to  $(\nu_e + \bar{\nu}_e)$  averaged over all zenith and azimuth angles versus neutrino energy. Solid, dashed and dotted lines show the prediction by [83], [84] and [85], respectively. All figures from Ref. [5].

geographical location of the experiment due to influence of the Earth’s magnetic field on the primary cosmic rays. Neutrinos of energy around 1 GeV are produced by cosmic rays of energy around 10 GeV. The primary fluxes of cosmic ray components are relatively well known at these energies. However, it is also known that primary cosmic rays of less than 10 GeV are affected by the geomagnetic field through a rigidity (momentum/charge) cutoff. Moreover, their fluxes are also modulated by the solar activity, with the minimum flux occurring at times of high solar activity. Geomagnetic and solar effects are not relevant for cosmic rays of energy greater than 1000 GeV, *i.e.* for neutrinos of energy above 100 GeV. However, primary fluxes of cosmic ray components at such high energies are not as well measured and there is greater uncertainty on their prediction.

Figure 2.7(a) shows the direction averaged atmospheric neutrino energy spectrum of  $(\nu_\mu + \bar{\nu}_\mu)$  calculated specifically for the Kamioka Observatory site. The solar and magnetic effects were incorporated into the calculations [83]. The flux was obtained for the period from summer 1996 to summer 2001. Besides the prediction by Honda *et al.* [83] also the calculations by Bartol [84] and Fluka collaborations [85] are shown for comparison. In figure 2.7(b) the ratio of these fluxes is presented as a function of neutrino energy. Below 10 GeV the agreement between various calculations is at the level of 10%. Above 10 GeV some discrepancies arise. They are related to the uncertainties in the measurement of cosmic ray components of the highest energies. Hence, different parametrizations of cosmic ray fluxes were adopted by the authors.

Existing differences between various predictions are not so much relevant in dark matter searches. Any dark matter induced neutrino signal in order to be confirmed has to be significantly different than background in the same energy range. It can be also

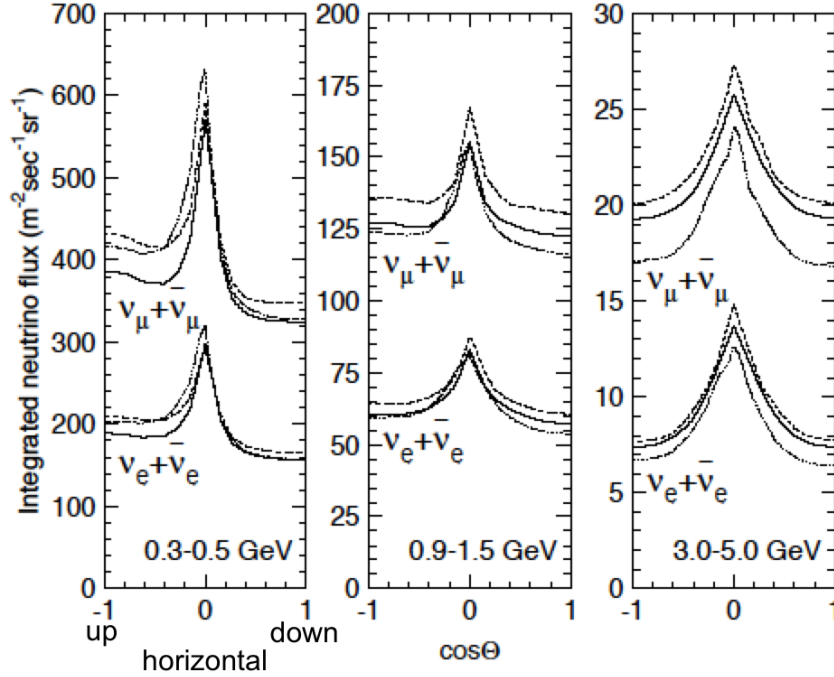


Figure 2.8: The flux of atmospheric neutrinos versus zenith angle calculated for Kamioka Observatory location for several neutrino energies (neutrino oscillations not included) [5]. Solid, dashed and dotted lines show the prediction by Honda [83], Bartol [84] and Fluka [85], respectively.  $\cos \theta = -1$  stands for the upward-going vertical tracks;  $\cos \theta = 0$  describes horizontal tracks; and  $\cos \theta = 1$  is for downward-going vertical tracks.

noticed that atmospheric neutrino flux is steeply falling with neutrino energy. Therefore, the greater the mass of DM particle is, the more likely that strong signal would be observed as the background is exponentially falling at high energy.

Figure 2.7(c) shows calculated flux ratio of  $\nu_\mu + \bar{\nu}_\mu$  to  $\nu_e + \bar{\nu}_e$  as a function of neutrino energy (integrated over solid angle). Predictions by various authors agree below 5 GeV. Above this energy there are some uncertainties related to kaon production in the hadronic showers. Kaons decay into neutrinos in a similar chain as pions do. Contribution of neutrinos originating from  $K$  decay in the atmosphere is more important at higher energies. There is only about 20% (10%) of kaon induced neutrinos for  $\nu_\mu + \bar{\nu}_\mu$  ( $\nu_e + \bar{\nu}_e$ ) at 10 GeV of  $\nu$  energy. But it increases to more than 30% at 100 GeV for both  $\nu_\mu + \bar{\nu}_\mu$  and  $\nu_e + \bar{\nu}_e$ . For a dark matter signal the ratio of neutrinos of various flavors could be essentially different than for atmospheric neutrinos. This issue is discussed more in the next chapter in Section 3.2.3.

There are also tau neutrinos produced in collisions of cosmic rays with nuclei in the atmosphere. The main source of tau neutrinos is related to charmed particle production and decay. The decay of  $D_s$  meson is the dominant source of tau neutrinos. For example, a leptonic channel  $D_s^+ \rightarrow \tau^+ \nu_\tau$  has a few percent branching ratio. In literature, the neutrino production from charmed hadrons is often referred to as prompt neutrino production. In addition to  $D_s$  decay, the tau lepton, produced in the process, has a short lifetime (around 290 femtoseconds) and decays immediately into many different final states. These final states consist always of a tau neutrino and some other particles like electrons ( $\sim 18\%$

BR), or muons ( $\sim 17\%$  BR), or one or more pions ( $\sim 65\%$  BR). Therefore, tau leptons from decays of  $D_s$  mesons contribute also to the total  $\nu_\tau$  flux.

Even though the value of a prompt tau neutrino flux is increasing with neutrino energy [86, 87], it remains several orders of magnitude lower than the value of the muon neutrino flux obtained for the same neutrino energy (for example, compare Fig. 7 in [87]). The above statement is valid up to the energy of several hundreds of TeV. Therefore, it is justified to neglect prompt tau neutrinos in the search for diffuse DM signal, as well as in neutrino oscillation analysis, as they yield a marginal fraction of observed atmospheric neutrino events. Separate issue is related to the flux tau neutrinos that may originate from oscillations of muon neutrinos. That case is explained in Section 5.4 at the stage when neutrino oscillations are included in the discussion of atmospheric neutrino properties.

Figure 2.8 shows zenith angle ( $\cos\theta$ ) distributions of atmospheric neutrinos as calculated for several neutrino energies. If not indicated otherwise, all zenith angle distributions presented in this thesis should be interpreted the following way: value  $-1$  of  $\cos\theta$  stands for the upward-going tracks;  $\cos\theta = 0$  describes horizontal tracks; and  $\cos\theta = 1$  is for downward-going vertical tracks. It can be seen that for Kamioka location some asymmetry between downward- and upward-going atmospheric neutrinos is expected at low energy range. That is due to the deflection of primary cosmic rays by the geomagnetic field. For neutrino energies higher than few GeV this effect is negligible and the calculated fluxes are symmetric.

There are more horizontal tracks than vertical ones as it can be observed in Fig. 2.8. Pions, kaons and muons which are produced in horizontal showers have larger effective path length than their counterparts produced in vertical showers. Therefore, more of them could decay into neutrinos while a larger fraction of the particles present in the vertical showers hit and stop in the ground without having a chance to decay in flight.

Angular distribution expected for dark matter induced neutrinos would be different than the one of atmospheric neutrinos. Signal events would either indicate some excess at the direction related to the source of enhanced DM annihilation. Or, their angular distribution would be isotropic (flat in  $\cos\theta$ ) in case of the uniform DM annihilation in the entire cosmic space. The search for a *point-like* signal is described in Section 3.1. The idea of a search for a diffuse annihilation signal is discussed in Section 3.2.

# Chapter 3

## Neutrinos from Dark Matter Annihilation

Neutrinos are expected to be produced in dark matter annihilation which is taking place in the entire cosmic space – both in the galactic halos as well as in the outer galaxy regions [1]. Recently, some authors have also postulated scenarios with decaying dark matter, e.g. [88, 89]. The decay of DM particles could also lead to appearance of neutrinos. Neutrinos originating from the annihilation (or decay) of the relic particles could be created directly or in a subsequent decays of mesons and heavy leptons. The energy spectrum of these neutrinos and branching ratio (BR) for their production is model dependent.

There are two main strategies in the search for dark matter induced neutrinos. They are related to the spatial distribution of a source:

1. *Point-like search.* In this type of search one is looking for neutrinos originating from a particular direction by comparing observed flux with expected background in the same angular range (for example with a flux of atmospheric neutrinos, in case of measurements on the Earth). In analyses of data from neutrino telescopes, the reconstructed direction of incoming neutrino is the main selection criterium.

Since DM annihilation rate is proportional to density squared of relic particles (Eq. 1.3), the searches focus on the regions where expected DM density could be larger. For instance, many models of galaxies anticipate increased DM concentration in their central regions. Such a cusp in DM density distribution is expected from numerical simulations of formation of the galaxies [16]. Moreover, it is also believed that massive celestial objects like the Sun, the Earth or the region of the Galactic Center (GC) could trap dark matter particles. Bound by the strong gravitational potential, DM particles accumulate inside such objects – their density is increasing there which results in enhanced annihilation rate [44].

2. *Diffuse search.* In the analysis of this type one seeks for the signal arising from all directions without distinguishing any particular source region. The relic particles are believed to be distributed randomly over the large cosmic volumes. This statement is also true for DM galactic halos. Apart from hypothetical cusps in density profiles foreseen for the central regions [16, 17, 18], the whole DM halo surrounding any galaxy like the Milky Way is a diffuse source of DM annihilation products [90]. Neutrinos originating from diffuse DM annihilation or decay would be isotropic in

coordinate system related to the Earth. The energy carried by these neutrinos is model dependent. However, if that energy could be specified, that would introduce a propitious factor in search for DM diffuse signal as the background events could have different energy characteristics.

The outline of this chapter is the following. Results of searches for neutrinos from DM annihilation in the Sun, core of the Earth and in the region of the Galactic Center are shown in the first part of the chapter. Presented results are based on the data from Super-Kamiokande detector and were published by the SK collaboration in 2004 [44]. The comparison of these results with limits on WIMP-nucleon cross section  $\sigma_{\chi N}$ , obtained in direct detection experiments, is also shown. In the last part of the chapter, the idea of search for diffuse neutrino signal from DM annihilation and DM decay is explained. Following this concept, the Super-Kamiokande data were analyzed by the author of the thesis, searching for the diffuse DM signal arising from the Milky Way. This analysis is discussed further in Chapters 6 and 7.

### 3.1 Neutrinos from Dark Matter Annihilation in Earth, Sun and Galactic Center

In the following section, search for neutrino signals arising from dark matter annihilation taking place in the Sun, core of the Earth or in the region of the Galactic Center is described. It is expected that WIMPs could accumulate inside these heavy objects due to scattering with nuclei and energy loss.

As it is explained in Section 1.3.1, one can distinguish two types of WIMP scattering: spin-dependent (SD) and spin-independent (SI) [27]. If the final WIMP velocity after scattering is less than its escape velocity, the particle will be gravitationally trapped inside the celestial object and eventually due to subsequent scattering will accumulate in the center of gravitational potential. Two WIMPs could annihilate there and produce, depending upon their mass and composition, primarily  $\tau$  leptons,  $b$ ,  $c$  and  $t$  quarks, gauge bosons or Higgs bosons [2]. In *supersymmetric* models, annihilating WIMPs most likely couple to the particles with masses closest to their mass. Finally, many kinds of particles, like neutrinos, positrons, antiprotons are produced via decay of primary annihilation products and these ones could be observed by certain terrestrial and satellite experiments.

Neutrinos are the only particles capable of escaping from very high density regions like the Earth's or the Sun's core. According to *supersymmetric* models, the mean energy of the neutrinos from neutralino annihilation would be in the range of 1/3 to 1/2 the mass of WIMP [44]. Hence, the searches are mostly focused on neutrinos of the energy from several GeV up to several TeV.

The search is performed by looking at the flux of neutrinos associated with the direction to investigated celestial object. If there were a dark matter annihilation taking place there, one would expect to observe an excess of particles above atmospheric neutrino background in that given angular range. In case of null observation, or when a signal is too weak and cannot exceed the background level, one could derive the limit on DM-induced neutrino flux. This limit corresponds to the flux that would have been observed if dark matter was there producing neutrinos via annihilation.

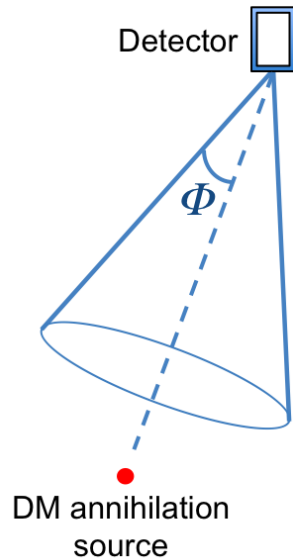


Figure 3.1: Illustration of a cone half-angle  $\Phi$  used to investigate the value of neutrino flux from a given angular region around the position of DM annihilation source.

The search of this kind was already performed using data from neutrino telescopes like AMANDA [91], Ice-Cube [43] and Super-Kamiokande [44]. Below, the main results from Super-Kamiokande detector are summarized.

### 3.1.1 Results from Super-Kamiokande

The search was performed using neutrino induced upward through-going muons and was published by the Super-Kamiokande collaboration in 2004 [44]. Upward-going muons (UPMU) are produced in the rock below the detector via charged current interactions of neutrinos. Downward-going muons are also produced in neutrino interactions above the detector but these are few comparing to overwhelming background of cosmic ray muons coming also from the same direction. However, flux of cosmic ray muons is completely stopped after traversing several kilometers in the ground. Therefore, upward-going muons cannot be produced in the atmosphere and must be neutrino induced. Neutrinos of energy greater than several GeV produce muons passing through the detector. The search was restricted only to such events. More information on UPMU events and other SK event samples is given in Chapter 5.

The data set used in the indirect search for WIMPs presented in Ref. [44] is based on 1679.6 days of data taking from April 1996 to July 2001. Currently, the new paper from Super-Kamiokande is in preparation with the results of the search based on statistics extended to 3109.6 live-days and collected until August 2008 [92]. No statistically significant excesses of events above the expected level of atmospheric neutrino background were seen in both analyses. The cones around the core of the Earth, the Sun, and the Galactic Center (Fig. 3.1) were investigated as the potential sources of DM-induced neutrinos.

Figures 3.2 show the zenith angle distributions of upward through-going muons with respect to the center of the Earth 3.2(a), the Sun 3.2(b) and the Galactic Center 3.2(c). Data from Super-Kamiokande are marked as dots with error bars. Expectation on the level of atmospheric neutrino background without oscillations is indicated as hatched

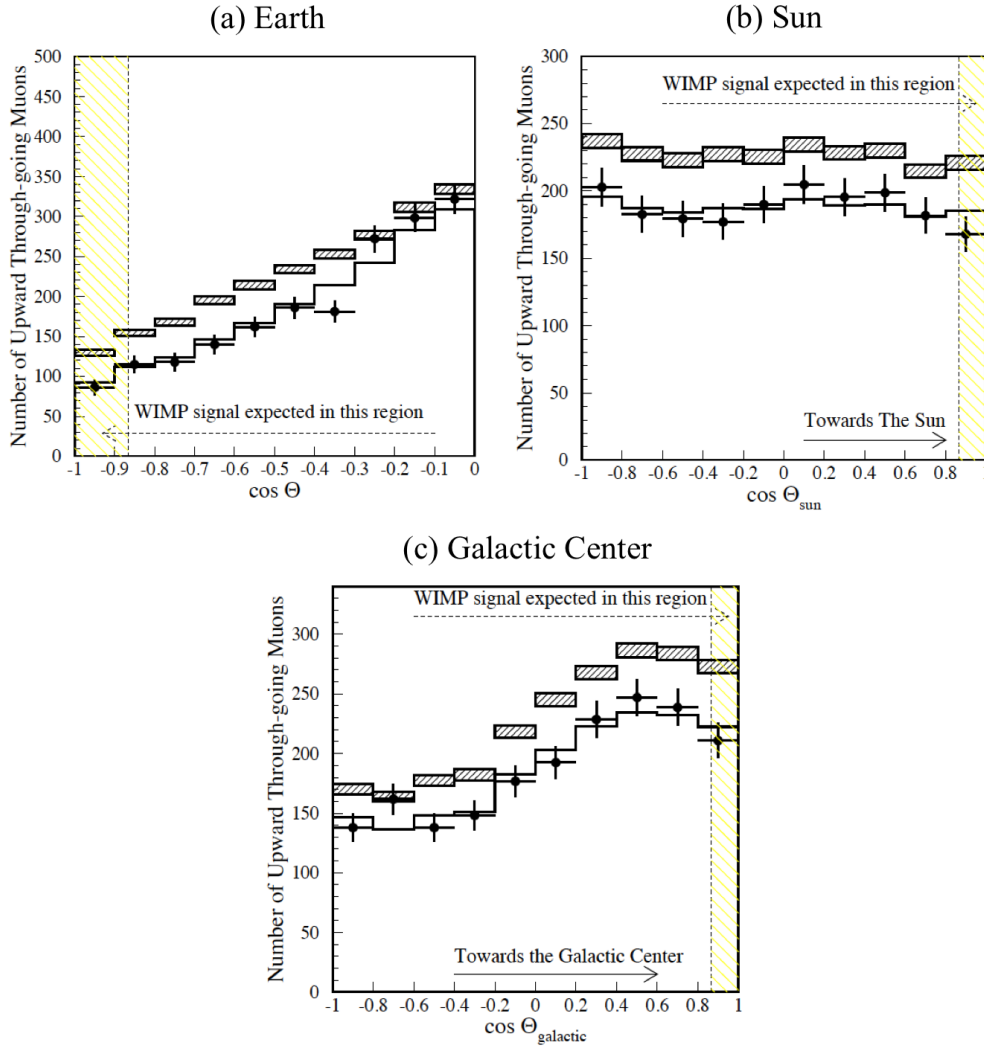


Figure 3.2: Zenith angle distributions of upward through-going muons at Super-K based on 1679.6 live days of exposure [44]. Distributions with respect to the center of the Earth (a), the Sun (b) and the Galactic Center (c) are shown. Points indicate observed data with statistical uncertainties. Hatched boxes mark atmospheric neutrino background expectation without  $\nu$  oscillations. The height of the box is related to statistical uncertainty. Solid lines indicate background after taking into account neutrino oscillations with  $\sin^2 2\theta_{23} = 1.0$  and  $\Delta m_{23}^2 = 2 \times 10^{-3} \text{ eV}^2$ . The angular region where DM-induced signal is expected is indicated on each plot as the hatched yellow area.

boxes. Solid lines mark the background expectation after taking into account oscillations with the following values of oscillation parameters:  $\sin^2 2\theta_{23} = 1.0$  and  $\Delta m_{23}^2 = 2 \times 10^{-3} \text{ eV}^2$ . More information on evaluation of atmospheric neutrino background can be found in Chapter 5.

The angular region where DM-induced signal is expected is indicated on each plot as the hatched yellow area. These regions were investigated using various cone half-angles around the potential source of annihilation (see Fig. 3.1). The simulation of a size of a cone's half-angle that contains 90% of the flux of neutrinos from DM annihilation in that given region was performed as function of a WIMP mass. Generally, the heavier the

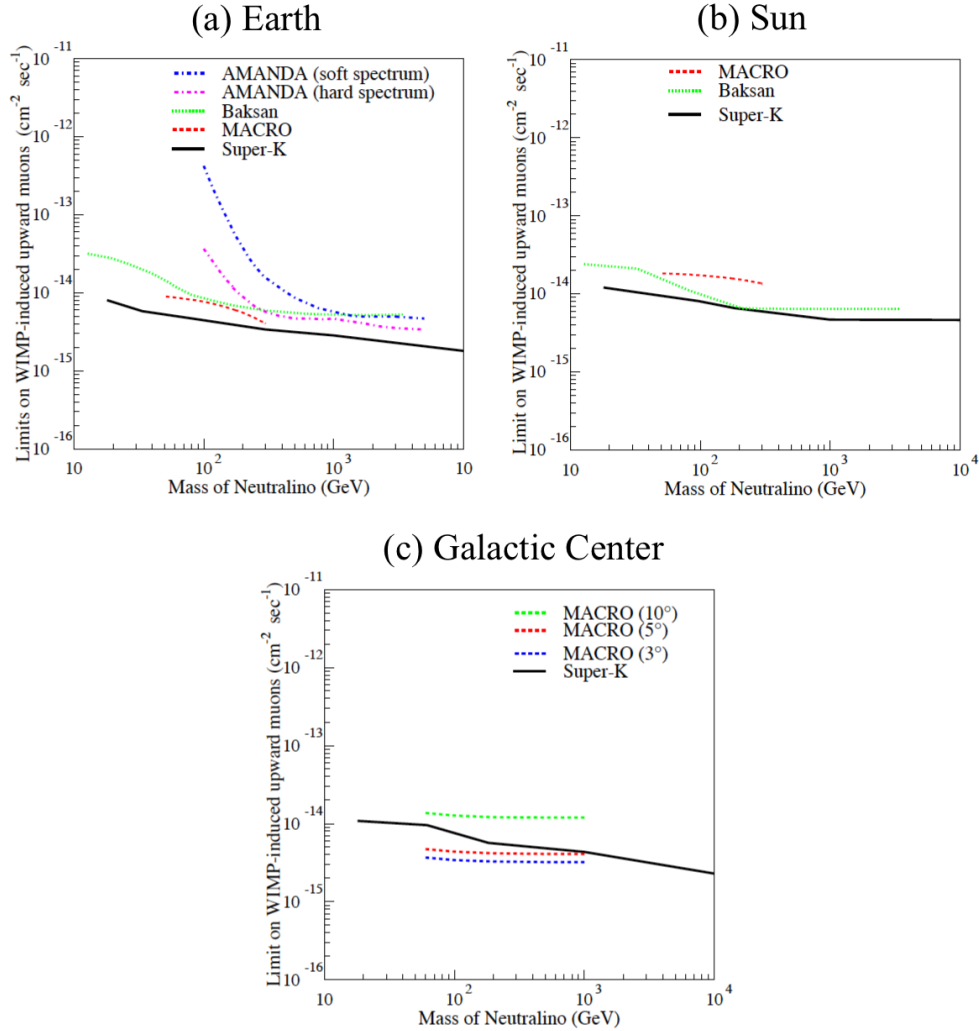


Figure 3.3: Super-Kamiokande DM-induced upward-going muon flux limits as a function of neutralino mass [44]. Upper 90% confidence limits from neutralino annihilations in the Earth’s core (a), the Sun’s core (b) and in the Galactic Center (c) are shown with corresponding limits from the other experiments. See text for a reference to the experiment’s publications.

DM particle is, the smaller is the half-angle that contains 90% of a resulting signal flux. That is mainly due to kinematics of neutrino interactions. Heavy neutralinos produce neutrinos of a harder spectrum and in case of their CC interactions the outgoing lepton follows closer the direction of a parent neutrino. Leptons produced in interactions of low energy neutrinos have wider spread of their directions with respect to direction of parent neutrinos. The simulations assumed that 80% of neutralino annihilations are into  $b\bar{b}$  quarks, 10% into  $c\bar{c}$  and 10% are into  $\tau^-\tau^+$  leptons. However, the neutrino-muon scattering angle depends mainly on the neutralino mass (via energy of produced neutrinos) and is not much sensitive to different annihilation branching ratios [93]. For the Earth, the cones of half-angles  $2^\circ$  and  $22^\circ$  contain 90% of the neutrino flux from WIMP annihilations with masses of 10 TeV and 18 GeV respectively. The corresponding numbers for the Sun are  $1.5^\circ$  and  $19^\circ$  for the same WIMP masses. The dependence of a cone half-angle versus WIMP mass for other intermediate masses can be found in [94, 95].

No excess of events was observed in neither case of a cone half-angle configuration and annihilation source. Therefore, it is possible to derive a 90% confidence limit on DM-induced neutrino flux as a function of neutralino mass. These limits are presented in figures 3.3. The comparison of Super-K flux limits with searches by other experiments is also shown there. The limits obtained in the AMANDA, BAKSAN and MACRO experiments are described in references [91], [96], [93], respectively. The lower bound of  $M_\chi = 18$  GeV in Super-Kamiokande analysis is the minimum WIMP mass for which at least 90% of the upward-going muons will be through-going rather than stopping in the detector. Upper bound is arbitrary.

### 3.1.2 Comparison with Direct Detection Results

Direct detection aims at observing WIMP scattering off nucleus in the detector medium (more on that can be found in Chapter 1.4). Indirect detection probes as well WIMP annihilation mechanism as their interactions with nuclei, when they scatter and are being trapped inside massive celestial objects. It is expected that WIMP density increases in the core of massive objects and the annihilation rate increases until equilibrium is achieved between capture and annihilation processes [44]. That makes the annihilation rate, which involves two captured WIMPs, half of the capture rate. Under these equilibrium conditions it is possible to compare rates in direct and indirect experiments as then, for a given DM halo model, they primarily depend on a WIMP-nucleon cross section  $\sigma_{\chi N}$  and WIMP mass.

One could calculate the ratio of direct detection rates to the flux of upward-going muons from WIMP annihilations in the Earth and the Sun [97]. To give an estimate of the sensitivities of the direct and indirect searches, the event rate in a 1 kg germanium detector is equivalent to the event rate in a  $10^5 - 10^7$  m<sup>2</sup> muon detector for neutralino with primarily scalar coupling to nuclei. And the event rate in a 50 gram hydrogen detector is roughly the same as in a  $10 - 500$  m<sup>2</sup> muon detector for a neutralino with pure axial vector coupling. The effective area corresponding to the Super-Kamiokande detector is equal 1200 m<sup>2</sup> and encompass the rock surrounding the detector (muons produced in CC  $\nu_\mu$  interactions outside detector can be observed in SK).

Using the maximum inferred ratio of the direct to indirect detection rates and Super-K limit on DM-induced upward-going muon flux (Fig 3.3), one can get conservative limits on WIMP-nucleon spin-independent (on oxygen) and spin-dependent (on protons) cross sections. To get a limit on spin-independent cross section, the DM-induced flux limits from the Earth and the Sun were used (compare Fig. 3.3). In the Earth, WIMPs undergo mainly scalar interactions due to large abundance of nuclei with even mass number [102]. In the Sun, WIMPs could interact through scalar as well as axial vector interactions. The fraction of spin-independent interactions in the total number of neutralino interactions in the Sun is unknown. Therefore, in order to get a conservative result it was assumed that all interactions were with scalar couplings. On the other hand, it is also possible to constrain a WIMP-proton spin-dependent cross section based on the WIMP flux limits from the Sun due to the large abundance of hydrogen in the star. In this case, it was assumed that all WIMP interactions in the Sun were with couplings to unpaired spin of the nucleon.

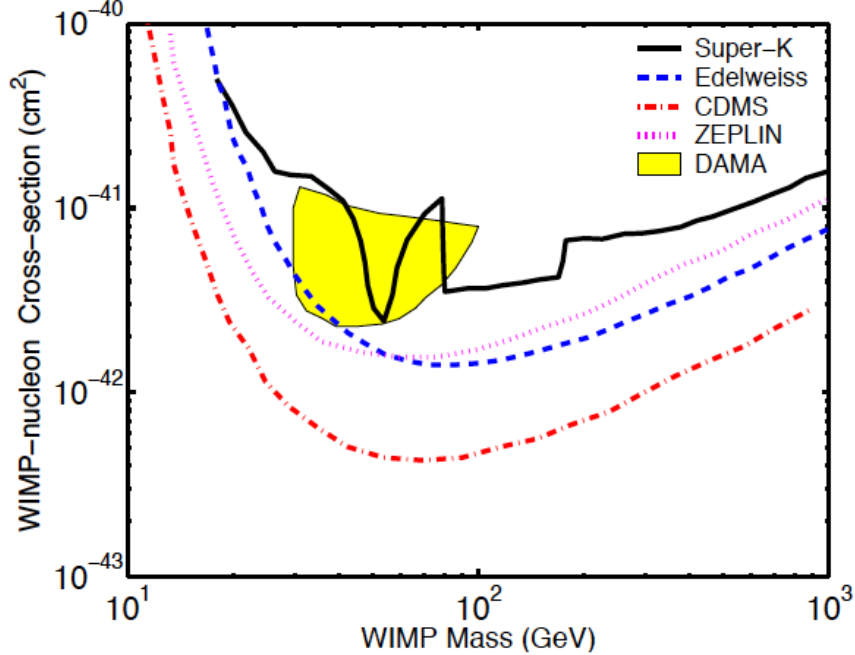


Figure 3.4: Exclusion plot in WIMP parameter space from Ref. [44]. Values of WIMP-nucleon cross section above lines are excluded. Super-Kamiokande 90% CL limit is indicated as a solid line and obtained for WIMP with scalar coupling using limits on WIMP-induced muons from the Sun and the Earth [44]. Also shown are DAMA  $3\sigma$  allowed region (filled) [98], 90% CL exclusion limit from CDMS (dot-dashed) [99], EDELWEISS (dashed) [100], and ZEPLIN (dotted) [101].

The following equation was used to derive the upper limit on WIMP-nucleon cross section from Super-K limit on flux of DM-induced upward-going mouns [44]:

$$\text{Max Ratio}(M_\chi) = \frac{\text{Direct Detection Rate}(M_\chi, \sigma_{\chi N})}{\text{Super-K flux limit}(M_\chi)}. \quad (3.1)$$

The quantity on the left is the maximum calculated ratio of direct to indirect detection rates for WIMPs with purely scalar or axial vector couplings [97]. The numerator on the right hand side indicates the event rate in a direct detection experiment as a function of WIMP mass and cross section. The denominator on the right hand side is the combined Super-K limit from the Sun and the Earth in case of spin-independent interactions or a single limit from the Sun in case of spin-dependent interactions. Equation 3.1 is solved for  $\sigma_{\chi N}$  to get the upper limit on spin-independent WIMP-nucleon cross section (Fig. 3.4) or on spin-dependent WIMP-proton cross section (Fig. 3.5). Derived limits on  $\sigma_{\chi N}$  from Super-K can be compared with those obtained from direct detection experiments.

The Super-K limit presented in Fig. 3.4 has a minimum around  $M_\chi = 56$  GeV. That corresponds to the mass of iron, the abundance of which in the Earth is about 30% [102]. There is expected enhancement in the 56 GeV WIMP capture rate in the Earth due to WIMP and iron mass matching – the WIMPs effectively lose most of their energy in the scattering when their mass matches the mass of target element.

In Fig. 3.4 and 3.5 it can be seen that constraints from Super-K have some discontinuity regions in addition to the structure observed around  $M_\chi = 56$  GeV for spin-independent scattering in the Earth in Fig 3.4. The first discontinuity occurs at around 80 GeV (mass

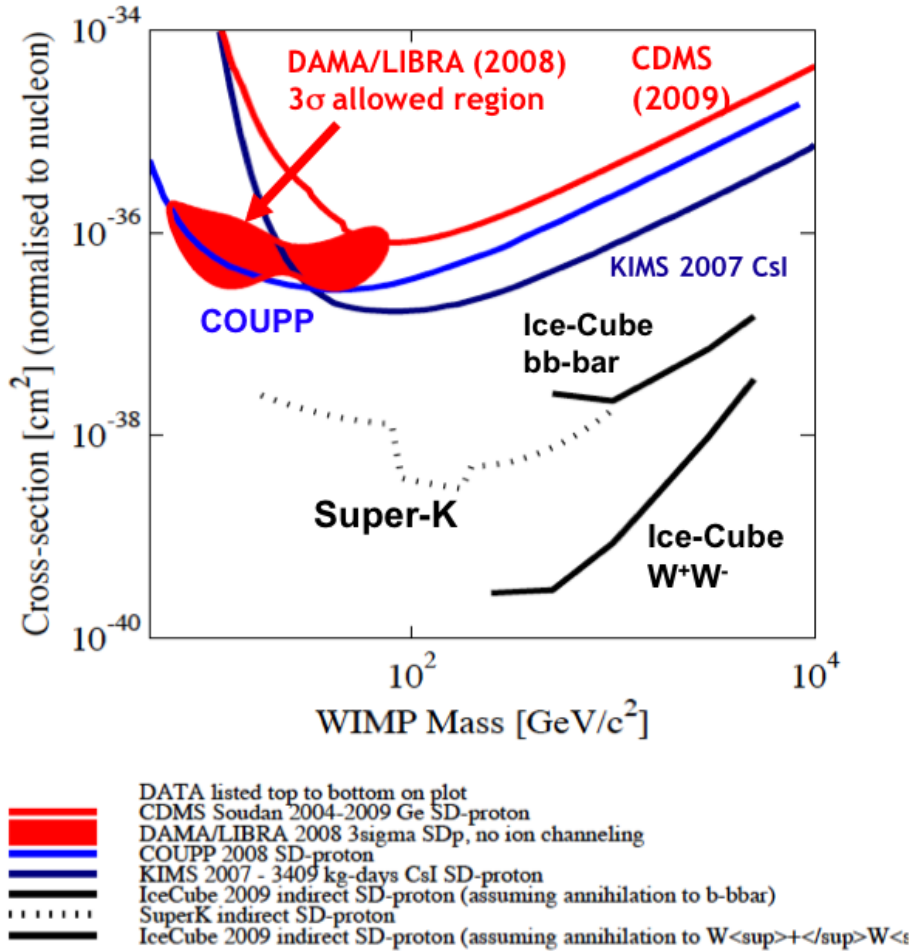


Figure 3.5: Exclusion plot in WIMP parameter space based on Ref. [34]. Values of WIMP-proton cross section above lines are excluded. Super-Kamiokande 90% CL limit is indicated as a black dashed line and obtained for WIMP with spin-dependent coupling using limits on WIMP-induced muons from the Sun [44]. 90% CL exclusion limits from other direct (CDMS, KIMS, COUPP) and indirect (Ice-Cube) experiments are shown. DAMA  $3\sigma$  allowed region (as interpreted in Ref. [30]) is partially excluded with constraints from Super-K.

of  $W^\pm$ ) and the other one at around 172 GeV (mass of top quark). They are related to the details of calculation of direct to indirect detection ratios [97]. For WIMPs more massive than the top quark, the most dominant annihilation channel is related to annihilation into  $t\bar{t}$  pairs. For WIMPs less massive than the top quark, the annihilation is mostly to gauge bosons. In case of WIMPs lighter than  $W$  boson, annihilation into  $\tau\bar{\tau}$  leptons governs the calculation in Ref. [97].

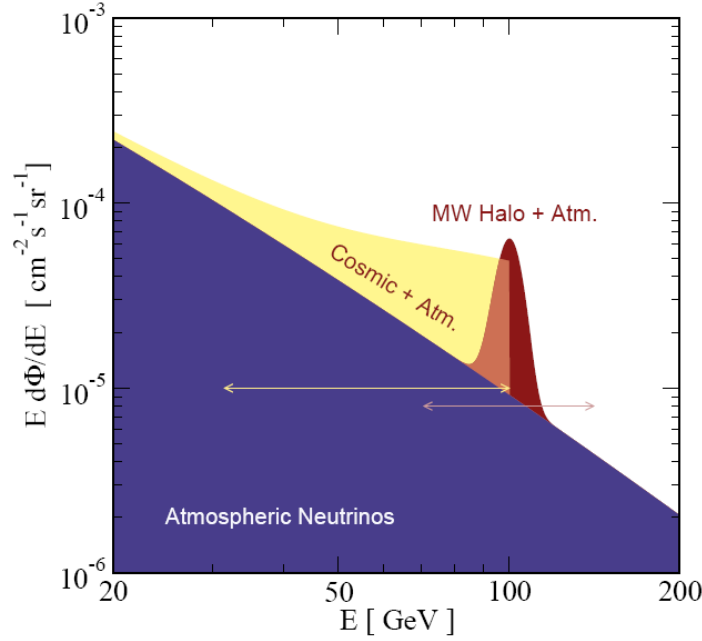


Figure 3.6: Expected signal from the diffuse annihilation of a 100 GeV DM particle, added to the atmospheric neutrino spectrum (blue region). Here, contributions of DM from the Milky Way halo (red) and large distance cosmic sources (yellow) are taken into account. The halo signal is sharply peaked, the cosmic signal is smeared due to the various redshift of the sources.  $E$  stands for neutrino energy. Figure taken from Ref. [90].

## 3.2 Neutrinos from Diffuse Dark Matter Annihilation

Detection of neutrinos from diffuse annihilation of dark matter particles is a challenging task as their expected flux should be much lower than the one of atmospheric neutrinos (main source of background in the search). Thus, in order to be able to find DM-induced neutrinos among collected atmospheric data one would need to specify and focus on some specific signatures of the expected signal.

In most typical *supersymmetric* scenarios with DM particles annihilating into quarks or charged leptons, neutrinos appear as a result of subsequent decays of these particles. The relation between DM annihilation rate and a resulting flux of neutrinos is then completely model dependent. Also, the energy of DM-induced neutrinos is regulated then by the unknown model and would be described by a continuous energy spectrum which most likely spans many orders of magnitude. As an alternative, one could consider scenario with dark matter particles annihilating directly and only to neutrinos, with equal probability that annihilation would lead to production of all neutrino flavors. It is illustrated with a following reaction:

$$\chi + \chi \rightarrow \bar{\nu} + \nu \quad (3.2)$$

In the further discussion it is assumed that the annihilation into pair of neutrinos has 100% branching ratio. Here, a neutralino is proposed as a dark matter candidate but the following discussion would be valid also for any dark matter candidate with the same phenomenology.

Neutralinos, as Majorana particles, could annihilate with each other. In the case described by Eq. 3.2, resulting neutrino energy would be the same as the mass of annihilating relic particles. Thus, annihilation induced neutrinos would introduce a characteristic modification to the observed atmospheric neutrino energy spectrum as illustrated in Fig. 3.6.

Moreover, neutrinos from diffuse dark matter annihilation are expected to have a flat zenith angle distribution (signal will be isotropic in the coordinate system related to the Earth). The annihilation takes place in the entire cosmic space as DM particles should be distributed randomly over a large cosmic volumes. Also, the signal related only to the Milky Way should be diffused due to the Earth's daily rotation and its motion around the Sun. However, the signal may not be isotropic in coordinate system related to the Galactic Center due to the hypothetical cusp in DM halo density anticipated for the central regions of the Galaxy [16, 18, 17].

Such distinctive signal signatures make the search for a diffuse signal feasible in the experiment with high statistics of collected neutrino interaction events. In the *golden channel* scenario described by Eq. 3.2, monoenergetic signal provides a strong hint in the search. The peak in the energy spectrum of collected neutrino events is expected for the signal at given  $M_\chi$ . Also, the angular distributions will have some admixture of isotropic component.

In case of other modes considered for DM annihilation than described by Eq. 3.2 and for other values of the branching ratio for a direct neutrino production, the search for diffuse signal will be more difficult. In typical *supersymmetric* annihilation modes (like 80% BR for neutralino annihilations into  $b\bar{b}$  quarks, 10% into  $c\bar{c}$  and 10% into  $\tau^-\tau^+$  leptons), the expected flux of DM-induced neutrinos decreases by 1-3 orders of magnitude as compared to case described by Eq. 3.2. Also, anticipated energy of the signal is not so much different then from the energy distribution of the atmospheric neutrino background.

The approach based on the DM annihilation mode described by Eq. 3.2 was originally proposed and discussed in more detail in Ref. [90]. The authors claim that no matter how the assumption on 100% BR for annihilation into a pair of neutrinos may look realistic and motivated by underlying theoretical model it allows to conclude a search with some conservative model independent constraints. With a null results coming from other indirect detection experiments investigating other annihilation products like  $\gamma$ ,  $e^{+/-}$ ,  $\bar{p}$ , the search for neutrinos is complementary and allows to probe the missing 'invisible' part of a phase space. If DM-induced signal is not seen also in neutrino data one could derive upper limit on a total DM self-annihilation cross section  $\langle\sigma_A V\rangle$  based on neutrino searches.

### 3.2.1 Galactic Neutrino Flux from Dark Matter Annihilation

The analysis presented in the thesis focuses on the search for diffuse DM annihilation signal originating in the Milky Way. The flux of particles from DM annihilation in the Milky Way is expected to be higher than the flux related to DM annihilation in the entire cosmic space (*cosmic signal*) [90].

As the dark matter annihilation rate is related to the density distribution of relic particles, a summary of DM galactic halo models is given in the following section. Further, it is explained how to link the galactic flux of DM annihilation products with DM annihilation cross section.

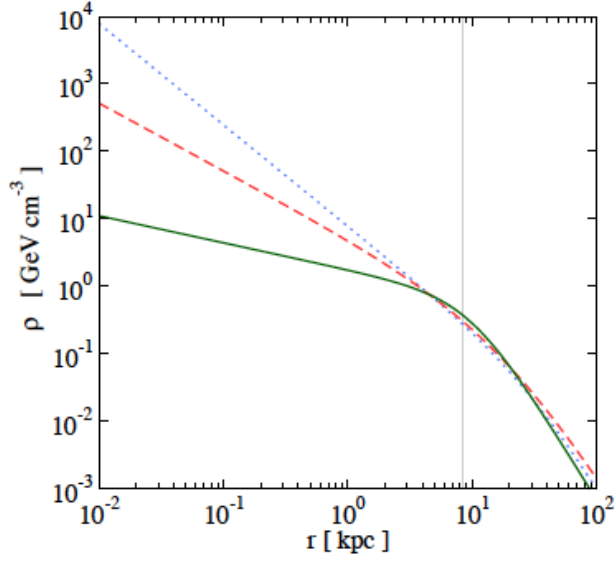


Figure 3.7: Dark matter density as a function of radius for different profiles considered: Moore, NFW and Kravtsov (in order of dotted, dashed and solid lines). The plot illustrates Eq. 3.3 with parameter values from Table 3.1. The vertical gray line indicates the Solar System distance from the GC (also, referred to as solar circle distance),  $R_{sc} = 8.5$  kpc. The normalizations are chosen to match the large scale properties of the MilkyWay. [90].

### Halo models

Cold dark matter simulations (*N-body simulations*) successfully predict the formation of large scale structures which involves DM assembled in the galactic halos [16]. A useful parametrization of DM density that fits the results of the simulations is the following:

$$\rho(r) = \frac{\rho_0}{(r/r_s)^\gamma [1 + (r/r_s)^\alpha]^{(\beta-\gamma)/\alpha}} \quad (3.3)$$

Here,  $r$  is a radius/distance from the center of the Galaxy. The values of variables  $\alpha$ ,  $\beta$ ,  $\gamma$ ,  $r_s$  for some commonly used profiles, like the Navarro-Frenk-White (NFW) [16], Moore [17], and Kravtsov [18] are listed in Table 3.1. Among above parameters,  $\gamma$  is so called inner cusp index and  $r_s$  is the scale radius.

Table 3.1: The parameters of Eq. 3.3 for the three profiles considered. Scale radius,  $r_s$ , is in [kpc] and DM density normalization at solar circle,  $\rho(R_{sc})$ , is in units of  $[\text{GeV cm}^{-3}]$  [90].

	$\alpha$	$\beta$	$\gamma$	$r_s$ [kpc]	$\rho(R_{sc})$
Moore	1.5	3	1.5	28	0.27
NFW	1	3	1	20	0.3
Kravtsov	2	3	0.4	10	0.37

Figure 3.7 shows the DM density,  $\rho(r)$ , as a function of distance from the Galactic Center for the different profiles. The normalizations are chosen such that mass contained within the solar circle ( $R_{sc} = 8.5$  kpc) provides the appropriate DM contribution to the

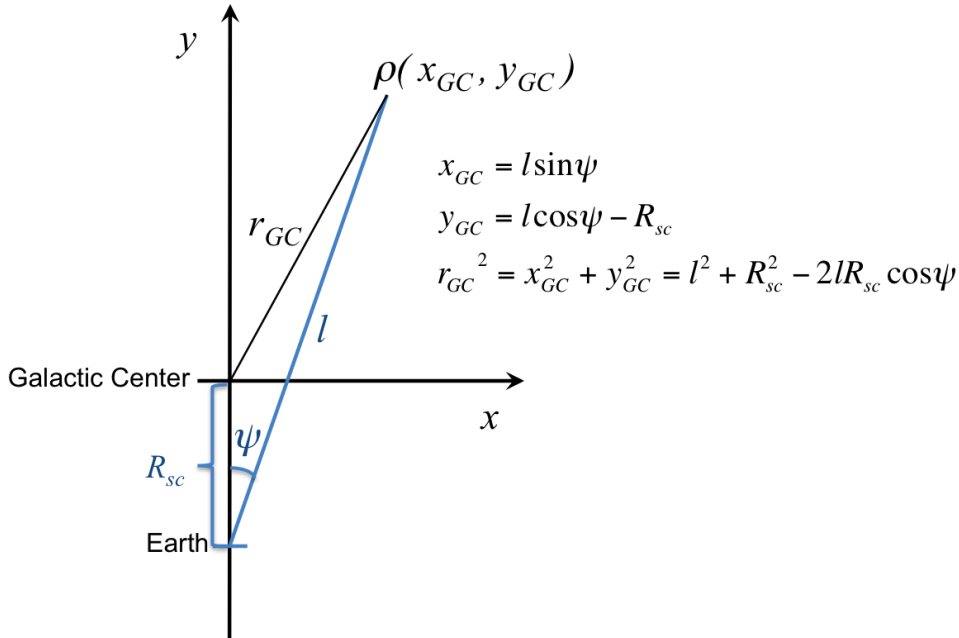


Figure 3.8: Illustration of line of sight  $l$  and viewing angle  $\psi$  in the coordinate system related to the Galactic Center.

local rotational curves. This yields the local DM density for NFW profile  $\rho_{NFW}(R_{sc}) = 0.3 \text{ GeV cm}^{-3}$ . The values of the local density for other profiles are listed in Table 3.1.

At large scales the distributions for all considered profiles are very similar. For the inner regions the discrepancy arises from the uncertainty in the prediction of the inner density cusp. The modeling of inner galactic regions is so far the most uncertain element due to the spatial resolution limit of the simulations. Baryons typically dominate the inner regions, and their impact has not yet been fully taken into account. They could either provide a mechanism that leads to increase of the inner cusp or the mechanism which flattens the profiles due to momentum transfer to DM particles.

### Annihilations in the Halo

The calculation of the spectrum of DM annihilation products from the halo is well established (e.g., Ref. [103]). For annihilations, the intensity (flux per solid angle) at an angle  $\psi$  with respect to the Galactic Center direction is proportional to the line of sight ( $l$ ) integration of the DM density squared:

$$\mathcal{J}(\psi) = \frac{1}{R_{sc}\rho_{sc}^2} \int_0^{l_{max}} \rho^2 \left( \sqrt{R_{sc}^2 - 2lR_{sc} \cos \psi + l^2} \right) dl. \quad (3.4)$$

The definition of angle  $\psi$  is shown in Fig. 3.8. The prefactor  $1/(R_{sc}\rho_{sc}^2)$  in Eq. 3.4 is an arbitrary scaling that is used to make  $\mathcal{J}$  dimensionless regardless of the underlying DM density profile. In that case the density is normalized at the solar circle ( $R_{sc} = 8.5 \text{ kpc}$ ) with value of  $\rho(R_{sc})$  appropriate for a given model (compare Table 3.1). The upper limit of the integration,

$$l_{max} = \sqrt{(R_{MW}^2 - 2 \sin^2 \psi R_{sc}^2) + R_{sc} \cos \psi}, \quad (3.5)$$

Table 3.2: Estimation of the various signal intensity factors,  $\mathcal{J}_{\Delta\Omega}$ , for the halo (as defined by Eq. 3.4 and 3.6). The last row lists canonical (average) values that are used by the authors in Ref. [90] to derive their constraints on the total DM annihilation cross section (see Section 3.2.2).

	$\mathcal{J}_{\Delta\Omega}^{Ang}$	$\mathcal{J}_{\Delta\Omega}^{Ave}$	$\mathcal{J}_{\Delta\Omega}^{Iso}$
Moore	102	8	0.3
NFW	26	3	0.4
Kravtsov	13	2.6	0.55
<b>Canonical</b>	<b>25</b>	<b>5</b>	<b>0.5</b>

depends on the adopted size of the halo,  $R_{MW}$ . However, contributions beyond the scale radius, typically about 20–30 kpc, are negligible.

In a further discussion it is useful to define the average value of intensity ( $\mathcal{J}$ ) in a cone with half-angle  $\psi$  around the GC that spans a field of view of  $\Delta\Omega = 2\pi(1 - \cos\psi)$ :

$$\mathcal{J}(\Delta\Omega) = \frac{1}{\Delta\Omega} \int_{\cos\psi}^1 \mathcal{J}(\psi') 2\pi d(\cos\psi'). \quad (3.6)$$

Then the average intensity of DM annihilation products from the field of view can be cast as [90, 103]

$$\frac{d\phi_{\Delta\Omega}}{dE} = \frac{\langle\sigma_A V\rangle}{2} \mathcal{J}_{\Delta\Omega} \frac{R_{sc}\rho_{sc}^2}{4\pi M_\chi^2} \frac{dN}{dE}, \quad (3.7)$$

The  $M_\chi$  is the assumed mass of the DM particle. The factor 1/2 on the right hand side of Eq. 3.7 accounts for DM being its own antiparticle and  $1/4\pi$  is for isotropic emission. The thermal average of the annihilation rate is proportional to  $\langle\sigma_A V\rangle$ , the product of the annihilation cross section and the relative velocity. The  $dN/dE$  is the spectrum of annihilation products. In adopted simple model in which DM particles directly annihilate into pairs of neutrinos (Eq. 3.2), the spectrum of neutrinos of a specific flavor is a monochromatic line with  $dN/dE = \frac{2}{3}\delta(E - M_\chi)$ . The prefactor 2/3 reflects the fact that 2 neutrinos ( $\nu + \bar{\nu}$ ) are produced per annihilated DM pair and that all neutrino flavors are equally populated. The latter statement means that neutrinos are produced with the same proportions of every flavor. The ratio of the flavors remains the same during neutrino propagation in space as neutrino oscillations affect equally all 3 flavors. For example, a part of  $\nu_\mu$  which will oscillate into  $\nu_\tau$  and  $\nu_e$  will be compensated by  $\nu_\mu$  from transitions of  $\nu_\tau$  and  $\nu_e$  neutrinos. That is true if initial contribution of each flavor is the same.

Figure 3.9 shows the behavior of  $\mathcal{J}(\psi)$  (thin lines) as a function of  $\psi$ , and  $\mathcal{J}_{\Delta\Omega}$  (thick lines) as a function of  $\Delta\Omega/4\pi$ , for the three considered halo profiles. For the innermost regions of the Galaxy ( $0.1^\circ$ , corresponding to  $\sim 0.015$  kpc) the flat cores are assumed in Fig. 3.9. The reason for this is that  $\mathcal{J}$  diverges for very cuspy profiles. It may be the artifact of the simulations which cannot resolve small spatial scales. Therefore, in this illustration, to avoid the numerical divergencies the flat core for all the profiles was assumed at the innermost regions.

Based on the Eq. 3.4 and 3.6 one could calculate the total expected signal intensity  $\mathcal{J}_{\Delta\Omega}$  from DM annihilation in the Galaxy. The results for the different profiles are summarized in Table 3.2 for the following components of the halo:

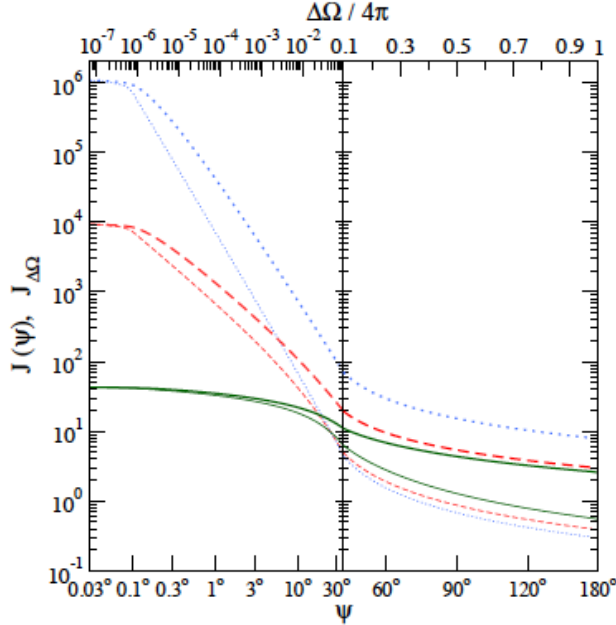


Figure 3.9: Line of sight integration  $\mathcal{J}(\psi)$  as a function of the pointing angle  $\psi$  (bottom axis) with respect to the Galactic Center direction for the three different profiles considered (Moore, NFW and Kravtsov in order of dotted, dashed and solid thin lines). Its average,  $\mathcal{J}_{\Delta\Omega}$ , inside a cone with half-angle  $\psi$  around the GC as a function of the visible fraction of the whole sky,  $\Delta\Omega/4\pi = (1 - \cos\psi)/2$  (top axis), is also presented (thick lines). The left side of the graph, below  $\Delta\Omega/4\pi = 0.1$ , is presented in log scale, the right side is in linear scale. [90].

- *Halo Average*. This is related to the average intensity of DM annihilation products,  $\mathcal{J}_{\Delta\Omega}$ , from the entire field of view (half-angle  $\psi = 180^\circ$ , whole sky). The differences between various halo models lead to the different values of the total estimated intensity (see Table 3.2). When a large field of view is considered, the average  $\mathcal{J}_{\Delta\Omega}$  is less sensitive to the chosen profile and to the uncertainties related to the inner cusp. *Halo Average* estimation of the average signal intensity is used as a baseline in the analysis presented in this thesis.
- *Halo Isotropic*. This calculation of the average signal intensity is related only to the regions of the Milky Way in the anti-GC direction. That would yield a minimal signal contribution which is comparable to the intensity related to the DM annihilation in the entire cosmic space (*cosmic signal*).
- *Halo Angular*. Here, one considers a  $30^\circ$  half-angle cone around the GC to define a source region for the signal. Thus, the average intensity  $\mathcal{J}_{\Delta\Omega}$  related only to the innermost region of the Galaxy is obtained.

The *Halo Average*, *Halo Isotropic* and *Halo Angular* estimations of  $\mathcal{J}_{\Delta\Omega}$  are used by the authors in Ref. [90] as a benchmark to derive their constraints on the total DM annihilation cross section  $\langle\sigma_A V\rangle$ .

### 3.2.2 Limit on Dark Matter Self-Annihilation Cross Section

The limit on dark matter self-annihilation cross section  $\langle\sigma_A V\rangle$  based on the search for diffuse neutrino signal from the Milky Way and cosmic space was obtained in Ref. [90] and is shown in Fig. 3.10. The limit was derived as a function of DM particle mass. The values of the cross section above the lines are excluded at 90% confidence level. The search is performed for a *golden channel* mode only (Eq. 3.2) – the energy spectrum of neutrinos per flavor is a monochromatic line equal to the mass of the annihilating relic particles.

In the search for DM signal in Ref. [90], authors investigated atmospheric neutrino energy spectrum (specifically,  $\nu_\mu + \bar{\nu}_\mu$ ) derived from measurements of the AMANDA [104], Frejus [105] and Super-Kamiokande [5] detectors. They had access only to the published data which are available up to  $10^5$  GeV of neutrino energy. This data are fully consistent with theoretically expected flux and energy spectrum shape for atmospheric neutrinos after their oscillations are taken into account. Thus, authors could derive a limit on allowed number of DM-induced neutrinos that could be accommodated by that data for each considered DM mass. They adopted conservative criteria and required that DM-induced neutrinos could double the total received intensity from atmospheric neutrinos in the energy bin width of  $\Delta\log_{10}E/\text{GeV} = 0.3$  around given  $E_\nu = M_\chi$  for the annihilations in the halo. In case of annihilations in the entire cosmic space the energy of neutrinos related to DM annihilation would be smeared due to the various redshift distribution of the sources. Then, a larger bin width of  $\Delta\log_{10}E/\text{GeV} = 0.5$  below  $E_\nu = M_\chi$  is considered for the integration. That procedure is illustrated in Fig. 3.6 where the expected energy distribution of DM-induced neutrinos is shown for the DM mass of 100 GeV and for both cases of halo and cosmic annihilation. The size of the integration bin in those two scenarios is indicated as yellow lines with arrows. The constraint on allowed number of DM-induced neutrino events could be translated into the flux limit and limit on total DM self-annihilation cross section  $\langle\sigma_A V\rangle$  (Fig. 3.10) using the Eq. 3.7.

### 3.2.3 Prospects for Dark Matter Diffuse Annihilation Search

As the existing limit for DM self-annihilation cross section  $\langle\sigma_A V\rangle$  is derived in a global analysis of combined atmospheric neutrino spectra published by certain neutrino experiments, it cannot fully exploit underlying features available in event-by-event analysis. There is a place for an improvement in any dedicated experimental search for dark matter diffuse neutrino signal.

Firstly, one could use more precise binning of the energy distributions when comparing a data with expectation on atmospheric neutrino production. As the dark matter signal is sharply peaked at the neutrino energy equal to DM particle mass it can be compared with data and expectation in much narrower bins than those used by the authors in Ref. [90]. Especially, in the range where a certain experiment has a precise information on incoming neutrino energy, high statistics and good resolution. Secondly, one could use also the angular distributions of neutrino events in the search as it is expected that a signal from DM diffuse annihilation would be isotropic while the atmospheric neutrino background is often peaked at the horizon (compare Fig. 2.8). Third, using both  $(\nu_\mu + \bar{\nu}_\mu)$  and  $(\nu_e + \bar{\nu}_e)$  samples in the search would place an additional constraint. Ratio of atmospheric neutrino fluxes –  $(\nu_\mu + \bar{\nu}_\mu)$  to  $(\nu_e + \bar{\nu}_e)$  – changes with energy. At 10 GeV it is around 3 and is rapidly increasing for higher energies (Fig. 2.7(c)) while the signal is expected to result

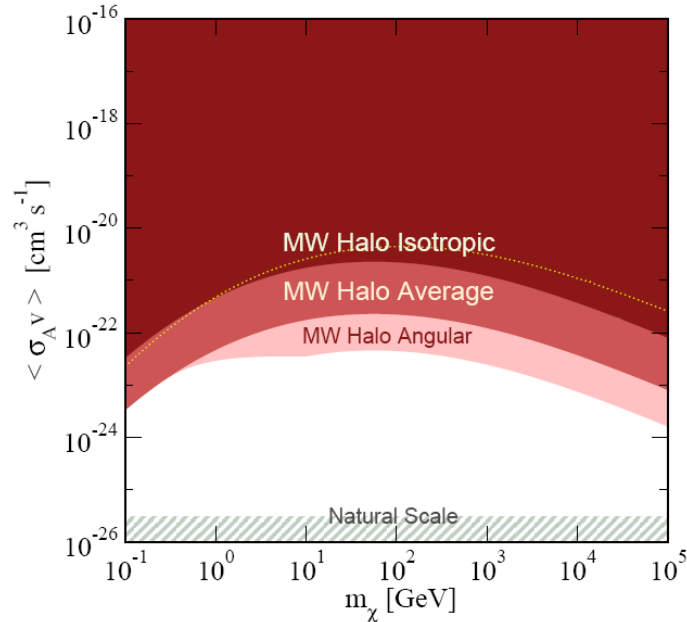


Figure 3.10: Limit on the DM total self-annihilation cross section from various components of the Milky Way halo (color regions excluded) and on the cosmic signal (region above the yellow dotted line excluded) [90]. These limits were derived under the assumption that the number of DM originating neutrinos cannot exceed the number of atmospheric neutrinos observed in a given energy interval. See text and Ref. [90] for details. For cross sections larger than the *natural scale*, the DM cannot be a thermal relic (see Section 1.2).

in the same flux for all neutrino flavors.

Dedicated experimental analysis could improve the existing constrains on the total self-annihilation cross section  $\langle \sigma_A V \rangle$  by 1-2 orders of magnitude by combing all that additional features. Thus, expected sensitivity could become closer to the natural scale expected for a thermal relic. It would be also possible to test some non-standard hypotheses which require values of  $\langle \sigma_A V \rangle$  to be enhanced comparing to the standard expectation which involves thermal evolution of the Universe. Such attempts are made by some authors in order to explain the results of the PAMELA and ATIC experiments [36, 37]. The significant excess of positrons/electrons was observed in those experiments which overwhelms the expected contribution from the cosmic rays. The effect could be interpreted as DM annihilation but only when some 'boost factors' related to increased value of  $\langle \sigma_A V \rangle$  or increased DM density are taken into account [48].

The search for diffuse neutrino signal from dark matter annihilation using neutrino data from the Super-Kamiokande detector has been performed by the author of this thesis and this analysis is presented in Chapters 6 and 7.

### 3.3 Neutrinos from Dark Matter Decay

The strategy of the search for neutrinos originating in Eq. 3.2, discussed in the previous section, can be also adopted to the search for neutrinos from decay of dark matter particles. The diffuse signal from direct DM decay into pair of neutrinos would have the similar characteristics as the annihilation signal. However, in case of such a decay, each neutrino

would carry the energy equal to half of the mass of the decaying DM particle,  $E_\nu = M_\chi/2$ . In case of annihilation described by Eq. 3.2,  $E_\nu = M_\chi$ . Any generic DM candidate that could directly decay into neutrinos could be addressed with this search.

It shall be noticed that a concept of decaying DM provides the extension to models with *Lightest Supersymmetric Particle* (LSP) as the DM candidate [89]. Due to the  $R$ -parity conservation postulated in most of the *supersymmetric* models [2], LSP is not allowed to decay into particles from the Standard Model only. Neither it can decay into any accompanying *supersymmetric* particles by the definition of being the lightest. However, it could be the case that DM is comprised of NLSP (*Next Lightest Supersymmetric Particle*) or even heavier *supersymmetric* particles. Then, in the decay of DM, both *supersymmetric* and Standard Model particles could be produced, including neutrinos. However, such a decay cannot be addressed with a search compliant with the adopted assumptions (Eq. 3.2) – the energy carried by neutrinos produced in 3-body decay is not fixed.

In case when  $R$ -parity is not conserved, any *supersymmetric* DM candidate could decay into the Standard Model particles only. In the following discussion one would be interested in direct neutrino production via DM decay. That can be allowed in some exotic scenarios, like the one based on Asymmetric Dark Matter (ADM) concept which is discussed in [89]. Here, modes with  $\chi \rightarrow \nu + \nu$  or  $\chi \rightarrow \bar{\nu} + \bar{\nu}$  are preferable. In this model, dark matter carries lepton and/or baryon number and the baryon asymmetry from Standard Model is transferred to the dark sector [89].

### Galactic neutrino flux from dark matter decay

The formula for signal intensity from DM decay in the Milky Way is similar to the one presented in Eq. 3.4 for DM annihilation. In case of decay, which involves only one DM particle, intensity is proportional to the DM density instead of density squared:

$$\mathcal{J}(\psi) = \frac{1}{R_{sc}\rho_{sc}} \int_0^{l_{max}} \rho \left( \sqrt{R_{sc}^2 - 2lR_{sc} \cos \psi + l^2} \right) dl. \quad (3.8)$$

The average flux of neutrinos of a given flavor originating from DM decay is then defined as:

$$\frac{d\phi_{\Delta\Omega}^{decay}}{dE} = \mathcal{J}_{\Delta\Omega} \frac{\Gamma_{decay} R_{sc} \rho_{sc}}{4\pi M_\chi} \frac{dN}{dE}. \quad (3.9)$$

$\Gamma_{decay}$  is the decay width to all neutrino flavors. It is related to DM lifetime  $\tau_{DM}$  as  $\Gamma_{decay} = 1/\tau_{DM}$  (if  $\hbar = c = 1$ ). Other symbols have similar definition as in Eq. 3.7.

# Chapter 4

## Super-Kamiokande Detector

This chapter contains an overview of the Super-Kamiokande detector (also referred to as SK or Super-K). The detector construction, principle of operation and history of the experiment are discussed. It is shown how interactions of neutrinos are observed at Super-K. The effect of Cherenkov radiation is explained. At the end of the chapter, the author's contribution to the experiment is presented.

### 4.1 Introduction

Super-Kamiokande is a water Cherenkov detector located at the Kamioka Observatory in Japan. The observatory is run by the Institute for Cosmic Ray Research, University of Tokyo. Experimental facility is located underground in the Mozumi mine, owned by the Kamioka Mining Company, at the depth of 1000 m. That corresponds to 2700 meters of water equivalent overburden (m w.e.).

Design of the Super-Kamiokande was originally motivated by the search for a proton decay. The detector showed its extraordinary capability to study interactions of solar and atmospheric neutrinos. It is also capable to observe muons produced in the atmosphere in the hadronic showers initiated by cosmic rays (cosmic ray muons). These muons pose a background in the search for neutrino interaction signals. Fortunately, the flux of cosmic ray muons at the Super-K underground location is suppressed as compared to that on the Earth's surface by around 5 orders of magnitude due to rock overburden [4].

Figure 4.1 shows a drawing of the Super-Kamiokande detector. The detector consists of two concentric, optically separated water Cherenkov detectors contained in a stainless steel tank 42 meters high and 39.3 meters in diameter. A mass of water contained in the entire volume is 50 000 tons. Inner detector (ID) is a large cylindrical region monitored with 11 146 hemispherical photomultiplier tubes (PMTs) which are mounted to the side, top and bottom walls of the support structure. Each tube is 20 inches in diameter and is facing towards the inside of the detector. Outer detector (OD) is a 2 meters thick water shield/outer veto instrumented with 1885 PMTs. OD detector tubes are smaller, 8 inches diameter each, and are facing outside.

The inner detector encompass a fiducial volume (FV) region of a mass 22.5 kton. The active volume is defined as a cylindrical region in the ID with borders 2 m away from the surface of PMTs. Its height is 32.2 m and diameter 29.8 m. In the experiment, it is required that each neutrino interaction event which is used in the physical analysis must have its interaction vertex in the fiducial volume. Neutrinos do not leave any detectable trace

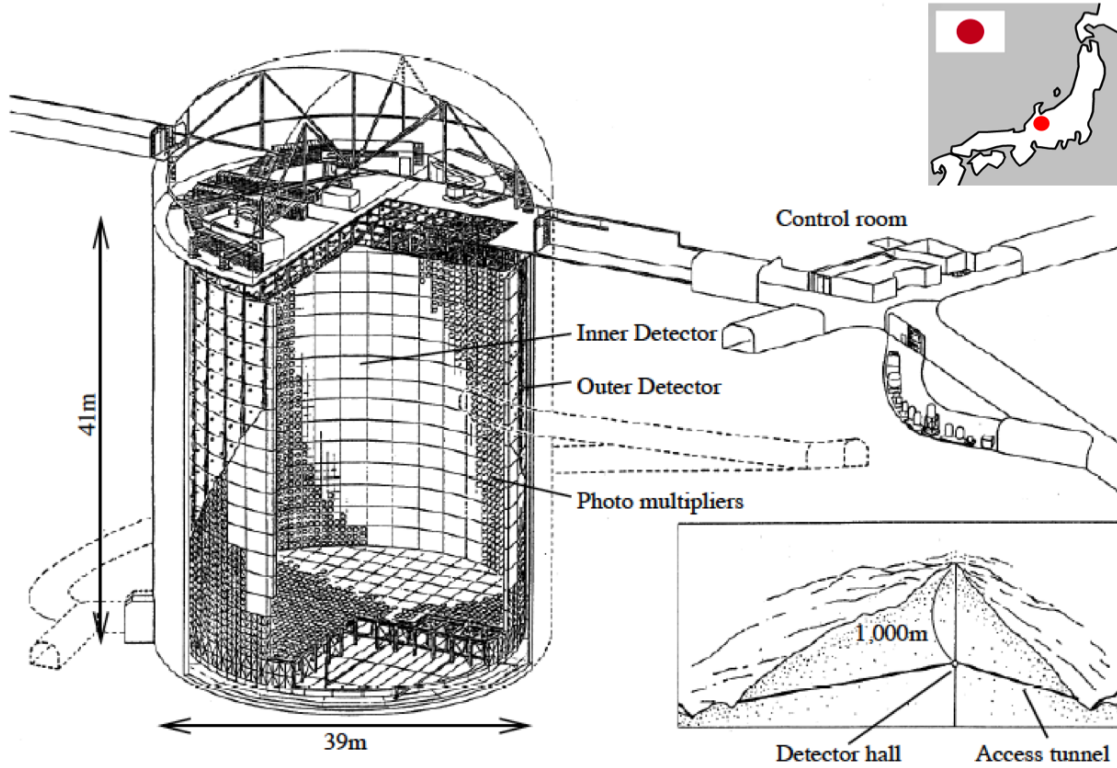


Figure 4.1: A schematic view of the Super-Kamiokande detector and the experimental hall [6]. The cutaway shows the inner detector which is monitored with photomultiplier tubes mounted on the stainless steel support structure. The outer detector contains outward-facing PMTs attached on the other side of the support structure. There are only 2 outer PMTs for every unit of 12 inner PMTs. The top of the detector, under the hemisphere, consists of electronics huts and open work area. The inset figure on the bottom-right shows the sectional view of Mt. Ikenoyama and the location of the experimental hall. The top-right inset figure shows the location of the Kamioka Observatory on the map of Japan.

in the detector while they pass. The signal is observable only when neutrinos interact and charged particles are produced as a result of that process. Therefore, events with no evidence of entering particles in the OD and with interaction vertices in the FV are considered good neutrino interaction candidates. The outer detector is used to identify incoming muons and particles outgoing from the interactions which originate in the fiducial volume.

The ID and OD detectors are separated with the sheets of a Tyvek<sup>®</sup><sup>1</sup> material, which is white on one side and black on the other. The black side is facing the ID and absorbs light. The white side is facing outside and reflects light produced in the OD. During a normal operation, the detector is closed (light-tightened) and filled with ultra-pure water. The water is constantly circulated and may flow between ID and OD regions. More details about the detector could be found in [4].

<sup>1</sup>Tyvek is a registered trademark of DuPont company.

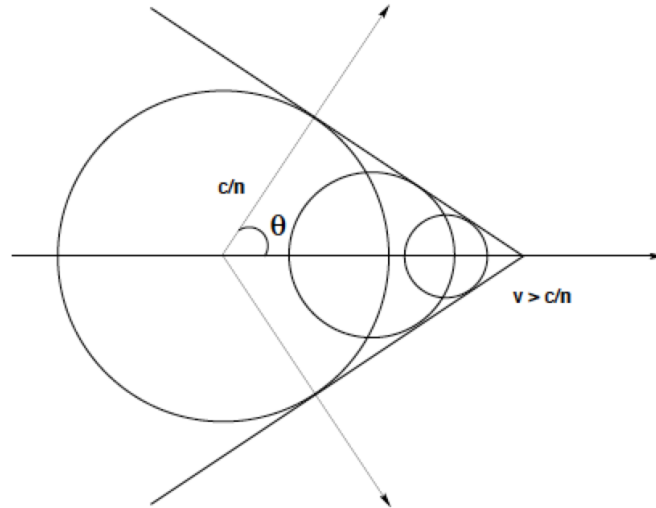


Figure 4.2: Construction of the wavefront of Cherenkov radiation. From [95].

## 4.2 Principle of Operation

The particle detection in the Super-K detector is based on the effect of Cherenkov radiation. When a high energy charged particle propagates through water (or other dielectric medium) with a speed greater than the speed of light in this medium, a Cherenkov effect occurs. The light is emitted by atoms excited by the passage of charged particle. The wavefront of electromagnetic wave propagates in form of a cone around the particle's direction of motion as shown in Figure 4.1. The opening angle of the cone, created in Cherenkov effect, is described with the following formula [71]:

$$\cos \theta = \frac{c}{vn}, v > \frac{c}{n} \quad (4.1)$$

where  $n$  is the refractive index of the medium,  $c$  is a speed of light in vacuum, and  $v$  is a velocity of the particle. For relativistic particles moving in water ( $n = 1.34$ ) the angle  $\theta$  is about 42 degrees. Charged particles emit Cherenkov light when their total energy is roughly 1.5 times higher than their mass. The threshold momenta are: for electrons – 0.57 MeV, for muons – 118 MeV, for pions – 156 MeV, for protons – 1049 MeV.

Neutrinos are mainly observed at SK via their charged current interactions (see Section 2.2 for a description of CC interactions). The charged lepton, which is produced in CC neutrino interaction, emits the Cherenkov light. That light projected on the walls of detector is recorded in PMTs in form of: (1) a ring if a charged particle stops in the ID; (2) or it may form a filled circle in case a particle exits to the outer detector. If multiple charged particles are produced in neutrino interaction, more than one ring could be observed. That happens for DIS and resonant pion production. Such events are then being referred to as multiple ring. The CC quasi-elastic neutrino interactions are seen as single ring events as recoiling proton usually has the energy below the Cherenkov light production threshold and only a charged lepton is visible. The example of such an event is shown in Fig 4.3. Here, the electron produced in CC quasi-elastic process initiated by  $\nu_e$  stops inside the detector and the resulting Cherenkov light forms a ring. This kind of

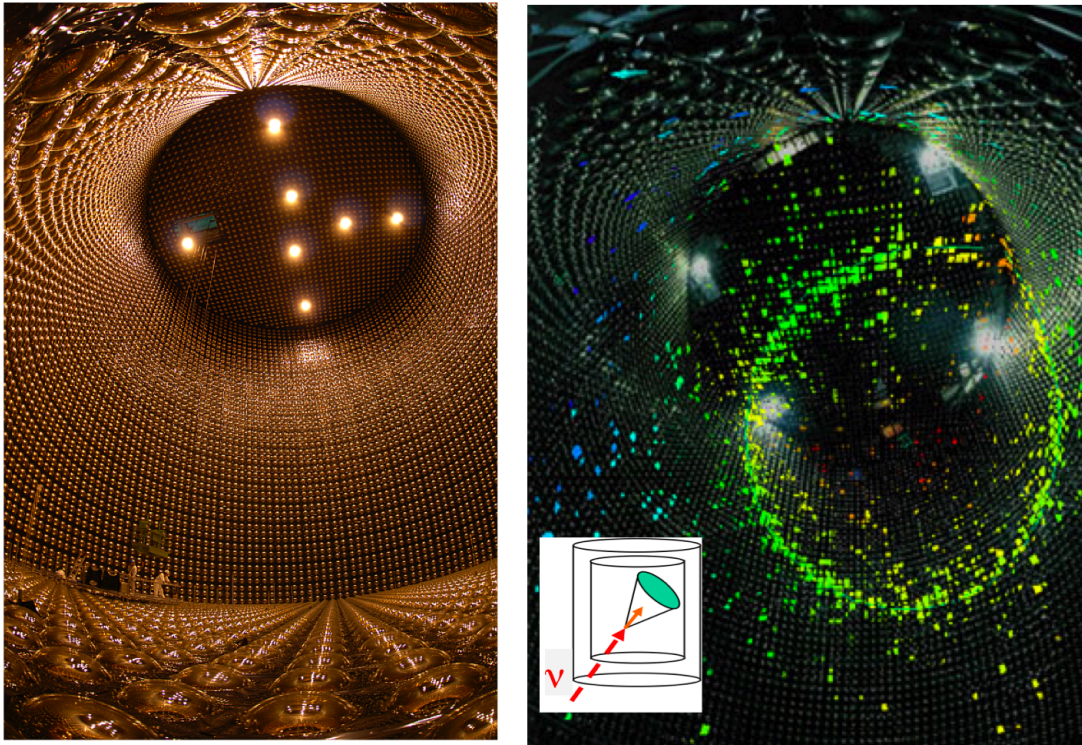


Figure 4.3: Left – Inside view of the Super-Kamiokande detector during the maintenance in 2006. Right – Illustration of Cherenkov ring produced in a charged current  $\nu_e$  interaction in water ( $\nu_e N \rightarrow e N'$ ). The cone in the inset figure indicates the trajectory of the emitted Cherenkov light, it does not show the wavefront shape.

event is classified also as a fully-contained event as the produced charged particle stops in the ID. More information on the classification of events at SK is given in Chapter 5.

For neutrinos with energies of the order of few GeV, their neutral current interactions are difficult to observe in water Cherenkov detector as there is no energetic charged particle produced in the final state. Recoiling protons are usually not sufficiently energetic to produce light and neutrons are undetectable due to lack of charge. In case of higher energies, additional particles could be produced in NC  $\nu$  reactions (for example in NC DIS and NC RES processes) and these charged particles could emit Cherenkov light. However, NC reactions of this type cannot be distinguished from charged current interactions of neutrinos – observable signatures are the same in both cases.

By using the information from PMTs, the energy deposited in the detector by particles, produced in neutrino interactions, could be determined. For CC quasi-elastic interactions the energy of incident neutrino could be reconstructed based on that information. It is also possible to distinguish what type of charged particle that emitted Cherenkov light and to reconstruct the position of its interaction vertex and direction of motion. These issues are discussed below in more detail.

## Energy

Cherenkov light emitted when a charged particle produced in  $\nu$  interaction traverse the water is recorded by photomultiplier tubes. The number of observed photoelectrons is related to the energy deposited in the detector (visible energy,  $E_{vis}$ ). For example, the

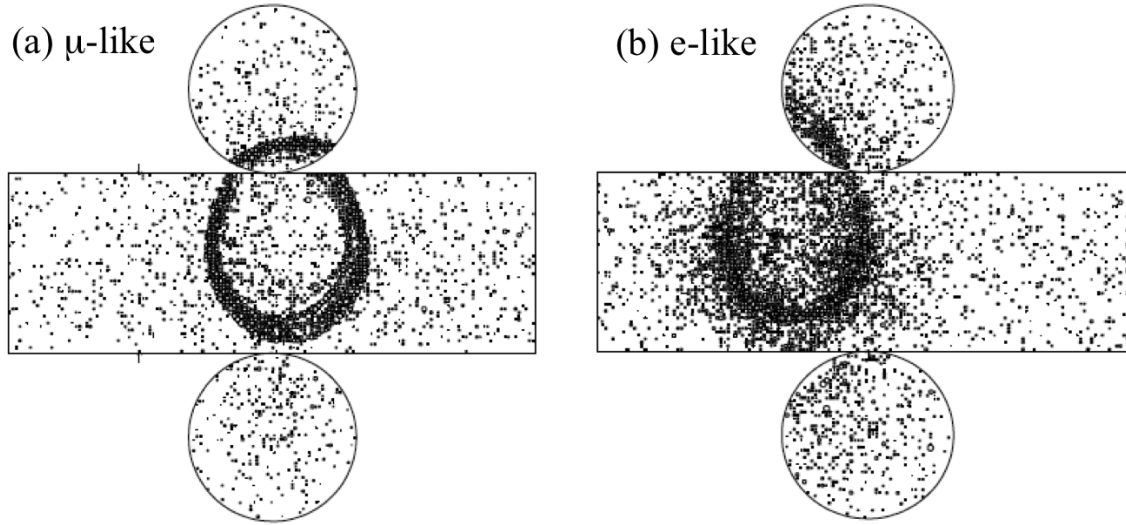


Figure 4.4: Figure (a) – An example event display of a single-ring  $\mu$ -like event. Each small circle represents a hit PMT and the size of the circle represents the number of photons that hit it. The boundary of the Cherenkov light is sharp as the muon travels relatively straight as it comes to a stop. Distant hit PMTs come from scattered light and Cherenkov light from delta-rays. Figure (b) – An example event display of a single-ring e-like event. In this event, the boundary of the Cherenkov light is smeared over many PMTs as the light comes from numerous positrons and electrons produced in the electromagnetic shower. [5].

energy loss,  $dE/dx$ , of a minimum ionizing particle going through the water is around 2 MeV per cm [56]. In the determination of particle's energy it is important to know the relation between the number of photoelectrons recorded in PMTs and the total deposited energy. That matching is called the energy scale determination. The energy scale of SK detector is evaluated in various calibration procedures [5]. The light attenuation in water is studied as well as geometrical uniformity of the detector response, and the efficiency of PMTs to detect photoelectrons.

Neutrino interaction candidates are recorded with different trigger conditions. Candidates for atmospheric neutrinos are required to have at least 30 hit PMTs in 200 nanosecond window (high energy trigger). That trigger condition corresponds to the mean number of hit PMTs generated by a 5.7 MeV electron. High energy trigger rate in the experiment is 10-12 Hz, but most of the observed events are background due to cosmic ray muons and low energy radioactivity from parents such as radon. There are only  $\sim 10$  interactions of atmospheric neutrinos per day expected to be observed at SK. Therefore, to extract neutrino interaction events from a sample of all collected events special selection procedures are applied as it is described in the next chapter. In particular, a 30 MeV energy threshold is used to extract candidate events which may contain interactions of atmospheric neutrinos. Solar neutrinos are expected to yield a visible energy lower than 15 MeV. The data selection procedures are described in the next chapter.

If all particles, that are produced in neutrino interaction, stop in the detector, the information on the total deposited energy is available. In case of CC quasi-elastic neutrino interactions it is enough to reconstruct the energy of a parent neutrino with a good accuracy. However, if some part of the incident neutrino energy is transferred to neutral

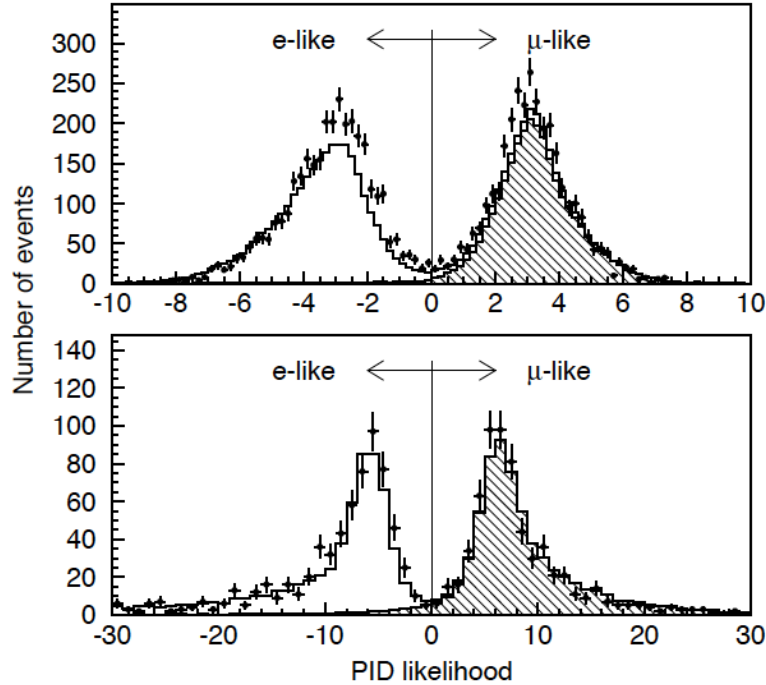


Figure 4.5: Particle identification likelihood distribution (PID) for single ring fully-contained events with visible energy  $< 1.3 \text{ GeV}$  (top) and  $> 1.3 \text{ GeV}$  (bottom) [5]. Points show the data (atmospheric neutrinos) and the histograms show the results of a Monte Carlo simulation. The hatched histograms show the charged current interactions of  $\nu_\mu$ , the plain histograms show the charged current interactions of  $\nu_e$ .

particles (like to other neutrino produced in NC reaction) or to particles which are not energetic enough to produce light in water, then the energy of interacting neutrino cannot be resolved. The same happens if some of the particles produced in the interaction exit the detector.

### Particle identification

The light pattern of the Cherenkov ring is associated with a type of particle produced in neutrino interaction. That is illustrated in Fig. 4.4. Two kind of rings are recognized: (1) muon-like ( $\mu$ -like) and (2) electron-like (e-like). The  $\mu$ -like rings are produced by muons, charged mesons and hadrons. The e-like rings are produced by electrons and gamma particles. Events which contain neutral pions would most likely be categorized as e-like because  $\pi^0$  decays immediately into two gamma particles. The most energetic ring in observed event determines its category electron or muon-like.

An electron (or a gamma particle) which is produced in neutrino interaction initiates electromagnetic cascades while propagating through water. Therefore, e-like rings have more diffuse light distribution than rings produced by muons/mesons. Muons (or mesons) propagate straight in water. Only when they are losing a large amount of energy due to Coulomb scattering change of direction can be observed. Therefore, the inner edges of the  $\mu$ -like rings could be more smeared than their outer edges. The width of a  $\mu$ -like ring is proportional to the energy of the particle which emits the Cherenkov light.

The separation for the e-like and  $\mu$ -like events is statistical. Each event at SK is being assigned a particle ID (PID) variable which value is being evaluated with advanced ring classification algorithm. Figure 4.5 shows the clear separation between electron and muon-like events obtained in this procedure. Based on this classification it is possible to tell the flavor of the parent neutrino – whether it is a muon or electron neutrino<sup>2</sup>.

Topological information about observed rings is also supplemented by information on the time of the hit of each PMT. Thus, it is possible to distinguish events containing decaying muon – a ring belonging to electron, which is produced in muon decay, is recorded later than the main muon ring.

### Interaction vertex and direction

The information on a time of hits in PMTs, shape and number of observed rings is used to determine the direction of a parent neutrino and its interaction vertex. This reconstruction is based on a set of specialized computer algorithms which investigate topology of each event and how it develops in time. Various configurations of neutrino directions and its interaction vertices are considered. The configuration that matches the best the observed pattern is used to determine the kinematics of the interaction.

## 4.3 History

Super-Kamiokande started operation in 1996 as a successor to the Kamiokande experiment. The latter one is famous of a direct observation of neutrinos from the supernova explosion (SN1987A) which occurred in February 1987 in the Large Magellanic Cloud [80]. The spokesman of the Kamiokande experiment, M. Koshiba, was awarded a Nobel prize in 2002 for the development of the experimental technique that resulted in observation of neutrinos of a cosmic origin.

Super-Kamiokande continued a line of discoveries started by its predecessor. SK discovered neutrino oscillations in atmospheric neutrino data in 1998 [65] and confirmed the oscillations of solar neutrinos [64]. It was also used as a far detector in a long baseline neutrino oscillation experiment K2K [79]. Currently, it is used as a far detector in the T2K project, a new generation oscillation experiment [6].

In November 2001 an accident happened at the experiment. During a refilling with water, at the end of reconstruction works which started in July 2001, one of the tubes located at the bottom of the detector imploded. That led to chain reaction. Very strong shock wave was produced and all photomultipliers which were in water at that time (around  $\sim 60\%$ ) were destroyed.

The experimental phase which started in April 1996 and ended in July 2001 (start of the maintenance) is being referred to as SK-I phase. After the accident, data taking was resumed in December 2001 with reduced number of PMTs (half comparing to SK-I configuration). That phase is referred to as SK-II. SK-II lasted until October 2005, then the detector reconstruction began. In 2006 the rest of the PMTs was put again in place and the detector returned to its original configuration from before the accident. SK-III

---

<sup>2</sup>As it is explained in Section 2.6, number of atmospheric tau neutrinos, expected to be observed at SK, is negligible. Nevertheless, interactions of tau neutrinos would lead to complex topology with the most energetic ring usually recognized as e-like (see Section 5.4).

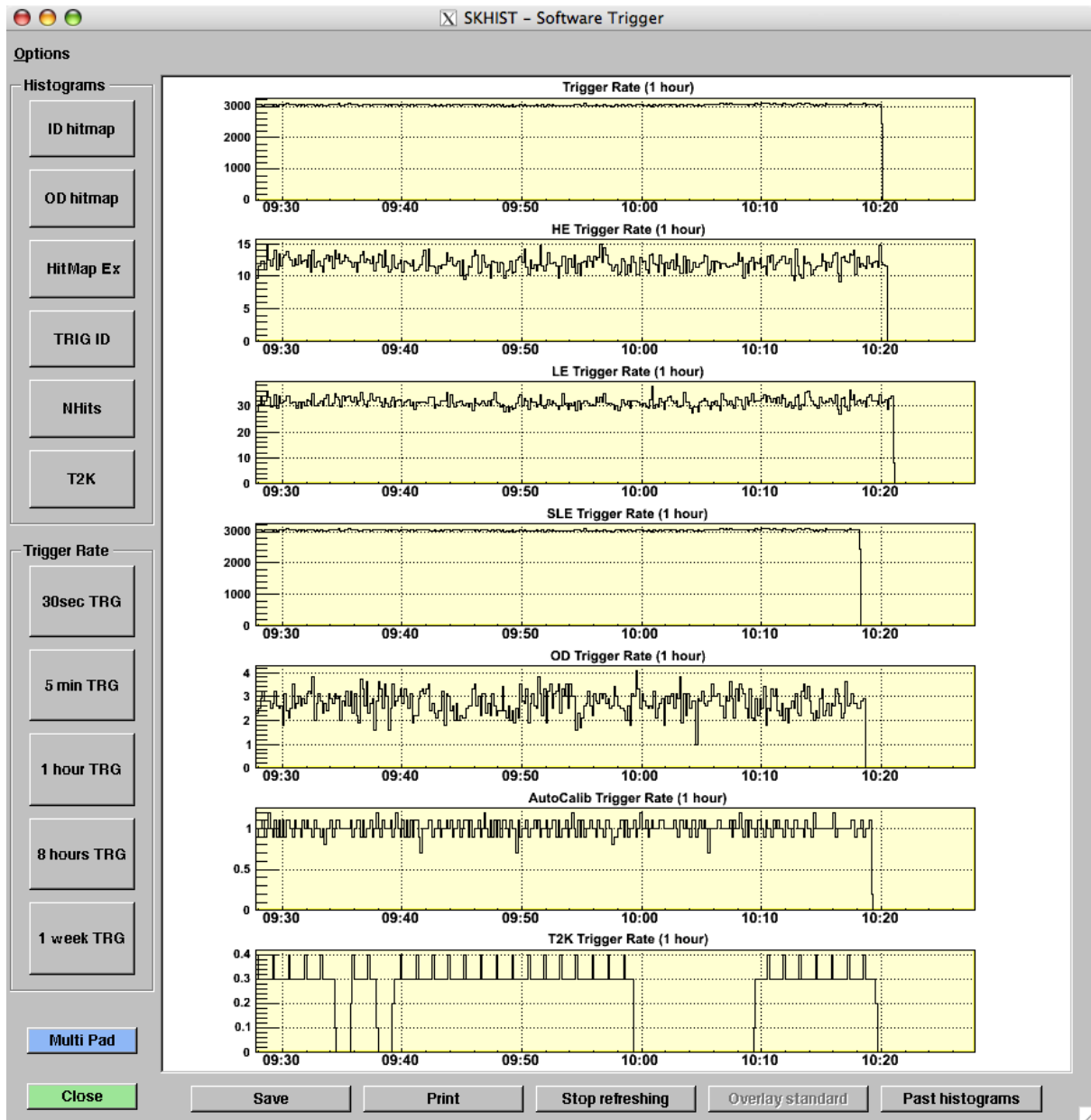
phase started in July 2006 and lasted until August 2008. The author of this thesis took part in the replacement of the PMTs in 2006. He also participated in the upgrade of the electronics which took place in summer 2008. He was involved in software development for a data acquisition system (DAQ). After the upgrade was completed in September 2008, SK-IV phase started with a configuration anticipated for the T2K project and future searches for neutrinos from supernovas.

## 4.4 DAQ Monitoring Software for SK-IV

The author of this thesis developed a software which enables to monitor the quality of the recorded data. The software is running *online*, using a realtime data streamed by the data acquisition system. It is specifically designed for the SK-IV experimental phase. After the upgrade of the electronics, the entire DAQ software had to be rewritten. The newly created components were developed using C++ programming language with an extensive use of ROOT data analysis libraries [106].

The DAQ monitoring software consists of three major components – *skhist*, *servhist* and *histogrammer*. *Skhist* is a graphical presenter of various data distributions and trigger rates. It is a network client program which gets histograms served over a local SK network by *histserv* (histogram server application). *Histserv* cooperates with the *histogrammer* component. The latter one directly connects to the DAQ stream and extracts the information needed to create histograms and data distributions. All histograms produced by the *histogrammer* reside in a dedicated shared memory region and are being constantly updated during a run.

Figure 4.6 presents the *skhist* window which contains the example set of distributions which could be visualized with it. *Skhist* is one of the standard programs used by people on the shifts to control the status of the detector and quality of recorded data. Program allows also to retrieve the history of distributions. It is possible to compare to past data with current ones or with a standard pattern. *Skhist* and the related applications have been used within the SK collaboration from September 2008.

Figure 4.6: *Skhist* application window.

# Chapter 5

## Atmospheric Neutrinos at Super-Kamiokande

The Super-Kamiokande data set was acquired during four phases of the experiment which are spanning the years 1996–2001 (SK-I), 2002–2005 (SK-II), 2006–2008 (SK-III) and 2008 onwards (SK-IV). The analysis presented in this thesis is based on data collected during SK-I, SK-II and SK-III periods. Data is separated into three categories following event topology: (1) neutrino events fully-contained inside the inner detector (FC events); (2) partially-contained events with an interaction vertex in the inner detector and some tracks recorded also in the outer detector (PC events); (3) and upward-going muon events from interactions of neutrinos beneath the detector (UPMU events). From triggers collected with average rate of 10 – 12 Hz, neutrino interaction candidates are selected in the procedure called data reduction. Data reduction is done separately for each category of events. The purpose of this procedure is to get rid of the background events and isolate neutrino interactions of the certain topological type. Special care is taken to ensure high efficiency of the selection.

In this chapter, basic characteristics and criteria for the selection of fully-contained, partially-contained and upward-going muon events are presented. These event samples constitute the final data set used in the physical analysis. Then, it is described how atmospheric neutrino data are modeled using simulations. With a help of simulations it is possible to investigate the effect of neutrino oscillations and to constrain the values of oscillation parameters  $\theta_{23}$  and  $\Delta m_{23}^2$ . The methodology and results of the atmospheric oscillation analysis are presented in the last part of this chapter. Also, short discussion on the origin of systematic uncertainties is included there. The similar methodology is in case of the oscillation analysis is applied later in the search for dark matter signal (see Chapters 6, 7).

### 5.1 Data Samples

The classification into the fully-contained, partially-contained, and upward-going muon event samples is based on the topology of neutrino induced signal.

### Fully-contained events

At the lowest energies, 100 MeV – 10 GeV, neutrinos are observed mainly via their charged current interactions with nuclei in the 22.5 kiloton water fiducial mass of the Super-Kamiokande detector. If the reconstructed neutrino interaction vertex is placed in the fiducial volume (FV) and all particles produced in the interaction stop inside the inner tank, then this type of event is classified as fully-contained. Moreover, if all particles produced in neutrino interaction emit Cherenkov light, the energy of a parent neutrino can be reconstructed with a good accuracy.

Fully-contained sample can be divided into specific subsamples. Basic criterium is related to visible energy ( $E_{vis}$ ) of event. Lower energy events are referred to as Sub-GeV ( $E_{vis} < 1.33$  GeV) and higher energy as Multi-GeV ( $E_{vis} \geq 1.33$  GeV). Sub-GeV and Multi-GeV events can be further divided into the events with a single visible ring (Single-Ring) and events with more than one visible ring (Multi-Ring). All that events are classified as either e-like or  $\mu$ -like based on the PID classification of the most energetic ring (most brightest ring) as it is explained in Section 4.2. In addition, Sub-GeV e-like and Sub-GeV  $\mu$ -like samples are subdivided into more detailed samples based on the number of electron rings (number of decay electrons) originating from delayed decays of directly produced muons or muons from pion decays. There are three categories of Sub-GeV  $\mu$ -like events based on number of decay electrons – 0, 1 and 2 (or more) decay electrons. In case of Sub-GeV e-like events only two such classes are distinguished – 0 and 1 (or more) decay electrons. That last classification affects Sub-GeV e-like samples and is based on a presence of decaying  $\pi^0$  mesons ( $\pi^0$ -like events). The corresponding samples are referred to as Sub-GeV  $\pi^0$ -like 1-Ring and Sub-GeV  $\pi^0$ -like Multi-Ring. The selection of events that belong to  $\pi^0$ -like samples is based on advanced classification algorithm tests various light patterns with a decaying  $\pi^0$  meson and estimates the probability that given event may contain only one visible  $\gamma$  ring from  $\pi^0$  decay (1-Ring  $\pi^0$ -like) or there are clearly two  $\gamma$  rings visible with energy matching the  $\pi^0$  mass (Multi-Ring  $\pi^0$ -like).

In total, one can distinguish 11 subsamples of fully-contained events which are listed in Table 5.1. These subsamples do not overlap – there are no events that contribute to more than one sample. All of the sets listed in Table 5.1 are considered in the neutrino oscillation analysis of SK data.

### Partially-contained events

Partially-contained sample consists of events which have a charged particle, produced in neutrino interaction in FV, which exits the inner detector. The Cherenkov light emitted by this particle is recored as well in the ID detector as in the outer veto region. The energies of neutrinos that produce partially-contained events are typically 10 times higher then those that produce fully-contained events. Electron neutrinos contribute only to FC samples as electron produced in CC neutrino interaction inside fiducial volume (2 meters from the walls of the inner detector) is very likely to stop inside the inner tank due to effective energy loss in water. The contribution of e-like events to partially-contained sample is estimated to be less than 2% [5].

Sample of partially-contained events can be divided into PC stopping and PC through-going subsamples. The first one includes particles that are depositing very little energy in the outer detector and most likely stopped there. The second sample consists of all the other PC events.

Table 5.1: Classification of the Super-Kamiokande atmospheric neutrino data samples. The information about the bin pattern of each sample is given as it is used in the oscillation analysis.

Sample	Subsample
<b>FC</b>	10 bins in $\cos\theta$ , 5 momentum bins [100-251, 251-398, 398-631, 631-1000, 1000-1330 MeV] : Sub-GeV $\mu$ -like 0-decay e, Sub-GeV $\mu$ -like 1-decay e, Sub-GeV e-like 0-decay e
	1 bin in $\cos\theta$ , 5 momentum bins [100-251, 251-398, 398-631, 631-1000, 1000-1330 MeV] : Sub-GeV $\mu$ -like 2-decay e, Sub-GeV e-like 1-decay e, Sub-GeV $\pi^0$ -like 1-Ring
	1 bin in $\cos\theta$ , 5 momentum bins [100-158, 158-251, 251-398, 398-631, 631-1330 MeV] : Sub-GeV $\pi^0$ -like Multi-Ring
	10 bins in $\cos\theta$ , 4 momentum bins [1.33-2.5, 2.5-5, 5-10, 10-100 GeV] : Multi-GeV e-like, Multi-Ring e-like
	10 bins in $\cos\theta$ , 2 momentum bins [1.33-2.5, 2.5-100 GeV] : Multi-GeV $\mu$ -like
	10 bins in $\cos\theta$ , 4 momentum bins [0.1-1.33, 1.33-2.5, 2.5-5, 5-100 GeV] : Multi-Ring $\mu$ -like
<b>PC</b>	10 bins in $\cos\theta$ , 2 momentum bins [0.1-2.5, 2.5-100 GeV] : PC stopping
	10 bins in $\cos\theta$ , 4 momentum bins [0.1-1.33, 1.33-2.5, 2.5-5, 5-100 GeV] : PC through-going
<b>UPMU</b>	10 bins in $\cos\theta$ , 3 momentum bins [1.6-2.5, 2.5-5, 5-100000 GeV] : UPMU stopping
	10 bins in $\cos\theta$ , 1 momentum bin [0.1-100000 GeV] : UPMU through-going non-showering, UPMU through-going showering

### Upward-going muon events

Some neutrino interactions in the rock surrounding the detector and in water of the outer detector can also be recorded and analyzed. High energy muons produced in charged current  $\nu_\mu(\bar{\nu}_\mu)$  interactions outside detector could intersect the tank, emitting Cherenkov light in the outer and in the inner detector. Downward-going cosmic ray muons cannot be distinguished here from downward-going muons produced in neutrino interactions. However, cosmic ray muon flux is almost entirely suppressed from the direction below the horizon at the detector underground location. Thus, upward-going muons must be of the neutrino interaction origin and can be used in the analysis involving muon neutrinos. In case of upward-going muons, as well as for partially-contained events, only part of the muon energy is deposited in the detector and energy of a parent neutrino cannot be resolved.

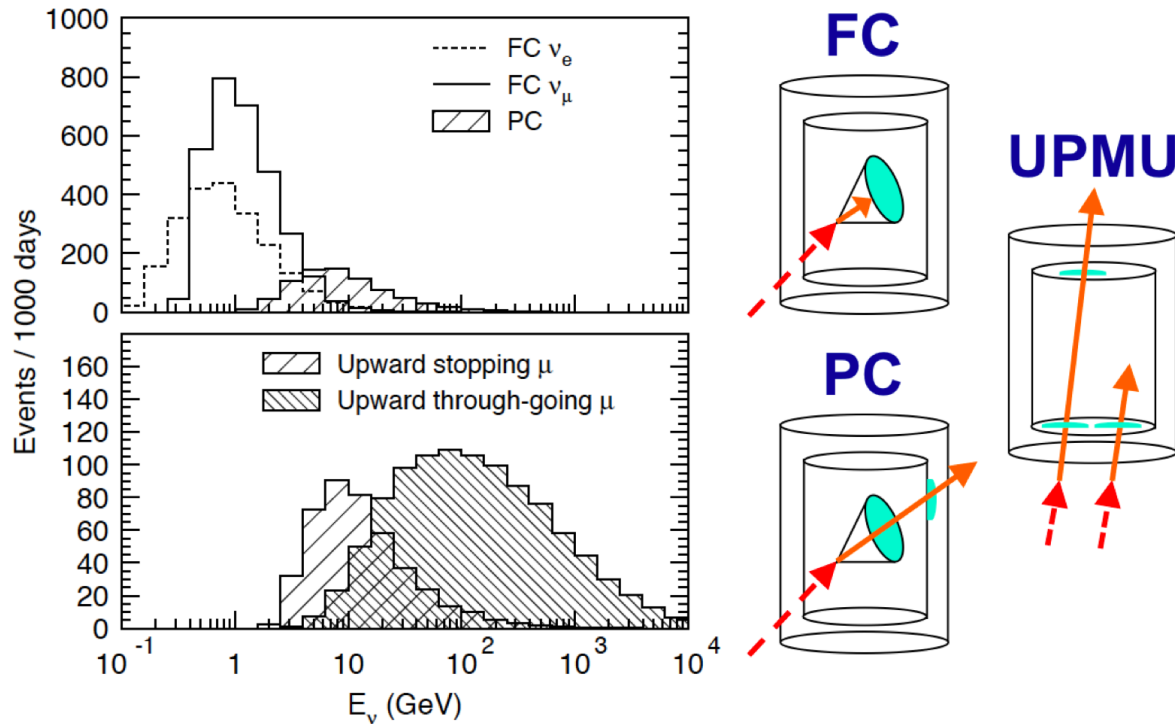


Figure 5.1: The simulated parent neutrino energy distributions for the fully-contained, partially-contained, upward stopping muon and upward through-going muon event samples of atmospheric neutrinos. Rates for the fully-contained and partially-contained samples are for interactions in the 22.5 kiloton fiducial volume. Figure taken from Ref. [5]

Upward-going muons can be divided into two main categories: those which enter the detector and stop inside (upward stopping muons) and those that entirely traverse the detector volume (upward through-going muons). Upward through-going muons could be additionally classified as non-showering or showering. That allows to isolate potentially most energetic neutrino sample which produce high energy showering muons with mean energy of hundreds GeV. The mean energy of neutrinos which produce stopping muons is roughly the same as for partially-contained events,  $\sim 10$  GeV. Upward through-going events are significantly more energetic than UPMU stopping events: the parent neutrino energy for these events is about 100 GeV on average and even more for the showering subsample. Energetic muon neutrinos produce muons which, within very good accuracy, have the same direction as their parent neutrino (see Fig. 2.3). Thus, upward-going muons compose the best sample suitable for any analysis where the good information about a position of neutrino source is important.

Figure 5.1 illustrates how FC, PC and UPMU event categories are being populated depending on a parent neutrino energy. The results are based on a simulation of atmospheric  $\nu_\mu$  and  $\nu_e$  interactions which were processed through the simulation of the detector response and event classification process of the same type as for the real data. For each simulated event the true neutrino energy is known and it spans many orders of magnitude as it is discussed in Section 2.5 (see Fig. 2.7).

## 5.2 Data Selection

In this section the basic idea for the selection of the fully-contained, partially-contained and upward-going muon events is shown. The background events dominate collected data and consist mainly of downward-going cosmic ray muons and low energy radioactivity from parents such as radon. The rate of background events in the collected samples overwhelms the rate of neutrino events by around 5 orders of magnitude. The reduction procedures which are applied to the data are usually based on sets of cuts arranged in the consecutive steps. The values of different group of variables are checked with computer algorithms and in each step it is decided whether the event has the characteristic typical for background (and then it is rejected) or it is more probable that it is due to neutrino interaction (and then the event is kept and passes to the next step). Selection criteria are chosen to assure the highest rejection of background events while keeping the highest number of neutrino events at the same time. After the entire reduction chain is applied and the final neutrino samples are isolated, the contribution of background events in them is less than 1%. As the last step, FC, PC, and UPMU events are scanned by physicists to check data quality and to verify the output of computer algorithms.

### Fully-contained event selection

The main criterium used to select neutrino events contained in the detector is the requirement of little activity in the outer detector used here as a veto region. That removes cosmic ray muons and distinguishes FC events from PC and UPMU events. One of the most important variables used in the selection is *nhitac* – number of photomultipliers which give signal in the largest OD cluster (number of OD hits). This variable is used to define whether the event is FC or PC. For the FC events *nhitac* should be  $<10$  in SK-I, and  $<16$  in SK-II and SK-III. The difference between SK-I and other experimental phases is due to changed configuration and different detector performance (Section 4.3). The distribution of *nhitac* variable of SK-I data is shown in Fig. 5.2.

Except the *nhitac*, also other more complex variables are checked in the process of selection. Detailed description of the whole procedure is provided in [5]. The rate of the fully-contained neutrino interactions is  $\sim 8$  events/day. Only the events with visible energy above 30 MeV are considered. This threshold is defined as the minimum energy of an electromagnetic shower that gives a certain amount of Cherenkov light.

The main sources of background for the FC sample consist of cosmic ray muons which pass the reduction cuts; neutrons generated by high energy cosmic ray muons which are captured in water and produce light; and false events generated by malfunctioning photomultipliers or electronics (flasher PMTs). The first mentioned source of background – cosmic ray muons – yields a background contamination of 0.07% in Sub-GeV  $\mu$ -like samples and 0.09% for Multi-GeV  $\mu$ -like events. The other sources of background contribute only to the e-like samples. Background related to neutrons is estimated to be 0.1% for Sub-GeV and Multi-GeV e-like events. The contamination from PMT flasher events is 0.42% for Sub-GeV e-like and 0.16% for Multi-GeV e-like events. All that numbers are estimated for SK-I [5] and they are similar for other experimental phases.

Examples of event display of e-like and  $\mu$ -like FC events with one clearly visible main ring are shown in Fig. 4.4 in Chapter 4. The classification for e-like and  $\mu$ -like events is based on the likelihood function which is illustrated in Fig. 4.5 (Section 4.2).

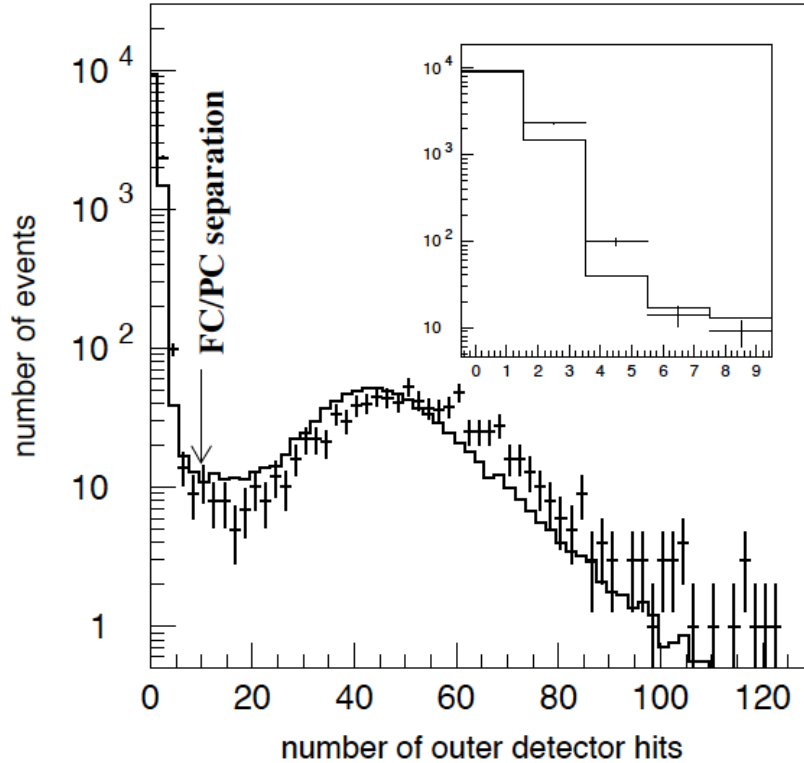


Figure 5.2: The number of hits in the largest outer detector cluster ( $n_{hitac}$ ). This variable is used to separate the fully-contained and partially-contained events. The histogram shows SK-I data (black points with errors) and prediction based on the Monte Carlo simulation (black histogram). The shift between the data and MC is due to the incomplete reflection of the outer detector performance in the simulation. It is one of the sources of the systematic uncertainty related to data reduction.

### Partially-contained event selection

Partially-contained events are selected based on a presence of light recorded in the outer detector. The most simple selection criteria are related to variables like the number of hit PMTs in the outer detector, number of clusters of hits, time structure of the signal. For the PC events it is required that event has to originate in the inner detector (vertex inside FV) and a charged particle (or particles), produced in neutrino interaction, must get to the outer detector and emit Cherenkov light there. The information about the time when the Cherenkov light is recorded in the outer detector PMTs and in the inner detector PMTs enables to distinguish PC events from UPMU events. The latter ones first enter the outer detector, deposit energy there, and then produce the light in the inner detector region (a sequence opposite to PC events). Also, in case of through-going UPMU events, more than one cluster of hits in the outer detector can be recognized corresponding to the entrance and exit point of a passing muon. PC events are distinguished from FC events based on the value of  $n_{hitac}$  variable as discussed in the previous section.

In order to reject background events which have non-trivial topology and not satisfactory timing information (mainly fast cosmic ray muons), more complex and time consuming criteria are applied during PC data selection using a specialized software.

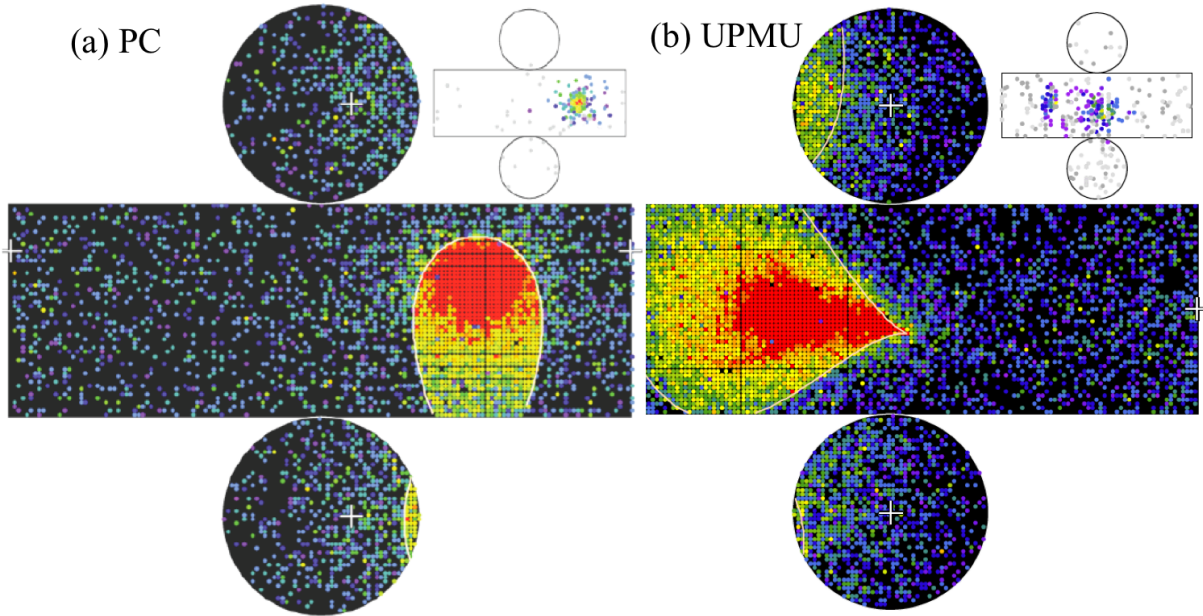


Figure 5.3: An example of event display of partially-contained (a) and upward through-going muon (b) events. Colors represent the charge deposited in PMTs. The scale is from red (maximum charge) to blue (minimum charge). Main canvas shows the hits in the inner detector. Inset corresponds to the outer detector.

There are dedicated computer algorithms, developed at SK, which are specialized to test the probability that observed event is due to interaction of a muon (muon fitters). Various muon fitters are used during selection procedure of PC events.

Even though advanced algorithms are used for the creation of the final PC data set, it still contains some unresolved background events. They consist mainly of stopping and through-going cosmic ray muons. In case of complex ring topologies, it is sometimes difficult to assign the correct ring direction and decide whether the event is a neutrino induced muon exiting the inner tank with an interaction vertex inside the ID or just a cosmic ray muon entering the tank from the outer detector and giving also a signal in the inner part. The rate of background events estimated in the eye-scanning of the final samples is less than 2%, similarly for all SK phases. The identified background events are not eliminated from the final samples and are also used in the analyses<sup>1</sup>. In the final sample, rate of PC events with a reconstructed vertex in the fiducial volume is  $\sim 0.6$  neutrinos/day. More details on the PC reduction are given in [5, 109].

An example of event display of the partially-contained event is shown in Fig. 5.3(a). Because the charged lepton, produced in neutrino interaction, exists the inner volume, the observed signal has a shape of a filled circle (as opposite to rings observed in case of FC events).

The author of this thesis maintained the partially-contained event selection during his work for the Super-K collaboration. He took responsibility for preparation of the official PC data sets based on SK-III data and estimated the systematic errors related to SK-III PC reduction. He worked also on PC event selection of SK-IV data.

<sup>1</sup>That is also true for FC samples, recognized background events are kept in the final FC samples. In case of UPMU samples, estimated rate of background events due to horizontal cosmic ray muons is subtracted from the final data set.

### Upward-going muon event selection

As it was stated before in Section 5.1, the upward-going muons observed at Super-K are classified into two categories: (1) upward stopping muon events having only an entrance signal in the OD; and (2) upward through-going muon events having both entrance and exit signals in the OD. The latter category can be divided into showering and non-showering events.

The UPMU selection is based on the identification of the entry and exit points in the OD using the information on the number hits in the OD, type of clustering and time structure of the signal. Entry and exit points are defined as minimum 10 OD PMTs that recorded signal. For the UPMU through-going events it is required that their geometrical trajectory in the inner detector is greater than 7 meters. For the UPMU stopping events it required that their visible energy must correspond to the energy loss of a minimum ionizing particle which traveled more than 7 meters in water.

To isolate the rate of about 1.5 neutrino induced upward-going muon per day from the remaining background of about  $2 \times 10^5$  cosmic ray muons, many different muon fitters are used. Some of these fitters are specialized to fit stopping muons, others are specialized to fit through-going muon events, or to fit muon events with bremsstrahlung *etc.* The fitters are applied to events in consecutive steps. Events that passed the previous step are then being tested with the next more complex set of fitters. The main logic behind that reduction is that if a muon fitter classifies an event as upward with a goodness of fit which was above the fitters goodness threshold then the event is automatically saved. Otherwise it is rejected.

After all computer tests are applied, the resulting sample is scanned by physicists. The aim is to check the data quality and to identify and remove background events that are due to unresolved PC or FC events. The last step is to estimate the fraction of cosmic ray muons in the most horizontal bins in  $\cos\theta$  (zenith angle of a muon). The obtained number is subtracted from the final UPMU sample which is later used in the physical analyses. The contribution of cosmic ray muons with  $\cos\theta < 0$  is non-zero because the Super-K detector is overburdened by a mountain which has some regions of thinner rock at certain azimuthal angles. Thus, the suppression of the cosmic ray muon flux is not even from all the directions. The contribution from horizontal cosmic ray muons is estimated using the events with  $\cos\theta$  slightly greater than zero. Then, it is assumed that horizontal muons coming from a little bit below the horizon have the same characteristics.

An example of event display of the upward through-going muon is shown in Fig. 5.3(b). In the OD region the entry and exit points are clearly visible. The direction of the muon could be estimated based on the number of photoelectrons recorded in PMTs (and also using time arrival information of the signal in PMTs).

## 5.3 Monte Carlo Simulation of Atmospheric Neutrino Interactions at Super-Kamiokande

The purpose of simulation of experimental data is to understand the physical processes that are responsible for the observation and a proof of understanding how data are collected and processed. Interactions of atmospheric neutrinos at Super-Kamiokande are simulated in large statistics corresponding to 500 years of livetime for each running period

Table 5.2: Reduction efficiency for each category of events in SK-I, SK-II and SK-III.

Sample	SK-I	SK-II	SK-III
FC	97.6%	99.2%	98.5%
PC	81.0%	74.8%	88.6%
Upward stopping $\mu$	98.0%	97.0%	98.2%
Upward through-going $\mu$	99.4%	98.1%	99.4%

of SK-I, SK-II and SK-III. These generated samples are being referred to as atmospheric Monte Carlo samples throughout the thesis.

Detailed description of atmospheric Monte Carlo generation for SK can be found in Ref. [5]. Below a brief overview is given. Atmospheric Monte Carlo is produced in a few steps. First, interactions of atmospheric neutrinos are simulated using NEUT neutrino interaction package [107]. The fluxes of neutrinos produced in the atmosphere in the cosmic ray showers are adopted from calculations of Honda *et al.* [83]. They are obtained for the Kamioka Observatory location, so the effects related to the Earth's magnetic field are included. The flux evaluation assumes no oscillations in neutrino propagation in the atmosphere and inside the Earth. Due to that fact, this MC is often referred to as *unoscillated MC*. To obtain *oscillated MC* each event from *unoscillated MC* is assigned the *oscillation weight* which corresponds to probability that neutrino characterized by a given flavor, energy and direction would change its flavor. The values of *oscillation weights* are obtained in the atmospheric oscillation analysis and are based on the fitted values of oscillation parameters (see Section 5.5). Next step in MC production is a simulation of the detector response for neutrino interaction products. Dedicated detector simulation was prepared using Geant3 package [108]. The production of Cherenkov light in water, transportation of all particles in the detector geometry and in the surrounding rock is included as well as the simulation of the electronic signal from photomultipliers. The last stage of the simulation is the data selection. Here, the same algorithms as for real data are applied to MC events to isolate fully-contained, partially-contained, and upward-going muon samples (and all of their subsamples as listed in Table 5.1). Atmospheric Monte Carlo obtained in that way provides a detailed expectation on the number of atmospheric events seen in the experiment (after scaling to the same livetime as data) and the information on the characteristics of atmospheric neutrinos.

Atmospheric Monte Carlo contains only neutrino events and no backgrounds. When one applies data reduction procedure to MC events, the efficiency of such selection can be estimated. One could answer the question how many neutrino events are rejected when the same procedure is applied to real data. The reduction efficiency for FC/PC samples is defined here as the percentage of neutrino events which have reconstructed vertex in the FV and which passed all the reduction steps getting into the final sample, to the number of all generated events with a true vertex in the FV. Reduction efficiency for UPMU events is based on the ratio of events which passed entire reduction chain, to all events which are traversing the detector. Table 5.2 contains summary of the reduction efficiency values for each category of events in SK-I, SK-II and SK-III.

## 5.4 Monte Carlo Simulation of Tau Neutrino Interactions at Super-Kamiokande

In addition to simulation of interactions of atmospheric neutrinos at SK, the simulation of interactions of tau neutrinos is performed for the reasons outlined below.

As it is explained in Section 2.5, there is very little tau neutrinos produced in the atmosphere from charmed mesons and they practically do not contribute to the observed data samples. The expected event rate from prompt tau neutrinos at SK could be estimated from [86] to be at the level of 4-7 events for SK-I+II+III running period. However, tau neutrinos could be produced also in oscillation of atmospheric muon neutrinos. The expected rate of those is low but could be attempted to observe. To give an estimate, expected contribution from CC  $\nu_\tau$  produced in oscillations of atmospheric  $\nu_\mu$  is 78 events for the SK-I data period for  $\Delta m_{23}^2 = 2.4 \cdot 10^{-3} \text{ eV}^2$ ,  $\sin^2 2\theta_{23} = 1.0$  [113].

In the experiment, it is impossible to distinguish CC  $\nu_\tau$  interactions from CC interactions of  $\nu_\mu$  and  $\nu_e$ . The tau lepton cannot be observed in water Cherenkov detector as it has very short lifetime of around 290 femtoseconds and decays into  $\nu_\tau$  and other particles, mostly pions. The recoiling hadronic state may additionally produce multiple particles. Therefore, the interactions of tau neutrinos are expected to lead to a complex topology observed at SK detector. These kind of events are difficult to reconstruct as they usually have many rings – some of them could be invisible and others may overlap. High average multiplicity results in production of hadronic showers, therefore these events would mostly be classified as e-like. Tau events of this characteristics cannot be told apart from DIS and a resonant pion production interactions of muon and electron neutrinos. Therefore, any search for tau neutrinos at SK can be performed only on the statistical basis. Then, it is useful to have a dedicated simulation of  $\nu_\tau$  interactions – tau MC. That allows to understand the detector response for tau neutrinos and to effectively study characteristics of these events.

A Monte Carlo simulation of  $\nu_\tau$  interactions is available for each running phase of SK-I, -II and -III. The generated MC sets contain only charged current interactions of tau neutrinos. The CC  $\nu_\tau$  interactions are mostly a deep inelastic scattering (approximately 63%) due to high energy threshold for a tau lepton production which is 3.5 GeV [113]. The tau MC uses the  $\nu_\tau$  cross section and assumes the flux of tau neutrinos to be the same as the flux of muon neutrinos. Decays of primary tau leptons are simulated with the tau decay library Tauola [114] which is used to choose the correct decay mode and kinematics of the outgoing particles. The detector response is simulated for all particles produced in tau neutrino interactions. Event reconstruction and data selection procedures are applied at the end of the process.

The simulated events of  $\nu_\tau$  interactions at SK are used in the oscillation analysis described the next section. Each event from tau MC is assigned the oscillation weight which is related to the probability that this event could be created from the muon neutrino that changed flavor during propagation. That probability depends on the energy and direction of a given neutrino. Events with non-zero weights contribute to the observed samples proportionally to the value of the obtained weight. They are used to model the SK data along with the muon and electron neutrinos from atmospheric MC set. The final contribution of tau events to the collected data is being determined in the oscillation analysis and is related to the obtained value of the oscillation parameters  $\theta_{23}$  and  $\Delta m_{23}^2$ .

## 5.5 Atmospheric Neutrino Oscillation Analysis

Atmospheric Monte Carlo and tau Monte Carlo sets are used to study neutrino oscillations. By changing the values of oscillation parameters (varying *oscillation weights* of *unoscillated MC*) one gets better or worse matching between the collected data and the obtained MC expectation. The model which matches data the best provides the best fit of underlying oscillation mechanism. The idea of such a fit is discussed in this section.

In the complete description of oscillations of neutrinos, the transitions between all neutrino flavors shall be considered (3 flavor oscillations). However, in Chapter 2 (Section 2.3) it is mentioned that neutrino oscillations in the atmospheric sector could be described as effective transitions only between muon and tau neutrinos (2 flavor oscillations). In this case, only the values of  $\theta_{23}$  and  $\Delta m_{23}^2$  parameters determine the effect. In case of 3 flavors transitions, additional oscillation parameters contribute such as  $\theta_{13}$ ,  $\theta_{12}$ ,  $\Delta m_{13}^2$ ,  $\Delta m_{12}^2$ . Among them,  $\theta_{13}$  governs the  $\nu_\mu \rightarrow \nu_e$  transitions ( $\nu_e$  appearance). The results of oscillation analysis based on the Super-Kamiokande atmospheric data showed no practical difference between 2 and 3 flavor approach. In the 3 flavor analysis, obtained value of  $\theta_{13}$  is consistent with zero and the values found for  $\theta_{23}$  and  $\Delta m_{23}^2$  parameters are similar to the ones obtained in 2 flavor analysis [110]. Therefore, for the simplicity of the discussion, the results of the 2 flavor analysis of SK data are presented in this section.

### 5.5.1 Livetime of Data Samples

The search is based on all SK samples listed in Table 5.1 and SK-I, SK-II, SK-III sets. The fully-contained and partially-contained data sets share a common set of good run selection criteria, and have identical livetime for each running period. The upward-going muon data set relies mostly on fitting long muon tracks. Thus, it depends less on detector effects resulting in looser data quality cuts and higher livetime. The livetime of each set corresponding to different experimental phases is given in Table 5.3.

Table 5.3: Livetime of SK-I, SK-II and SK-III data sets.

Sample	SK-I	SK-II	SK-III
FC/PC	1489.2 days	798.6 days	518.1 days
UPMU	1646.0 days	828.0 days	635.6 days

### 5.5.2 Fit

The data are compared against the Monte Carlo expectation using a "pulled"  $\chi^2$  [111] method based on a Poisson probability distribution:

$$\chi^2 = 2 \sum_n \left( N_n^{MC} \left( 1 + \sum_i f_i^n \epsilon_i \right) - N_n^{data} + N_n^{data} \ln \frac{N_n^{data}}{N_n^{MC} (1 + \sum_i f_i^n \epsilon_i)} \right) + \sum_i \left( \frac{\epsilon_i}{\sigma_i} \right) \quad (5.1)$$

where  $n$  indexes the data bins,  $N_n^{MC}$  is the MC expectation with oscillations, and  $N_n^{data}$  is the number of observed events in the  $n^{th}$  bin. When 2 flavor oscillations are considered,

$N_n^{MC}$  depends on the values of 2 oscillation parameters,  $\theta_{23}$  and  $\Delta m_{23}^2 - N_n^{MC}(\theta_{23}, \Delta m_{23}^2)$ . These parameters governs the probability that a muon neutrino characterized by a given energy and direction, will change into the tau neutrino. That probability is calculated for each  $\nu_\mu$  ( $\bar{\nu}_\mu$ ) event present in the atmospheric Monte Carlo (disappearance probability) and for each  $\nu_\tau$  ( $\bar{\nu}_\tau$ ) event from tau MC (appearance probability). When MC expectation is compared against data as in Eq. 5.1, each event in MC contributes with the *oscillation weights* corresponding to the obtained value of oscillation probability. During a fit, the values of oscillation parameters are varied and the configuration with the best matching between the data and MC expectation implies the best oscillation model. The values of  $\theta_{23}$  and  $\Delta m_{23}^2$  are determined in this procedure.

Systematic errors are incorporated into the fit via the systematic error parameter  $\epsilon_i$ , where  $i$  is the systematic error index and  $f_i^n$  is the fractional change in the MC expectation in bin  $n$  for a  $\sigma_i$  change in the  $i^{th}$  systematic error. During a fit, equation 5.1 is minimized with respect to the  $\epsilon_i$  at each point in a fit's oscillation parameter space according to  $\frac{\partial \chi^2}{\partial \epsilon_i} = 0$  [111]. The best fit point is defined as the global minimum  $\chi^2$  on the grid of oscillation points. The index  $i$  spans from 1 to 120 as there are 120 sources of systematic uncertainty applicable in the atmospheric neutrino analysis of SK data. The sources of systematic uncertainty are discussed in the next section.

There are 16 data samples used in the analysis, including both e-like and  $\mu$ -like event categories. These include all samples into which FC, PC and UPMU events could be subdivided as shown in Table 5.1. Each sample is binned in the zenith angle and momentum of event. In case of the single ring events, the value of a zenith angle is reconstructed from observed Cherenkov ring which is produced by a charged particle created in neutrino interaction. In case of events with multiple rings the direction of event is obtained as the weighted average of directions of individual rings. The weights used in the averaging depend on the reconstructed momentum of each particle. For each ring the particle type (PID) is assigned on the basis of ring type (e-like or  $\mu$ -like) and cone opening angle (see Section 4.2). Therefore, the momenta of rings are either related to electrons (e-like rings) or muons ( $\mu$ -like rings). The momentum of a multi-ring event is a sum of individual ring momenta. The only exception from this rule is the momentum estimation of  $\pi^0$ -like events which is based only on the most energetic gamma-induced ring which is e-like. In case of events with decay electrons, the delayed electron ring is not included in the estimation of an event direction and momentum.

If there are  $X$  angular bins considered for a given sample and  $Y$  momentum bins, it can be said that each bin in the zenith angle distribution is investigated in the fit independently  $Y$  times correspondingly to different momenta bins. In total, there would be  $X \times Y$  bins considered in the fit for that given sample.

The FC and PC samples are divided into 10 bins in the zenith angle ranging from  $-1 \leq \cos \theta \leq 1$  with the exception for Sub-GeV  $\pi^0$ -like Multi Ring, Sub-GeV  $\pi^0$ -like Single Ring, Sub-GeV e-like 1 decay electron, and Sub-GeV  $\mu$ -like 2 decay electron samples. These samples contain rings that are very poorly correlated with a parent neutrino direction (low energy events with a complex topology), therefore only 1 bin in the zenith angle is used. There are 10 angular bins for the UPMU events, but the considered zenith angle is from  $-1 \leq \cos \theta \leq 0$ . The binning in the momentum differs among the subsamples and can be consult in Table 5.1.

Samples are binned separately for SK-I, SK-II and SK-III and bins with low number of expected MC events are merged with the neighboring bins. That strategy was adopted

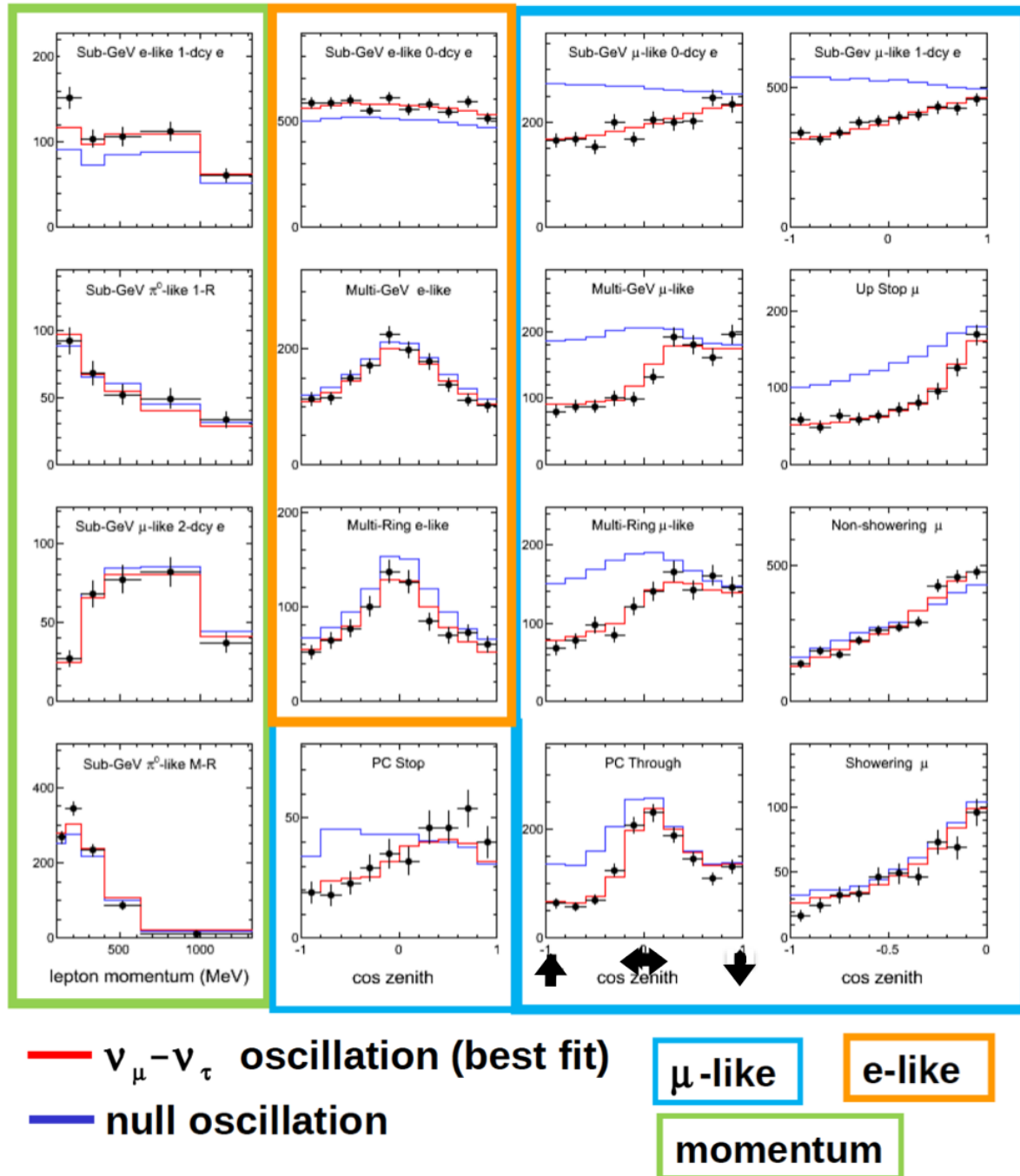


Figure 5.4: The illustration of the zenith angle and momentum distributions of the data samples used in the neutrino oscillation analysis. The Sub-GeV  $\pi^0$ -like Multi Ring, Sub-GeV  $\pi^0$ -like Single Ring, Sub-GeV e-like 1 decay electron, and Sub-GeV  $\mu$ -like 2 decay electron samples have no assigned parent neutrino direction and in case of these samples the momentum distributions of events are shown. The black dots represent the SK-I+II+III data with statistical errors. The red lines stand for the Monte Carlo expectation at the best fit oscillation model. The blue lines are the expectation without oscillations. The impact of the systematic uncertainties is included in the expectation of the best fit oscillation model. From [112].

to ensure the stability of function 5.1. As a result, there are 420 bins considered for each experimental phase. The index  $n$  spans from 1 to 1260.

When data in the considered bin are compared with the Monte Carlo expectation, the normalization of the Monte Carlo sample is scaled to match the livetime of the data separately for SK-I, SK-II and SK-III sets. However, the normalization of MC samples is allowed to slightly vary in the fit via the values of systematic uncertainty parameters. The procedure ensures that various relations between samples (bins), like a relative normalization, are held during a fit. That is a strong bounding condition as changing the normalization of events in one sample always affects characteristics of other samples.

### 5.5.3 Sources of systematic uncertainty

There are 120 systematic uncertainty terms applicable in the oscillation analysis. These systematic errors could be separated into two categories, those that are common to all of the SK run periods and those that differ.

There are 33 errors classified as common for all experimental phases. They are either related to neutrino flux prediction or to interactions of particles that affect neutrino production in the atmosphere. It shall be noticed that these group of uncertainties effectively regulate the normalization of Monte Carlo samples. Directly, as independent parameters which stand behind neutrino flux normalization of low energy ( $< 1$  GeV) and higher energy ( $> 1$  GeV) neutrinos. And indirectly, through impact of uncertainty parameters which are related to neutrino production in the atmosphere like meson production cross sections and nuclear effects in the hadronic showers, ratio of neutrinos of different flavors, ratio of neutrinos to anti-neutrinos *etc.*. Some of these uncertainty parameters depend on the considered energy scale, therefore resulting fluxes of neutrinos of different energies may be affected by different set of uncertainty parameters. The complete list of these errors could be found in Tables V and VI of Ref. [110].

Systematic errors that are independent for SK-I, SK-II, and SK-III represent uncertainties related to the detector performance in each era. Particle reconstruction and identification uncertainties, as well as energy scale and fiducial volume uncertainties, differ for SK-I, SK-II, and SK-III because of their different geometries and performance. One can distinguish  $29 \times 3$  such uncertainty parameters. Their complete list is in Table VII in [110].

The effect of the systematic uncertainties is introduced by the coefficients  $f_i^n$  which are computed for every bin and error in the analysis. For common systematic uncertainties there is a coefficient for every bin in the analysis. On the other hand, independent systematic errors specific to SK-I (II, III) have non-zero coefficients for the SK-I (II,III) analysis bins and are zero otherwise.

### 5.5.4 Results

Figure 5.4 presents the zenith angle distributions of events in various samples used in the search. The Sub-GeV  $\pi^0$ -like Multi Ring, Sub-GeV  $\pi^0$ -like Single Ring, Sub-GeV e-like 1 decay electron, and Sub-GeV  $\mu$ -like 2 decay electron samples have no assigned event direction and in case of these samples the momentum distributions of events are shown instead. The SK+I+II+III data are shown on the plots along with the Monte Carlo expectation without oscillations and best fit oscillation model which is obtained in this

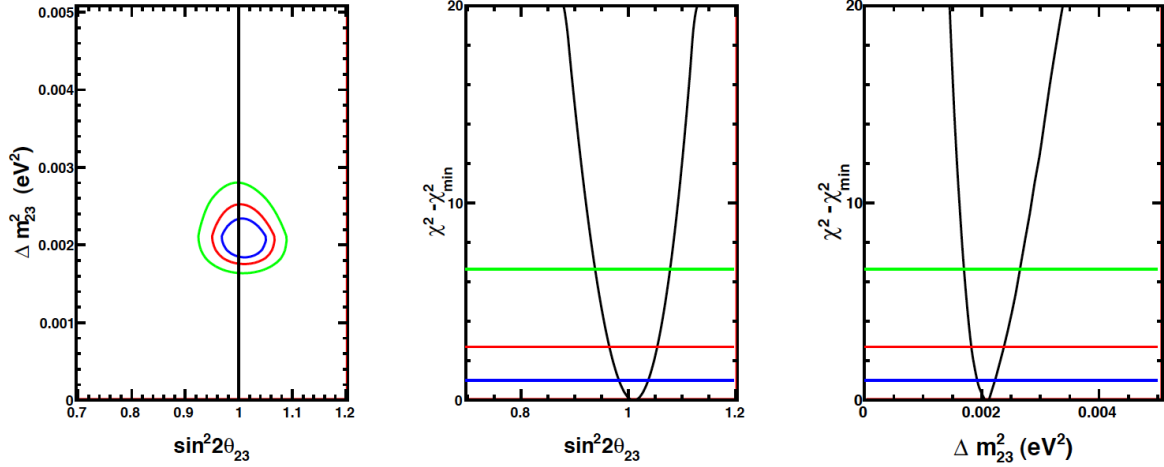


Figure 5.5: *Left figure* – Best fit contour for the values  $\Delta m_{23}^2$  and  $\sin^2 2\theta_{23}$  oscillation parameters in the 2 flavor analysis of SK-I+II+III data. 68% confidence level (CL) allowed region is encircled with the blue line, 90% CL with the red line, and 99% CL with the blue line. *Middle figure* –  $\chi^2 - \chi_{min}^2$  distribution as a function of  $\sin^2 2\theta_{23}$ . For each point in  $\sin^2 2\theta_{23}$ ,  $\Delta m_{23}^2$  is chosen so that  $\chi^2$  minimized. The horizontal lines correspond to the 68% (blue), 90% (red) and 99% (blue) confidence level. *Right figure* –  $\chi^2 - \chi_{min}^2$  distribution as a function of  $\Delta m_{23}^2$  minimized over the values of  $\sin^2 2\theta_{23}$ . The meaning of horizontal lines is the same as in the middle plot.

analysis. It is clearly seen that the measured shape of zenith angle distributions for e-like events is consistent with expectations, but the FC  $\mu$ -like and PC samples show significant zenith-angle dependent deficits of events as compared to model without oscillations. The effect of oscillations in the UPMU sample is not visible (except UPMU stopping sample) due to high mean energy of parent neutrinos – at this configuration of their energy and path length their transitions are not favored.

Fitted values of the oscillation parameters in 2 flavor approach are as follows:  $\sin^2 2\theta_{23} = 1.007$  and  $\Delta m_{23}^2 = 0.00211$  [110]. Since the obtained value for  $\sin^2 2\theta_{23}$  is in the unphysical region, the value  $\sin^2 2\theta_{23} = 1.00$  is adopted as the best physical result. The fit converges at the minimum  $\chi^2/NDF = 469.6/418 = 1.12$ , where NDF stands for Number of Degrees of Freedom. Figure 5.5 shows the best fit contours for  $\sin^2 2\theta_{23}$ ,  $\Delta m_{23}^2$  and a one dimensional  $\chi^2 - \chi_{min}^2$  distributions. The latter ones are obtained separately for each one of the fitted parameters while minimizing the values of the other parameters.

# Chapter 6

## Methodology of Search for Diffuse Dark Matter Annihilation Signal

This chapter presents the methodology of the search for a signal from diffuse dark matter annihilation using Super-Kamiokande atmospheric neutrino data. It is assumed that Super-K data could have one additional source as compared to contribution related to atmospheric neutrinos. Some fraction of collected data may be due to interactions of neutrinos originating from DM annihilation in the cosmic space. The goal of the search is to evaluate the allowed contribution from such source.

The analysis discussed in this chapter would be referred to as the *simplified approach* as it is based on limited number of data samples and systematic uncertainties are not addressed at this stage. The scope of such an approach is to explain the idea of the procedure based on some simple examples and to test the capacity of the method to discover potential signal. The complete search for the diffuse signal, referred to as *global approach*, is presented in the next chapter. The discussion presented in this chapter refers to DM annihilation, but the same approach can be used for studies of a decay of DM particles.

### 6.1 Introduction

The searches presented in this and the next chapter are focused on the scenario with dark matter particles annihilating directly and only to neutrinos, equally to all flavors (see Eq. 3.2). The analysis of this kind was proposed by H. Yuksel *et al.* [90]. In the considered model, resulting neutrino energy is the same as the mass of the annihilating relic particles. Thus, annihilation induced neutrinos would introduce a characteristic modification to the observed atmospheric neutrino energy spectrum as it is discussed in Section 3.2 (compare Fig. 3.6). Moreover, one could also expect that neutrinos from diffuse dark matter annihilation would have an isotropic zenith angle distribution. The Super-Kamiokande data set consisting of interactions of atmospheric neutrinos could be investigated for the presence of admixture with such distinctive signatures.

The aim of the search is to test the hypothesis of presence of DM signal in to collected data and to evaluate the allowed contribution related to dark matter induced neutrinos. In order to achieve this goal the following approach is adopted. It is assumed that Super-Kamiokande data could be described by two components: dark matter induced neutrinos

(signal) and atmospheric neutrinos (background). For each tested mass of DM particles, the best combination of signal and background is found that the best matches the data. The background and signal contributions are evaluated based on the Monte Carlo simulations.

The simulation of interactions of atmospheric neutrinos (atmospheric Monte Carlo) is available for the Super-Kamiokande data in large statistics – 500 years of livetime for each running period of SK-I, SK-II and SK-III. Atmospheric events are classified into three main event categories – fully-contained (FC), partially-contained (PC), and upward-going muons (UPMU). Chapter 5 contains description of SK data samples. The explanation of Monte Carlo simulations of atmospheric neutrinos is also contained there.

The simulation of diffuse neutrino signal is developed for the purpose of this analysis and is described in the next section.

## 6.2 Simulation of Diffuse Dark Matter Annihilation Signal

Dark matter induced neutrino signal is simulated assuming several neutrino energies corresponding to different masses of relic particles. The large set of generated events is already available for atmospheric neutrinos (atmospheric MC). Simulation of the detector response is done and the data selection procedures are already applied to all events from atmospheric MC. The same simulation conditions for the signal and background events can be assured, with all apparatus details included, if events from atmospheric MC are used to mimic signal events. However, one has to remember that atmospheric MC events have certain characteristics different than the ones expected for the signal. These effects shall be taken into account and corrected for as it is described below.

### Energy

In the investigated model of DM annihilation, the signal is monoenergetic and atmospheric neutrinos are described by continuous energy spectrum as shown in Fig. 2.7. Therefore, only  $\nu$  events from atmospheric MC with the true energy close to the considered mass of the annihilating relic particles are used to mimic signal events.

The number of events in SK-I atmospheric Monte Carlo (500 years of livetime) is shown in Fig. 6.1 as a function of the energy of atmospheric neutrinos. Decrease of the number of events in MC samples, observed for higher energies, reflects the dependence of the neutrino flux on the value of the flux of primary cosmic rays, which can be described as  $E^{-2.7}$  function of energy (E) [56]. It can be seen that the higher the energy of neutrinos is, the wider bins should be considered in order to have sufficient statistics to simulate signal events at this given energy.

### Direction

The signal is expected to be isotropic in coordinate system related to the Earth as it is discussed in Section 3.2. The  $\cos\theta$  distribution of atmospheric neutrinos is not isotropic – compare figure 2.6. Thus, in order to properly mimic signal events with atmospheric neutrino events, the latter ones are assigned special *isotropic weights*. These weights are

Number of events in SK-I MC (500 years livetime)

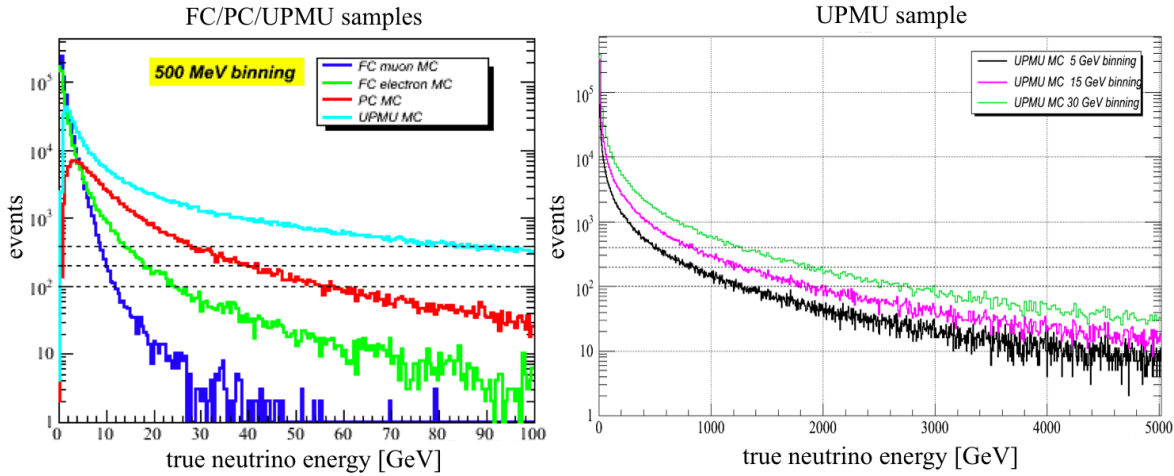


Figure 6.1: Number of events in atmospheric neutrino Monte Carlo as a function of true neutrino energy. Left panel shows the number of FC/PC/UPMU events in energy bins of 500 MeV. Right panel presents the total number of UPMU events using bins of different sizes as indicated on the plot. The data shown on the plots correspond to SK-I Monte Carlo set of 500 years of livetime.

evaluated on the basis of  $\cos\theta$  distributions of atmospheric neutrinos of a given energy before any effects related to the signal observation are taken into account. Purpose of the weights is to make the distribution of events, which are used to mimic DM signal, isotropic (flat in  $\cos\theta$ ).

Figure 6.2 shows the  $\cos\theta$  distribution of atmospheric neutrinos of energy of 4 GeV before any effects related to detection and acceptance of events are taken into account. Based on that information, one could calculate the value of a weight that should be assigned to each event, selected to simulate DM signal from atmospheric MC, that would yield the isotropic  $\cos\theta$  distribution. The weights depend on the value of  $\cos\theta$  and are determined for each neutrino energy separately. In Figure 6.2, the flux value of the illustrated signal is arbitrary and does not reflect the fact that the same flux value for all neutrino flavors is expected in case of the signal.

## Neutrino flavor

One expects that dark matter annihilation would result in equal fluxes of neutrinos for every flavor. That is not true for atmospheric neutrinos – fluxes ratio for different flavors are not the same and change with energy (compare Fig. 2.7). Therefore, atmospheric neutrino events that are selected to mimic signal events of the certain energy are assigned additional weights to assure the criterium of  $\phi(\nu_e) = \phi(\bar{\nu}_e) = \phi(\nu_\mu) = \phi(\bar{\nu}_\mu) = \phi(\nu_\tau) = \phi(\bar{\nu}_\tau)$ . This requirement means that the flux of DM-induced neutrinos before the detection should be the same for every flavor and also for neutrinos and anti-neutrinos.

Table 6.1 shows the number of muon and electron neutrino events in SK-I+II+III atmospheric Monte Carlo set (1500 years of livetime) in selected energy intervals. The production of atmospheric MC is discussed in Section 5.3. The number of tau neutrino events is also shown in the table. The interactions of tau neutrinos are simulated as explained in Section 5.4 ( $\phi(\nu_\tau/\bar{\nu}_\tau) = \phi(\nu_\mu/\bar{\nu}_\mu)$ ) and correspond to the same livetime as

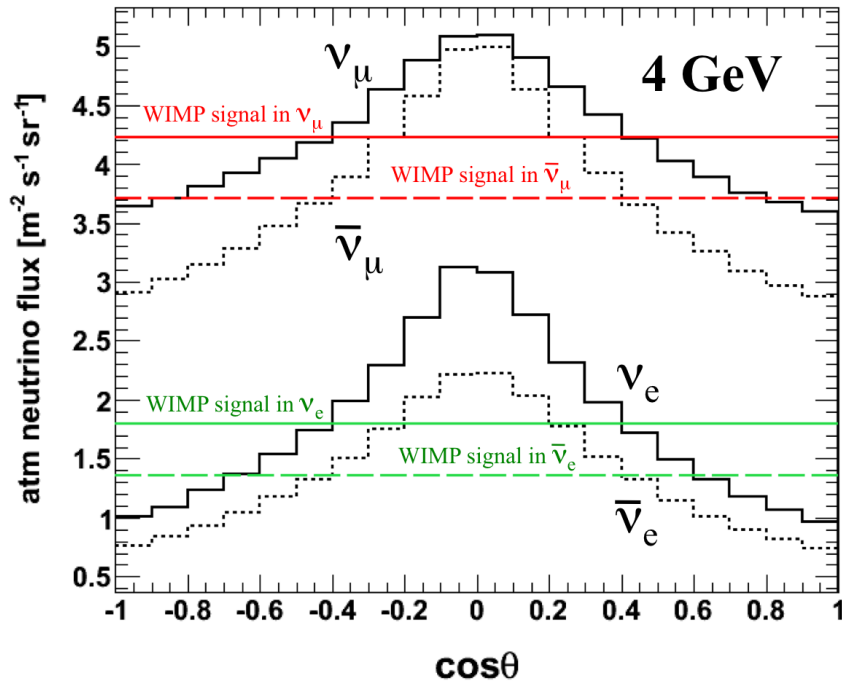


Figure 6.2: Zenith angle distribution of  $\nu_\mu$ ,  $\bar{\nu}_\mu$ ,  $\nu_e$ , and  $\bar{\nu}_e$  atmospheric neutrinos of the energy of 4 GeV. The expected distributions of DM-induced neutrinos are indicated as *WIMP signal*  $\nu_\mu/\bar{\nu}_\mu/e/\bar{e}$  lines. The normalization of each signal distribution is arbitrary and does not reflect the fact that equal flux value is expected for neutrinos of every flavor as well as for neutrinos and anti-neutrinos. The distributions of  $\nu_\tau$  and  $\bar{\nu}_\tau$  are not shown on the plot as the production of tau neutrinos in the atmosphere is negligible at these energies.

simulation of muon neutrinos in SK-I+II+III MC sets.

Table 6.1 presents numbers of simulated events which passed data selection. These numbers are not corrected for a livetime and neutrino oscillation effects are not included. Also, the numbers are not corrected for the requirement of the same flux value of neutrinos of different flavors. They show how many events are available in the simulated sets that can mimic signal events of each neutrino flavor for various neutrino energies.

It was decided that there should be at least 300 events in the MC set at a given energy, in order to use these events to simulate the signal. Therefore, in the final analysis presented in the next chapter, the charged current signal in electron neutrinos is simulated only up to 56 GeV of DM mass. The charged current signal in tau neutrinos can be simulated only up to 130 GeV of DM mass. In case of neutral current interactions of electron and tau neutrinos, they can be simulated for every neutrino energy even though that there may be too few events of this type in the corresponding MC set as NC interactions of electron and tau neutrinos can be mimic by NC interactions of muon neutrinos (after applying special weights).

Table 6.1: Number of observed events (which passed data selection) in atmospheric MC (SK-I+II+III) and in tau MC (SK-I+II+III) sets. Column CC  $\nu_\tau\bar{\nu}_\tau$  contains only charged current interactions of tau neutrinos, while columns  $\nu_\mu\bar{\nu}_\mu$  and  $\nu_e\bar{\nu}_e$  show number of CC and NC interactions. Null contribution of  $\nu_\tau\bar{\nu}_\tau$  events at 3 GeV is due to a 3.5 GeV threshold for a tau lepton production. Column Energy shows selected values of DM particle masses and Bin Range interval used in the atmospheric MC and tau MC to imitate signal.

Energy [GeV]	Bin Range [GeV]	$\nu_\mu\bar{\nu}_\mu$	$\nu_e\bar{\nu}_e$	CC $\nu_\tau\bar{\nu}_\tau$	$\nu_\tau\bar{\nu}_\tau / \nu_\mu\bar{\nu}_\mu$ [%]
3	2.9–3.1	52276	20106	0	-
4	3.9–4.1	33448	11383	448	<b>1.3</b>
5.6	5.4–5.8	38244	11132	1613	<b>4.2</b>
10	9.5–10.5	37257	7490	2885	<b>7.7</b>
20	19–21	27239	2769	2198	<b>8.1</b>
30	29–31	15655	1102	1167	<b>7.5</b>
56	54–58	14537	431	837	<b>5.8</b>
90	87–93	12151	157	480	<b>4.0</b>
130	125–135	12512	132	339	<b>2.7</b>
200	192–208	11716	45	221	<b>1.9</b>
600	580–620	6437	4	38	<b>0.6</b>
1000	970–1030	4404	1	23	<b>0.5</b>
2000	1800–2200	8711	1	22	<b>0.25</b>

## Tau neutrinos

The simulation of DM signal in tau neutrinos shall be discussed as a separate issue as neutrinos of this flavor are very rarely produced in the atmosphere and additional sample – tau MC – need to be used to mimic their interactions. The main characteristics of tau events as DM signal are outlined here.

In the tau MC production only the charged current interactions of  $\tau$  and  $\bar{\tau}$  are considered. The value of the flux of the simulated tau neutrinos is assumed to be the same as the flux value of muon neutrinos in the atmospheric MC. That is very convenient and compatible with the investigated DM annihilation model which requires same flux of neutrinos of every flavor. Therefore, it is possible to directly compare number of muon neutrinos in the atmospheric MC with number of tau neutrinos in the tau MC for each considered neutrino energy and derive some conclusions on the detection efficiency of tau events.

The last column in Table 6.1 contains information on the ratio of tau to muon neutrinos. Even though, that assumed values of fluxes of muon and tau neutrinos are the same in the simulation, tau neutrinos constitute a little fraction of muon events for all illustrated energies at the stage when it is counted how many of generated events are observed. That is regulated by two factors: (1) difference in the CC  $\nu_\tau$  cross section ( $\sigma_{\nu_\tau N}$ ) as compared to CC  $\nu_\mu$  cross section ( $\sigma_{\nu_\mu N}$ ); (2) detection efficiency to observe tau events.

Below the energy of 3.5 GeV there are no CC  $\nu_\tau$  interactions in the tau MC sample, due to a threshold for a tau lepton production. For energies below several tens of GeV, the ratio of CC  $\sigma_{\nu_\tau N}$  to  $\sigma_{\nu_\mu N}$  is less than 0.7 as it shown in Fig. 6.3, while being even  $< 0.4$  for energies below 20 GeV. It can be inferred from Table 6.1 that the highest contribution

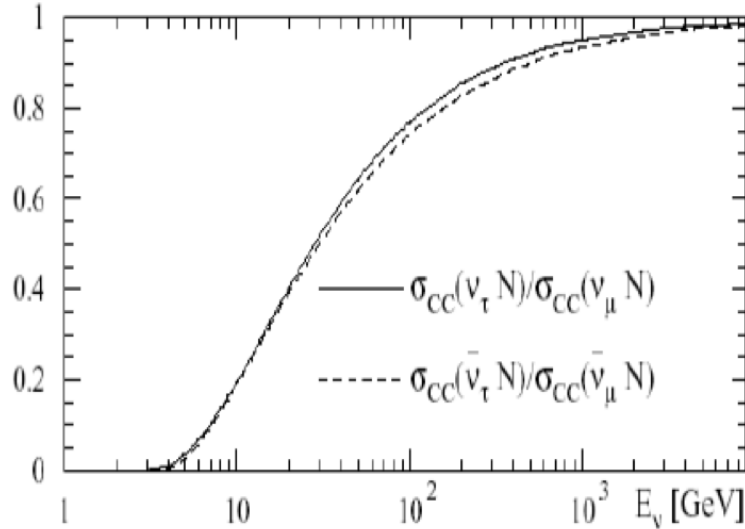


Figure 6.3: The ratio of the charged current  $\nu_\tau$  cross section to  $\nu_\mu$  cross section a function of neutrino energy. The results for  $\nu_\tau$  and  $\bar{\nu}_\tau$  are shown.

Table 6.2: Fraction of  $\nu_\tau\bar{\nu}_\tau$  events contributing to Multi-GeV and Multi-Ring e-like samples as compared to all observed  $\nu_\tau\bar{\nu}_\tau$  interactions in all SK samples.

Energy [GeV]	$\nu_\tau\bar{\nu}_\tau$ in Multi-GeV e-like sample [%]	$\nu_\tau\bar{\nu}_\tau$ in Multi-Ring e-like sample [%]
4	26	19
10	33	40
30	43	50
56	49	47
90	55	43
200	68	31
600	87	13
1000	91	9

of  $\nu_\tau$  events with respect to  $\nu_\mu$  events is expected in the range from approximately 10 to 50 GeV. That means that the efficiency to observe  $\nu_\tau$  events at SK detector is the best at these energies, despite the fact that the value of CC  $\sigma_{\nu_\tau N}$  increases as a function of neutrino energy. Tau neutrinos of the energy of several tens of GeV contribute to FC samples, while atmospheric neutrinos of the same energy rather are observed as PC or UPMU events. That is explained by the fact that the  $\nu_\tau$  energy is spread among many particles which are produced the interaction. Tau lepton produced in CC  $\nu_\tau$  interaction decays immediately and  $\tau$  energy is transferred to multiple decay products. At the higher energies of neutrinos the contribution from tau events is decreasing comparing to muon events. That is due to the fact that high energy  $\nu_\tau$  events are rejected and cannot be fully resolved during data selection procedure.

In Figure 6.4, the zenith angle distributions of  $\nu_\tau$  events due to interactions of 10 GeV tau neutrinos are shown for all SK data samples. It can be seen how the monoenergetic tau signal contributes to various samples. The distribution of  $\cos\theta$  of the simulated tau

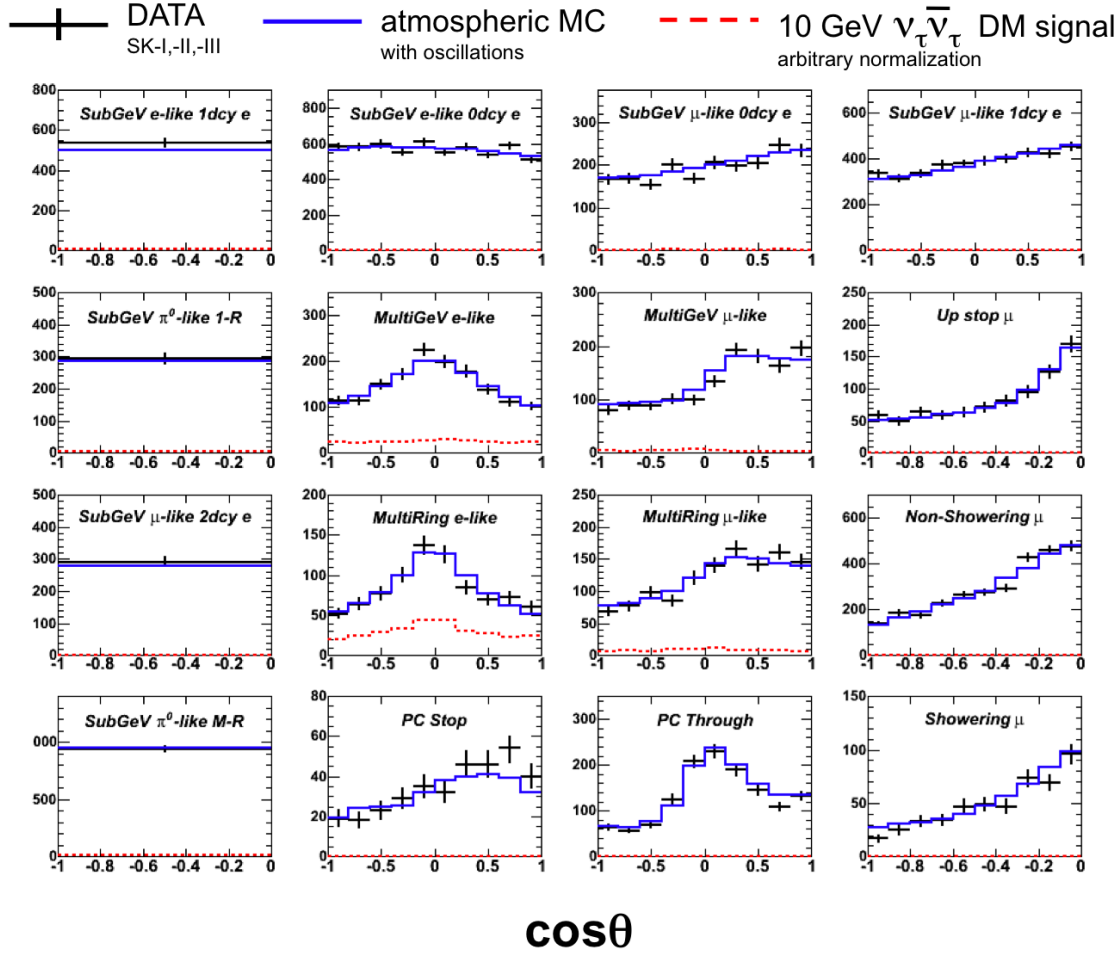


Figure 6.4: The zenith angle distributions (red dashed lines) of  $(\nu_\tau + \bar{\nu}_\tau)$  signal from annihilation of 10 GeV DM particle as seen in various SK data samples. The black points represent the SK-I+II+III data with statistical errors. The blue lines stand for the Monte Carlo expectation at the best fit oscillation model. The contribution of  $(\nu_\tau + \bar{\nu}_\tau)$  signal is enhanced 50 times as compared to the event rate in the tau MC.

events is presented (red dashed line) along with SK data (black points) and with the expected contribution from atmospheric neutrinos – best fit Monte Carlo model (blue lines). At the tau neutrino energy of 10 GeV it is estimated that 73% of all CC  $\nu_\tau$  interactions that are observed are in the Multi-GeV e-like and Multi-Ring e-like samples. Table 6.2 shows the contribution of the  $\nu_\tau \bar{\nu}_\tau$  events to these samples for other energies considered.

It can be concluded that any monoenergetic DM signal observed in tau neutrinos will populate mostly Multi-GeV e-like and Multi-Ring e-like samples. That is different than in case of muon and electron neutrinos of the DM origin which will be spread more uniformly over e-like and  $\mu$ -like samples.

## 6.3 Methodology

Main goal of the studies presented in this chapter is to test sensitivity of SK data to DM signal contribution. The other purpose is to illustrate the strategy of the analysis based

on some simple examples. For simplicity, limited number of SK samples is used here and impact of systematic uncertainty parameters is not included. With the obtained results it is possible to understand which data samples constrain the fit for a tested range of DM particle masses and to find out which constraints are the most important.

The method of the search for DM signal is very similar to the one discussed in Section 5.5 used for the atmospheric neutrino oscillation analysis. Similarly, the SK data are modeled with a Monte Carlo simulation of atmospheric neutrino production, propagation, oscillation and detector response. The atmospheric MC set described in Section 5.3 is used for that purpose. Additionally, the contribution from simulated DM annihilation signal is considered. This signal is mimic as described in Section 6.2.

In order to test the hypothesis of dark matter annihilation signal contribution to the Super-Kamiokande atmospheric neutrino data one can use the method of minimum  $\chi^2$ . The formula adopted in this study is more simple as the one used in case of the oscillation analysis (compare Eq. 5.1):

$$\chi^2 = \sum_{i=1}^{n\text{bins}} \frac{(N_i^{\text{data}} - (\alpha \cdot N_i^{\text{atmMC}} + \beta \cdot N_i^{\text{DM}}))^2}{\sigma_i^2} \quad (6.1)$$

The visible energy and  $\cos \theta$  distributions of various SK data samples are investigated with above formula, in order to find the combination of atmospheric neutrino MC ( $N^{\text{atmMC}}$ ) and simulated DM signal ( $N^{\text{DM}}$ ) which would match the data ( $N^{\text{data}}$ ) the best. The minimum value of  $\chi^2$  is expected for the best configuration. The parameter  $\alpha$  in Eq. 6.1 stands for the global normalization of atmospheric MC and parameter  $\beta$  is the normalization factor of simulated DM signal. Values of  $\alpha$  and  $\beta$  are varied in the fit. The value of  $\sigma$  is the statistical uncertainty of the data.

The  $N^{\text{atmMC}}$  in Eq. 6.1 depend on the oscillation parameters (see Section 5.3). The oscillation model is not being determined in the studies presented in this chapter. The values of oscillation parameters  $\theta_{23}$ ,  $\Delta m_{23}^2$  are fixed at the best fit values obtained in the oscillation analysis. However, it shall be noticed that these parameters are not the only ones which determine the contribution related to atmospheric MC. Also, the systematic uncertainty terms are responsible for the matching between atmospheric MC and SK data – their impact is included in the "best fit" oscillation model presented in Fig. 5.4 as red histograms. They can affect the value of each bin considered in the analysis in addition to the impact of oscillation parameters. The normalization of atmospheric MC is regulated by some of these uncertainty parameters as it is discussed in Section 5.5.3.

In the approach presented in this chapter, the matching between the MC model and the SK data is based only on the criterium of the same livetime of all considered samples and on a fitted value of a normalization of each MC set. The global normalization of atmospheric MC ( $\alpha$ ) and normalization of DM signal MC ( $\beta$ ) are determined in the fit. Only SK-I data are used in the examples presented in this chapter – livetime of SK-I FC/PC set is 1489.2 days, and SK-I UPMU set livetime is 1646 days.

## 6.4 Search for Low Energy Signal

In the first part of this section, the examples of a fit of a signal from annihilation of WIMPs with  $M_\chi = 5.6$  GeV are discussed. It is shown how the fit results change depending on the number of samples which are included in the search and their characteristics. First

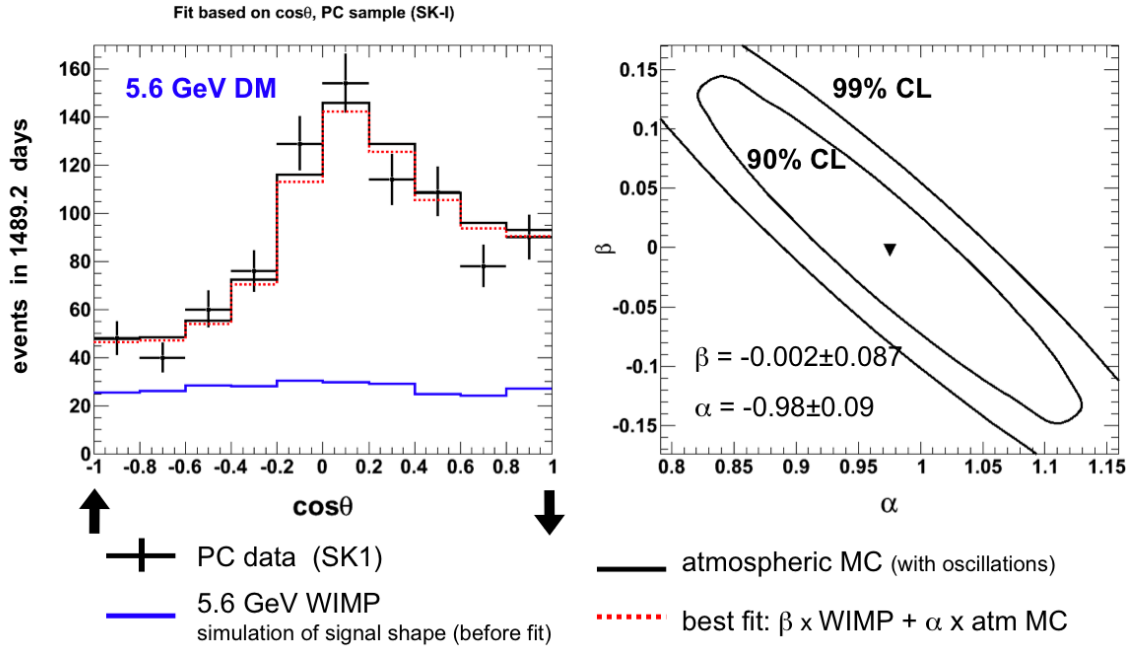


Figure 6.5: Left panel –  $\cos\theta$  distribution of SK-I PC events. Data are represented by black points. Oscillated Monte Carlo expectation for atmospheric neutrinos is marked as the black line. The illustration of a shape of a signal from annihilation of  $M_\chi = 5.6$  GeV WIMP is shown as the blue line (arbitrary normalization). The best found configuration of atmospheric MC and DM-induced signal is shown as the red dotted line. Right panel – 90% and 99% confidence level contours for  $\alpha$  and  $\beta$  parameters determined in the fit.

examples are based on a fit to single sample and are illustrated with partially-contained events — signal is well represented in PC events at this energy. Later, the addition of more samples to the fit is discussed. At the end, the results for other values of  $M_\chi$  are presented. These results are obtained using the zenith angle and visible energy distributions of FC and PC events.

The FC and PC samples presented in this section are not subdivided into the samples like Mutli-GeV, Sub-GeV, Multi-Ring *etc.*, which are all listed in Table 5.1. Only one set containing FC events of all categories and one sample including all types of PC events are used. The signal is fitted only in muon neutrinos and muon anti-neutrinos.

### Fit based only on zenith angle distribution of PC events

Results of the fit based on PC events are presented in Fig 6.5. There are 10 bins considered in this example ( $N_{bins} = 10$ ). Number of Degrees of Freedom (NDF) equals 8 as there are two fitted parameters. The following values for  $\alpha$  and  $\beta$  parameters are obtained:  $\alpha = 0.98 \pm 0.09$ ,  $\beta = -0.002 \pm 0.087$  with  $\chi^2/NDF = 1.2$ . Parameter  $\beta$  is normalized in a way that it matches the normalization of atmospheric MC. Therefore, resulting value of  $\beta$  can be interpreted as a fraction of atmospheric MC that can be added as a WIMP signal. Knowing the total number of atmospheric MC events in the sample, one can calculate the number of fitted DM-induced neutrinos that correspond to obtained value of  $\beta$ . Here, preferred DM signal contribution is consistent with zero and fitted number of signal events equals  $-2 \pm 79$ . The large error on that number reflects the fact that values of  $\alpha$  and  $\beta$

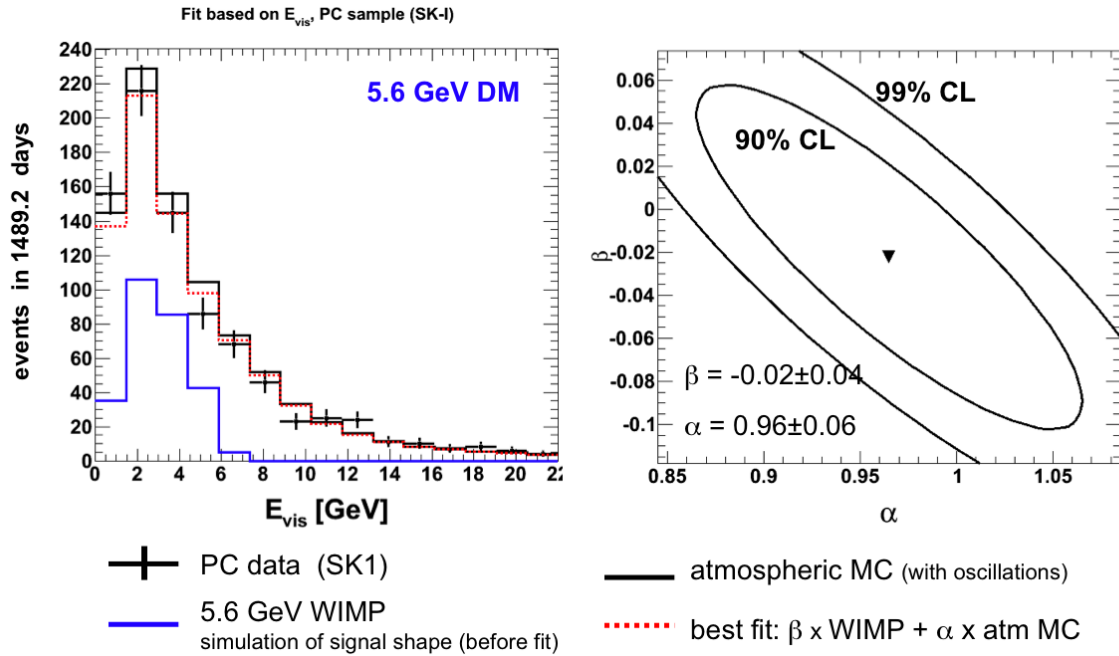


Figure 6.6: Left panel – visible energy distribution of SK-I PC events. Data (black points), oscillated Monte Carlo (black line), shape of a signal from annihilation of  $M_\chi = 5.6$  GeV WIMP (blue line) and the best found configuration of oscillated MC and DM-induced signal (red dotted line) are shown. Right panel – 90%, 99% confidence level contours for  $\alpha$  and  $\beta$  parameters determined in the fit.

are poorly constrained in the fit.

During a fit, it is not required that  $\alpha + \beta = 1$ . One assumes that initial normalization of atmospheric MC, which is described as  $\alpha = 1$ , is not the best one that can be obtained for this sample. For example, this normalization can be fine-tuned with the inclusion of systematic uncertainty terms and this effect is mimicked in the presented approach as a fit of  $\alpha$  parameter. Also, some part of the contribution related to atmospheric neutrinos could be replaced with a contribution coming from DM-induced neutrinos.

In the presented example, it is favored to decrease the total normalization of atmospheric MC. The fact that matching between the data and initial atmospheric MC model is improved with the new found configuration, reflects the fact that atmospheric MC model used in the search is not optimized to have the best matching with this particular PC sample considered. The "best fit" atmospheric MC expectation is optimized to match all SK samples such as FC, PC, UPMU (and all of their subsamples). It is also required that information on relations between samples is included in that expectation – one cannot freely change the normalization of one sample without affecting the normalization of other samples.

#### Fit based only on visible energy distribution of PC events

Results of the fit are presented in Fig 6.6. Here,  $N_{bins} = 15$ ,  $NDF = 13$ . The best fit values are:  $\alpha = 0.96 \pm 0.06$ ,  $\beta = -0.02 \pm 0.05$  ( $\chi^2/NDF = 1.0$ ). At this configuration of atmospheric MC and shape of DM-induced signal, preferred contribution of a signal is negative. It seems to be good to slightly decrease overall normalization of atmospheric

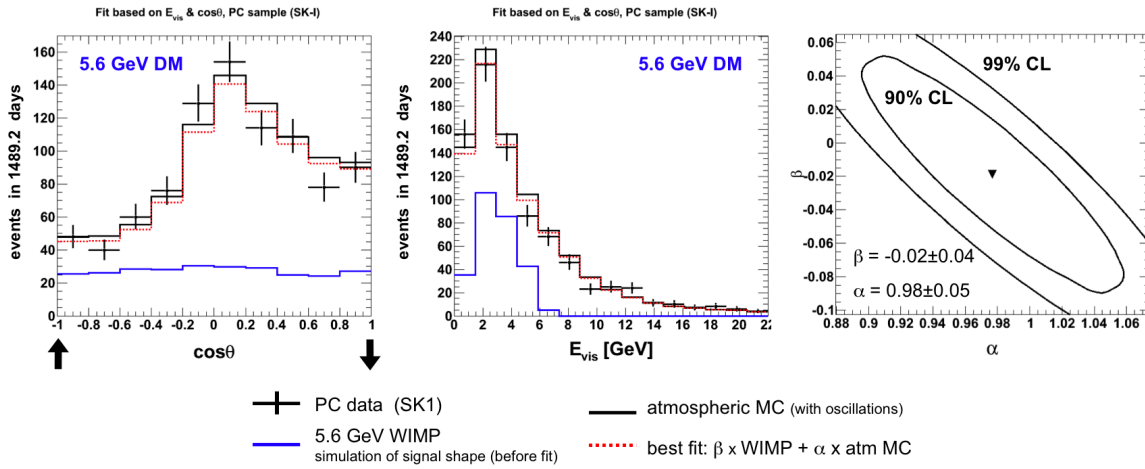


Figure 6.7: Zenith angle distribution (left panel), visible energy distribution (middle panel) of SK-I PC events and resulting  $\chi^2$  contour (right panel) of a fit of  $\alpha$  and  $\beta$  parameters to the zenith and visible energy distributions. Data (black points), oscillated Monte Carlo (solid black line), shape of a signal from annihilation of  $M_\chi = 5.6$  GeV WIMP (blue solid line) and the best found configuration of oscillated MC and a signal (solid red line) is shown on the left and middle panel. Right panel shows the 90%, 99% CL fit contours for  $\alpha$  and  $\beta$  parameters.

MC and to subtract some events in the 2nd and 3rd bin (counting from the left) as can be seen on Fig. 6.6 to have the better matching with distribution of collected data. There are  $-20 \pm 44$  signal events found.

The information on the energy of events gives stronger constraint in the fit than the angular information. The resulting errors on the values of fitted parameters are lower as compared to values obtained in a fit which is based only on  $\cos\theta$  distribution. The fit contours presented on the right plot in Fig. 6.6 show that parameters  $\alpha$  and  $\beta$  are better constrained in the approach which based on visible energy of events.

### Fit based on zenith angle and visible energy distributions of PC events

Results of the simultaneous fit which is based on two distributions are presented in Fig 6.7. There are 25 bins considered in this example ( $NDF = 23$ ). The best fit values are:  $\alpha = 0.98 \pm 0.05$ ,  $\beta = -0.02 \pm 0.04$  ( $\chi^2/NDF = 1.0$ ). The obtained results are similar as in the case of a fit with a visible energy distribution only. There are  $-17 \pm 39$  DM-induced neutrinos expected in this example.

For a comparison, the fit based on  $\cos\theta$  and visible energy distributions of FC  $\mu$ -like events yields the following values of normalization parameters:  $\alpha = 1.11 \pm 0.01$ ,  $\beta = -0.011 \pm 0.003$  ( $\chi^2/NDF = 1.7$ ). That corresponds to  $-41 \pm 10$  DM-induced neutrinos. Large value of fitted  $\alpha$  parameter means that around 10% atmospheric MC events shall be added. It is related to the fact that in case of FC samples the large fraction of systematic uncertainty is related to the normalization. In the presented *simplified approach*, that effect is compensated with obtained value of  $\alpha$ .

The visible energy and zenith angle distributions of FC  $\mu$ -like events are presented in Fig. 6.8(a) and Fig. 6.8(b), respectively. The data, atmospheric MC and DM signal shape before the fit are presented there. There is no graphical representation of the best found MC configuration for the FC results discussed above.

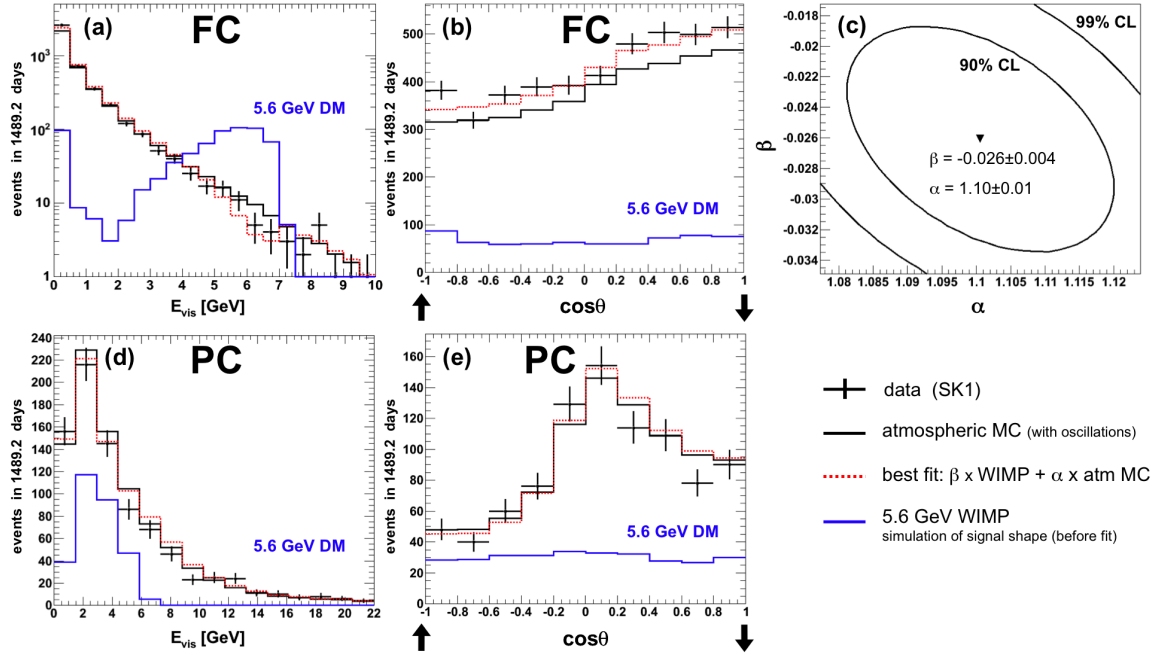


Figure 6.8: Simultaneous fit of the signal from annihilation of 5.6 GeV DM particle to PC and FC samples. All symbols have the same meaning as indicated in previous figures (example Fig 6.7). Note changes of scale for the contour plot.

### Fit based on $\cos\theta$ and visible energy distributions of PC and FC $\mu$ -like events

Results are shown in Fig. 6.8. The fit in this case is based on 4 distributions,  $N_{bins} = 55$  ( $NDF = 53$ ). When two samples are used in the fit additional constrain is given by a relative contribution of each sample (kept constant during the fit). The following values of normalization parameters are obtained:  $\alpha = 1.10 \pm 0.01$ ,  $\beta = -0.026 \pm 0.004$  ( $\chi^2/NDF = 1.5$ ). The value of  $\beta$  corresponds to  $-246 \pm 42$  DM-induced neutrinos.

Here, the constraints on the values of  $\alpha$  and  $\beta$  are much stronger, originating from number of bins considered in the fit as well as from relative contribution to different samples. The energy distribution of the DM signal in FC sample (Fig. 6.8(a)) is very distinctive and gives a strong constraint. On the other hand, the zenith angle distribution of FC events is not as strongly peaked as PC  $\cos\theta$  distribution and both the signal and the data tend to have the similar shape there. For that reason the zenith angle distribution of FC events does not effectively bound the fit.

The best found configuration favors the negative value of the  $\beta$  parameter with a relatively small uncertainty. That seems to be an effect related to the signal shape at this energy and the fact how it compares with the data and atmospheric MC distributions of the investigated samples. The overall normalization of MC expectation wants to be increased as clearly seen on the example of FC sample. Therefore, the fitted value of  $\alpha$  parameter is large. At the same time it is suitable to subtract some events in selected bins to have better matching with the data. That can be realized with negative DM signal contribution. In particular, energy distributions of FC and PC events contain bins which show the excess of atmospheric MC events over data events. It happens to be the case that simulated signal from annihilation of 5.6 GeV WIMP is also expected in the same bins.

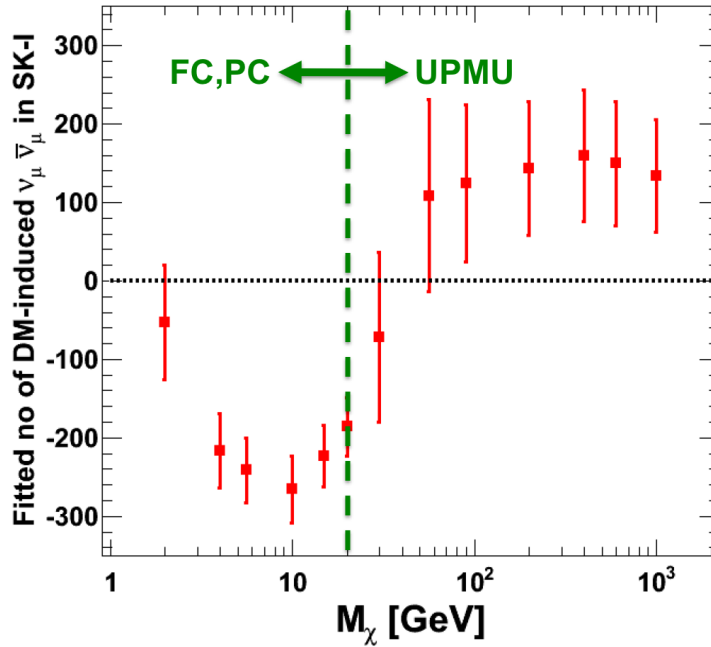


Figure 6.9: Fitted number of DM-induced ( $\nu_\mu + \bar{\nu}_\mu$ ) events for various masses of relic particles considered in the search. The points with errors were obtained from fit (search) based on FC/PC samples for  $M_\chi < 20$  GeV and based on UPMU stopping and through-going samples for  $M_\chi \geq 20$  GeV.

Therefore, obtained negative contribution related to DM-induced neutrinos is specific for considered mass of WIMPs. The effect is at around 5 standard deviations from a null DM signal contribution. That rises a question whether such a result is reliable.

With more samples used in the search the fit is better constrained. The strong constraints are the relations/proportions between various samples. In the presented examples the limited number of samples is used and information about them is not complete. In addition, UPMU samples could be used with FC/PC samples and each of them could be subdivided into subsamples. Also, the existing discrepancies between Monte Carlo and data, present in selected bins, can be related to systematic uncertainties. They could impact only selected bins, similarly as DM signal corresponding to given  $M_\chi$ . Therefore, to confirm obtained results, the *full approach fit* need to be conducted. The results of this approach are presented in Chapter 7.

### Results for range of dark matter particle masses

The fitting procedure is repeated for the set of DM particle masses using both  $\cos \theta$  and  $E_{\text{vis}}$  distributions of FC and PC samples. The value of  $\beta$  parameter for each DM particle mass is translated into the event rate of DM-induced neutrinos which corresponds to SK-I running period. That results are shown in Fig. 6.9. This search, based on FC and PC sets, is done up to  $M_\chi = 20$  GeV. Above that energy only a fraction of events remain in FC/PC samples.

The preferred solutions correspond to negative, unphysical DM contribution for the entire energy range considered. That is related to the fact that the shape of DM signal

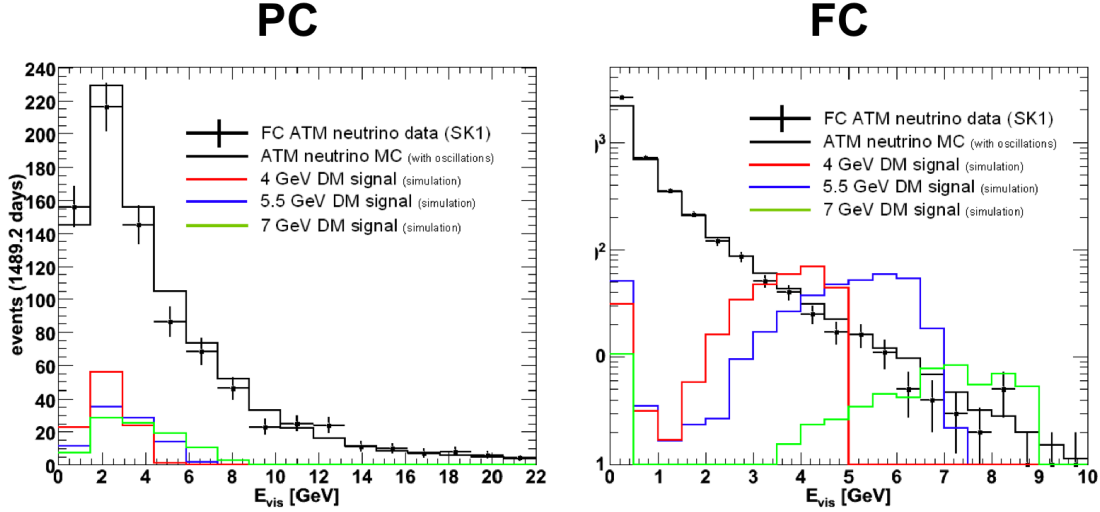


Figure 6.10: Visible energy distribution of SK-I PC (left plot) and SK-I FC (right plot) events. Data are indicated as points, atmospheric MC as black lines and DM signal corresponding to different values of  $M_\chi$  as color lines. The normalization of DM signal is arbitrary (before fit) and different than in previous figures. The low energy tail of DM signal visible in the distribution for FC events is related mostly to neutral current interactions of neutrinos in which only part of the incident neutrino energy is recorded (from a recoiling proton or other particles produced in NC DIS or NC RES processes).

does not vary a lot with DM particle mass and the same data are used in the fit for every considered relic particle mass. Figure 6.10 presents the visible energy distributions of simulated DM signal events which correspond to various  $M_\chi$ . The zenith angle distributions are not shown because the shape of DM signal corresponding to different  $M_\chi$  is similar (expected signal is isotropic) for every considered case and is illustrated in Fig. 6.8(b,e).

Results presented in Fig. 6.9 for different masses of DM particles are not independent as every time the same set of data is used. Therefore, obtained results indicate the range of  $M_\chi$  which can be excluded by SK data (strong negative contribution). From the simulation of DM signal shape for various  $M_\chi$  in this range (Fig. 6.10), it can be seen that such signals overlap and yields similar signatures. Therefore, one can exclude the whole range of sources – if there were a signal from a direct DM annihilation into neutrinos at some  $M_\chi$  which is not considered, such a signal would not be omitted.

Results give strong negative contribution (sometimes more than 5 times, as in can be seen in Fig. 6.9). It may suggest that the adopted approach is not complete and these results need to be confirmed in the *full approach*.

## 6.5 Search for High Energy Signal

In this section, the search for a signal from the high energy signal neutrinos, above 20 GeV, is shown. The upward-going muon samples are used. As it can be seen in Fig. 5.1, for neutrino energies above several tens of GeV, practically only UPMU samples may contribute to the search. Thus, the fit is based on the angular distributions of UPMU events.

The UPMU samples could be divided into subcategories of *stopping*, *through-going non-showering* and *through-going showering* muons. There is a correlation between a

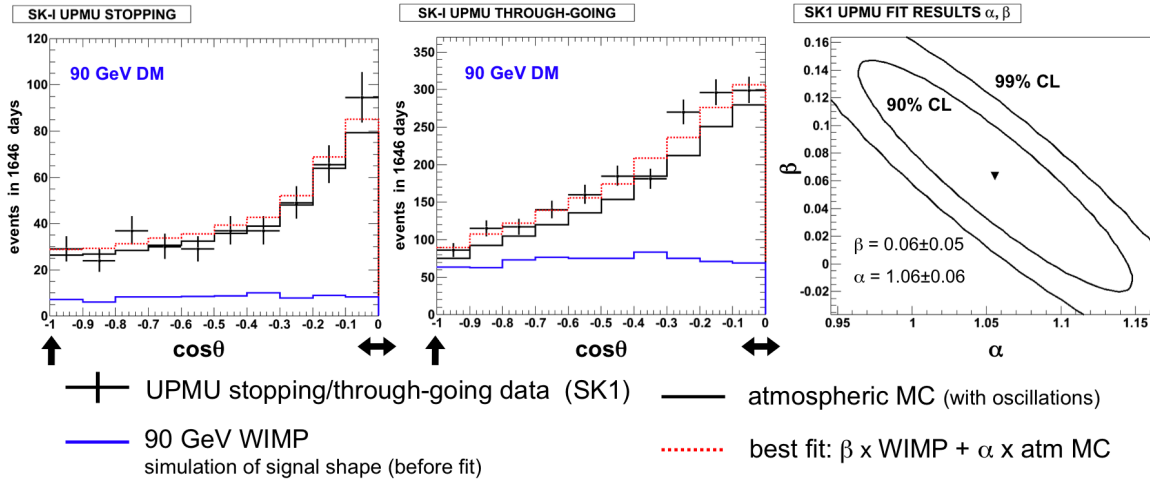


Figure 6.11: The zenith angle distributions of UPMU stopping events (left panel) and UPMU through-going events (middle panel) are shown for the SK-I data (black points), best fit atmospheric Monte Carlo model (black lines), shape of a signal from annihilation of  $M_\chi = 90$  GeV (blue solid lines) and the best found configuration of oscillated MC and DM signal (dotted red line). Right hand side plot shows fit result with a  $\chi^2$  contour for  $\alpha$ ,  $\beta$  parameters.

parent neutrino energy and a class of *upward-going* muons into which the event would be classified. Very energetic muons will more likely produce showers. Lower energy muons could stop inside the detector. So, neutrinos of a different energies would populate the samples of *stopping*, *through-going non-showering* and *through-going showering* differently. That places additional constraint for a fit. In the approach described below, UPMU set is divided into 2 categories only – *stopping* and *through-going* samples.

### Fit based on UPMU *stopping* and *through-going* muon events, $M_\chi = 90$ GeV

This section presents the fit which uses UPMU events in the search for a signal from annihilation of WIMP with  $M_\chi = 90$  GeV. The results of the fit of a  $\nu_\mu \bar{\nu}_\mu$  signal are shown in Fig. 6.11. The fit is based only on the zenith angle distributions of stopping and through-going muons. The shape of the simulated DM signal does not depend on the energy of neutrinos. DM particles of other masses would yield different proportions of the signal contribution to UPMU samples. The relative proportions of the signal in different UPMU samples are kept in the fit. The best fit values are:  $\alpha = 1.06 \pm 0.06$ ,  $\beta = 0.06 \pm 0.05$  ( $\chi^2/NDF = 1.0$ ). The fit is moving the overall normalization significantly up. It is related to normalization of UPMU samples which is largely controlled by the systematic uncertainty parameters and their values are fitted in the oscillation analysis. The fitted contribution of DM-induced neutrinos is  $124 \pm 100$  events and is consistent with zero within the obtained error.

### Results for range of dark matter particle masses

The fit based on the UPMU stopping and through-going samples is repeated for the set of other DM particle masses. The number of DM-induced neutrinos is obtained for seven considered WIMP masses. That results are presented in Fig. 6.9. Fitted number of signal events is positive. For the entire range of tested  $M_\chi$  masses (for neutrino energies

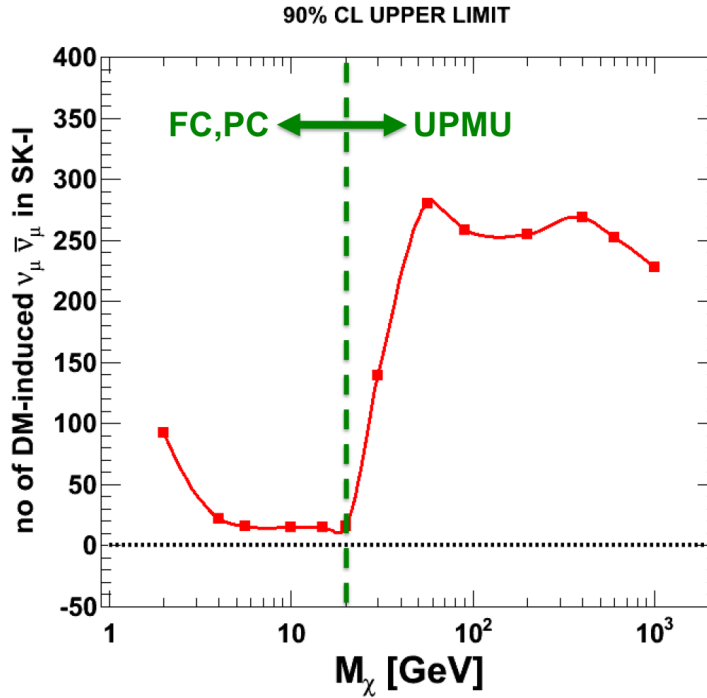


Figure 6.12: 90% CL upper limit on the number of DM-induced ( $\nu_\mu + \bar{\nu}_\mu$ ) events in SK-I. The results are based on the *simplified approach* discussed in this chapter. The limit from the analysis based on FC/PC samples is shown on the left and the limit based on the analysis which uses UPMU sample is presented on the right.

$\geq 20$  GeV), the results are consistent with zero within 2 sigma. Therefore, these results should also be interpreted as an exclusion of the  $M_\chi$  region as the points in Fig. 6.9 are not independent.

### Tests of fitting procedure to variation of signal properties

Stability of the fit against binning in  $\cos \theta$  and also against details of DM signal simulation were checked. Different sizes of the energy interval used to extract candidates for signal events from atmospheric MC were applied. Also, isotropic weights were modified. No signs of instability of the obtained results were found.

## 6.6 Upper Limit on Fitted Number of DM-Induced Neutrinos

The results of the searches presented in this chapter show that no signal of DM-induced neutrinos is found. Therefore, one could derive the upper limit on the number of signal events allowed by the fit. That limit is presented in Fig. 6.12 as a function of a mass of DM particle.

It is important to discuss the procedure of a limit calculation when this one is based on the negative number of fitted signal events as it is the case for a couple of DM particle masses considered in the search. This method is adapted from [115] and referred in literature to as *Bayesian approach* or *PDG 1996 adjusted*. Below, the brief overview of the

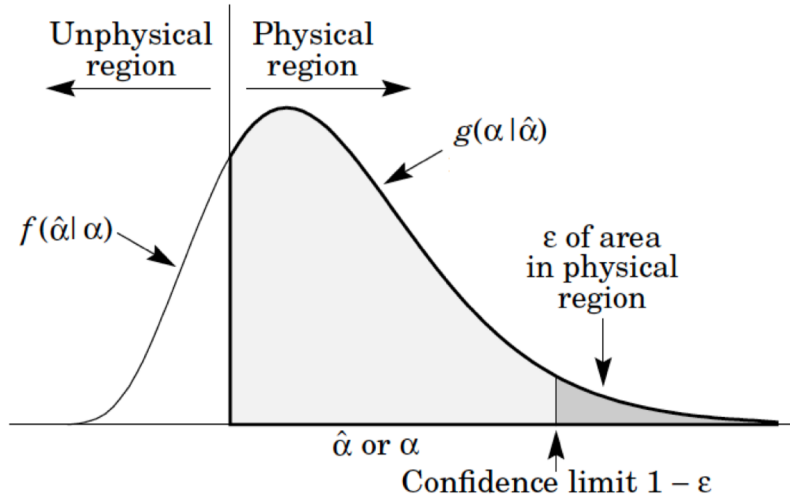


Figure 6.13: An example of a measurement  $\hat{\alpha}$  which can give unphysical results [115]. If one assumes that  $\alpha$ , the quantity one tries to measure, cannot lie in the unphysical region (0 probability) but can lie anywhere in the physical region (constant probability), then the new knowledge of distribution of  $\alpha$  is given by the shaded function after appropriate normalization. See text for details.

limit calculation is given for a general case of a measurement of physical value  $\alpha$  which results in estimator  $\hat{\alpha}$ .

### Upper limit in the Bayesian approach

In this approach, the physical constant  $\alpha$  is treated as statistical variable and one claims no prior knowledge of its value – every value from the physical region is equally probable for  $\alpha$  (flat prior distribution). Any measurement provides the information about estimator  $\hat{\alpha}$  for a fixed and unknown value of  $\alpha$ . This can be described by the conditional probability density function  $f(\hat{\alpha}|\alpha)$ . In order to derive a confidence limit on the value of  $\alpha$ , one would like to get inverse information – given our measurement is  $\hat{\alpha}$ , the "true answer"  $\alpha$  lies between  $\alpha$  and  $\alpha + d\alpha$  with probability  $g(\alpha|\hat{\alpha})d\alpha$ . The connection between  $f$  and  $g$  functions is provided by Bayes' theorem:

$$g(\alpha|\hat{\alpha}) = \frac{f(\hat{\alpha}|\alpha)\pi(\alpha)}{\int f(\hat{\alpha}|\alpha)\pi(\alpha)d\alpha} \quad (6.2)$$

Function  $\pi(\alpha)$  represents prior knowledge of  $\alpha$  value. However, it is assumed that before experiment all physically reasonable values of  $\alpha$  are equally probable. Therefore,  $\pi(\alpha)$  is constant over the region of interest and zero in the unphysical region. This leads to the following formula:

$$g(\alpha|\hat{\alpha}) = \begin{cases} f(\hat{\alpha}|\alpha)/\int f(\hat{\alpha}|\alpha)\pi(\alpha)d\alpha & \text{if } \alpha \text{ is in the physical region} \\ 0 & \text{otherwise} \end{cases} \quad (6.3)$$

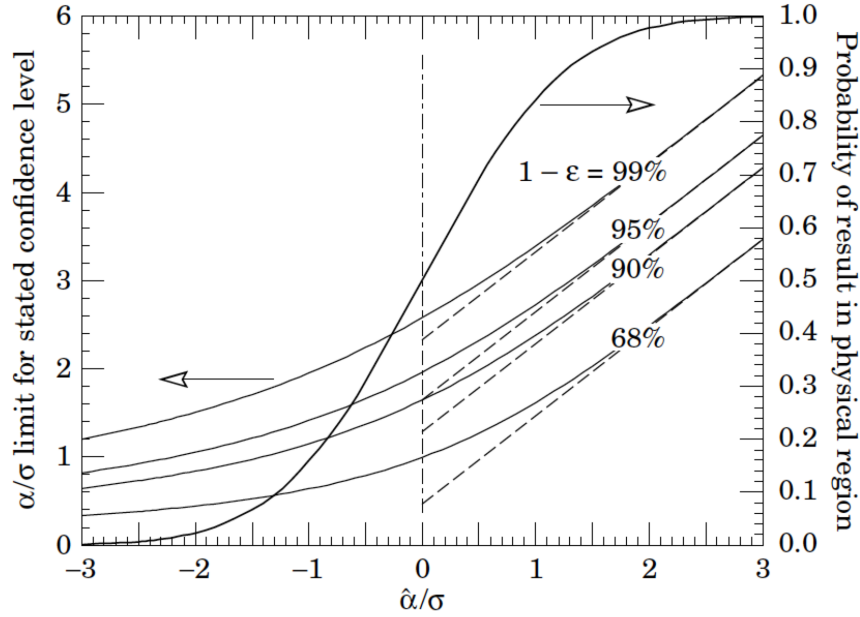


Figure 6.14: Application of the Bayesian scheme shown in Fig. 6.13 to the case of Gaussian  $f(\hat{\alpha}|\alpha)$ . See text for details. Figure from [115].

In Figure 6.13 it is assumed that  $f(\hat{\alpha}|\alpha)$  distribution of  $\hat{\alpha}$  is obtained in a set of measurements. In the illustrated case, there is a significant probability of obtaining the results in the unphysical region. To derive an upper limit on the value of  $\alpha$ , one needs to replace the  $f(\hat{\alpha}|\alpha)$  distribution with the  $g(\alpha|\hat{\alpha})$  distribution which is defined in Eq. 6.3. In Fig. 6.13, the  $g(\alpha|\hat{\alpha})$  is shown by the shaded region, except it needs to be normalized to 1. In order to derive a 90% confidence level limit on the value of  $\alpha$ , one needs to find such a value of  $\alpha_{90\%}$  that integral  $\int_0^{\alpha_{90\%}} g(\alpha|\hat{\alpha})d\alpha$  yields 90% of the total area of  $g(\alpha|\hat{\alpha})$  distribution. That is for an assumption that physically allowed values of  $\alpha$  are  $\geq 0$ . Confidence limit level is indicated as  $(1 - \epsilon)$  and equals 0.9 in the considered case. In Fig. 6.13, 90% of the area in the physical region of distribution  $g(\alpha|\hat{\alpha})$  is shown as the light shaded region.

In the analysis presented in this thesis it is assumed that  $\hat{\alpha}$  – what would mean fitted number of DM-induced neutrinos – is a random number from a Gaussian distribution. In this case, the  $f(\hat{\alpha}|\alpha)$  distribution discussed in Fig. 6.13 should be Gaussian. Then, the upper limit for the value of  $\alpha$  can be obtained based on the curves in Fig. 6.14 [115]. For example, if obtained value of  $\hat{\alpha}$ , which has uncertainty  $\sigma$ , is one standard deviations negative ( $\hat{\alpha}/\sigma = -1.0$ ), then it can be concluded that  $\alpha < 1.15\sigma$  with 90% probability. To get this estimate one should check the value on the left vertical axis for the 90% curve at the value of  $\hat{\alpha}/\sigma = -1.0$ . The right vertical axis shows the probability that value as low as  $\hat{\alpha}/\sigma$  would occur in the experiment.

By using the method described above, the upper limit on the fitted number of DM-induced neutrinos can be obtained for the negative (unphysical) and positive (physical) fit result. The upper limit calculation is computed numerically for the results of the fits which are presented in the following and next chapter.

## 6.7 Summary

The results presented in this chapter are illustrative. They reveal information on the properties of different samples. What bounds the fit is mainly the energy information, and proportions of a signal in different samples which change with energy of neutrino events. Less bounds are coming from angular distributions.

It shall be mention that a whole spectrum of additional factors should be included in the full analysis approach. By incorporating more information to the fit, one could get more reliable results:

- The right strategy towards the full approach analysis seems to require more samples used in the analysis. Since the search constrains also the atmospheric neutrino background contribution, not only contribution related to DM signal, all samples listed in Table 5.1 shall be used, similarly as in case of the oscillation analysis. Moreover, all available knowledge of relations/proportions between SK data samples shall be incorporated.
- It would be better to directly determine the values of the oscillation parameters  $\Delta m_{23}^2$ ,  $\theta_{23}$  which stand behind oscillated atmospheric MC contribution.
- There are 120 sources of systematic uncertainty considered in the oscillation analysis of the Super-Kamiokande atmospheric neutrino data. They are valid also for this analysis. Thus, in the final approach their impact on the fit results need to be included as well. Some of these uncertainties have a character of normalization parameters. Therefore, when systematic uncertainties are included in the fit there is no need to fit parameter  $\alpha$ .
- Fitted contribution of dark matter signal shall be based on all neutrino flavors requiring  $\phi(\nu_e) = \phi(\bar{\nu}_e) = \phi(\nu_\mu) = \phi(\bar{\nu}_\mu) = \phi(\nu_\tau) = \phi(\bar{\nu}_\tau)$ . Then, the best use of the e-like nad  $\mu$ -like samples can be made. Tau neutrinos would mostly contribute to Multi-GeV e-like and Multi-Ring e-like samples what can additionally bound the fit – excessive number of events in those samples could indicate a presence of strong tau signal which is not expected for atmospheric neutrinos.

Such approach was used in the final set of fits and is presented in the next chapter.

# Chapter 7

## Search for Diffuse Dark Matter Annihilation Signal at Super-Kamiokande

This chapter presents a search for a signal from diffuse dark matter annihilation (or dark matter decay) using atmospheric neutrino data from Super-Kamiokande-I, -II and -III. All available information on data samples and experience from atmospheric neutrino analysis (see Chapter 5) is used in the combined fit of oscillation parameters and DM signal contribution. The search is focused on the signal arising from a diffuse source of dark matter annihilation (or decay) in the Milky Way halo. The investigated model assumes that two neutrinos are directly produced in the process of dark matter annihilation as described in Eq. 3.2.

The results of the search for dark matter induced neutrino signal are shown in the first part of this chapter. The number of signal events which could be accommodated by the Super-Kamiokande data is obtained separately for each mass considered for DM particles in a range from 3 GeV to 3 TeV. It is shown that no significant DM signal contribution is allowed by the data which are consistent with atmospheric neutrino oscillation effect. Comparison with results obtained in the *simplified approach* presented in Chapter 6 is shown. Further, a corresponding limit on dark matter induced diffuse neutrino flux is derived as a function of mass of relic particles. Finally, the limits on DM decay lifetime  $\tau_{DM}$  and DM self-annihilation cross section  $\langle\sigma_A V\rangle$  are obtained. These constitute the main results of this thesis.

### 7.1 Diffuse Dark Matter Annihilation Search

The strategy of the search for dark matter induced diffuse signal is similar to the method used in the analysis of atmospheric neutrino oscillations (see Chapter 5). Similarly, the search is based on a fit of the Monte Carlo expectation to the Super-Kamiokande data. The same data samples are used and the same sources of the systematic uncertainty are addressed in the fit. The only difference, comparing to oscillation analysis, is the fact that in case of DM diffuse search one assumes that collected data are described by two sources of neutrinos instead of a one. These components are: dark matter induced neutrinos (signal) and atmospheric neutrinos (background). The goal is to find the best combination of

a signal and background that fully explains the data. The fits are repeated assuming masses of DM particles in a range from 3 GeV to 3 TeV. The oscillation parameters that are related to estimation of atmospheric neutrino background contribution are allowed to vary in the fit as well as the normalization of the simulated dark matter signal.

### 7.1.1 Data Sample

The sample of neutrino interactions in which we search for DM signal consists of the atmospheric neutrinos. The search is based on SK-I, -II, -III data sets. As it was stated in Chapter 5, based on the topology of neutrino induced signal and parent neutrino energy, events can be assigned to three main categories: fully-contained (FC), partially-contained (PC), and upward-going muons (UPMU). Because the DM particle mass is not constrained, the search should cover the widest possible range of neutrino energies. Therefore, all main SK data samples and their corresponding subsamples, listed in Table 5.1, are taken into account in the following search. These are the same samples as used in the atmospheric oscillation analysis. The information about the livetime of each data set is given in Section 5.5.1. Total livetime of SK-I, -II, and -III sets is 2805.9 days of FC/PC events and 3109.6 live-days of UPMU events.

For the atmospheric neutrino interactions (background), the Monte Carlo simulation of the detector response is available in large statistics corresponding to 500 years of livetime separately for SK-I, -II and -III sets (1500 years of livetime in total).

### 7.1.2 Dark Matter Induced Signal

Dark matter induced signal and the detector response are simulated assuming several neutrino energies corresponding to different DM particle masses. The considered range of  $M_\chi$  is from 3 GeV to 3 TeV. The investigated model of direct DM annihilation (or decay) into pair of neutrinos assumes equal flux ( $\phi$ ) of neutrinos of every flavor. Therefore, for each mass of a relic particle considered, the signal is simulated in  $\nu_e/\bar{\nu}_e$ ,  $\nu_\mu/\bar{\nu}_\mu$  and  $\nu_\tau/\bar{\nu}_\tau$  and the requirement of  $\phi(\nu_e) = \phi(\bar{\nu}_e) = \phi(\nu_\mu) = \phi(\bar{\nu}_\mu) = \phi(\nu_\tau) = \phi(\bar{\nu}_\tau)$  is imposed. The details of that procedure are provided in Section 6.2.

The illustration of a signal contribution from annihilation of DM particle with a mass of 5.6 GeV is shown in Fig. 7.1. All data samples which are being used in the analysis are presented there. The zenith angle and the momentum distributions are shown. Plots contain the SK-I+II+III atmospheric neutrino data (black points), the fitted contribution from atmospheric neutrinos obtained in 2 flavor oscillation analysis (blue solid lines), and the shape of the simulated DM-induced signal (red dashed lines). The signal is enhanced arbitrary for the illustration purpose, its proportions to different samples are reflected.

The DM-induced signal from the Milky Way halo is expected to be isotropic in coordinate system related to the Earth (flat in  $\cos\theta$ ). The distributions in Fig. 7.1 incorporate the detector effects and data selection. Therefore, the angular shape of the signal shown on plots in Fig. 7.1 is not flat. That shape is determined by many factors such as detector efficiency to observe neutrinos from a given direction (acceptance), dimensions of the detector's fiducial volume (FV), details of the data selection. For example, even in case of a uniform detector acceptance in  $\theta$ , what is expected for some samples like Multi-GeV e-like and Multi-GeV  $\mu$ -like, the observed signal may not be isotropic. The SK fiducial volume is a cylinder with a height of about 29.8 m and a diameter of 32.2 m. The dimen-

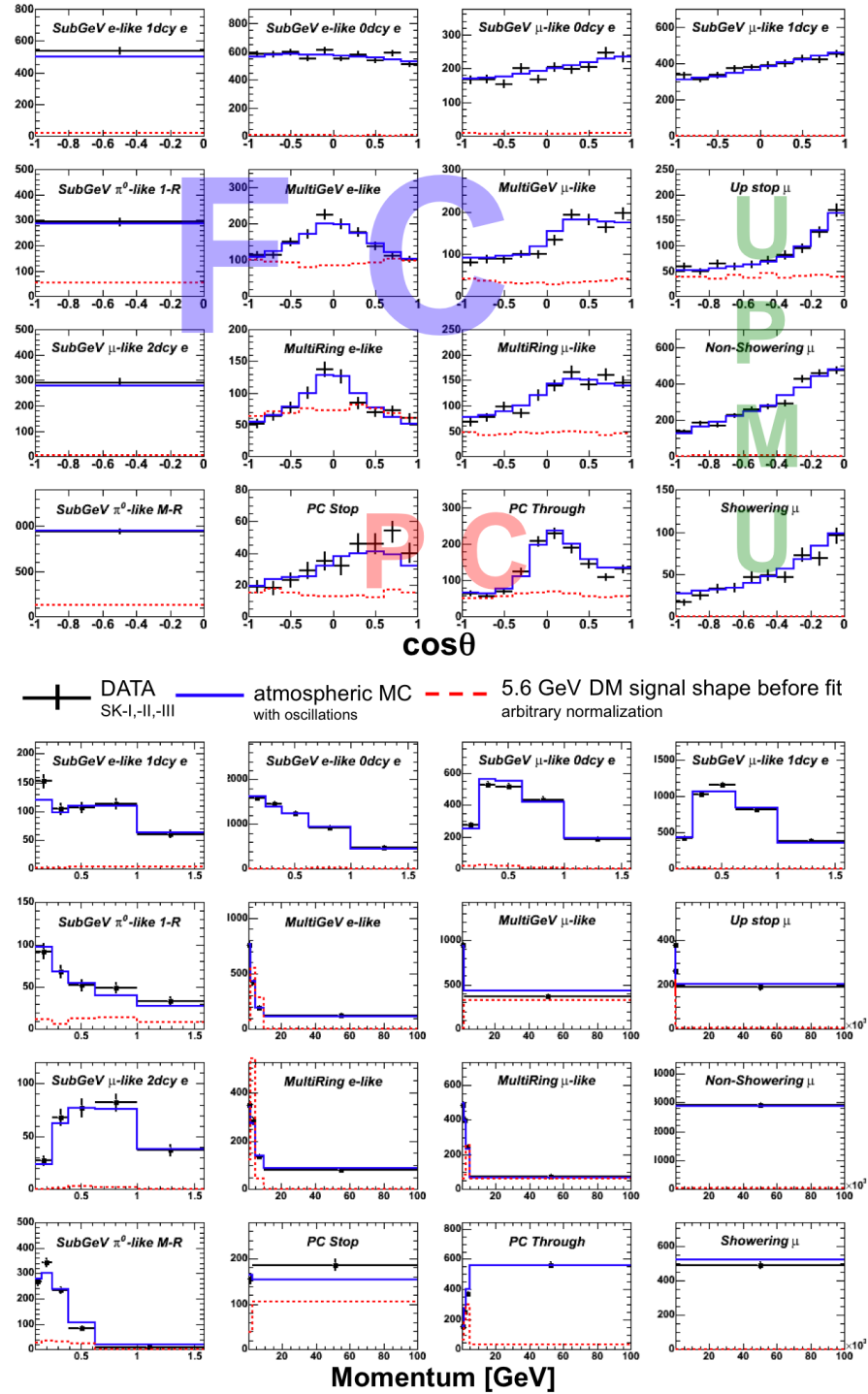


Figure 7.1: Illustration of a signal from annihilation of 5.6 GeV DM particle. All Super-Kamiokande samples used in a fit are presented. SK-I+II+III data (black points), best fit atmospheric MC (blue solid lines) and DM signal (red dashed lines) are shown in  $\cos\theta$  (upper panel) and lepton momentum distributions (lower panel). Equal flux of all neutrino flavors is assumed for the illustrated signal –  $\phi(\nu_e) = \phi(\bar{\nu}_e) = \phi(\nu_\mu) = \phi(\bar{\nu}_\mu) = \phi(\nu_\tau) = \phi(\bar{\nu}_\tau)$ . The signal contribution is before fit and its normalization is enhanced for the illustration purpose. Relative contribution of samples is conserved during a fit.

sions of the FV are not equal. It was checked in the separate study that this situation may lead to less FC events observed in the horizontal than vertical direction. Horizontal leptons, produced by neutrinos interacting in the SK's active volume, have shorter path length than vertical leptons and more of them exit the inner detector volume contributing rather to PC sets than FC. That may result in the concave shape of the observed angular signal in case of some FC samples. On the other hand, the convex shape in  $\cos\theta$  distributions of PC events was also confirmed in the study. In addition, other factors related to acceptance of events may play role in the determination of the shape of the observed angular distributions, depending on the sample considered.

Figures 7.2, 7.3, 7.4, and 7.5 show the signal illustration for  $M_\chi = 1.3, 20, 40,$  and  $130$  GeV, respectively. Each figure contains a complete set of 16 data samples used in the analysis. In case of the Sub-GeV  $\pi^0$ -like Multi Ring, Sub-GeV  $\pi^0$ -like Single Ring, Sub-GeV e-like 1 decay electron, and Sub-GeV  $\mu$ -like 2 decay electron samples, the lepton momentum distributions are shown. Other samples are illustrated with the zenith angle distributions. It can be seen how the contribution of the signal to various samples changes depending on the considered mass of DM particle. In case of low energy WIMPs ( $< 6$  GeV) the FC samples are mostly populated giving a strong constraint in the fit. That is due to many momentum bins considered for FC events and numerous subsamples – the proportions of the signal among all used samples are being kept in the fit. For the higher masses of DM particles, the PC and UPMU samples contribute more. In case of PC and UPMU events only some part of  $\nu$  energy is deposited in the detector and there are less momentum bins considered here than for FC sets. Therefore, PC and UPMU samples provide mainly angular information in the search. For the neutralinos with masses greater than several tens of GeV, the signal is practically present in the UPMU samples only. The UPMU through-going showering muon sample is the set with the highest average energy of parent neutrinos, while UPMU stopping muon sample contains the events with statistically the lowest energy of neutrinos among the UPMU sets. The information on the relative contribution of the signal to various UPMU samples depends on  $M_\chi$  and is an important constraint in the fit.

As it is explained in Section 6.2 (see Table 6.1), the signal in electron and tau neutrinos can be simulated only up to  $M_\chi = 56$  GeV in case of  $\nu_e/\bar{\nu}_e$  and up to  $M_\chi = 130$  GeV for  $\nu_\tau/\bar{\nu}_\tau$ . That is due to the insufficient number of electron and tau neutrino events in the *atmospheric* and *tau Monte Carlo* sets which are being used to mimic DM signal events. Above  $M_\chi = 130$  GeV, only the  $\nu_\mu/\bar{\nu}_\mu$  events are used to for signal simulation.

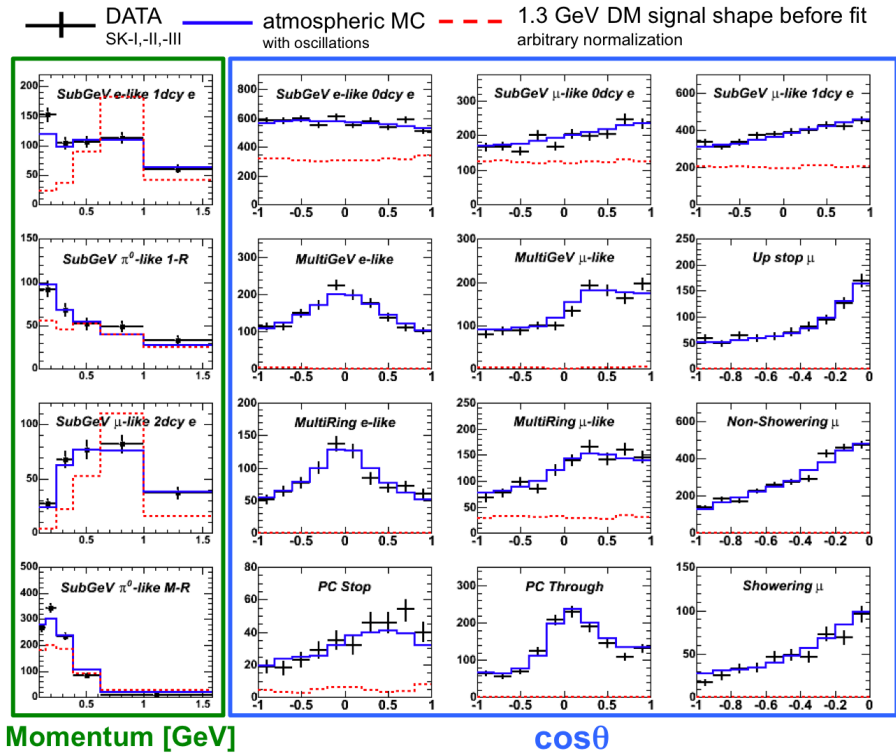


Figure 7.2: Illustration of a signal from annihilation of 1.3 GeV DM particle.

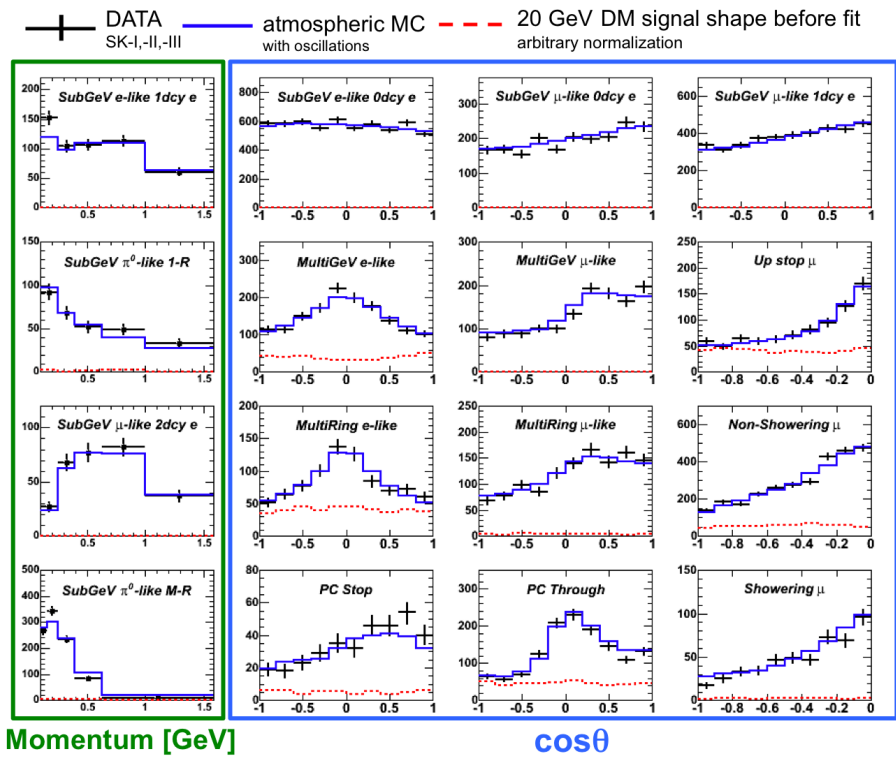


Figure 7.3: Illustration of a signal from annihilation of 20 GeV DM particle.

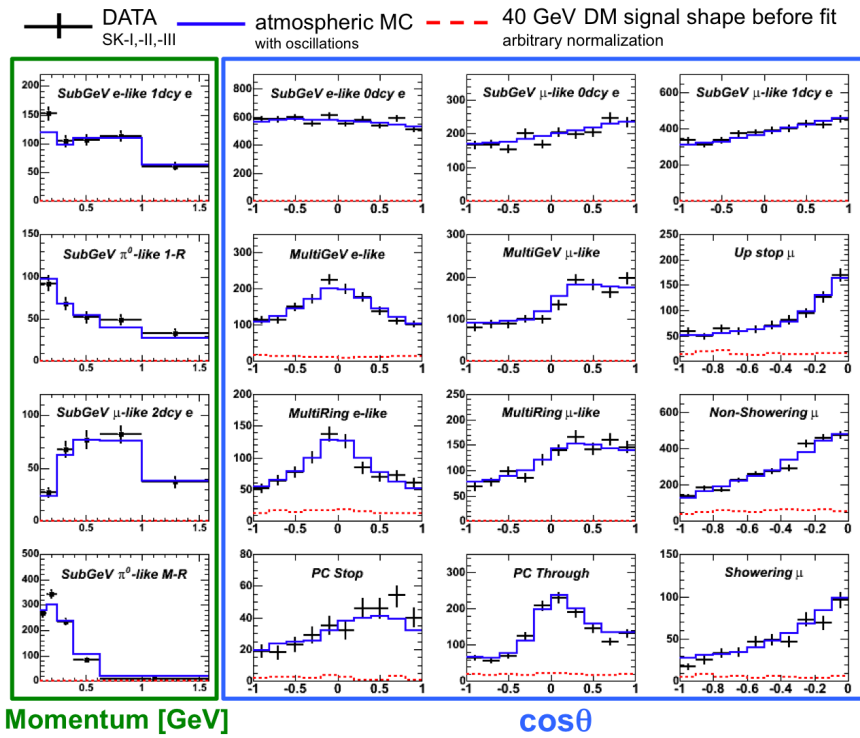


Figure 7.4: Illustration of a signal from annihilation of 40 GeV DM particle.

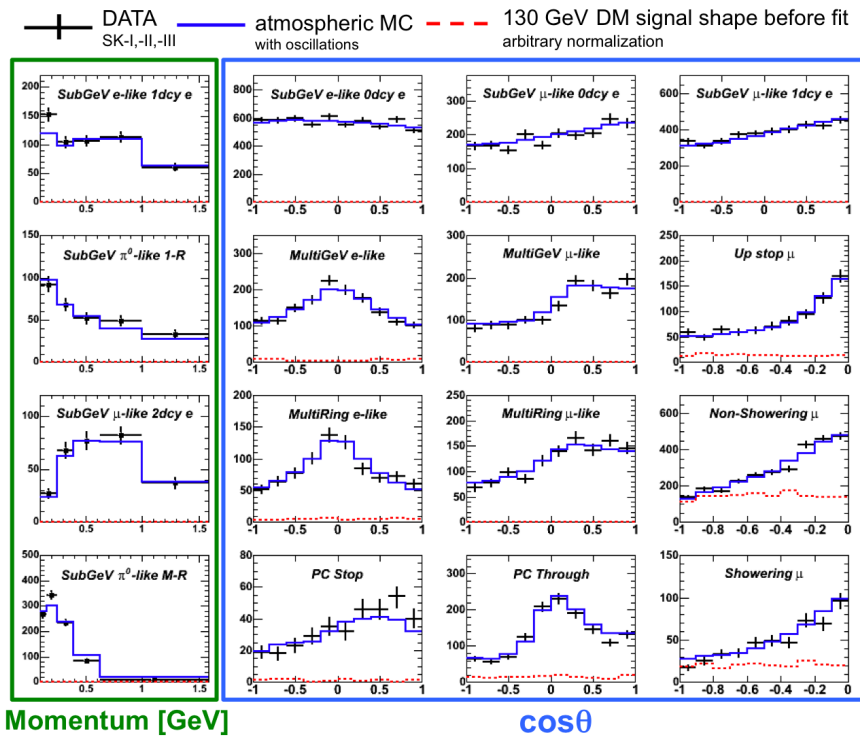


Figure 7.5: Illustration of a signal from annihilation of 130 GeV DM particle. Notice different signal normalization than on the previous figures.

### 7.1.3 Fit

In order to find the allowed contribution of DM-induced neutrinos in the SK data, method of minimum  $\chi^2$  is used, the same as in case of the analysis of oscillations of atmospheric neutrinos. The equation 5.1 needs to be slightly modified to include the contribution from DM-induced signal:

$$\chi^2 = 2 \sum_n \left( \left( N_n^{MC} + \beta N_n^{DM} \right) \left( 1 + \sum_i f_i^n \epsilon_i \right) - N_n^{data} + N_n^{data} \ln \frac{N_n^{data}}{(N_n^{MC} + \beta N_n^{DM}) (1 + \sum_i f_i^n \epsilon_i)} \right) + \sum_i \left( \frac{\epsilon_i}{\sigma_i} \right) \quad (7.1)$$

All symbols in Eq. 7.1 have the same meaning as described in Section 5.5.2. Additional parameter  $\beta$  stands for the normalization of the simulated DM signal. For each considered mass of a relic particle the values of the following parameters are determined in the fitting procedure based on Eq. 7.1:

- $\beta$  – normalization of the simulated DM signal. This parameter represents the fraction of unoscillated MC events that could be added as DM-induced neutrinos for considered mass of DM particles. Error on the value of  $\beta$  comes from the intersection of 1-sigma line with the resulting  $\chi^2 - \chi_{min}^2$  distribution (compare Fig. 7.6).
- $N_n^{MC}(\sin^2 2\theta_{23}, \Delta m_{23}^2)$  – oscillation parameters –  $\Delta m_{23}^2$ ,  $\sin^2 2\theta_{23}$  – which governs the value of  $N^{MC}$  are allowed to vary in the fit and their values are determined defining the contribution of atmospheric neutrinos (background) to the samples.
- $\epsilon_i$  – 120 parameters of the systematic uncertainties. Normalization of the background is regulated by some of these systematic terms as described in Section 5.5.3.

In total, values of 123 parameters could be fitted using Eq. 7.1 –  $\beta$ ,  $\Delta m_{23}^2$ ,  $\sin^2 2\theta_{23}$ , and 120  $\epsilon_i$  parameters. However, the value of  $\sin^2 2\theta_{23}$  is not being determined in the final analysis presented further in this chapter. That is due to precedent study which showed that for a number of tested  $M_\chi$ , the results of the fit of the oscillation parameters  $\Delta m_{23}^2$ ,  $\sin^2 2\theta_{23}$  are almost identical with the values obtained in the 2 flavor oscillation analysis –  $\Delta m_{23}^2 = 0.0021 \text{ eV}^2$ ,  $\sin^2 2\theta_{23} = 1$  (see Section 5.5.4). Moreover, the values of  $\chi^2$  obtained in the neutrino oscillation studies do not differ significantly from the ones obtained when DM-induced signal is also included in the fit. It means that adding the DM signal does not improve much the matching between the data and underlying model related to oscillation of atmospheric neutrinos.

It was concluded that the oscillation parameter  $\sin^2 2\theta_{23}$  does not need to be varied in the fit as the resulting best fit values have a strong preference to be in the unphysical region above 1 or at 1 (see Fig. 7.6). Thus, the value of  $\sin^2 2\theta_{23}$  is fixed at 1 during the procedure. The values of  $\Delta m_{23}^2$  parameter, obtained in the precedent study, are also very close to the value obtained in 2 flavor oscillation analysis. Therefore, in the final analysis this parameter is allowed to vary only within the 90% CL region determined in the 2 flavor analysis (compare Fig. 5.5). Above assumptions allow to fasten the computation of the fit. In summary, 122 parameters are being determined for each tested  $M_\chi$  in the final analysis –  $\beta$ ,  $\Delta m_{23}^2$  and 120 parameters related to systematic uncertainty.

The fitting procedure described in this chapter is based on all SK data samples listed in Table 5.1 and illustrated in Fig. 7.1. SK-I, -II and -III sets are used. The fact how the

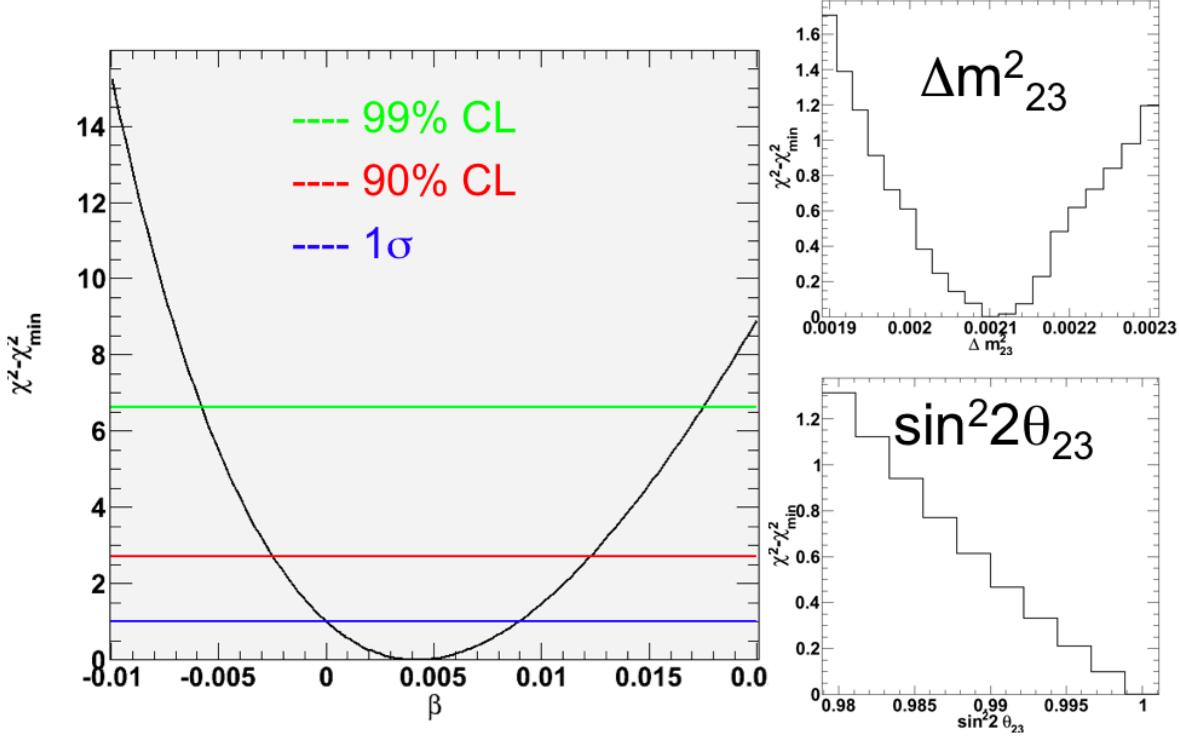


Figure 7.6: Illustration of a fit for a signal from annihilation of 90 GeV DM particle using the Eq. 7.1 based on all SK data samples listed in Table 5.1.  $\chi^2 - \chi_{\min}^2$  distributions are shown as a function of  $\beta$ ,  $\Delta m_{23}^2$  and  $\sin^2 2\theta_{23}$  parameters.  $\chi^2 - \chi_{\min}^2$  distribution for a given parameter is obtained so that the values of  $\chi^2$  of the other 2 fitted parameters are minimized. The resulting best fit values are very close to SK results of the 2 flavor atmospheric oscillation analysis –  $\Delta m_{23}^2 = 0.0021 \text{ eV}^2$ ,  $\sin^2 2\theta_{23} = 1$ .

signal is distributed among the subsamples is important and these proportions are being held in the fit. The momentum and  $\cos\theta$  distributions are used in the search with the binning described in Section 5.5.2. Both e-like and  $\mu$ -like samples are used. Index  $n$  in Eq. 7.1 spans 420 bins as in case of the oscillation analysis. The signal is simulated using all neutrino flavors and contribute as charged current and neutral current interactions of neutrinos and anti-neutrinos. The procedure described above is being referred to as a *global approach*. The results of this search, done for a range of DM particle mass considered from 3 GeV to 3 TeV, are presented further in this chapter. The lower threshold of the analysis,  $M_\chi = 3 \text{ GeV}$ , is based on the precedent studies. It was noticed that Sub-GeV samples, which mostly contain the signal for  $M_\chi < 3 \text{ GeV}$ , do not constrain the fit effectively due to rather flat angular distributions of the atmospheric neutrino data which resemble the expected shape of DM signal. If the data, atmospheric MC and signal have similar characteristics the fit is not working effectively. Some other approach is anticipated for the  $M_\chi < 3 \text{ GeV}$  as discussed at the end of this chapter. The upper analysis threshold,  $M_\chi = 3 \text{ TeV}$ , is related to limited statistics in the MC samples which are used to simulate DM signal at such high neutrino energies.

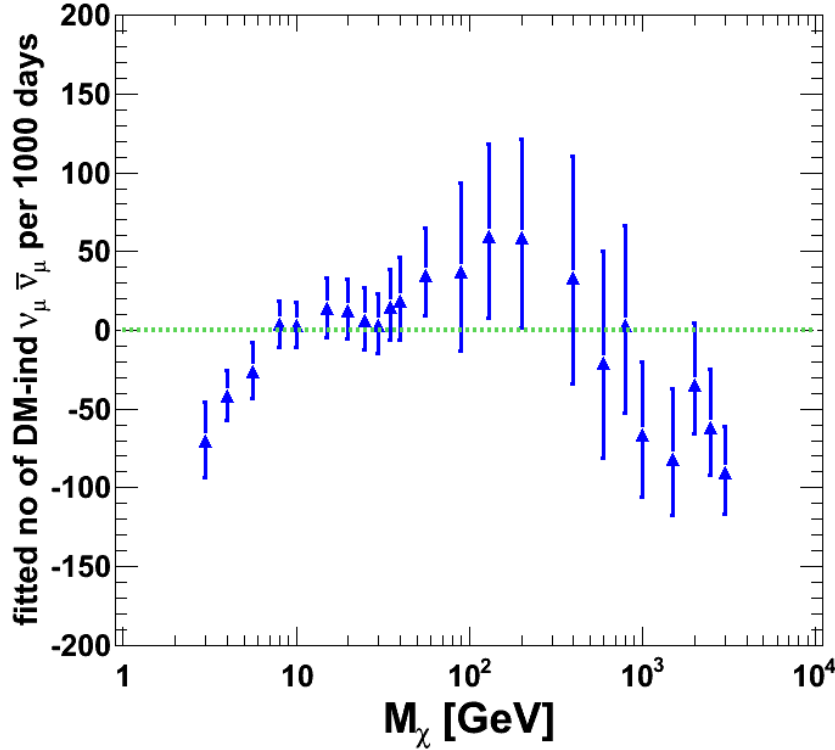


Figure 7.7: Fitted number of  $(\nu_\mu + \bar{\nu}_\mu)$  events from DM annihilation per 1000 days of exposure of Super-Kamiokande detector. The SK-I, -II, and -III data sets, corresponding to 2805.9 days of livetime of FC/PC events and 3109.6 live-days of UPMU events, are used to obtain this result.

## 7.2 Fitted Number of Dark Matter Induced Neutrinos

Fitted number of DM-induced neutrinos is based on the best found configuration of atmospheric MC and DM signal for each tested  $M_\chi$ . The way to obtain that number is to integrate the fitted signal over all bins that are used in the search. This accounts for the proper treatment of the systematics in the fit as the systematic uncertainty terms could increase or decrease the number of events in the given bin additionally to the fitted global normalization of the signal which is governed by the  $\beta$  parameter. One could also independently evaluate the number of fitted neutrinos of every flavor. Even though the e-like and  $\mu$ -like samples are not entirely pure and contain some contamination from other species of neutrinos, the information on the true flavor of the signal neutrinos is stored during the fitting procedure. The signal shape, for example the one shown in Fig. 7.1, could be decomposed into the contribution related to every neutrino flavor.

The fitted number of  $(\nu_\mu + \bar{\nu}_\mu)$  is shown in Fig. 7.7 for a sampling values of  $M_\chi$  in the range 3 GeV – 3 TeV. The result is consistent with a null admixture from DM-induced neutrinos for the entire considered mass range of  $M_\chi$ . The errors on the points correspond to 1-sigma error on the fitted value of the  $\beta$  parameter and are obtained from resulting  $\chi^2 - \chi_{min}^2$  distributions (compare Fig. 7.6).

The results presented in Fig. 7.7 are not independent as for every tested  $M_\chi$  the same

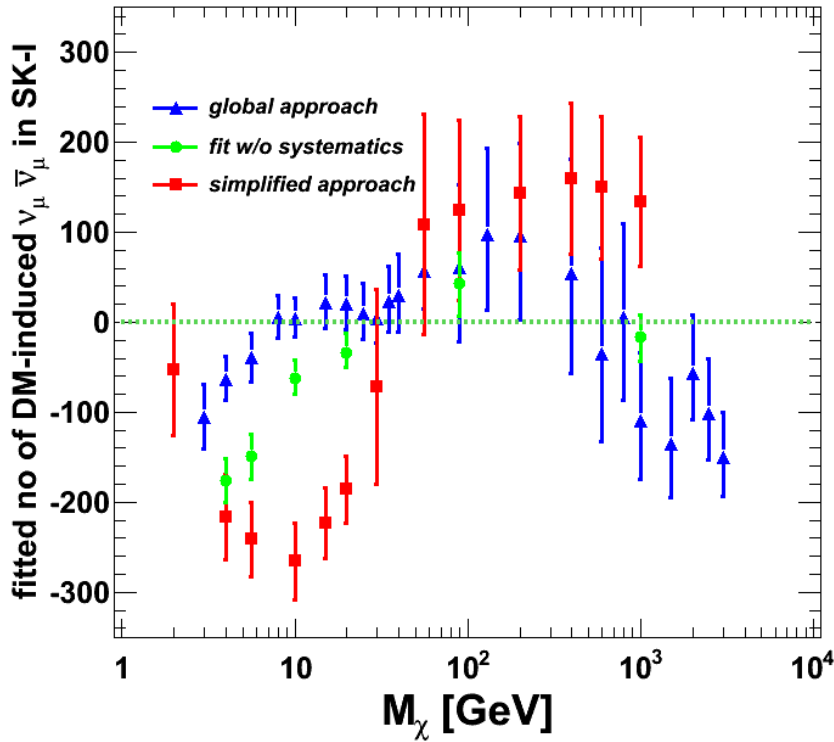


Figure 7.8: Number of  $(\nu_\mu + \bar{\nu}_\mu)$  events from DM annihilation obtained in the *global approach* (blue points), in the *simplified approach* described in Chapter 6, Fig. 6.10 (red points) and in the fit without systematic uncertainty terms (green points). Numbers correspond to SK-I phase.

data set is used. The results indicate some characteristic ranges of  $M_\chi$  for which different fitted DM contributions are obtained:

- $M_\chi < 10$  GeV – Expected number of DM-induced neutrinos is negative. The fit is very well constrained at these energies, but the signal shape favors negative number of fitted signal events. There are numerous fully-contained samples into which signal contributes and the strong constrains are related to momentum distributions. Also, the signal is expected in both e-like and  $\mu$ -like samples.
- $10$  GeV  $< M_\chi < 30$  GeV – Fitted number of signal neutrinos is very close to zero. The Multi-GeV FC and PC samples bound the fit.
- $30$  GeV  $< M_\chi < 600$  GeV – Fitted number of signal neutrinos is above zero with rather large errors resulting from the limited number of samples where the signal is present and the fact that a fit is based mostly on the angular information in that case.
- $M_\chi > 600$  GeV – Signal is present only in the UPMU samples. Signal shape favors negative number of fitted DM-induced neutrinos.

Number of DM-induced neutrinos of other flavors,  $(\nu_e + \bar{\nu}_e)$ ,  $(\nu_\tau + \bar{\nu}_\tau)$ , was calculated as a cross check of obtained results and gives the same conclusions on the null DM signal

contribution. The number of fitted ( $\nu_\mu + \bar{\nu}_\mu$ ) events from DM annihilation is presented as the most representative result.

As an additional cross check that a signal is not hidden by a systematic error contribution, simpler fit was performed where only the normalization parameter  $\alpha$  was fitted in addition to oscillation parameters ( $\sin^2 2\theta_{23}$ ,  $\Delta m_{23}^2$ ) and to signal normalization parameter  $\beta$  (4 fitted parameters, all  $\epsilon_i = 0$ ). Parameter  $\alpha$  stood for the global normalization of atmospheric MC (background). Only few  $M_\chi$  were checked with a fit without systematic uncertainty terms. The results, shown in Fig 7.8, give the same conclusions as the fit which includes systematic errors. The smaller errors on the green points reflect the fact that  $\epsilon_i$  parameters are not included in this expectation and resulting  $\chi^2 - \chi_{min}^2$  distributions are more narrow than in case of fit with systematics included. In Figure 7.8, the comparison with results of the *simplified approach* presented in Chapter 6 is also shown. Fitted number of signal neutrinos correspond to SK-I period.

### 7.2.1 Upper Limit on DM-Induced Neutrinos

Based on the null results of a search for DM signal in the considered range of  $M_\chi$ , one could derive the upper limit on the fitted number of DM-induced neutrinos (assuming 100% branching ratio for  $\chi + \chi \rightarrow \bar{\nu} + \nu$ ). The limit obtained for the results of the *global approach* is presented in Fig. 7.9 for ( $\nu_\mu + \bar{\nu}_\mu$ ). The statistical procedure used to evaluate the upper limit when the fitted value falls into the unphysical region (fitted number of signal neutrinos is below zero) is described in Section 6.6.

## 7.3 Upper Limit on DM-Induced Neutrino Flux

Based on the fitted number of DM-induced neutrinos and the upper limit on that event number, the corresponding limit on DM-induced neutrino flux can be evaluated.

In order to match the fitted number of signal events with the value of DM-induced neutrino flux, the following procedure has been used. In case of atmospheric MC events, the true value of the neutrino flux is known for any neutrino energy. From a fit it is known how many signal neutrinos could be added to the atmospheric neutrinos (background) to have the best expectation on the SK data. The upper limit on that fitted number is then derived as explained in Section 7.2.1. Thus, a ratio of the upper limit on the number of signal neutrinos at a given energy, corresponding to certain  $M_\chi$ , to the number of background events of the same energy<sup>1</sup> should be the same as the ratio of the upper limit on the signal flux to the atmospheric neutrino flux. The upper limit on DM-induced neutrino flux can be derived from this proportion as values of all other parameters are known.

The limit on DM-induced neutrino flux is shown in Fig. 7.10 for neutrinos of one flavor. This limit can be evaluated independently based either on the fitted number of  $\nu_\mu \bar{\nu}_\mu$ ,  $\nu_e \bar{\nu}_e$  or  $\nu_\tau \bar{\nu}_\tau$  neutrinos. Calculations based on different neutrino flavors yield the same results. This provides a consistency check of the obtained results and of the procedure used to calculate this limit. The same limit obtained for every neutrino species reflects the input condition of the search which assumes that annihilation leads to equal flux ratio of neutrinos of every flavor.

<sup>1</sup>The number of events is compared in the energy bins of the same width.

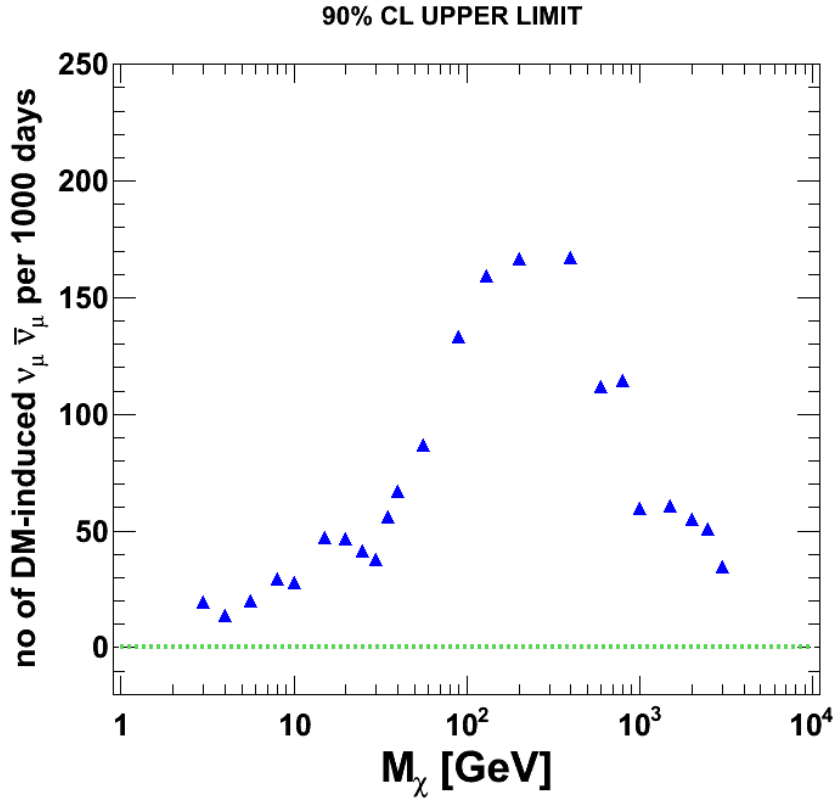


Figure 7.9: 90% CL upper limit on the number of  $(\nu_\mu + \bar{\nu}_\mu)$  from DM annihilation per 1000 days.

In figure 7.10, the atmospheric  $(\nu_\mu + \bar{\nu}_\mu)$  flux ( $\phi_{\nu_\mu + \bar{\nu}_\mu}$ ) is shown as a function of neutrino energy/ $M_\chi$ . It is seen that the upper limit on DM-induced neutrino flux is the same as the atmospheric neutrino flux at the  $\nu$  energy around 14 GeV. It means that DM-induced signal from annihilation of 14 GeV WIMP would be observed at 90% CL if its flux were of the same value or higher than flux of atmospheric neutrinos of the energy of 14 GeV. For energies greater than 14 GeV, the DM-induced flux of neutrinos shall be significantly higher than  $\phi_{\nu_\mu + \bar{\nu}_\mu}$  of neutrinos of the same energy in order to be observed at SK. At 100 GeV it needs to be at least 35 times higher than  $\phi_{\nu_\mu + \bar{\nu}_\mu}$ , and at 1 TeV it must be even 400 times  $\phi_{\nu_\mu + \bar{\nu}_\mu}$ . It shall be noticed that in case of neutrinos of energies above roughly 14 GeV, their energy cannot be resolved at SK – they mainly contribute to PC and UPMU samples. Therefore, high energy DM signal will be hidden in a sample of atmospheric neutrino events spanning many energies. That leads to a high requirement on the signal flux value for  $M_\chi > 14$  GeV as compared to the value of atmospheric neutrino flux which decreases rapidly with energy. It can be said that the upper limit on the value of DM-induced neutrino flux is rather constant for  $M_\chi > 100$  GeV – no matter what energy of the signal neutrinos is, they must be observed in a number of events significantly larger as compared to the number of atmospheric neutrino events of all energies.

The limit on the DM-induced neutrino flux could be related to a certain physical model responsible for neutrino production in the mechanisms such as annihilation or decay of dark matter particles. In the next part of this chapter the limits on DM decay lifetime  $\tau_{DM}$  and DM self-annihilation cross section  $\langle \sigma_A V \rangle$  are derived based on the limit

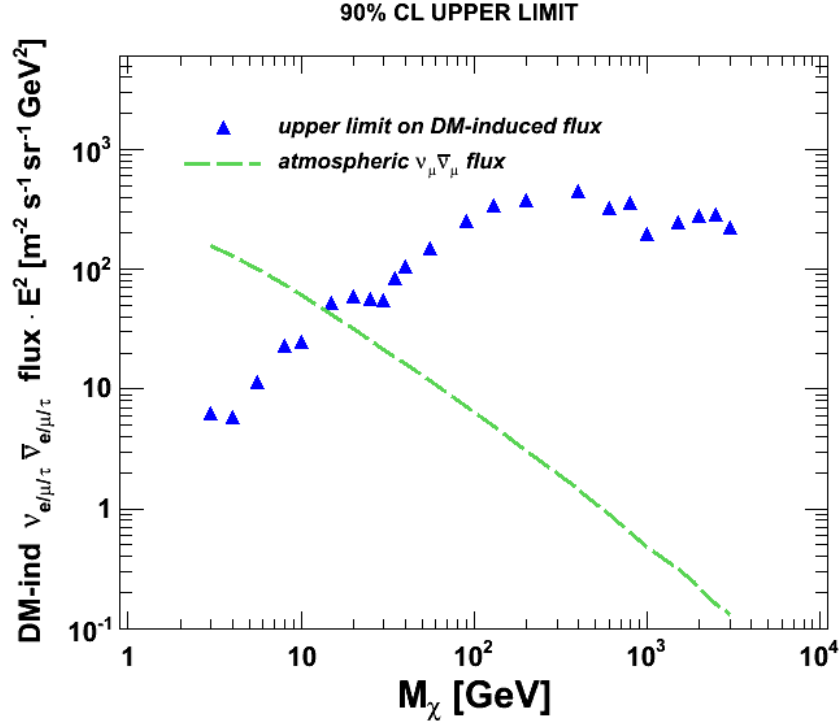


Figure 7.10: 90% CL upper limit on DM-induced neutrino flux (any flavor) is indicated as blue points corresponding to the tested values of  $M_\chi$ . Green dashed line is the flux of atmospheric ( $\nu_\mu + \bar{\nu}_\mu$ ), in this case horizontal axis corresponds to the energy of neutrinos.

on DM-induced neutrino flux.

## 7.4 Limit on Dark Matter Lifetime

Any generic DM candidate that could directly decay into neutrinos could be addressed with this search as it is discussed in Section 3.3. The upper limit on the DM-induced neutrino flux is related to the value of DM lifetime  $\tau_{DM}$  as described in Eq. 3.9. The SK limit on  $\tau_{DM}$  obtained in this analysis is presented in Fig. 7.11. Values of  $\tau_{DM}$  below the lines are excluded at 90% confidence level.

The other limit presented in Fig 7.11 is approximate and taken from Ref. [116]. Authors assume simple dependence of the limit as function of  $M_\chi$ . Their limit was derived using a limit on DM self-annihilation cross section  $\langle\sigma_A V\rangle$  obtained in the analysis by H. Yuksel *et al.* [90] (presented also in Fig. 3.10).

In the evaluation of the SK limit on  $\tau_{DM}$ , the entire Milky Way is considered as the source of the signal and NFW halo profile is assumed. The average signal intensity,  $\mathcal{J}_{\Delta\Omega}$ , which is present in Eq. 3.9 and used in this calculation is related to the *Halo Average* scenario described in Section 3.2.1. In Table 3.2, this parameter is referred to as  $\mathcal{J}_{\Delta\Omega}^{Ave}$  and for NFW profile equals 3.

In case of DM decay into two neutrinos, energy of each neutrino corresponds to half of the mass of decaying particle. Therefore, the limit on DM lifetime constrains range of  $M_\chi$  twice as larger as in case of other figures presented in this chapter which refer to DM annihilation.

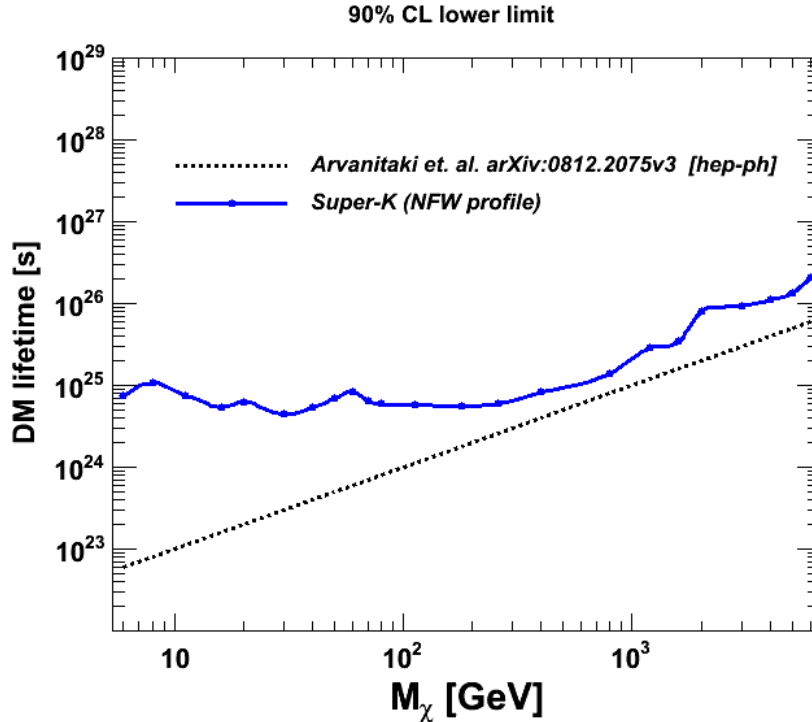


Figure 7.11: 90% CL lower limit on DM lifetime. The values below the lines are excluded.

## 7.5 Limit on Dark Matter Self-Annihilation Cross Section

The limit on the DM-induced neutrino flux could be translated into the limit on DM self-annihilation cross section  $\langle\sigma_A V\rangle$  as described in Eq. 3.7. The SK limit obtained in the *global approach* analysis is shown in Fig. 7.12 as a function of DM mass. The values of the cross section above the lines are excluded.

The average signal intensity,  $\mathcal{J}_{\Delta\Omega}$ , used to evaluate the limit, corresponds to the *Halo Average* scenario discussed in Section 3.2.1. The entire Milky Way is considered here as a source of the signal and the NFW [16], Moore [17] and Kravtsov [18] DM halo profile models are adopted to derive constraints on the value of  $\langle\sigma_A V\rangle$ . The separate limit is presented for each of the DM halo profiles considered.

Super-Kamiokande limit obtained in this work can be compared with the limit presented in Ref. [90]. The search described in [90] is based on the energy distributions of atmospheric neutrinos published by AMANDA [104], Frejus [105] and Super-Kamiokande experiments [5]. The limit from [90] is derived under the assumption that the number of DM-induced neutrinos cannot exceed the number of atmospheric neutrinos observed in a given energy interval (see Section 3.2.2). The analysis presented in Ref. [90] is based on the same assumptions on the origin of the signal as this work. Similarly, the signal is related to the diffuse annihilation in the entire Milky Way (*Halo Average* scenario). Instead of deriving a separate constraint for each DM halo profile, authors of Ref. [90] used only one value of the signal intensity,  $\mathcal{J}_{\Delta\Omega}$ , chosen as the most representative for all DM halo profiles. That average intensity adopted in Ref. [90] is indicated as the *canonical* in Table 3.2 and corresponds to the  $\mathcal{J}_{\Delta\Omega}^{Ave}$  column.

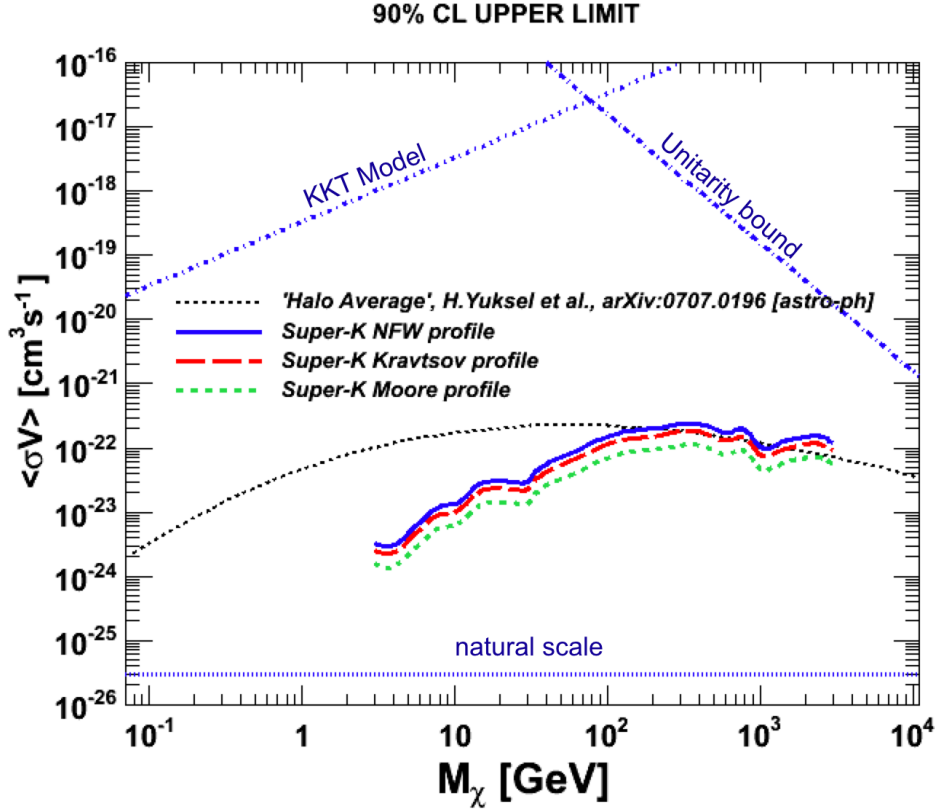


Figure 7.12: 90% CL upper limit on DM self-annihilation cross section  $\langle\sigma_A V\rangle$  for the NFW [16] (blue solid line), Kravtsov [18] (red dashed line) and Moore [17] (green dashed line) DM profiles. Values of  $\langle\sigma_A V\rangle$  above the lines are excluded. The limit obtained in Ref. [90] is indicated as black dotted line (*Halo Average*). The *natural scale* line is related to the maximum value of DM self-annihilation cross section for which DM can still be produced as a thermal relic. The *KKT* and *Unitarity bound* correspond to the upper limits on the value of  $\langle\sigma_A V\rangle$  derived in the course of theoretical predictions (see text for explanation).

The Super-Kamiokande limit, obtained in this search, improves the results presented in Ref. [90] for  $M_\chi < 100$  GeV. That is due to dedicated event-by-event analysis and simulation of a detector response for DM signal. The best improvement is observed for the mass of DM particles below  $\sim 30$  GeV where one could effectively use momentum distributions of FC and PC events (along with their angular distributions). Also, the signal is fitted in e-like and  $\mu$ -like neutrino samples requiring equal flux of all neutrino flavors before the detection. For the higher energies, where mainly UPMU samples contribute, only angular distributions can be investigated and tested against expected signal signatures. There is only one global momentum bin considered for the UPMU through-going event sample as shown in Table 5.1. Above 100 GeV the limit from this work gives similar predictive power as a combined result from [90]. It should be noticed that analysis presented in Ref. [90] uses narrower energy bins for neutrino energies above several hundreds of GeV than the ones considered in the analysis of the SK data. That is due to usage of a data from the AMANDA neutrino telescope which is larger than SK detector and more suitable for resolving energies of high energy neutrinos.

It is expected that dedicated analysis of AMANDA/Ice-Cube data could improve the

existing limits on the value of  $\langle\sigma_A V\rangle$  for  $M_\chi > 100$  GeV due to high statistics of observed neutrino events in this experiments. The Super-Kamiokande data samples are most valuable for the range of DM particle masses below 30 GeV due to numerous subsamples and extensive information on the energy and direction. Therefore, searches for diffuse DM annihilation signal conducted in various experiments are complementary and help to constrain the broad range of  $M_\chi$ .

The obtained constraints on the value of  $\langle\sigma_A V\rangle$  can be discussed within the framework of some theoretical models of DM properties with their upper limit expectations shown in Fig. 7.12:

- *KKT model.* This limit is provided by the model of Kaplinghat, Knox and Turner [117] (KKT) which is related to the evolution of DM halos. Here, the significant DM annihilation is invoked to resolve a conflict between predicted sharp cusps of DM density at the central galaxy regions (in some simulations) and observed rather flat cores of halo profiles. In this model, the cusps in DM density at the inner regions of the galaxies are expected to flatten at the values of  $\langle\sigma_A V\rangle$  indicated as *KKT model* in Fig. 7.12. However, the constraints of the *KKT model* could be relaxed [1], and predictions of the model could be reinterpreted as an upper bound allowing only the values of  $\langle\sigma_A V\rangle$  below a *KKT line* [118]. The results of this analysis rules out the proposal of KKT that DM annihilation have a strong macroscopic effect on galactic halos.
- *Unitarity bound.* This limit is related to the general principles of quantum mechanics and description of DM scattering amplitudes [119, 120]. The requirement on the unitarity of the scattering matrix, together with an assumption of non-relativistic velocities of DM particles in the halos, impose constraints on the value of cross section for self-scattering DM which can be also related to the value of DM self-annihilation cross section. This model yields the prediction on the value of  $\langle\sigma_A V\rangle$  smaller then indicated as *unitarity bound* in Fig. 7.12.
- *Natural scale.* In the standard thermal relic expectation of the Universe evolution and freeze-out mechanism (see Section 1.2) one expects the value of  $\langle\sigma_A V\rangle$  to be at the maximum level of  $3 \cdot 10^{-26}$  cm<sup>3</sup>/s in order to agree with the observed DM contribution to the mass of the Universe [1, 118]. However, larger cross sections (not exceeding obtained limit) are possible if dark matter is produced non-thermally or acquires mass only in the late Universe from decays of heavier particles [117].

Detailed expectations on the DM density distribution in the central regions of galaxies differ among the models as it is discussed above. However, most of these models agree that DM density in the central galactic regions is increased as compared to the outer regions and flux of DM-induced particles should be greatly enhanced from the direction of the Galactic Center due the fact that annihilation rate is proportional to  $\rho_{DM}^2$  (Eq. 3.7). Therefore, the analysis presented in this chapter can be extended in future and conducted with different set of variables used in the fit. The angular distributions of events in the Galactic Center coordinates can be used instead of zenith angle distributions. That could make a better use of the expected signal shape in the fit and will allow to cross check the results of the other DM analysis of SK data which is focused on the search of a signal from the Galactic Center with UPMU events [44] (see Section 3.1). The tools developed for the

purpose of this work could extend the existing point-like analysis with the capability to test low energy samples in a global approach so that entire knowledge of the SK data is incorporated in the search.

Moreover, the lower energy threshold of the current analysis, 3 GeV, shall be extended in future down to few hundreds MeV with the Galactic Center coordinates approach. The zenith angle distributions of the SK data in the sub-GeV range are almost isotropic, the same as the signal. Therefore, the fit of three components – data, signal and background – with similar characteristics is not very effective and does not provide reliable results in a sub-GeV range. Therefore, this analysis will be extended in future with a fit based on the Galactic Center coordinates.

# Chapter 8

## Neutron Background Studies for ArDM

The Argon Dark Matter (ArDM), aims at developing and operating a 1 ton-scale liquid argon detector for a direct detection of Weakly Interacting Massive Particle as dark matter in the Universe. In the first part of this chapter, the main features of the detector are presented. The second part includes a discussion on expected experimental background and on the work done by the author in preparation for the construction of the detector. Simulations of neutron background were performed in order to derive some constraints on the design of the neutron shield. The simulation of neutron production by muons is also discussed. The content of this chapter is independent from the material presented in other parts of the thesis.

### 8.1 Dark Matter Search with ArDM Detector

In 2004, a new initiative for direct detection of dark matter started – Argon Dark Matter experiment. The goal of this project is to design, assemble and operate an underground dual-phase 1 ton argon detector and to demonstrate the feasibility of a noble gas ton scale experiment in terms of efficient performance and sufficient background discrimination capabilities.

The experimental technique is based on detecting low energy recoils of argon nuclei induced by collisions of dark matter particles in the detector. Deposited energy leads to production of scintillation light and ionization charge in the medium. Typical kinetic energy of argon recoils induced by WIMPs is expected in the range of 10–100 keV. Therefore, the signal is quite elusive and requires very good background rejection. In addition, due to the very small WIMP-nucleus interaction cross section, a very low (event) rate is expected.

#### 8.1.1 Detector Description

The conceptual layout of the detector is shown in Fig. 8.1. One of the key features of the design is to independently detect the primary S1 (scintillation) and secondary S2 (charge) signals induced by recoils in the liquid argon (LAr). The light produced in the scintillation and recombination of free electrons is detected by a light readout system located on the bottom of the detector, behind the transparent high voltage (HV) cathode.

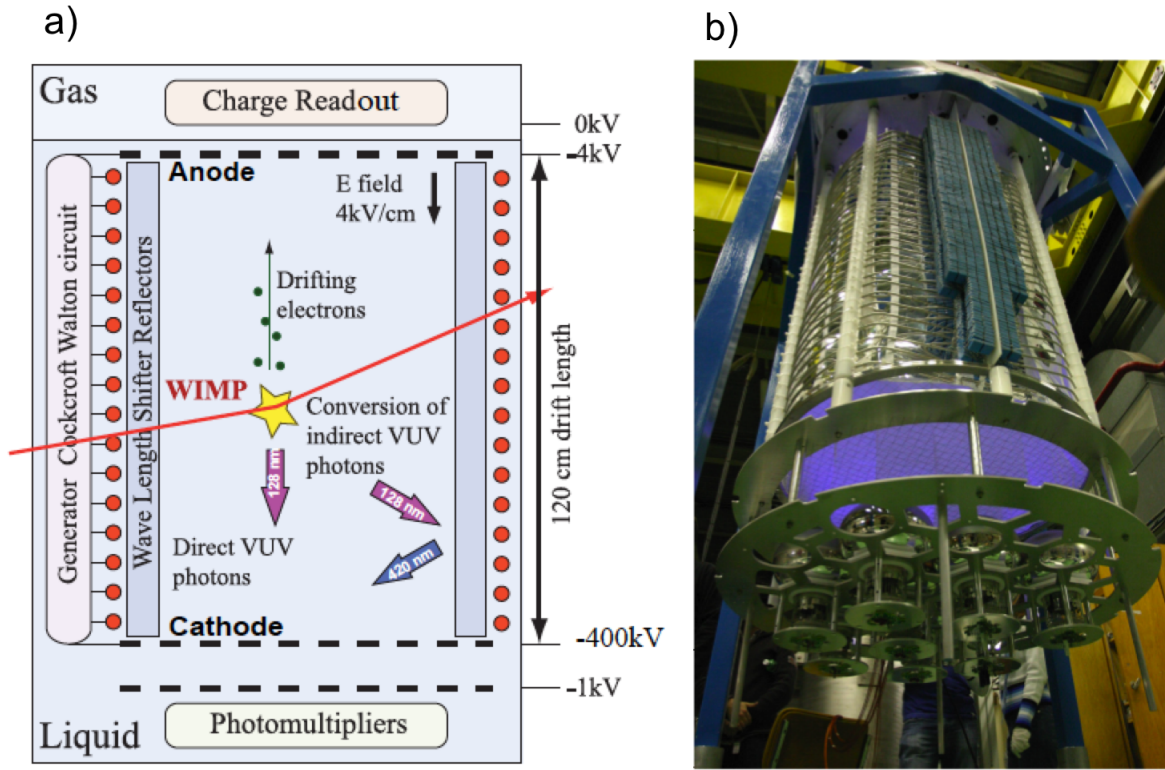


Figure 8.1: (a) Principle of operation of the ArDM detector [3]. (b) Inside view of the ArDM detector. [122].

Since the primary VUV scintillation light of argon (128 nm) cannot be detected with good efficiency using commercially available PMTs, it is convenient to shift its wavelength to the visible part of the spectrum. This is realized with TPB (TetraPhenyl Butadiene) coating on the surface of the PMTs [121]. TPB shifts the wavelength of VUV light to 420 nm bandwidth. To increase the light collection efficiency, the scintillation light is reflected by specially conceived high reflectivity plates placed around the field shaping electrodes which encompass the fiducial volume. These plates are also covered with the TPB wavelength-shifter.

Electrons produced in the ionization are drifted towards the top of the detector, extracted to the gaseous phase and amplified there by a charge readout system. The design of the charge readout system has not been concluded. One of the possible realizations uses a Large Electron Multiplier (LEM) system [122]. By segmenting the LEM it is possible to obtain 2 dimensional image of an event. The time correlation between scintillation and charge, related to drift of electrons, could provide the information on the third coordinate, thus allowing a full spatial event reconstruction.

The ratio of the primary S1 to the secondary signal S2 allows to distinguish effectively between nuclear recoils and other backgrounds as it is discussed more in Section 8.1.2.

In Figure 8.2 the design of the ArDM detector is shown. More detailed information on the detector and its operation can be found in Ref. [3].

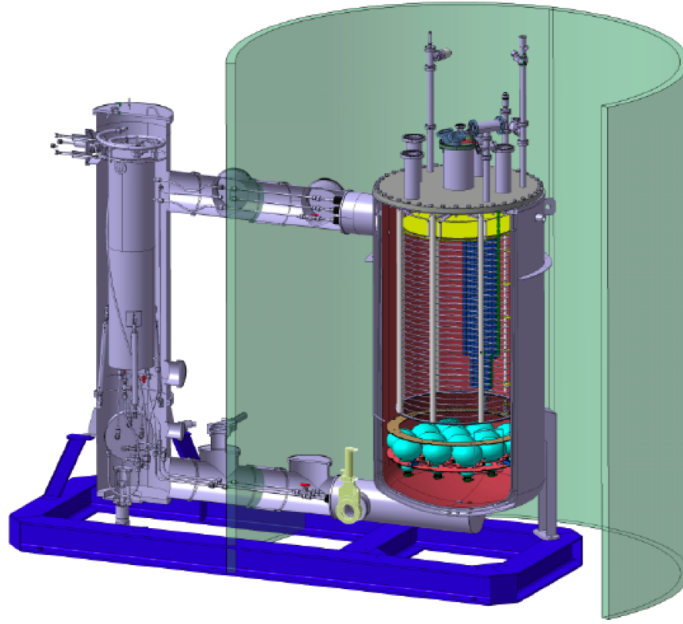


Figure 8.2: Schematic layout of the ArDM detector and its main components. The inner detector vessel has a diameter of 100 cm and the maximal vertical drift length of 120 cm. Charge readout system is indicated with yellow color; light readout PMTs with cyan. Electric field shaping rings of the HV system are visible inside detector, they encompass the fiducial volume region. Outer neutron shield is marked with green. On the left, outside, a cryogenic system dewar is shown. [3].

### 8.1.2 Experimental Background

The background particles produce nuclear and electron recoils inside the detector. The dominant electron/gamma background leads to production of electron recoils and could be rejected by the ratio of the scintillation to the ionization signals ( $S1/S2$ ), which is much lower in that case than the  $S1/S2$  ratio for nuclear recoils induced by neutrons/ $\alpha$ 's and expected also for WIMP interactions.

In case of nuclear recoils a large amount of light is emitted as dense ionization leads to production of light from recombination of electrons in addition to prompt scintillation. For that reason, the  $S2$  signal related to electrons drifted into gaseous phase is then relatively smaller than the  $S1$  signal because large fraction of electrons do not leave the region of ionization. In case of recoils induced by electrons/gammas the situation is opposite, the  $S1$  signal is small due to weak ionization and  $S1/S2$  fraction is lower than for heavy recoils.

In addition to the method based on comparison of  $S1$  and  $S2$  signals, the time structure of the scintillation light in argon can be also used to provide background discrimination as the time rise of the signal is different in case of electron and nuclear recoils [124]. By combining these two methods, efficient rejection of  $e/\gamma$  background can be achieved. This is required in the experiment which uses LAr due to the presence of  $^{39}\text{Ar}$  beta-emitter in natural argon liquefied from the atmosphere.  $^{39}\text{Ar}$  isotope is produced in the collisions of cosmic rays with a stable  $^{40}\text{Ar}$  isotope.  $^{39}\text{Ar}$  decays with a half life of 269 years and a value  $Q = 565$  keV. Its activity in LAr has been measured and it is expected to induce a background rate of around 1 kHz in a 1 ton detector [125]. The alternative way to

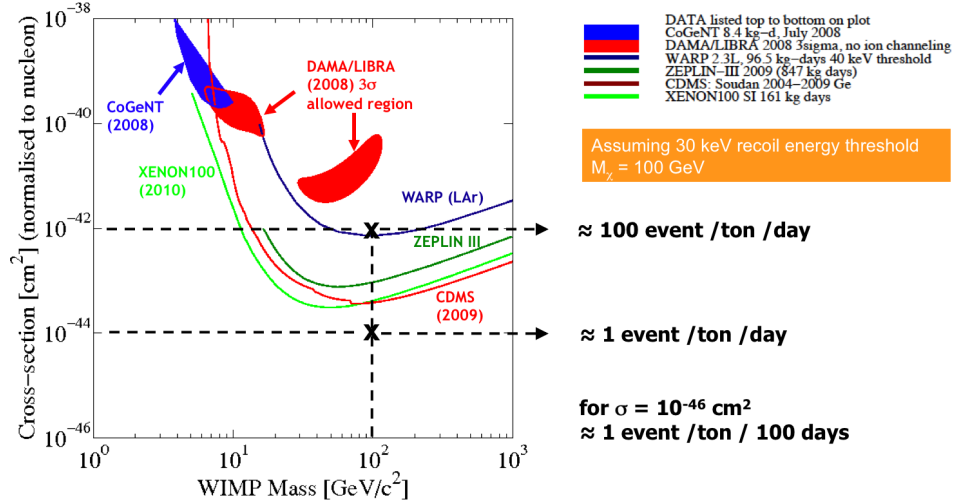


Figure 8.3: Cross section normalized to nucleon as a function of WIMP mass. Exclusions from various experiments are indicated with lines – region above the line is excluded by certain experiment. DAMA NaI best fit 90% CL contour is indicated as red region. The event rates, expected in ArDM, for  $M_\chi = 100 \text{ GeV}$  and various cross section values are indicated with crosses. [123].

suppress radioactivity related to  $^{39}\text{Ar}$ , is to obtain  $^{39}\text{Ar}$ -depleted material by extracting argon from well gases rather than from the atmosphere.

Apart from electrons, the other relevant sources of background consist mainly of neutrons and  $\alpha$  particles. Background events associated with electron and nuclear recoils induced by muons and neutrinos are reported to be negligible [126]. Moreover, muons passing through the detector can be usually tagged by an active veto detector. Alpha particle interactions usually can be rejected as they deposit a few MeV energy in the detector and their interactions occur only near the vessel walls, thus could be eliminated by a good fiducial volume definition. Multiple elastic scattering of neutrons is also a clear indication of the background events, as WIMPs, due to the weak coupling, do not undergo multiple interaction in the detector. Only the single elastic scattering of low energy neutrons would be indistinguishable from expected WIMP scattering. That provides a solid argument for a careful neutron background studies (see Section 8.2).

### 8.1.3 ArDM prospects

Currently, the ArDM group is operating a 1 ton prototype detector on the surface at CERN. The installation at the Canfranc underground laboratory is planned in 2011.

The expectation on the event rates for the ArDM 1 ton prototype operating underground is shown in Fig. 8.3. Expected number of WIMP events for a detector with energy threshold 30 keV, in case of  $M_\chi = 100 \text{ GeV}$  and for a WIMP-nucleon cross section ( $\sigma_{\chi N}$ ) of  $10^{-42} \text{ cm}^2$  ( $10^{-6} \text{ pb}$ ) is around 100 events per day per ton. Providing that sufficiently low electron and neutron background levels can be reached, the values of WIMP-nucleon cross section equal  $10^{-8} \text{ pb}$  can be probed expecting  $\sim 1$  WIMP event per ton per day. For the year of operation the values of  $\sigma_{\chi N} = 10^{-10} \text{ pb}$  could be addressed in a search expecting  $\sim 1$  WIMP event per ton per 100 days.

## 8.2 Neutron Background Studies

Neutrons at deep underground locations are either produced in cosmic-ray muon interactions, or by natural radioactivity. The first ones are induced by the high energy muons passing the rock and elements surrounding the detector. Neutrons from local radioactivity are caused by U/Th traces in the rock and detector components. They are produced in spontaneous fission of  $^{238}\text{U}$  or via  $(\alpha, n)$  reactions initiated by alpha particles from decays of radioactive isotopes in  $^{238}\text{U}/^{232}\text{Th}$  chains.

Following the approach presented in Ref. [127] one could consider three classes of neutron sources depending on the place of their origin:

1. neutrons from radioactivity in the surrounding rock,
2. neutrons from radioactivity in the detector elements,
3. muon-induced neutrons.

Energy spectra, flux, and methods of suppression are different for each case of neutron source listed above. The overall flux of neutrons from the surrounding rock is expected to be the most dominant,  $\phi_{rock} = 3.8 \times 10^{-6} \text{ cm}^{-2}\text{s}^{-1}$  at the Canfranc site [128]. However, the event rate related to rock neutrons can be reduced by external neutron shield placed around the detector. Neutrons scatter effectively in the hydrocarbon materials and lose large fraction of their energy. Therefore, neutron flux after passing such moderator is significantly reduced and energy spectrum of these particles is shifted towards much smaller energies as compared to the initial spectrum before the moderator. The mean energy of neutrons associated with the radioactivity is typically of the order of 1-2 MeV, depending on the composition of the rock.

The flux of neutrons from detector components depends strongly on the choice and radiopurity of the materials used in the construction. This type of background is considered to be the most difficult to reject as it cannot be suppressed by any shield and it is also not possible to estimate its flux and energy spectrum with high precision. Contamination of U/Th cannot be measured for all detector elements, it shows a variation between the samples of the same kind, and converting it to the resulting neutron flux is not an easy task and often requires some simplifying assumptions. In the ArDM experiment, the glass parts of PMTs, glass fibres in Vetrinite plates of the LEM system, and capacitors in the HV system are recognized as the major internal sources of neutrons. Typical traces of U/Th isotopes in those elements can lead to production of even up to  $3 \cdot 10^3$  neutrons per year with their mean energy around 1 MeV. Therefore, after the successful operation of the ArDM prototype, detector elements will be scanned in order to determine their actual radioactivity contamination and if possible better ultra-low radioactivity materials will be used.

The flux of muon-induced neutrons,  $\phi_{\mu-ind}$ , is usually three orders of magnitude lower than  $\phi_{rock}$  at various underground locations ( $\phi_{\mu-ind} = 1.7 \times 10^{-9} \text{ cm}^{-2} \text{ s}^{-1}$  at the Canfranc site [128]). However, the energy spectrum of muon-induced neutrons is hard, extending to GeV scale. This fact has the following consequences: muon-induced neutrons can reach the detector from large distances, they can pass through the shield and produce higher energy recoils. Most of the events which are induced by neutrons produced by muons can be tagged with the active veto system using a time correlation with the passing muon.

The problematic events are caused by neutrons which originated in a large distance from a muon track. Then, such muon cannot be observed with the active veto detector.

Investigations on neutron background sources and simulations of their propagation and interactions inside the detector are being performed within the ArDM group [129]. Their purpose is to evaluate the expected number of events with a single scattering in the detector and a help to specify requirements for a veto system, shield project and for purity of the detector materials. Below, the results of the author's simulation of neutrons related to radioactivity in the rock of the new Canfranc experimental hall are discussed. The ArDM installation is planned there in 2011. At the end of the chapter, some considerations regarding production of neutrons by muons underground are presented.

### 8.2.1 Rock Neutron Simulations for Canfranc

The energy of neutrons produced underground depends on the composition of the rock surrounding the experimental hall. An example of such a spectrum obtained for the Boulby underground laboratory located in United Kingdom is shown in Fig. 8.4(a) [127]. This figure describes the combined neutron energy spectra from  $^{238}\text{U}$  spontaneous fission and  $(\alpha, n)$  reactions in NaCl (NaCl is the main component of the rock at the Boulby laboratory). The spectrum shown in Fig. 8.4(a) is obtained in simulations and corresponds to the energy of neutrons at the point of creation. Its shape depends on the elements which are in the rock and its normalization is regulated by the contamination of radioactive isotopes.

The energy spectrum of neutrons at the walls of the experimental hall (rockface) is different than their production spectrum. It is a combined spectrum of energies of neutrons after they propagated in the surrounding rock and lost some part of their energy for interactions. The simulated energy of neutrons at the rockface is shown in Fig. 8.4(b) for the Boulby laboratory [127]. The shape of that spectrum is less sensitive to the composition of the rock as initial energy of neutrons is smeared after propagation. Therefore results of simulations presented in Ref. [127] can be adopted in studies of neutrons related to radioactivity in other laboratories. Especially, if effects related to usage of neutron shields are discussed. Energy spectra of neutrons after they passed moderators of different widths are shown in Fig. 8.4(b). The resulting distributions are more regular than the rockface spectrum.

The energy spectrum of rock neutrons presented in Fig. 8.4(b) was parametrized and used in the simulation developed by the author for the Canfranc laboratory. The rockface spectrum from Fig. 8.4(b) was scaled to match the flux of rock neutrons  $\phi_{rock} = 3.8 \times 10^{-6} \text{ cm}^{-2}\text{s}^{-1}$ . This flux value was derived for the old Canfranc cavern in Ref. [128] and in the following search it is assumed that its value is similar in a new experimental hall where ArDM installation is planned. The simulation was developed using Geant4 simulation package [130]. The realistic dimensions of the experimental hall are included in the simulation with an anticipated position of the ArDM experimental setup (Fig. 8.5).

The goal of the studies presented in this section is to evaluate the effect of the polyethylene shield placed around the detector. The thickness of the shield, planned by engineers as 50 cm, needed to be confirmed in the simulations as sufficient to stop neutrons coming from the walls. Also, the effect of 2 holes present in the shield, which are necessary to install pipes of the cryogenic system, needed to be investigated. Hence, two configurations of the external polyethylene shield are considered in the simulations: (1) ideal setup

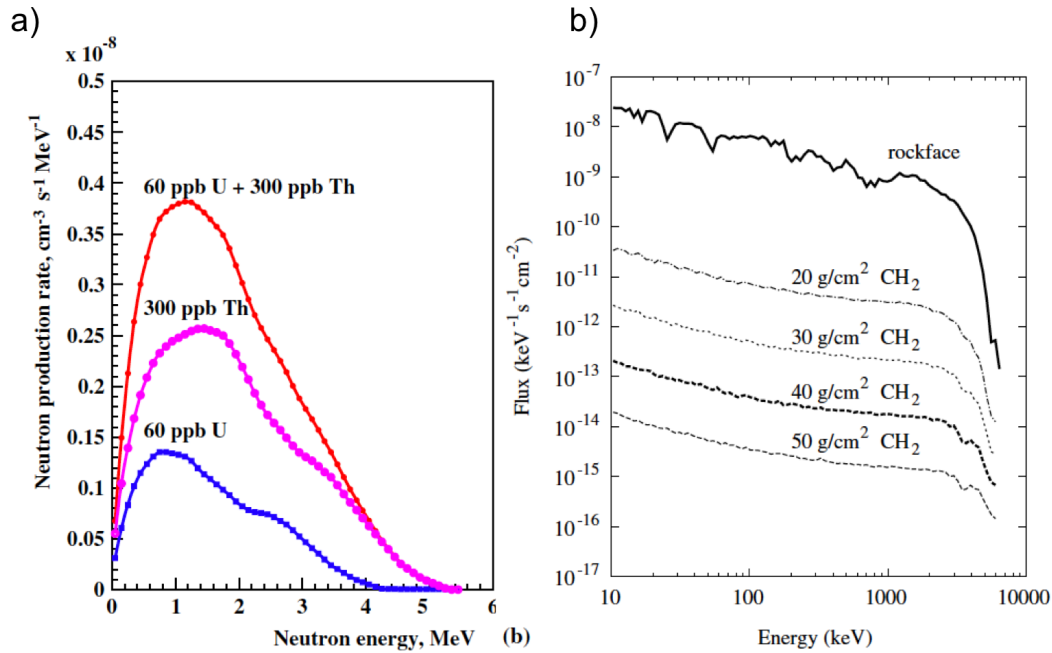


Figure 8.4: (a) Energy spectra of neutrons produced from U/Th traces in the rock as calculated for the Boulby laboratory [127]. The spectra correspond to the energy of neutrons at the point of creation. (b) Neutron energy spectra from radioactivity in the rock obtained at the walls of the Boulby laboratory [127]. Simulated energies of neutrons at the rockface were obtained using the neutron production spectrum from (a). Dotted curves show the spectra after passing hydrocarbon neutron moderators of various thickness.

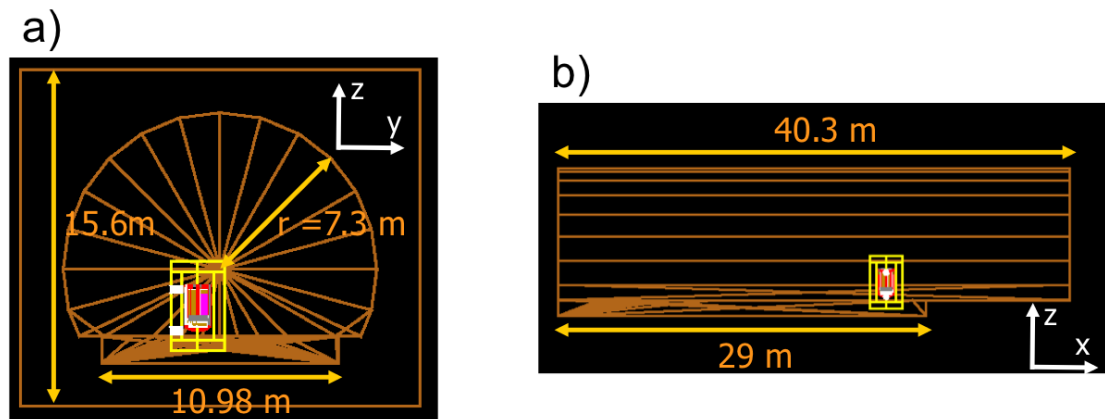


Figure 8.5: Illustration of the geometry included in the simulation of neutrons related to radioactivity in the rock of the Canfranc laboratory. Figures a) and b) show different sectional views of the experimental hall. The position of the ArDM experimental setup is indicated.

without any holes, (2) and configuration with two holes of 30 cm diameter each.

The shield is simulated as a cylinder with a height of 3.124 m and external diameter of 2.52 m. The top and bottom lids of the barrel are included in the simulation with the ArDM detector placed inside. Detailed simulation of the detector geometry has been developed by the collaboration with the details of that work described in Ref. [131]. For the purpose of the following Monte Carlo study, only the main characteristics of the

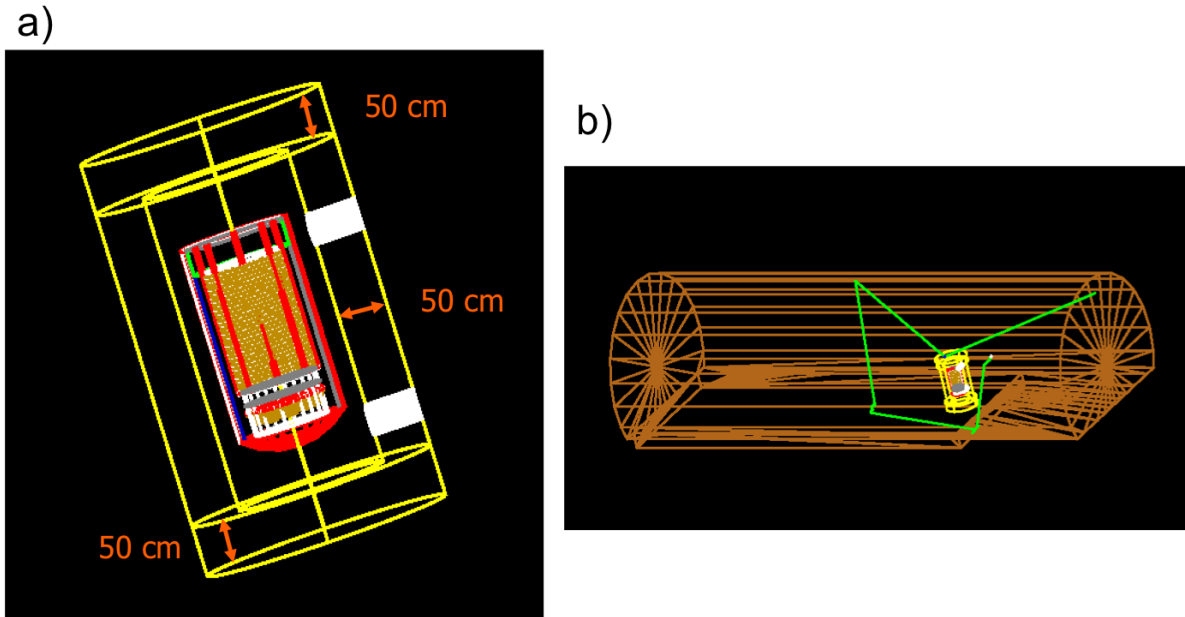


Figure 8.6: (a) Illustration of the simulated polyethylene shield setup for the ArDM detector. The neutron moderator is marked with yellow. White color marks the holes in the shield expected for the pipes of the cryogenic system. (b) Example of simulated background event: neutron of energy 2 MeV originate in the wall of the experimental cavern, hit the external shield, scatter in the laboratory and finally is captured in the wall after losing most of its energy.

detector, like external dimensions, type of construction materials used on the outside, and size of the fiducial volume with LAr are needed. The response of the detector for neutron interactions is not simulated at this stage. Illustration of the simulated shield setup with the ArDM detector placed inside is shown in Fig. 8.6(a).

For each simulated event, initial position of neutron is generated randomly on one of the walls of the experimental hall assuming isotropic particle emission. A few meters of rock behind the walls of the experimental cavern are included in the simulation to account for the effect of backscattering. The example of simulated trajectory of neutron with energy 2 MeV is shown in Fig. 8.6(b). It can be seen that neutrons scatter several times during their propagation in the laboratory.

The simulation of neutron's propagation in the experimental hall and its interactions in the shield is CPU time consuming process. In order to have sufficient statistics of events that passed the shield, many simulated events are required. The number of generated neutron events in both considered configurations without (1) and with holes (2) is shown in Table 8.1, along with the rates of neutrons which reach various parts of the simulated setup. By using the information on the total expected flux from Ref [128], number of events can be translated into the event rates.

Based on the numbers shown in Table 8.1 it can be concluded that configuration without holes seems to provide sufficient protection against neutrons. In this configuration, expected number of neutrons which can get through the shield and reach detector external container is around 0.66 event per day. For the configuration with holes, the corresponding rate is 3 orders of magnitude higher, showing that any gaps in the shield are significantly ruining its performance. If a neutron gets into the gap, it scatters there very effectively and

Table 8.1: Summary of the simulation of neutrons related to radioactivity in the rock of the new Canfranc hall. Results are obtained for the ArDM experimental setup with the 50 cm thick shield. All quoted errors are statistical.

	with holes	without holes
generated events	$3.7 \cdot 10^8$ livetime: 26.57 days 637.74 hours	$1.5 \cdot 10^9$ livetime: 106.77 days 2562.41 hours
events which hit external plane of the shield	$\sim 55 \cdot 10^3$ per hour	$55 \cdot 10^3$ per hour
events which get inside holes in the shield	$\sim 237$ per hour	–
events which get through the shield and hit detector external container	<b><math>35.9 \pm 0.2</math></b> per hour $861 \pm 6$ per day	<b><math>0.027 \pm 0.003</math></b> per hour $0.66 \pm 0.08$ per day
events which get through the shield and hit detector external container with energy above <b>100 keV</b>	<b><math>4.1 \pm 0.1</math></b> per hour	<b><math>0.08 \pm 0.03</math></b> per day
events which get inside active volume (all energies)	$17.7 \pm 0.2$ per hour $424 \pm 4$ per day	$0.012 \pm 0.002$ per hour $0.3 \pm 0.05$ per day

propagates along the hole. The fact that the holes will contain stainless steel pipes does not make the obtained results conservative. Construction materials that will be inside the holes are not placing any barrier in terms of neutron propagation.

Various parameters of neutrons that passed the shield and reached external surface of the detector are saved in the simulation. For each event, the position where neutron enters the detector container is recorded along with its momentum vector at this point. If a given neutron hits detector many times due to scattering inside the setup, its parameters are saved only once while it enter the detector volume for the first time. Recorded events can be used in the separate Monte Carlo studies of their interactions inside the ArDM with more detailed detector geometry included and simulation of the detector response, but that is not the scope of following studies.

The positions of the hits of neutrons on the surface of detector container are shown in Fig. 8.7 for the two considered configurations of the shield setup. The position of the gaps with respect to the coordinates  $x$ ,  $y$ ,  $z$  can be inferred from Fig. 8.5. It is clearly seen that in the configuration with holes neutrons most likely hit detector opposite to the position of the hole which proves that they are effectively transported through the gaps.

The energy of neutrons when they reach the ArDM external container is shown in Fig. 8.8 for both considered shield setup configurations. Most of the events have energy below 1 keV. It is far below the detection threshold which will be in the range 10-30 keV at best. It has been estimated in the separate Monte Carlo study that maximum recoil energy induced by neutrons is about 10% of their kinetic energy [123]. Therefore, the events that may be observed in the experiment should have minimum neutron energy of 100 keV and these compose only 12–13% of all events which reach the external container. The rate of such neutrons is shown in Table 8.1 (second row from the bottom). In the

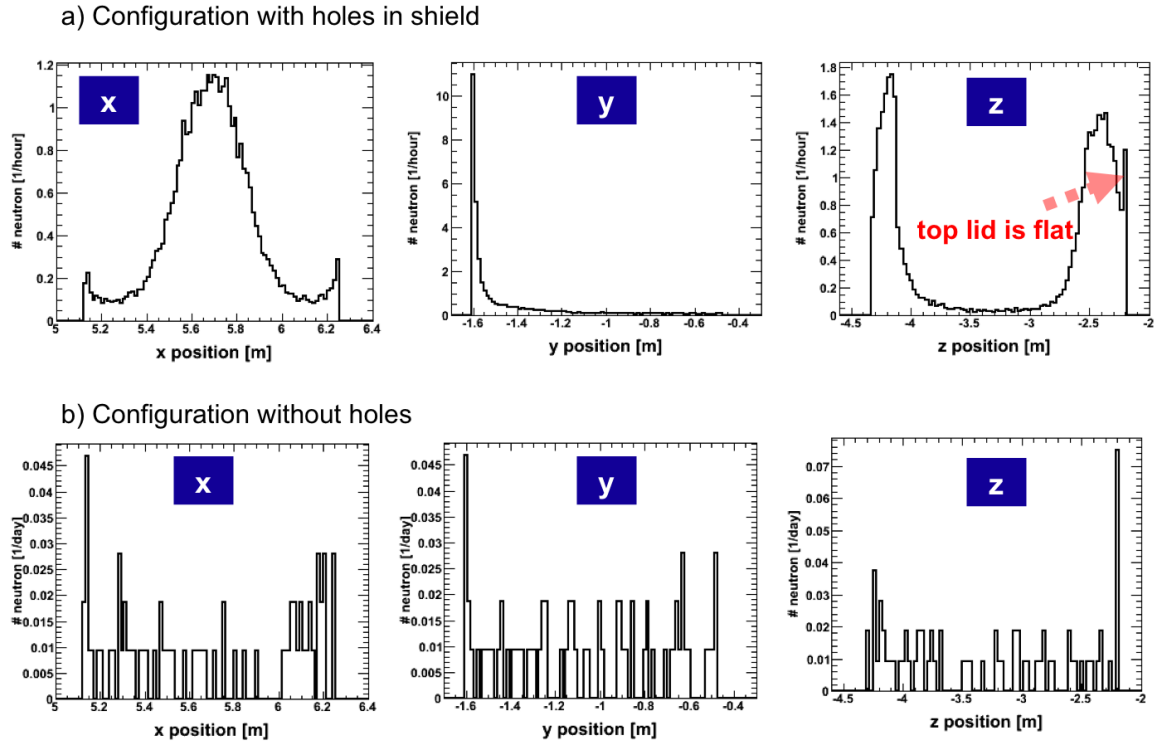


Figure 8.7: The entrance position of neutrons that reach detector external container are shown for the two considered configurations of the shield setup: (a) with holes and (b) without holes. The position of the holes with respect to the coordinates  $x$ ,  $y$ ,  $z$  can be inferred from Fig 8.5. Note the different units of vertical axes in (a) and (b).

configuration with holes around 4 events with energy  $> 100$  keV are expected per hour and in the ideal setup without gaps less than 0.1 event is expected per day. The rate of events in the configuration with holes is of the same level as expected rate of neutrons produced from radioactivity in the detector elements.

Event rates, quoted above, can be further reduced in the experiment as not every neutron entering the detector will interact inside the active volume. The probability of interaction has been estimated to be around 50% for the simulated events. Moreover, among the interacting neutrons some will scatter more than once. Such events can be distinguished from WIMP-induced events which are expected to have only one interaction point. The probability of multiple scattering for interacting neutrons has been estimated in the separated studies of interactions of neutrons in the LAr tank having the ArDM detector dimensions and for similar neutron energies [123]. That probability is around 50%.

It can be concluded that rate of neutron events which passed the shield and may be observed in the experiment with interactions similar to the ones expected for WIMPs is  $0.5 \times 0.5 = 0.25$  fraction of their initial rate obtained on the walls of the detector external container. Around 1 event per hour in the configuration with holes is expected and less than 0.02 event per day in case of ideal setup. The latter number confirms that 50 cm thick shield provides sufficient protection against background. However, the expected rate of 1 event per hour in the configuration with holes can limit the sensitivity of the detector to observe rare interactions of WIMPs. Therefore, the effect of the holes which effectively

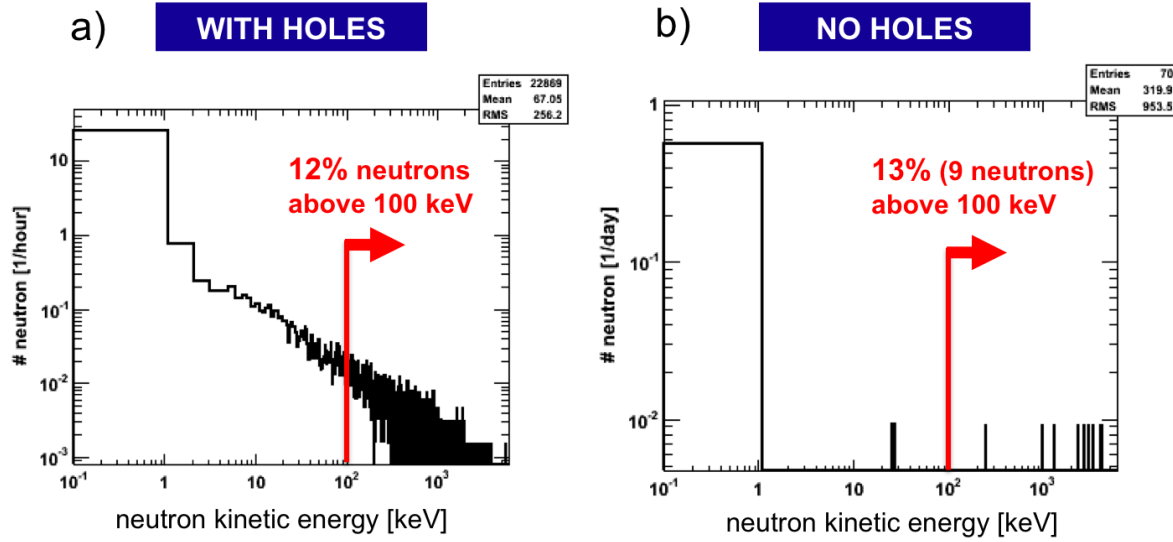


Figure 8.8: Energy spectrum of neutrons related to radioactivity in the wall of the experimental hall while they enter the external detector container after passing a shield. Note the different units of vertical axes on the plots.

transmit neutrons should be reduced in the experiment. Additional shield around the entrance to the holes should be conceived or some neutron absorbing material that can be placed inside the gaps or inside the pipes (like bags filled with polyethylene sand) is recommended.

## 8.2.2 Muon-Induced Neutron Simulations

The goal of the studies presented in the following section is to develop and validate a simulation of neutron production by muons underground based on Geant4 package. Created tool can be later used by the ArDM collaboration to study interactions of muon-induced neutrons in the shield.

It is widely accepted in the literature that neutron production at a certain depth can be approximated by assuming that neutrons are produced by monoenergetic muons (see Ref. [132], and references therein). Mean energy of muons underground,  $\langle E_\mu \rangle$ , is related to the depth. For example,  $\langle E_\mu \rangle = 250$  GeV corresponds to 2700 m w.e. overburden which is adequate for the Canfranc laboratory;  $\langle E_\mu \rangle = 50$  GeV corresponds to the depth of around 230 m w.e.; and  $\langle E_\mu \rangle = 280$  GeV to 3 km w.e. [132].

Neutron production by muons is related to the following processes:

- *direct muon-induced spallation* – muons can directly interact with nuclei leading to production of hadrons (including neutrons) in the spallation process.
- *muon-induced electromagnetic cascades* – neutrons are produced here in interactions of photons with nuclei, in photonuclear reactions ( $\gamma, n$ ). These photons are abundantly created in the electromagnetic showers initiated by muons during their radiative processes such as bremsstrahlung.
- *muon-induced hadronic cascades* – neutrons can be created in inelastic processes of hadrons which were produced in spallation or in photonuclear reactions.

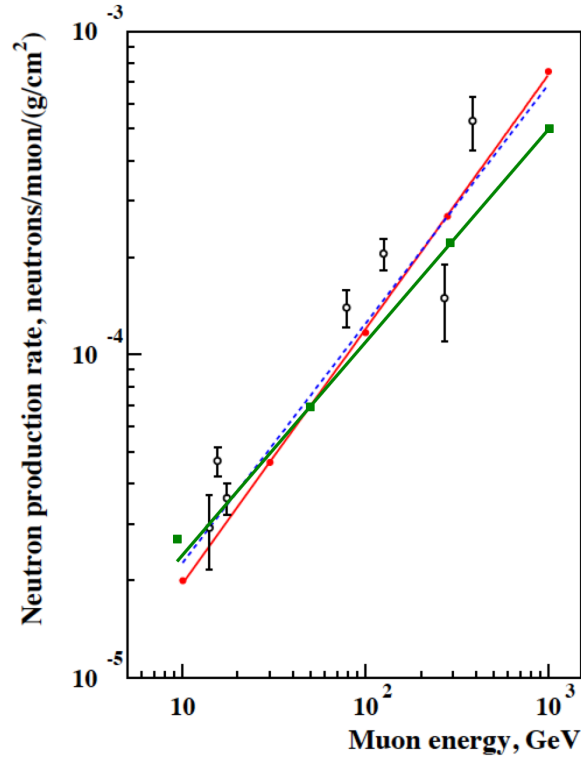


Figure 8.9: Average number of neutrons produced by a muon per unit path length ( $1/\text{g}/\text{cm}^2$ ) in scintillator as a function of muon energy. The results of this simulation are marked with green points and approximated using a fitted function (green line). The parameterization of results of other simulations based on the FLUKA code are indicated as red [132] and blue dashed lines [134]. For a reference of measurements see [132] (and references therein).

- *negative muon capture at rest* – this process contributes at very low energies of muons.

In order to check the validity of the simulation of neutrons by muons in those processes, the neutron production rates were checked for the interactions of muons in the scintillator  $\text{C}_{10}\text{H}_{20}$  of density  $\rho = 0.8 \text{ g}/\text{cm}^3$  and compared with other results available in the literature for the same material. The comparison of this work with the results obtained using older simulation codes based on the FLUKA package [133] is shown in Fig. 8.9. The Geant4 based simulation yields slightly higher neutron production rate expected at energies below several tens of GeV, and slightly lower yield at energies above  $\sim 100 \text{ GeV}$  as comparing to other codes. The comparison of simulations with a few available measurements shows good agreement and it is difficult to judge which ones better describes the data.

As a next step, neutron production in the rock by muons is checked for a few fixed energies  $E_\mu$  corresponding to different depths. Mean energies of neutrons induced by muons are presented in Fig 8.10(a). It can be seen that there is a very weak dependence of resulting mean neutron energy ( $\langle E_n \rangle$ ) on the energy of the muon. Figure 8.10(b) shows the value of the neutron production rate as a function of  $E_\mu$ . Here, the correlation with the muon energy is more important.

The main point of interest of this study is a neutron production by muons in the rock around the Canfranc laboratory. The mean energy of neutrons induced by muons at

## neutron production in rock by muons

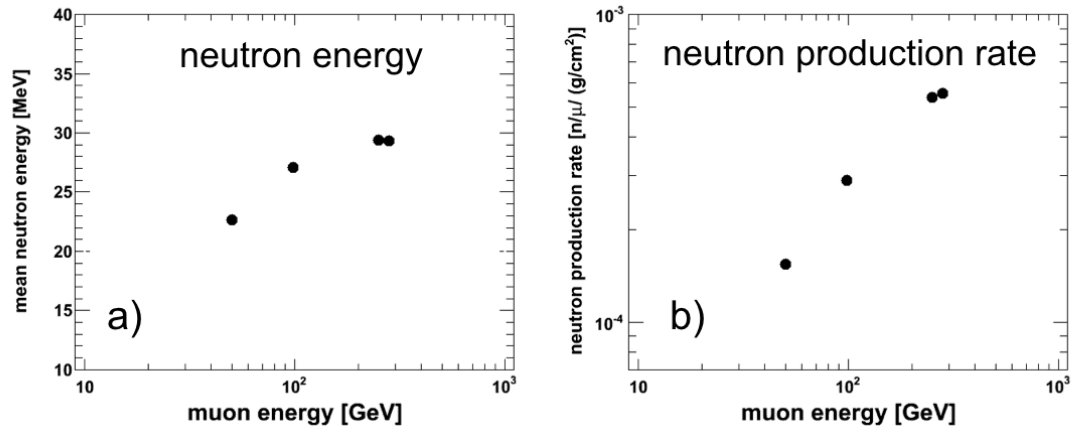


Figure 8.10: Results of the simulation of a neutron production by muons in the rock as a function of muon energy. The mean energy of created neutrons is shown (a) and the neutron production rate per unit path length of a muon (b).

these depth is 27 MeV and the resulting spectrum reaches up to GeV scale as shown in Fig. 8.11(a). Such energetic neutrons can pass the shields and imitate WIMP events in the experiment. Especially, if they are created at large distance from a muon track, it may happen that the muon is not detected by any veto system placed above the DM detector. The distribution of a distance of a neutron's production point with respect to the muon track is shown in Fig. 8.11(b). The mean value of the distance expected for neutrons produced in the Canfranc rock is around 0.7 m. However, there are also neutrons which can be created in long developing cascades at the distances of several meters away from passing muons.

This result shows that any future simulation of muon-induced neutrons performed for the detector experimental setup at the Canfranc laboratory should include a region of rock several meters away from the walls of the cavern. On the other hand, it shall be noticed that the flux of neutrons associated with muons is expected to be 3 orders of magnitude lower than the flux of neutrons related to the radioactivity in the rock. The exact expectation on the contribution of muon-induced neutrons to the sample of collected single-scattering recoils in the experiment is necessary but these events are not expected to limit the sensitivity of the detector as much as events related to the neutrons from radioactivity which are passing the shield through the holes in the setup.

### 8.2.3 Conclusions on the neutron background studies for ArDM

In this chapter, two studies of neutron background simulations for the ArDM detector were presented. Firstly, the simulation of neutrons from radioactivity in the rock of the Canfranc laboratory confirmed that anticipated 50 cm thick polyethylene shield provides sufficient protection against neutrons produced by radioactive isotopes. It was also noticed that any holes in the polyethylene material will limit the shield performance and induce a rate of background events at the external surface of the detector of around 4 events per hour (rate of events with  $E_n > 100$  keV) which is comparable to the event rate of neutrons

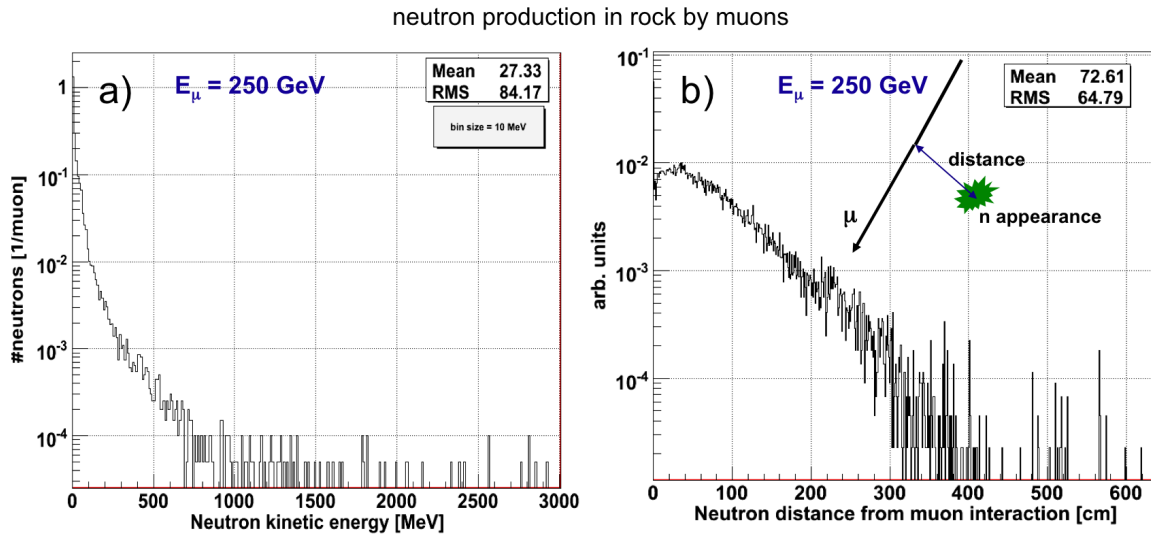


Figure 8.11: (a) Energy spectrum of neutrons produced by muons. (b) Distance of a neutron production point from muon trajectory. Both distributions are obtained in the simulation of interactions of muon with  $E_\mu = 250$  GeV (mean energy of muons at the depth of 2700 m w.e.).

from radioactivity in the elements of the detector. That event rate can be reduced further in the experiment: only a half of these neutrons are expected to interact in the active volume and half of the interacting ones should scatter more than once. Therefore, the effective rate of such neutrons observed in the experiment should be approximately at the level of 1 event per hour.

The other presented studies aimed to develop and test a software tool which can be used to simulate production of neutrons by cosmic ray muons underground. It was shown that neutrons produced by muons can be created in at long distance from a muon track and can have relatively high energy. Therefore, any future study regarding their production should take into account a region of rock several meters away from the walls of the experimental hall and estimate their background depending on the active veto installed around the detector.

# Summary and outlook

The main outcome of this thesis is the result of the search for a signal from diffuse dark matter annihilation in the Milky Way using neutrino data from the Super-Kamiokande-I, -II, -III. No signal contribution is allowed by the Super-Kamiokande data which are consistent with the expectation on the background level comprised of atmospheric neutrinos. Considered masses of DM particles in the search are ranging from 3 GeV to 3 TeV. The analysis is based on assumption that DM particles are annihilating directly into neutrino and anti-neutrino pairs. Adopted approach could be also related to the search for neutrinos from decay of DM particles.

Presented search for neutrinos is complementary to the other indirect detection experiments, investigating other annihilation products like  $\gamma$ ,  $e^{+/-}$ ,  $\bar{p}$ . It allows to probe the missing 'invisible' part of a phase space and to derive some general constraints. The upper limits on the value of DM-induced neutrino flux and on the value of DM self-annihilation cross section  $\langle\sigma_A V\rangle$  have been obtained as a function of mass of relic particles. With this analysis, the existing limit on the value of  $\langle\sigma_A V\rangle$  (based on neutrino data) has been improved for  $M_\chi < 100$  GeV. That is due to the dedicated simulation of a response to DM signal and a usage of entire knowledge related to each observed and simulated event. Information on reconstructed energy of neutrinos, their direction, flavor, relations between various event samples, systematic uncertainties are included in the search. Data samples containing the most complete information on interacting neutrinos cover the range of neutrino energies from several GeV to several tens of GeV at which neutrinos are observed as partially- or fully-contained events and populate numerous event subsamples. In this energy region the most significant improvement as compared to the existing results has been achieved – even up to 2 orders of magnitude better limit on the value of  $\langle\sigma_A V\rangle$ .

Recent observations of a positron excess by PAMELA [36], and anomalous ( $e^- + e^+$ ) spectrum by ATIC [37], as well as electron spectra from FERMI [35] are inconsistent with each other and with a standard electron-positron production models in the Galaxy [47]. That fact demonstrates the importance of a multi-messenger approach to investigation of the fluxes of cosmic particles. The observed excess of electrons/positrons could be related to nearby astrophysical sources such as pulsars [53], but it could be also explained by DM annihilation within a distance of few kpc from the Solar System [48]. If the latter hypothesis is true, that indicates an existence of leptophilic dark matter particles [50, 51]. In such a scenario significant flux of DM-induced neutrinos from decays of muons and tau leptons is expected. A large fraction of that flux could be also related to neutrinos directly produced in DM annihilation. Validation of this scenario with a search for neutrinos produced in the Milky Way is currently of a great interest of the scientific community. The analysis performed in the thesis have shown that no excess of neutrinos of DM origin has been observed in the diffuse flux as compared to the level of background consisting of

atmospheric neutrinos. The results exclude a range of DM self-annihilation cross sections  $\langle\sigma_A V\rangle$  larger than approximately  $10^{-22} \text{ cm}^3 \text{ s}^{-1}$  for WIMPs heavier than 100 GeV. For  $M_\chi$  in a range from 10 to 100 GeV, the upper limit on allowed cross section varies between  $10^{-23} \text{ cm}^3 \text{ s}^{-1}$  and  $8 \times 10^{-23} \text{ cm}^3 \text{ s}^{-1}$  correspondingly, and for very light WIMP candidates with  $M_\chi < 10 \text{ GeV}$  values of  $\langle\sigma_A V\rangle$  larger than  $\sim 7 \times 10^{-24} \text{ cm}^3 \text{ s}^{-1}$  are not allowed. It does not mean that observed electron/positron fluxes cannot be due to DM annihilation. The models which are used to explain the PAMELA/ATIC spectra by DM annihilation are not strongly constrained and in some cases a large expected value  $\langle\sigma_A V\rangle$  can be compensated in them by hypothetical clumps of DM density in the structure of the halo [48]. Taking into account the limits obtained in this thesis, some values of DM-self annihilation cross section should not be considered in theoretical models which are trying to explain PAMELA/ATIC results with leptophilic dark matter.

Based on the tools developed for the purpose of this analysis, additional search for DM signal will be conducted in future using the Galactic Center coordinates. The flux of DM-induced neutrinos should be greatly enhanced from the direction of the Galactic Center due to the increased DM density expected for the central galactic region as compared to the outer halo [16, 17, 18]. Analysis that uses angular distributions defined in the Galactic Center coordinate system instead of the zenith angle distributions, could make a good use of the expected signal shape in the fit. Such an approach will allow to extend existing SK searches for upward-going muon events from the direction of the GC by addition of lower energy samples and by incorporating the full knowledge of SK data samples and systematic uncertainties. Also, it may be possible to extend the lower limit of the presented analysis,  $M_\chi = 3 \text{ GeV}$ , down to the sub-GeV range.

# Bibliography

- [1] G. Bertone, D. Hooper, J. Silk, "Particle dark matter: Evidence, candidates and constraints", Phys. Rept. **405**, 279-390 (2005), arXiv:hep-ph/0404175.
- [2] G. Jungman, M. Kamionkowski, K. Griest, "Supersymmetric dark matter", Physics Reports **267**, 195-373 (1996).
- [3] C. Amsler *et al.* (The ArDM Collaboration), "First results on light readout from the 1-ton ArDM liquid argon detector for dark matter searches", J. of Instr. **5**, 11003 (2010).
- [4] S. Fukuda *et al.* (The Super-Kamiokande Collaboration), "The Super-Kamiokande detector", Nucl. Instruments and Methods A **501**, 418 (2003).
- [5] Y. Ashie *et al.* (The Super-Kamiokande Collaboration), "A Measurement of Atmospheric Neutrino Oscillation Parameters by Super-Kamiokande I", Phys. Rev. Lett. D **71**, 112005 (2005), arXiv:hep-ex/0501064.
- [6] Y. Hayato *et al.* (The T2K Collaboration), "Letter of Intent: Neutrino Oscillation Experiment at JHF", <http://neutrino.kek.jp/jhfnu/loi/loi.v2.030528.pdf>.
- [7] A. Vacheret for the T2K Collaboration, "The T2K beam line and near detectors", Proceedings of the NuInt 07 conference (2007).
- [8] D. Larson *et al.*, "Seven-Year Wilkinson Microwave Anisotropy Probe (WMAP) Observations: Power Spectra and WMAP-Derived Parameters", Astrophys. J. Suppl. **192**, 16 (2011), arXiv:astro-ph.CO/1001.4635.
- [9] G. Hinshaw *et al.*, "Five-Year Wilkinson Microwave Anisotropy Probe(WMAP) Observations: Data Processing, Sky Maps & Basic Results", Astrophys. J. Suppl. **180**, 225-245 (2009), arXiv:astro-ph/0803.0732.
- [10] A. Borriello, P. Salucci, "The Dark Matter Distribution in Disk Galaxies", Mon. Not. Roy. Astron. Soc. **323**, 285 (2001), arXiv:astro-ph/0001082.
- [11] F. Zwicky, "Spectral displacement of extra galactic nebulae," Helv. Phys. Acta. **6**, 110-127 (1933).
- [12] H. Dahle, "A compilation of weak gravitational lensing studies of clusters of galaxies", arXiv:astro-ph/0701598.
- [13] K. A. Olive, G. Steigman, T. P. Walker, "Primordial Nucleosynthesis: Theory and Observations", Phys. Rept. **333**, 389 (2000), arXiv:astro-ph/9905320.
- [14] M. Tegmark *et al.*, "The 3D power spectrum of galaxies from the SDSS", Astrophys. J. **606**, 702 (2004), arXiv:astro-ph/0310725.

- [15] L. Bergstrom, A. Goobar, "Cosmology and Particle Physics", Chichester (UK), John Wiley & Sons (1999).
- [16] J. F. Navarro, C. S. Frenk and S. D. M. White, "The Structure of Cold Dark Matter Halos", *Astrophys. J.* **462**, 563 (1996), arXiv:astro-ph/9508025.
- [17] B. Moore, T. Quinn, F. Governato, J. Stadel, G. Lake, "Cold collapse and the core catastrophe", *Mon. Not. Roy. Astron. Soc.* **310**, 1147 (1999), arXiv:astro-ph/9903164.
- [18] A. V. Kravtsov, A. A. Klypin, J. S. Bullock, J. R. Primack, "The Cores of Dark Matter Dominated Galaxies: theory vs. observations", *Astrophys. J.* **502**, 48 (1998), arXiv:astro-ph/9708176.
- [19] D. Clowe *et al.*, "A direct empirical proof of the existence of dark matter", *Ap. J. L* **648**, 109 (2006), arXiv:astro-ph/0608407.
- [20] R. Massey *et al.*, "Dark matter maps reveal cosmic scaffolding", *Nature* **445**, 286-290 (2007).
- [21] M. Kamionkowski, "Particle Dark Matter" (1996), arXiv:hep-ph/9609531.
- [22] N. Fornengo, S. Scopel, A. Bottino, "Discussing direct search of dark matter particles in the minimal supersymmetric extension of the standard model with light neutralinos", *Phys. Rev. D* **83**, 015001 (2011), arXiv:hep-ph/1011.4743.
- [23] J. Edsjo, P. Gondolo, "Neutralino Relic Density including Coannihilations", *Phys. Rev. D* **56**, 1879-1894 (1997), hep-ph/970436.
- [24] L. J. Rosenberg, K. A. van Bibber, "Searches for invisible axions", *Phys. Rept.* **325**, 1 (2000).
- [25] G. Servant, T. M. P. Tait, "Is the Lightest Kaluza-Klein Particle a Viable Dark Matter Candidate?", *Nucl. Phys. B* **650**, 391-419 (2003).
- [26] G. Bertone *et al.*, "Identification of Dark Matter particles with LHC and direct detection data", *Phys. Rev. D* **82**, 055008 (2010), arXiv:hep-ph/1005.4280
- [27] M. Goodman and E. Witten, "Detectability of certain dark-matter candidates", *Phys. Rev. D* **31**, 3059 (1985).
- [28] R. Bernabei *et al.* (The DAMA Collaboration), "First results from DAMA/LIBRA and the combined results with DAMA/NaI", *Eur. Phys. J. C* **56**, 333-355 (2008), arXiv:astro-ph/0804.2741.
- [29] R. Bernabei *et al.* (The DAMA Collaboration), "Dark Matter particles in the galactic halo: results and implications from DAMA/NaI", *Int. J. Mod. Phys. D* **13**, 2127-2160 (2004), arXiv:astro-ph/0501412.
- [30] C. Savage *et al.*, "Compatibility of DAMA/LIBRA dark matter detection with other searches", *JCAP* 0904, 010 (2009), arXiv:astro-ph/0808.3607.
- [31] C. E. Aalseth *et al.* (The CoGeNT Collaboration), "Results from a Search for Light-Mass Dark Matter with a P-type Point Contact Germanium Detector", arXiv:astro-ph.CO/1002.4703.

- [32] Z. Ahmed *et al.*, "Dark Matter Search Results from the CDMS II Experiment", *Science* **327**, 1619 (2010).
- [33] E. Aprile *et al.*, "First Dark Matter Results from the XENON100 Experiment", *Phys. Rev. Lett.* **105**, 131302 (2010).
- [34] R. Gaitskell, V. Mandic, Dark Matter Limit Plot Generator:  
<http://dendera.berkeley.edu/plotter/entryform.html>.
- [35] A. A. Abdo *et al.* (The Fermi LAT Collaboration), "Measurement of the Cosmic Ray  $e^+ + e^-$  spectrum from 20 GeV to 1 TeV with the Fermi Large Area Telescope", *Phys. Rev. Lett.* **102**, 181101 (2009), arXiv:astro-ph.HE/0905.0025.
- [36] O. Adriani *et al.* (The PAMELA Collaboration), "Observation of an anomalous positron abundance in the cosmic radiation", *Nature* **458**, 607-609 (2009), arXiv:astro-ph/0810.4995.
- [37] J. Chang *et al.*, "An excess of cosmic ray electrons at energies of 300–800 GeV", *Nature* **456**, 362-365 (2008).
- [38] S. W. Barwick *et al.* (The HEAT Collaboration), "Measurements of the Cosmic-Ray Positron Fraction From 1 to 50 GeV", *Astrophys. J.* **482**, L191 (1997), arXiv:astro-ph/9703192.
- [39] W. de Boer, C. Sander, V. Zhukov, A. V. Gladyshev, D. I. Kazakov, "EGRET Excess of Diffuse Galactic Gamma Rays as Tracer of Dark Matter", *Astron. Astrophys.* **444**, 51 (2005), arXiv:astro-ph/0508617v1.
- [40] F. Aharonian *et al.* (The HESS Collaboration), "Very high energy gamma rays from the direction of Sagittarius A\*", *Astron. Astrophys.* **425**, L13-L17 (2004), arXiv:astro-ph/0408145.
- [41] J. Albert *et al.* (The MAGIC Collaboration), "Observation of Gamma Rays from the Galactic Center with the MAGIC Telescope", *Astrophys. J.* **638**, L101 (2006), arXiv:astro-ph/0512469.
- [42] H. Motz, "Indirect Search for Dark Matter with the ANTARES Neutrino Telescope", *Proceedings of 7th International Heidelberg Conference*, Hackensack NJ, 504 (2009).
- [43] D. Hubert (for the IceCube Collaboration), "Neutralino Dark Matter Searches with Neutrino Telescopes: AMANDA Results and IceCube Prospects", *Nuclear Physics B (Proceedings Supplements)* **173**, 87-90, (2007).
- [44] S. Desai *et al.* (The Super-Kamiokande Collaboration), "Search for Dark Matter WIMPs using Upward Through-going Muons in Super-Kamiokande", *Phys. Rev. D* **70**, 083523 (2004), arXiv:hep-ex/0404025.
- [45] A. W. Strong, I. V. Moskalenko, O. Reimer, "Diffuse continuum gamma rays from the Galaxy", *Astrophys. J.* **537**, 763-784 (2000), arXiv:astro-ph/9811296.
- [46] A. W. Strong, I. V. Moskalenko and O. Reimer, "Diffuse Galactic continuum gamma rays. A model compatible with EGRET data and cosmic-ray measurements", *Astrophys. J.* **613**, 962 (2004).
- [47] I. V. Moskalenko, A. W. Strong, "Production and Propagation of Cosmic-Ray Positrons and Electrons", *Astrophys. J.* **493**, 694 (1998), arXiv:astro-ph/9710124.

- [48] D. Hooper, A. Stebbins, K. M. Zurek, "The PAMELA and ATIC Excesses From a Nearby Clump of Neutralino Dark Matter", *Phys. Rev. D* **79**, 103513 (2009), arXiv:hep-ph/0812.3202.
- [49] O. Adriani *et al.* (The PAMELA Collaboration), "A new measurement of the antiproton-to-proton flux ratio up to 100 GeV in the cosmic radiation", *Phys. Rev. Lett.* **102**, 051101 (2009), arXiv:astro-ph/0810.4994.
- [50] P. Meade, M. Papucci, A. Strumia, T. Volansky, "Dark Matter Interpretations of the Electron/Positron Excesses after FERMI", *Nucl. Phys. B* **831**, 178 (2010), arXiv:hep-ph/0905.0480.
- [51] M. Cirelli, M. Kadastik, M. Raidal, and A. Strumia, "Model-independent implications of the  $e^+$ ,  $e^-$ , anti-proton cosmic ray spectra on properties of Dark Matter", *Nucl. Phys. B* **813**, 1 (2009), arXiv:hep-ph/0809.2409.
- [52] H. C. Cheng, , J. L. Feng, K. T. Matchev, "Kaluza-Klein dark matter", *Phys. Rev. Lett.* **89**, 211301 (2002).
- [53] H. Yuksel, M. D. Kistler, T. Stanev, "TeV Gamma Rays from Geminga and the Origin of the GeV Positron Excess", *Phys. Rev. Lett.* **103**, 051101 (2009), arXiv:astro-ph/0810.2784.
- [54] W. Pauli, "The letter to the Physical Society of Tubingen" reproduced in *Neutrino Physics* by K. Winter (editor), Cambridge University Press (1991).
- [55] E. Fermi, "An attempt of a theory of beta radiation", *Z. Physik* **88**, 161-177 (1934).
- [56] K. Nakamura *et al.* (The Particle Data Group), "Review of Particle Physics", *J. Phys. G* **37**, 075021 (2010).
- [57] A. Achterberg *et al.*, "Detection of Atmospheric Muon Neutrinos with the IceCube 9-String Detector" , *Phys. Rev. D* **76**, 027101 (2007).
- [58] L.-L. Chau, W.-Y. Keung, "Comments on the Parametrization of the Kobayashi-Maskawa Matrix", *Phys. Rev. Lett.* **53**, 1802 (1984).
- [59] C. Giunti, C. W Kim, "Fundamentals of Neutrino Physics and Astrophysics", Oxford University Press, USA (2007).
- [60] P. Przewłocki, "A study of neutrino interactions constituting the background to electron neutrino appearance in T2K experiment", Ph.D. thesis, The Andrzej Soltan Institute for Nuclear Studies, Otwock-Swierk, (2010), <http://neutrino.fuw.edu.pl/system/files/plik/2010/pp-phd-final-corrected240310.pdf>.
- [61] G. P. Zeller, "Low energy neutrino cross sections from K2K, MiniBooNE, SciBooNE, and MINER $\nu$ A", *J. of Phys.: Conference Series* **136**, 022028 (2008).
- [62] D. Casper, "The Nuance Neutrino Simulation, and the Future", *Nucl. Phys. Proc. Suppl.* **112**, 161 (2002).
- [63] Q. R. Ahmad *et al.* (The SNO Collaboration) "Measurement of Day and Night Neutrino Energy Spectra at SNO and Constraints on Neutrino Mixing Parameter", *Phys. Rev. Lett.* **89**, 011302 (2002).

- [64] J. Hosaka *et al.* (The Super-Kamiokande Collaboration), "Solar neutrino measurements in Super-Kamiokande-I", Phys. Rev. D **73**, 112001 (2006), arXiv:hep-ex/0508053.
- [65] Y. Fukuda *et al.* (The Super-Kamiokande Collaboration), "Evidence for oscillation of atmospheric neutrinos", Phys. Rev. Lett. **81**, 1562-1567 (1998), arXiv:hep-ex/9807003.
- [66] S. Abe *et al.* (The KamLAND Collaboration), "Precision Measurement of Neutrino Oscillation Parameters with KamLAND", Phys. Rev. Lett. **100**, 221803 (2008), 0801.4589
- [67] N. Agafonova *et al.*, "Observation of a first  $\nu_\tau$  candidate in the OPERA experiment in the CNGS beam", Phys. Lett. B **691**, 138-145, (2010).
- [68] B. Pontecorvo, "Mesonium and anti-mesonium", Sov. Phys. JETP **6**, 429, (1957).
- [69] Z. Maki, M. Nakagawa, and S. Sakata, "Remarks on the Unified Model of Elementary Particles", Prog. Theor. Phys. **28**, 870-880 (1962).
- [70] M. Bilenky and B. Pontecorvo, "The lepton-quark analogy and muonic charge", Sov. J. Nucl. Phys., **24**, 316319 (1976).
- [71] D. H. Perkins, "High Energy Physics", Cambridge University Press (2000).
- [72] T. Schwetz, M. Tortola, J. Valle, "Three-flavor neutrino oscillation update", New J. Phys. **10**, 113011 (2008), arXiv:hep-ph/0808.2016.
- [73] P. Lipari, "Neutrinos, a Different Way to Look at the Sky", Acta Phys. Polon. B **37**, 2411-2418 (2006).
- [74] J. N. Bahcall, M. H. Pinsonneault, S. Basu, "Solar Models: current epoch and time dependences, neutrinos, and helioseismological properties", Astrophys. J. **555**, 990-1012 (2001), arXiv:astro-ph/0010346.
- [75] B.T. Cleveland *et al.*, "Measurement of the solar electron neutrino flux with the Homestake chlorine detector", Astrophysical Journal **496**, 505-526 (1998).
- [76] T. Araki *et al.*, "Experimental investigation of geologically produced antineutrinos with KamLAND", Nature **436**, 499-503 (2005).
- [77] G. Bellini *et al.* (The Borexino Collaboration), "Observation of Geo-Neutrinos", Phys. Lett. B **687**, 299-304 (2010), arXiv:hep-ex/1003.0284.
- [78] P. Adamson *et al.* (The MINOS Collaboration), "Measurement of Neutrino Oscillations with the MINOS Detectors in the NuMI Beam", Phys. Rev. Lett. **101**, 131802 (2008), arXiv:hep-ex/0806.2237.
- [79] S. H. Ahn *et al.* (The K2K collaboration), "Measurement of Neutrino Oscillation by the K2K Experiment", Phys. Rev. D **74**, 072003 (2006).
- [80] K. S. Hirata *et al.*, "Observation of a neutrino burst from the supernova SN1987a", Phys. Rev. Lett. **58**, 1490 (1987).
- [81] D. Lynden-Bell, "Galactic Nuclei as Collapsed Old Quasars", Nature **223**, 690694, (1969).
- [82] M. Ziembicki *et al.*, "The SMRD subdetector at the T2K near detector station", Acta Phys. Polon. B **41**, 1579-1584 (2010).

- [83] M. Honda, T. Kajita, K. Kasahara, and S. Midorikawa, "A New calculation of the atmospheric neutrino flux in a 3-dimensional scheme", Phys. Rev. D **70**, 043008 (2004), arXiv:astro-ph/0404457.
- [84] G. D. Barr, T. K. Gaisser, P. Lipari, S. Robbins, T. Stanev, "A three-dimensional calculation of atmospheric neutrinos", Phys. Rev. D **70**, 023006 (2004), arXiv:astro-ph/0403630.
- [85] G. Battistoni, A. Ferrari, T. Montaruli, and P.R. Sala, "High energy extension of the FLUKA atmospheric neutrino flux", arXiv:hep-ph/0305208.
- [86] L. Pasquali, M.H. Reno, "Tau neutrino fluxes from atmospheric charm", Phys. Rev. D **59**, 093003 (1999).
- [87] A. D. Martin, M. G. Ryskin, A. M. Stasto, "Prompt neutrinos from atmospheric  $c\bar{c}$  and  $b\bar{b}$  production and the gluon at very small  $x$ ", Acta Phys. Polon. B **34**, 3273-3304 (2003), arXiv:hep-ph/0302140.
- [88] M. R. Buckley *et al.*, "High-Energy Neutrino Signatures of Dark Matter Decaying into Leptons", Phys. Rev. D **81**, 016006 (2010), arXiv:astro-ph.HE/0907.2385v2.
- [89] B. Feldstein, A.L. Fitzpatrick, "Discovering Asymmetric Dark Matter with Anti-Neutrinos", arXiv:hep-ph/1003.5662.
- [90] H. Yuksel, S. Horiuchi, J.F. Beacom, S. Ando, "Neutrino Constraints on the Dark Matter Total Annihilation Cross Section", Phys. Rev. D **76**, 123506 (2007), arXiv:astro-ph/0707.0196.
- [91] J. Ahrens *et al.* (The AMANDA Collaboration), "Limits to the muon flux from WIMP annihilation in the center of the Earth with the AMANDA detector", Phys. Rev. D **66**, 032006 (2002).
- [92] T. Tanaka, Ph.D. thesis, Nagoya University (2011).
- [93] M. Ambrosio *et al.* (The MACRO Collaboration), "Limits on dark matter WIMPs using upward-going muons in the MACRO detector", Phys. Rev. D **60**, 082002 (1999).
- [94] M. Mori *et al.* (The Kamiokande Collaboration), "Search for neutralino dark matter heavier than the W boson at Kamiokande", Phys. Rev. D **48**, 5505 (1993).
- [95] S. Desai, "High energy neutrinos astrophysics with Super-Kamiokande", Ph.D. thesis, Boston University (2004).
- [96] M. M. Boliev *et al.* (The Baksan Collaboration), Proceedings of 24th International Cosmic Ray Conference in Rome **1**, 722 (1995).
- [97] M. Kamionkowski, K. Griest, G. Jungman, B. Sadoulet, "Model-Independent Comparison of Direct versus Indirect Detection of Supersymmetric Dark Matter", Phys. Rev. Lett. **74**, 5174-5177 (1995).
- [98] R. Bernabei *et al.* (The DAMA Collaboration), "Search for WIMP annual modulation signature: Results from DAMA / NaI-3 and DAMA / NaI-4 and the global combined analysis", Phys. Lett. B. **480**, 23 (2000).

- [99] D. S. Akerib *et al.* (The CDMS Collaboration), "First Results from the Cryogenic Dark Matter Search in the Soudan Underground Lab", Phys. Rev. Lett. **93**, 211301(2004), arXiv:astro-ph/0405033.
- [100] A. Benoit *et al.* (The EDELWEISS collaboration), "Improved Exclusion Limits from the EDELWEISS WIMP Search", Phys. Lett. B. **545**, 43 (2002).
- [101] D. Cline *et al.*, "ZEPLIN II liquid xenon dark matter detector", Proceedings of 4th International Workshop on the Identification of Dark Matter, edited by N. J. C. Spooner and V. Kudryavtsev (2003).
- [102] D. L. Anderson, "Theory of the Earth", Blackwell Scientific Publications, Boston (1989).
- [103] L. Bergstrom, P. Ullio, J. H. Buckley, "Observability of  $\gamma$  Rays from Dark Matter Neutralino Annihilations in the Milky Way Halo", Astropart. Phys. **9**, 137 (1998), arXiv:astro-ph/9712318.
- [104] J. Ahrens *et al.* (The AMANDA Collaboration), "Observation of High Energy Atmospheric Neutrinos with the Antarctic Muon and Neutrino Detector Array", Phys. Rev. D **66**, 012005 (2002), arXiv:astro-ph/0205109.
- [105] K. Daum *et al.* (The Frejus Collaboration), "Determination of the atmospheric neutrino spectra with the Frejus detector", Z. Phys. C **66**, 417-428 (1995).
- [106] R. Brun and F. Rademakers, "ROOT: An object oriented data analysis framework", Nucl. Instrum. Meth. A **389**, 8186 (1997).
- [107] Y. Hayato, "NEUT", Nucl. Phys. Proc. Suppl. **112**, 1711-176 (2002).
- [108] R. Brun and F. Carminati, "GEANT - Detector Description and Simulation Tool CERN Program", CERN Programming Library Long Writeup W5013 (1993).
- [109] F. Dufour, "Precise Study of the Atmospheric Neutrino Oscillation Pattern Using Super-Kamiokande I and II", Ph.D. thesis, Boston University (2009).
- [110] R. Wendell *et al.* (The Super-Kamiokande Collaboration), "Atmospheric neutrino oscillation analysis with sub-leading effects in Super-Kamiokande I, II, and III", Phys. Rev. D **81**, 092004 (2010), arXiv:hep-ex/1002.3471v2.
- [111] G. L. Fogli, E. Lisi, A. Marrone, A. Palazzo, A. M. Rotunno, "Hints of  $\theta_{13} > 0$  from global neutrino data analysis", Phys. Rev. Lett. **101**, 141801 (2008), arxiv:hep-ph/0806.2649.
- [112] R. Wendell, "Super Kamiokande", presentation given at the 11th International Workshop on Next Generation Nucleon Decay and Neutrino Detectors, Toyama, Japan (2010), <http://www-sk.icrr.u-tokyo.ac.jp/NNN10/slides/14am-Wendell.pdf>.
- [113] K. Abe *et al.* (The Super-Kamiokande Collaboration), "A Measurement of Atmospheric Neutrino Flux Consistent with Tau Neutrino Appearance", Phys. Rev. Lett. **97**, 171801 (2006), arXiv:hep-ex/0607059v2.
- [114] S. Jadach, Z. Was, R. Decker, J.H. Kuhn, "The  $\tau$  decay library TAUOLA, version 2.4", Comput. Phys. Commun. **76**, 361 (1993).
- [115] R.M. Barnett *et al.* (The Particle Data Group), "Review of Particle Physics", Physical Review D **54**, 1 (1996).

- [116] A. Arvanitaki *et al.*, "Astrophysical Probes of Unification", Phys. Rev. D **79**, 105022 (2009), arXiv:hep-ph/0812.2075.
- [117] M. Kaplinghat, L. Knox, M.S. Turner, "Annihilating Cold Dark Matter", Phys. Rev. Lett. **85**, 3335 (2000).
- [118] J. F. Beacom, N. F. Bell, G. D. Mack, "Upper Bound on the Dark Matter Total Annihilation Cross Section", Phys. Rev. Lett. **99**, 231301 (2007), arXiv:astro-ph/0608090v2.
- [119] K. Griest and M. Kamionkowski, "Unitarity limits on the mass and radius of dark-matter particles", Phys. Rev. Lett. **64**, 615 (1990).
- [120] L. Hui, "Unitarity Bounds and the Cuspy Halo Problem", Phys. Rev. Lett. **86**, 3467 (2001).
- [121] V. Boccone *et al.* (The ArDM Collaboration), "Development of wavelength shifter coated reflectors for the ArDM argon dark matter detector", J. of Inst. **4**, P06001 (2009), arXiv:0904.0246.
- [122] A. Marchionni *et al.* (The ArDM Collaboration), "ArDM: a ton-scale LAr detector for direct Dark Matter searches", Proceedings of 1st International Workshop towards the Giant Liquid Argon Charge Imaging Experiment (2010), arXiv:1012.5967.
- [123] P. Mijakowski, "The search of dark matter with ArDM detector", Acta Phys. Pol. B **37**, 2179-2185 (2006), <http://th-www.if.uj.edu.pl/acta/vol37/pdf/v37p2179.pdf>.
- [124] A. Hitachi *et al.*, "Effect of ionization density on the time dependence of luminescence from liquid argon and xenon", Phys. Rev. B **27**, 52795285 (1983).
- [125] P. Benettii *et al.* (The WARP Collaboration), "Measurement of the specific activity of  $^{39}\text{Ar}$  in natural argon", Nucl. Instrum. Meth. A **574**, 83-88 (2007), arXiv:astro-ph/0603131v2.
- [126] R. Brunetti *et al.* (The WARP Collaboration), "Experiment Proposal" (2004), <http://warp.pv.infn.it/>.
- [127] M. J. Carson *et al.*, "Neutron background in large-scale xenon detectors for dark matter searches", Astropart. Phys. **21**, 667 (2004).
- [128] J.M. Carmona *et al.*, "Neutron background at the Canfranc Underground Laboratory and its contribution to the IGEX-DM dark matter experiment", Astropart. Phys. **21**, 523-533 (2004).
- [129] L. Kaufman, "Detector Performance and Background Studies for the ArDM Experiment", Ph.D. thesis, ETH Zurich (2008).
- [130] S. Agostinelli *et al.* (The Geant4 Collaboration), "GEANT4: A simulation toolkit", Nucl. Instrum. Meth. A **506**, 250303 (2003), <http://geant4.web.cern.ch/geant4/>.
- [131] M. del Carmen Carmona-Benitez, "Direct Dark Matter Searches with Noble Liquid Detectors: The ArDM Experiment", Ph.D. thesis, Universidad de Granada (2009).
- [132] V. A. Kudryavtsev, N. J. C Spooner, J. E McMillan, "Simulations of muon-induced neutron flux at large depths underground", Nucl. Instrum. Meth. A **505**, 688-698 (2003), arXiv:hep-ex/0303007.

- [133] A. Fasso, A. Ferrari, P. R. Sala. "FLUKA: Status and Prospective for Hadronic Applications", Proceedings of the MonteCarlo 2000 Conference, Lisbon (2000).
- [134] Y-F. Wang, V. Balic, G. Gratta, "Predicting Neutron Production from Cosmic-ray Muons", Phys. Rev. D **64** 013012 (2001), arXiv:hep-ex/0101049.